Flipping the Narrative: ATP10A's Multifaceted Influence on Lipid Metabolism, Endothelial Function, and Fertility.

By

Adriana Norris

Dissertation

Submitted to the Faculty of the

Graduate School of Vanderbilt University

in partial fulfillment of the requirements

For the degree of

DOCTOR OF PHILOSOPHY

in

Biological Sciences

May 10, 2024

Nashville, Tennessee

Approved:

Antonis Rokas, Ph.D. (chair)

John Stafford, MD, Ph.D.

Richard O' Brien, Ph.D.

Maulik Patel, Ph.D.

ACKNOWLEDGEMENTS

I extend my heartfelt gratitude to the Graham Lab, particularly to Dr. Todd Graham, for his exceptional mentorship and guidance throughout this journey. Special thanks to Dr. Eugenia Yazlovitskya for her support during moments of doubt, to Alex Mansueto for being my fellow mouseketeer, to Mariana Jimenez for her attentive ear and encouragement, and to Bhawik Jain for being an excellent conference buddy.

I express my appreciation to past lab members Dr. Swapneeta Date, Davia Watkins, and Dr. Jordan Best, as well as to Dr. Bart Roland, for his great mentorship and for welcoming me to the Graham lab and encouraging me to join. A sincere thank you to Dr. John Stafford and his lab members for sharing their expertise, lab space, and resources, crucial for the successful execution of our mouse work. Gratitude also extends to the entire team at Vanderbilt University and Vanderbilt University Medical Center cores, including veterinarians and animal technicians, for their availability, willingness to answer questions as well as provide resources.

My deepest thanks to my parents, Angela and Kenneth Norris, for their unwavering support, encouragement, and for instilling patience and perseverance in me. A special acknowledgment to my mom, Angela, the first Black woman to graduate from the Coast Guard Academy, a true role model in breaking barriers and never giving up. Thanks to my sisters, Brittany and Michelle Norris, for being my role models, for always making me laugh, and for encouraging me to travel and see the world!

I am grateful to friends both at Vanderbilt and beyond, for bringing laughter and joy during challenging times. Lastly, immense gratitude to my best friend and husband, Ryan Mims, for his constant encouragement and laughter. Special mentions to my cat, Squeak, and dog, Boscoe, for their adorable and silly companionship.

Table of Contents

List of Tables

List of Figures

Chapter I: Introduction

Biological Membranes

Biological membranes are lipid bilayers that serve as barriers; separating the interior of the cell and organelles from the external environment and cytosol, respectively. This division creates distinct biological niches that underlie the diverse functions of tissues, cells, and organelles, making membranes an essential component of all living cells [1]. The composition of these membranes plays a crucial role in their functionality, with approximately half of their mass being comprised of proteins and the other half of lipids [2]. The effects of this protein-lipid interaction are bidirectional, influencing the function, positioning within the membrane, and physical properties of both the proteins and lipids [3, 4]. The composition of membranes is essential for various cellular processes, such as vesicle transport, the establishment and dissipation of ion gradients, and responses to stimuli, including the formation of signaling platforms.

The model of biological membranes being lipid bilayers was first proposed by Gorter and Grendel in 1925 [5]. Years later, Mark S. Bretscher expanded on the discovery of membranes being lipid bilayers and proposed the idea of membrane asymmetry by labeling phosphatidylethanolamine (PE) in the membranes of erythrocytes and ghosts with a non-permeant reagent [6]. In 1972, Bretscher proposed that there was an asymmetrical distribution of several lipids within the membrane; where phosphatidylcholine (PC) and sphingomyelin (SM) are located mostly in the outer leaflet and phosphatidylserine (PS) and PE in the inner leaflet [7]. Treatment of erythrocytes with various phospholipases [8] and non-penetrating probes [9] supported this idea of an asymmetric distribution of SM, PC, PS, and PE in the bilayer. Two years later, in 1974, Sheetz and Singer proposed the bilayer couple hypothesis that suggested a structural and functional interdependence of the two leaflets in biological membranes [10]. By treating erythrocytes with different amphipathic molecules that intercalate within different sides of the membrane; they showed that “two halves [of a biological

membrane] can respond differently to a perturbation while remaining coupled together." Their discoveries elaborated on the idea of lipid asymmetry in the membrane; now demonstrating a functional asymmetry. Despite these discoveries, how lipid asymmetry was set within a membrane was still unknown. The occurrence of spontaneous lipid flip-flop has been demonstrated, but it operates on the order of hours to days [11-15], rendering it too slow to hold biological significance. Therefore, an input of energy is necessary to facilitate this process. Indeed, Seigneuret and Devaux, showed that that spin-labeled analogs of PS and PE underwent rapid transverse diffusion in erythrocytes, resulting in cell morphology changes, and this process was inhibited by ATP depletion. They proposed that "an ATP-driven transport of amino phospholipids toward the inner leaflet could be the major cause of the phospholipid asymmetry in the erythrocyte membrane" and that this process was carried out by an "energy-driven aminophospholipid translocase (APLT)" [13, 16]

The search for flippases

In 1988, Moriyama and Nelson purified a 115 kD protein with vanadate-sensitive ATPase activity, from chromaffin granule membranes, named "ATPase II" [17]. One year later, Zachowski, Henry, and Devaux demonstrated a flippase activity in chromaffin granules and proposed it was catalyzed by ATPase II [18]. They reported that "This is the first evidence for an ATP-dependent specific phospholipid 'flippase' in intracellular organelles." The 'APLT' from human erythrocytes [16, 19] was later partially purified [20] and reconstituted into proteoliposomes and exhibited PS-specific translocase activity [21]. In 1993, *Drs2,* a budding yeast ortholog of the 'APLT', was identified in a screen aimed at discovering mutants defective in assembly or function of ribosomes and was initially thought to be a calcium ATPase [22]. Several years later, ATPase II (now known as ATP8A1), from bovine chromaffin granules, was cloned and found to be 50% identical to *Drs2* [23]; however, the experiments they did to show Drs2/ATPase II was a flippase couldn't be reproduced and there was quite a bit of controversy as to whether these proteins were flippases or not. However, subsequently, years of research from the Graham lab and others using *Saccharomyces cerevisiae*, *Arabidopsis*

thaliana, as well as cell culture and mouse models provided evidence that supported a direct role for these flippases in phospholipid translocation [24-29]. These findings expanded the known function of proteins in the primordial P-type ATPase family of ATP-fueled pumps, that were previously only thought to transport ions [30]. In 1998, Axelson and Palmgren performed a phylogenetic analysis on this family of proteins and categorized these newly discovered eukaryotic aminophospholipid flipping pumps as type IV P-type ATPases (P4-ATPases) [31]. Importantly, the maintenance of membrane asymmetry is orchestrated not only by flippases, but also by floppases and scramblases (Figure 1). Floppases facilitate the outward transport of lipids [32] and scramblases enable bidirectional lipid transport, operating independently of an input of energy [33]. The focus of this thesis will be on flippases, which regulate the ATP-mediated inward movement of lipids from the outer leaflet to the cytosolic leaflet.

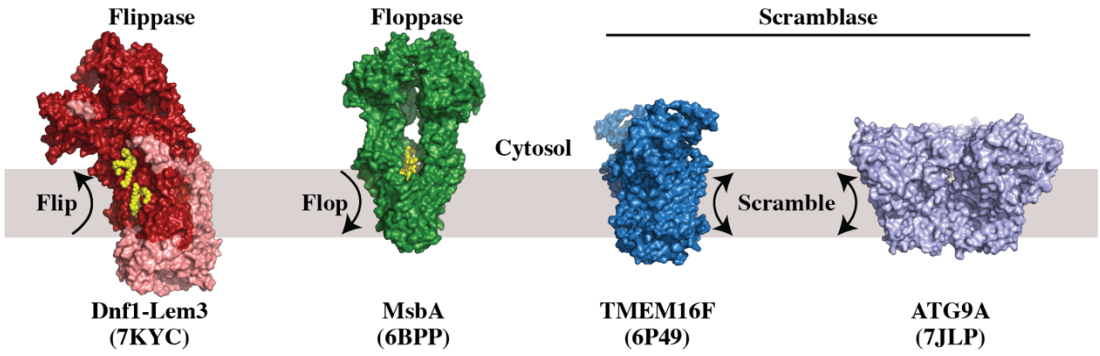

Figure 1. Membrane asymmetry is controlled by flippases, floppases and scramblases. A few examples of lipid transporter structures with Protein Data Bank Identifiers. Substrate lipid is shown in yellow for Dnf1-Lem3 and MsbA. Schematic created by Dr. Todd R Graham.

Flippases in the Cell: Structure and Function

The structure and function of flippases has been extensively reviewed elsewhere [34-36, schematic of phylogenetic relationships can be found in ref 34]. Briefly, P4-ATPases adopt a four-domain structure similar to other ATPases. These domains include nucleotide-binding (N), phosphorylation (P), actuator (A), and membrane (M) domains. P4-ATPases undergo E1 to E2 conformational transitions during ATP hydrolysis, driving conformational changes in the substrate-binding membrane domain. The catalytic subunit of P4-ATPases forms a heterodimer with a Cdc50

beta subunit, resembling Na+/K+-ATPase subunits. The beta subunit acts as a chaperone for ER exit and influences lipid translocation. Additionally, flippases are essential components of the plasma membrane, Golgi, and endosomal system. These enzymes have roles in membrane remodeling, vesicular transport, membrane biogenesis, sorting and localization of proteins in the secretory and endocytic pathway, cytoskeletal dynamics, cell division, lipid metabolism and lipid signaling. At the organismal level, the significance of these flippases is underscored by the adverse health consequences resulting from mutations and deficiencies in these lipid transport proteins [37, 38] (Figure 2).

Dyslipidemia

Dyslipidemia is a medical condition characterized by an abnormal level of lipids (fats) in the blood, including elevated levels of free fatty acids and triglycerides [39]. Maintaining homeostasis of these lipids is essential for normal physiological functioning, as they serve as critical energy sources and contribute to cellular structure. The regulation of lipid levels in the body is a complex process involving intricate metabolic pathways, hormonal signals, and genetic factors.

Free fatty acids (FFA) are primarily derived from the breakdown of triglycerides (TGs), which are stored in adipose tissue. Hormones such as insulin and glucagon, along with other factors, tightly control the release and utilization of FFAs. Dyslipidemia can arise when this balance is disrupted, often associated with conditions such as obesity and diabetes. Obesity, characterized by excessive accumulation of adipose tissue, is a major contributor to dyslipidemia. Enlarged adipocytes release increased amounts of FFAs into the bloodstream, leading to elevated lipid levels [40]. In diabetes, insulin resistance further complicates lipid metabolism, impairing the ability of insulin to regulate FFA release and storage [41].

The consequences of dyslipidemia are significant and extend beyond altered blood lipid profiles. High levels of circulating lipids, particularly low-density lipoprotein cholesterol (LDL-C) and triglycerides, contribute to the development of atherosclerosis—a condition characterized by the buildup of fatty plaques in arterial walls. Atherosclerosis is a major risk factor for cardiovascular diseases, including

coronary artery disease, heart attacks, and strokes. Understanding the mechanisms underlying dyslipidemia is crucial for developing effective interventions and preventive strategies.

Insulin signaling

The insulin signaling pathway plays a pivotal role in regulating glucose and lipid metabolism, cell growth, and overall energy homeostasis [42]. The insulin signaling pathway begins when insulin binds to the insulin receptor (INSR) on cell membranes and this binding activates the receptor's intrinsic tyrosine kinase activity and tyrosine residues on the insulin receptor and insulin receptor substrate (IRS) proteins become phosphorylated. Phosphorylated IRS proteins activate phosphoinositide 3-kinase (PI3K) and subsequently Akt, which promotes glucose uptake by cells, primarily muscle and adipose, through the translocation of glucose transporter proteins, primarily GLUT4, to the cell membrane. Akt also stimulates glycogen synthesis and promotes protein synthesis by inhibiting glycogen synthase kinase 3 beta (GSK3β) and activating the mammalian target of rapamycin (mTOR), respectively. Insulin inhibits lipolysis, which reduces the release of fatty acids from adipose tissue. In endothelial cells, insulin promotes the release of nitric oxide (NO) which leads to vasodilation [43]. These orchestrated responses ensure that glucose and lipid levels are within a tightly regulated range, preventing hyperglycemia and excessive lipolysis. Dysregulation of the insulin signaling pathway is associated with conditions like insulin resistance, type 2 diabetes, and metabolic syndrome.

Endothelial cells and Cholesterol Metabolism

Cholesterol homeostasis is a tightly regulated process in the body, involving synthesis, uptake, and efflux of cholesterol to maintain optimal cellular and systemic cholesterol levels [44]. A key organ involved in this process is the liver, where cholesterol synthesis and conversion to bile acids occur. Additionally, endothelial cells, lining the inner surface of blood vessels, play a crucial role in vascular

function and health and their functions are intertwined with cholesterol homeostasis in several ways. Dysfunction in endothelial cells, often associated with high cholesterol levels, can lead to inflammation and contribute to the development of atherosclerosis. Additionally, endothelial cells are involved in the transport of lipoproteins, including LDL and HDL, across blood vessel walls and disruptions in cholesterol homeostasis can impact this transport. Taken together, cholesterol homeostasis is vital for maintaining cellular and vascular health. Dysregulation can lead to endothelial dysfunction and contribute to cardiovascular diseases, emphasizing the importance of balanced cholesterol metabolism for overall well-being. Interestingly, there is evidence for a role for flippases in cholesterol metabolism as well as other important metabolic processes and this is described in the next section.

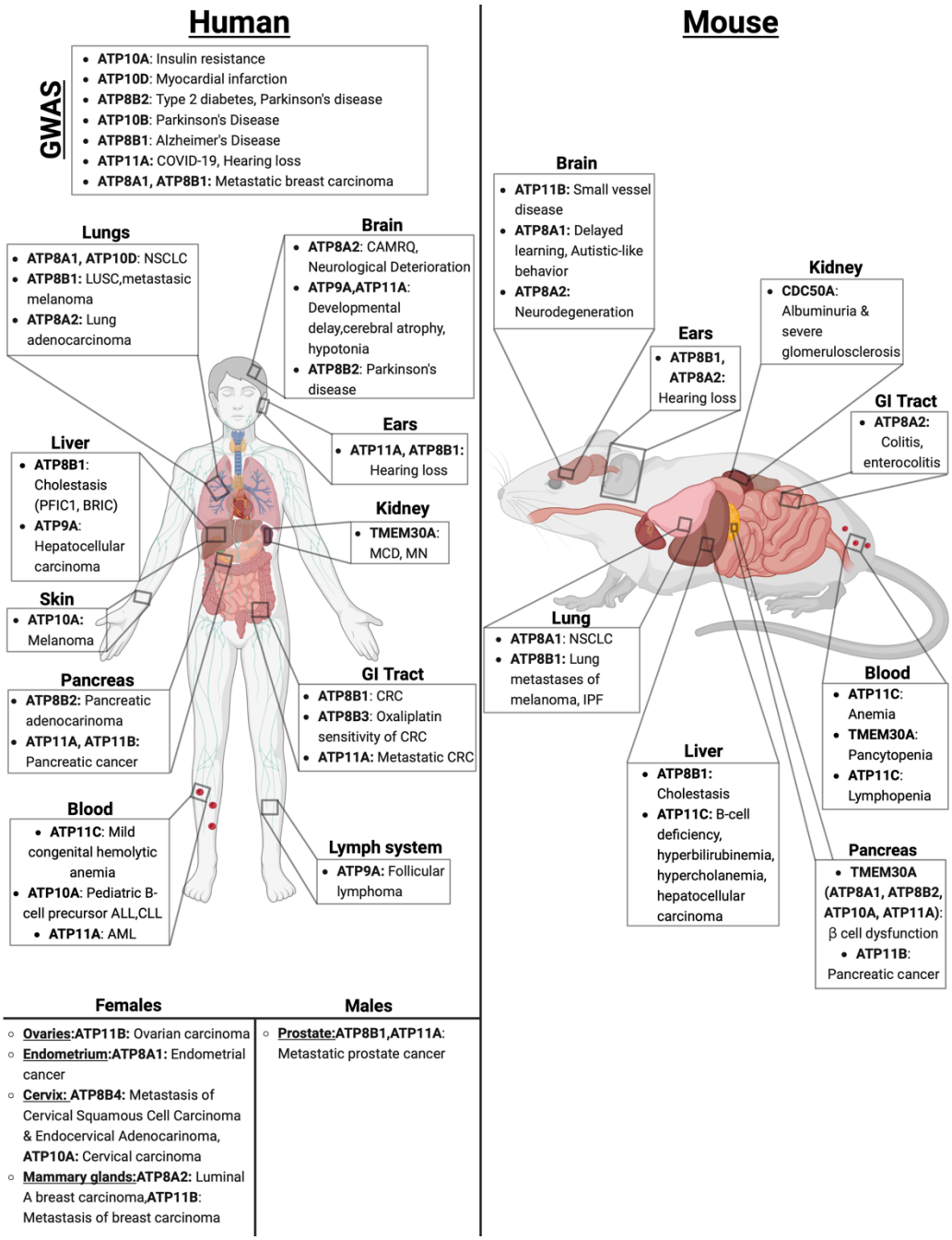

Figure 2. Involvement of P4-ATPases in human and mouse pathologies. The contribution of P4-ATPases to various pathologies in humans and mice is well established and can affect several locations in the body; including the lungs, brain, liver, skin, kidney, pancreas, GI tract,ears, blood and lymph, as well as female and male reproductive organs. Schematic created using Biorender.com. NSCLC= Non-small cell lung cancer, LUSC= lung squamous cell carcinoma, PFIC1= progressive familial intrahepatic cholestasis type 1, BRIC1= benign recurrent intrahepatic cholestasis type 1, MCD= minimal change disease, MN=Membranous nephropathy, CRC= Colorectal cancer, ALL=Acute lymphocytic leukemia, CLL= Chronic lymphocytic leukemia, AML=acute myeloid leukemia, IPF= Idiopathic pulmonary fibrosis, CAMRQ=Cerebellar ataxia, impaired intellectual development, and disequilibrium syndrome.

Role of flippases in cholesterol homeostasis

The action of the flippase, ATP8B1, a broad-specificity lipid transporter [45-47], has been reported to be important in bile acid homeostasis in humans. Mutations in the *ATP8B1* gene lead to impaired bile flow, also known as cholestasis, which can result in extensive liver damage. Two forms of inherited cholestasis, benign recurrent intrahepatic cholestasis type 1 (BRIC1) and progressive familial intrahepatic cholestasis type 1 (PFIC1) were previously mapped to 18q21 and haplotype analysis was then used to identify the mutated gene as FIC1 (familial intrahepatic cholestasis 1), also known as ATP8B1 [48]. Moreover, *Atp8b1*-deficient mice display an increase in the biliary extraction of cholesterol from the canalicular (apical) membrane of hepatocytes, affecting the activity of the bile salt transporter, ABCB11, and resulting in cholestasis [48]. The etiology of ATP8B1-associated cholestasis has been extensively covered elsewhere [38, 49].

The structure of ATP8B1 was recently solved, allowing for the structural implications of disease-causing mutations in this flippase to be further analyzed [50]. The authors mapped mutations found in PFIC1 and BRIC1 on the structure of ATP8B1 and found that the mutations are homoegenously distributed along the protein sequence. They found two mutations, D445N and H535L, in the nucleotide binding pocket that could potentially alter ATP binding. Additionally, the D445 residue is at an interacting distance with the autoinhibitory C-terminus so its alteration could potentially affect the autoregulation of ATP8B1. They also found several mutations in the P-domain that would abolish autophosphorylation of the catalytic aspartate (D454) and result in an inactive flippase; these mutations include S453Y, D454G, and T546M. PFIC1 patients exhibit an S403Y mutation that is located in the PISL motif that is conserved in all P4-ATPases. Mutation at this residue could potentially diminish ATPase activity and substrate affinity. Interestingly, they found that phosphoinositides, specifically $PI(3,4,5)P_3$ stimulate the activity of ATP8B1 with no C-terminus. $PI(3,4,5)P_3$ is created by the enzyme, phosphoinositide 3-kinase (PI3K) and this enzyme has been shown to be activated by several different bile acids [51, 52].This observation in conjunction with the structural data that shows that $PI(3,4,5)P_3$ stimulates the activity of ATP8B1, could be evidence for a novel mechanism for bile acid homeostasis,

whereby bile acids regulate their own movement from the hepatocyte into the canalicular space. This loop would be characterized by bile acids in the hepatocyte activating PI3K, which creates $PI(3,4,5)P_3$,which then activates ATP8B1, which in turn regulates ABCB11, the major bile acid transporter responsible for moving bile salts from the hepatocyte to the canalicular space. This hypothesis will need to be further explored.

There is also evidence for ATP11C, a flippase that translocates PS, having a role in bile acid homeostasis. *ATP11C* deficiency in mice causes hyperbilirubinemia and hypercholanemia [53]. These pathologies could arise in *ATP11C* deficient mice because ATP11C mediates the transport of bile acids and organic anions across the sinusoidal membrane [54] and is essential for basolateral membrane localization of multiple bile salt transport proteins in hepatocytes [55].

Clearly, mutations and deficiencies in several flippases result in changes to cholesterol and bile acid homeostasis in humans and mice. Studies in yeast have also revealed roles for flippases in cellular sterol homeostasis. A yeast mutant of three flippases and their corresponding beta subunit, Dnf1-Lem3, Dnf2-Lem3. Dnf3-Crf1 and a membrane protein, Sfk1, resulted in cells that could not maintain ergosterol in the plasma membrane and instead accumulated the sterol in lipid droplets [56]. The authors concluded that Dnf1, 2, and 3 work cooperatively with Sfk1 to maintain phospholipid asymmetry in the plasma membrane and this preserves the membrane's ability to retain sterols at high concentrations. Altogether, flippase maintenance of phospholipid asymmetry has a role in whole-body and cellular sterol homeostasis.

Role of flippases in glucose homeostasis

As previously mentioned, P4-ATPases are heterodimers that require a noncatalytic beta subunit for proper localization and function. This beta subunit is known as TMEM30 or CDC50. There are three isoforms of the beta subunit, TMEM30A, TMEM30B, and TMEM30C, where TMEM30A is the most abundantly expressed isoform and interacts with 11 of the 14 P4-ATPAses. A popular method to determine how P4-ATPases generally affect a biological process is to create TMEM30 knockouts and

measure the resulting phenotypes. This methodology does not elucidate which specific flippase(s) are important in a process, however, it does show how globally affecting P4-ATPase localization and function can affect different biological processes across many tissues and cell types. This methodology was utilized to discover that P4-ATPases play a role in insulin secretion and glucose sensing in pancreatic β cells [57]. The authors created a mouse line where *Tmem30a* was knocked out specifically in pancreatic β cells and found that the mice exhibited glucose intolerance that worsened with age, abnormally large islets with increased beta cell mass, and hyperglycemia with impaired glucose stimulated insulin secretion. Additionally, using islet cell culture models, they found that *Tmem30a* deficiency lead to impairments in insulin maturation, the formation of mature insulin secretory granules, and less GLUT2 at the surface of β cells. The authors found that these phenotypes were ultimately caused by a reduction in clathrin-mediated exocytic vesicles budding from the TGN due to the *Tmem30a* deficiency. Lastly, they found that *Tmem30a* deficiency in MIN6 cells resulted in reduced expression of *Atp8a1, Atp8b2, Atp10a, and Atp11a*, providing some evidence for what flippases' location and function could have been disrupted to cause the observed β cell phenotypes. In the case of *Atp10a,* there is additional evidence that this flippase has a role in glucose homeostasis. SNPs in *ATP10A* have been shown to correlate with increased risk of insulin resistance in a human population [58]. Additionally, *Atp10A* deficiency in mice has been shown to result in glucose intolerance, reduced insulin sensitivity, and hyperinsulinemia [59, 60]. However, whether these phenotypes arise from *Atp10A* deficiency specifically in the pancreas needs to be further explored.

Role of flippases in the maintenance of red blood cells

Phosphatidylserine (PS) exposure on the outer leaflet of erythrocyte membranes is a determinant for apoptosis because PS acts as an 'eat me' signal to splenic macrophages [61]. Therefore, modulating plasma membrane PS localization by flippase (substrate-specific internal translocation) and scramblase (non-specific internal and external translocation [62] activity can have

broad effects on erythrocyte longevity and thus the body's capacity to effectively deliver oxygen to tissues. ATP8A1 was originally thought to be responsible for the majority of the flippase mediated PS translocation in murine erythrocytes [63], however it was later found that *Atp8a1-/-* mice do not display increased PS exposure on their erythrocytes, most likely due to compensation by other flippases expressed in this cell type [64]. One such compensatory flippase is ATP11C and *Atp11c* deficient mice exhibit anemia [65]. The authors that made this observation later explored the role of ATP11C in erythrocyte longevity [66]. They found that *Atp11c* deficient mice exhibited impaired flippase activity during erythropoiesis and that circulating erythrocytes in the mutant mice had increased PS exposure that increased with age. The erythrocytes from the mutant mice also had shortened life spans and abnormal shapes, also known as stomatocytosis. This abnormal stomatocyte shape most likely occurred due to the implications of the bilayer couple hypothesis [10, 16] and/or altered interaction with PS and skeletal proteins at the plasma membrane [67, 68].

There are established differences between human and murine erythrocytes [63], therefore it is important to study the role of ATP11C in human erythrocytes as well. A potential role for ATP11C in human erythrocytes was precipitated by the finding that a mutation in *ATP11C* inherited as an X-linked recessive trait, corresponding to Thr418Asn, in a male patient resulted in mild congenital hemolytic anemia without morphological abnormalities [70]. Thr418 is near Asp412, the phosphorylation site for forming the phosphate intermediate that is essential for the flippase to translocate PS. The authors found that PS internalization in the patient's erythrocytes was decreased 10-fold compared to controls. Flippase and scramblase activity alter PS localization at the plasma membrane, therefore the authors wanted to elucidate the contribution of ATP11C to PS distribution during conditions of low intracellular [Ca2+] (scramblases inactive) and conditions of high intracellular [Ca2+] (scramblases active), as seen in senescent cells. They found that ATP11C maintenance of PS in the inner leaflet was more important during conditions where scramblase activity is high, as seen in senescent cells, but less important in cells with low scramblase activity.

Indeed, ATP11C activity is highly regulated in senescent erythrocytes. For example, there is lower expression of ATP11C in senescent erythrocytes, partly due to it being cleaved by caspase [71] and/or calpain [72]. Additionally, a decrease in intracellular [K+] and [ATP], as well as an increase in [Ca2+] results in reduced ATP11C activity and ultimately an increase in PS exposure in senescent erythrocytes [73]. These authors proposed that there was an additional unknown factor involved in the reduction of flippase activity in senescent erythrocytes. Indeed, it was later discovered that increased plasma membrane tubulin results in lower flippase activity [74]. Additionally, sickle-shaped erythrocytes incubated with the PKCζ activator, phorbol myristate acetate (PMA), had a twofold increase in scramblase activity compared to normal erythrocytes incubated with PMA, however PS exposure was almost four times greater in the normal erythrocytes, revealing that PS exposure does not depend mainly on scramblase activity [75]. Interestingly, PMA also induces tubulin polymerization [76], an activity that is hypothesized to have a negative effect on flippase activity. Altogether, negative regulation of flippase activity (most likely ATP11C) is an important factor contributing to PS exposure during erythrocyte senescence. Interestingly, there is evidence that ATP11C is tightly regulated in non-senescent/non-apoptotic cells as well. Following treatment with PMA in human and mouse cell lines, ATP11C underwent clathrin-mediated endocytosis [77]. The authors found that this endocytic event occurred through Ca2+ induced PKC activation, which most likely results in phosphorylation of a serine residue in the C-terminal region of ATP11C that creates a functional dileucine motif that induces endocytosis. The authors concluded that the endocytosis of ATP11C functionally sequesters the protein and thus acts as a negative regulatory mechanism, however this phenotype has yet to be established in erythrocytes.

ATP11C is the most abundant flippase in human red blood cells, and ATP11A and ATP11B are also detected at low levels [78]. Additionally, ATP11C and ATP8A1 are the most abundant flippases in mouse red blood cells and ATP11B is detected at low levels. The authors that made these discoveries, as well as another group [79], investigated mechanistic details of different mutations in *ATP11C* in human red blood cells, specifically T415N and T418N. T418N is the mutation seen in the patient with

mild congenital hemolytic anemia and T415N is very close to it. The T415N mutation reduced ATP11C expression due to protein misfolding, increased retention of the misfolded protein in the ER, and more broadly, decreased ATPase activity by 61% relative to WT controls. In mice, ATP11C mutations result in several phenotypes, including B-cell deficiency, anemia, hyperbilirubinemia, cholestasis, and hepatocellular carcinoma [53, 55, 65, 80]. Additionally, conditional KO of *Tmem30a* results in pancytopenia in mice [81], further highlighting the importance of proper function and localization of flippases to the maintenance of blood cell homeostasis in mice. However, the phenotypes seen in humans due to *ATP11C* mutation are much milder, perhaps because there is some residual activity of the mutant ATP11C in erythrocytes, there is compensation by other lowly expressed erythrocyte flippases (ATP11A and ATP11B), or maybe, ATP11C has a more important role in mouse physiology versus humans and this is still an open area of research. Alternatively, one possibility is that the importance of flippases in human erythrocyte function is better precipitated in people with flippase mutations in conjunction with other pathologies, such as cancer, diabetes and hypertension. It was recently discovered that erythrocytes treated with a microtubule stabilizing chemotherapy drug, Paclitaxel, exhibit PS exposure, most likely due to the drug increasing the amount of tubulin at the plasma membrane, thus inhibiting flippase activity [74]. There is also an increase in PS exposure in erythrocytes from people with diabetes and hypertension, conditions that also result in changes to tubulin dynamics and post-translational modification [82-85]. Interestingly, Paclitaxel treatment can result in several vascular malignancies, including stroke, deep vein thrombosis, and pulmonary embolism. Additionally, anemia [86] and hypercoagulability [87] are common in diabetic and hypertensive patients, respectively. Therefore, the contribution of flippase dysregulation and deficiency to the underlying causes of different hemorheological dysfunctions in cancer patients taking drugs that affect microtubule dynamics (such as Paclitaxel) as well as diabetic and hypertensive patients needs to be further explored and could help elucidate the potential importance of erythrocyte flippases in maintaining blood cell and vascular health in humans.

Role of flippases in Metabolism

SNPs in *ATP10A* have been shown to correlate with increased risk of insulin resistance in a cohort of African Americans [58]. SNPs in *ATP10D* result in increased circulating levels of hexosylceramides (HexCer) [88] and increased incidences of myocardial infarction in an elderly Japanese population [89]. This increase in plasma HexCer levels measured in people with *ATP10D* SNPs was quite mysterious until our lab discovered that ATP10D, in addition to ATP10A, translocates glucosylceramide (GlcCer), a member of the HexCer family [90].

Studies in mice have also suggested metabolic roles for several flippases. *Atp10A* deficiency in mice results in glucose intolerance, reduced insulin sensitivity, and hyperinsulinemia [59,60]. C57BL/6J mice, a popular mouse strain used in metabolic studies due to their susceptibility to metabolic disorders [91], has a premature stop codon in *Atp10D* and is therefore an *Atp10D* null mouse [92]. Reintroducing *Atp10D* into C57BL/6J mice results in mice having a more favorable metabolic profile on a high fat diet, characterized by less weight gain, lower plasma triglyceride, glucose, insulin and HexCer levels, and improved whole-body insulin sensitivity [93]**.** These studies provided some evidence that ATP10A and ATP10D have roles in metabolism however, the mouse models used were flawed.

The previous mouse model of *Atp10A* deficiency [59] were mice generated at Oak Ridge National Laboratory that had radiation-induced chromosomal deletions at the *pink-eyed dilution (p)* locus on mouse chromosome 7 (MMU-7). Assessment of body fat in mice with two of the distally extending heterozygous deletions, $p^{23DFiOD}$ and p^{30PUb}, revealed that the *p-linked-obesity-locus 1* (*plo 1*) region on proximal MMU-7 contained gene(s) influencing body fat. Therefore, the authors wanted to investigate potential metabolic phenotypes in these mice. p^{30Pub} represents the most extensive distal extension of the *p* deletion; situated between ubiquitin protein ligase E3A (*Ube3a*) and the imprinted gene in the Prader-Willi syndrome region (*Ipw*). *Atp10A* (previously known as *Atp10C)* sits within this deletion interval and the authors suggested that this gene may be responsible for the body fat phenotypes. In the $p^{23DFiOD}$ heterozygotes, the first two exons including the 5′ promoter region of *Atp10c* are deleted, whereas in

the p^{30PUb} heterozygotes, the complete gene of 21 exons and the 5′ and 3′ flanking regions are deleted. In the first report, the authors placed the p^{30Pub} mice on a high fat diet and found that the female mutants exhibited increased body weights and fat accumulation on a 45% fat diet and that maternal inheritance of the p^{30Pub} deletion was linked to altered glucose tolerance, increased adiposity, and non-alcoholic fatty liver disease [59]. In a subsequent study, the authors found that female $p^{23DFiOD}$ mice, when fed a HFD for 4 weeks, showed increased body weights, plasma insulin levels, and insulin resistance without changes in food intake. After 12 weeks on the same diet, insulin resistance persisted, accompanied by altered expression of genes in the insulin signaling pathway, in both adipose tissue and skeletal muscle [60]. While these reports offered some evidence for a sex-specific involvement of *Atp10A* in metabolism, it's important to note that the mice utilized in these studies carried extensive chromosomal deletions, encompassing genes beyond *Atp10A* within the deletion interval. Consequently, the observed phenotypes cannot be solely ascribed to *Atp10A* deficiency. Furthermore, attempts to establish homozygosity for the chromosomal deletion proved unsuccessful due to embryonic lethality, limiting the examination to heterozygotes only [59,60].

The *Atp10D* correction model was created by integrating a BAC-derived WT *Atp10D* into an undefined chromosomal position in the C57BL/6J background and the study mice were all males and were hemizygous for the transgene and homozygous for $Atp10d^{-/-}$ [93]. The authors were not able to generate a control strain and did not study littermates to control for maternal effects. Taken together, the existing mouse models for both *Atp10A* and *Atp10D* failed to clearly define these genes' influence on metabolism and more work is needed to answer this interesting question.

Defining the role of ATP10A and ATP10D in Metabolism

The metabolic syndrome is characterized by abdominal obesity, insulin resistance, hypertension, and dyslipidemia, and an increased risk of developing type 2 diabetes mellitus and atherosclerotic cardiovascular disease (ASCVD) [94]. This syndrome affects 33% of Americans and on a global scale, over 1 billion people [95]. Therefore, there is a need to further understand the genetic

basis for this disease. There is evidence that deficiency in *ATP10A* and *ATP10D* can impact components of the metabolic syndrome. Additionally, both flippases translocate GlcCer [90] and this glycosphingolipid has been implicated as an independent antagonist to the insulin signaling pathway [96]. Pharmacological inhibition of GlcCer synthesis improves insulin sensitivity in cultured adipocytes and mice, where it has also been shown to resolve buildup of fat in the liver, also known as hepatic steatosis [97].

To determine the role of these flippases, that translocate a bioactive lipid, in metabolic disease, we generated new murine models of *Atp10A* and *Atp10D*. We used CRISPR/Cas9 guide RNA sequences targeted to regions flanking exon 2 of *Atp10A* to create a whole-body knockout. For *Atp10D* we used CRISPR/Cas9 to correct the nonsense mutation found in C57BL/6J mice, to the WT sequence found in other mouse models [92]. We hypothesize that *Atp10A* deficiency will lead to worsened metabolic outcomes and that correcting the *Atp10D* deficiency in C57BL/6J mice will protect the mice from diet-induced obesity and other metabolic perturbations. To test this hypothesis, we placed these different mouse models on high fat diets for 12-16 weeks and measured weight gain over time as well as other metabolic parameters; including glucose tolerance, insulin signaling in tissues, energy expenditure, and lipid tolerance.

Overview of thesis contents

This thesis covers the functions of ATP10A, across distinct physiological domains. The initial chapter explores the role of ATP10A in preserving endothelial cell insulin sensitivity and safeguarding female mice from diet-induced dyslipidemia, and parts of this work have been published [98]. Subsequently, the investigation extends to male-specific infertility resulting from ATP10A deficiency, unraveling molecular intricacies underlying reproductive impairments, and parts of this work have also been published [99]. The third chapter explores lipoprotein lipase (LPL) activity and localization within *Atp10A* knockout mice. Chapter four investigates the impact of correcting *Atp10D*, a closely related flippase, on metabolic phenotypes, offering insights into potential compensatory mechanisms. The final

chapter describes further metabolic profiling of *Atp10A*-deficient mice, examining feces lipid content, gene expression patterns, and blood pressure dynamics. This thesis describes the diverse facets of the influence ATP10A has on cellular function, metabolism, and reproduction, providing an understanding of its physiological ramifications.

Chapter 2: ATP10A promotes endothelial cell insulin sensitivity and protects against diet-induced dyslipidemia in female mice

INTRODUCTION

The metabolic syndrome is a complex condition that affects 33% of Americans and on a global scale, over 1 billion people [95]. This syndrome is characterized by abdominal obesity, insulin resistance, hypertension, and dyslipidemia, and an increased risk of developing type 2 diabetes mellitus and atherosclerotic cardiovascular disease (ASCVD) [94] By promoting oxidative stress and inflammation, these conditions can cause damage to the vascular endothelium. A damaged vascular endothelium is more susceptible to atherosclerosis, aneurysms, and arteriosclerosis, which increases risks of developing chronic diseases. It is well established that vasculature damage can be a consequence of these disorders, interestingly, there is also evidence for vasculature dysfunction playing a causal role in promoting these disorders [100]. Therefore, there is a need to develop a comprehensive understanding of the 'crosstalk' that occurs between the endothelium and resident tissues in the context of the metabolic syndrome. This will provide insight into how to maintain a healthy vasculature as well as inform the development of therapeutics that can help heal a damaged vasculature.

ATP10A is a potential effector of endothelial cell (EC) and tissue crosstalk. ATP10A shows the highest expression in human arterial tissue (GTEx) and murine brain ECs (Tabula Muris). Commonly found variants in *ATP10A* have been linked to increased risk of insulin resistance [58] and variants within a related gene, *ATP10D*, have been linked to increased atherosclerosis risk [89]. ATP10A and ATP10D are P4-ATPases, also known as lipid flippases, that translocate lipids from the exoplasmic or luminal leaflets to cytosolic leaflets of cell membranes. This creates an asymmetric distribution of lipids within membranes that has several implications for the cell [101], including in apoptosis [71], vesicular trafficking [102], signal transduction [103], as well as in generating signaling lipids.

Interestingly, most of the 14 human P4-ATPases have established roles in disease, such as in severe neurological disease and intrahepatic cholestasis [38]. These enzymes transport specific lipid substrates, which are closely related to their cellular and physiological functions. ATP10A flips phosphatidylcholine (PC) [45] and glucosylceramide (GlcCer) [90]. PC has structural roles in membranes [104] and is involved in protein trafficking [105]. Its metabolites, such as lysophosphatidylcholine (LysoPC) and eicosanoids produced from arachidonic acid (AA), have roles in modulating inflammation and various disease states [106-109]. GlcCer is a bioactive lipid that can also affect insulin signaling and energy homeostasis [110], as well as inflammation [111]. Inhibiting GlcCer synthase enhances insulin sensitivity [112] and protects against cardiac hypertrophy [113]. GlcCer can be broken down into ceramide or built up into gangliosides, which also have established roles in metabolism [114-116].

Previous reports described a role for murine ATP10A in diet-induced obesity and insulin resistance, however, the mouse model used in these studies contained a large chromosomal deletion that included *Atp10A* (previously named *Atp10C)* and several other genes [59, 60]. Homozygosity resulted in embryonic lethality, so the authors used mice heterozygous for the deletion. It was unclear whether *Atp10A* deficiency caused the metabolic perturbations observed, but they did find that mice that inherited the chromosomal deletion maternally had more severe metabolic phenotypes compared to those who inherited the deletion paternally. This observation suggested that the *Atp10A* locus was imprinted to suppress expression of the paternal allele, however several studies failed to detect imprinted expression of the *ATP10A* gene [117-119]. It appears that *ATP10A*'s expression pattern is complex and dependent on multiple factors including gender, genetic background, and tissue type.

Although correlations between *ATP10A* deficiency and insulin resistance, diet-induced obesity, and glucose uptake [120] have been reported, it is unclear whether this flippase plays a causative role in these processes or has any function in ECs, where its expression has been detected. Here, we generated a gene-specific deletion and tested the impact of *Atp10A* deficiency in mice during high fat diet (HFD) feeding. *Atp10A* deficient mice display female-specific diet-induced dyslipidemia, disruptions

in liver insulin signaling, and broad changes to lipid metabolism. Additionally, we found that ATP10A is expressed in ECs in liver and visceral fat (VF) and that ATP10A knockdown in ECs results in perturbations to insulin-dependent signaling as well as alterations to the regulation of an important vasodilator, endothelial nitric oxide synthase (eNOS), suggesting a potential role for ATP10A in endothelial and resident tissue 'crosstalk' as well as in vascular maintenance and health.

MATERIALS AND METHODS

Animals. All mouse experiments were approved under the Vanderbilt University Institutional Animal Care and Use Committee. Mice were housed in 12 h light/dark cycles in temperature and humidity-controlled facilities with ad-libitum access to diet and water (in the Barrier facility).

Creating the mouse model. The *Atp10A* mouse model (knockout allele name: *Atp10Aem1(Vtrg)*) was created via CRISPR-Cas9 in collaboration with the Vanderbilt Genome Editing Resource. Guide RNAs (crRNA) were created to target *Atp10A* on chromosome 7: Target Intron 1-2: TGACTGCTTAATGATTCGAGG, GAGTGACTGCTAATGATCG, Target Intron 2-3: GGAAAAAGCCCAATTCCACAC, AGCCCAATCCACACAGGAAC. CRISPR editing reagents were delivered into the pronuclei of one-cell fertilized mouse zygotes (C57BL/6J). Approximately 608 bp were deleted using this method: nucleotides 58389679-58390287 (NCBI reference sequence: NC_000073). The resulting pups were biopsied and screened by PCR and Sanger sequencing. The predicted founders were bred to WT C57BL/6J animals and the offspring were genotyped (N1 generation). The offspring with the appropriate genotype were then backcrossed two more times.

Genotyping. Mice were genotyped using tail DNA. *Atp10A* DNA products were detected via a multiplexed PCR (Lucigen EconoTaq PLUS GREEN,Biosearch Technologies) followed by gel electrophoresis; *Atp10A-F* (GTGCACTGTATTTGTCTGCC), *Atp10A-R1 (*CAAAGTCGCCCACTCGGATTTC), *Atp10A-R2* (CCAACCTACGTAAGAACAGG).

Body composition, body length, and tissue mass. WT and experimental mice were fed standard chow or 60% HFD (D12492, Research Diets) ad libitum, starting at the age of 3-12 weeks old (see Supplemental Table 1). Mice were weighed once per week to measure body weight gain over time. On the 12th week on the HFD, body composition was assessed via NMR (LF50 Body Composition Mice Analyzer, Bruker, stock # E140000501). Mice were sacrificed with CO_2, the body lengths were measured and the mass of the wet tissue was measured using an analytical scale. Tissues were collected and flesh frozen when mice were sacrificed.

Oral glucose tolerance tests (OGTT) and fasting blood glucose/insulin measurements. Mice were fasted for 5 hours (7AM-12PM) and then an OGTT was performed. Mice were gavaged with 20% w/v dextrose (final 2g/kg body weight), and a tail-vein blood glucose was measured via a glucometer (Accu-Chek, Accu-Chek Aviva Plus Meter) at baseline, 15, 30, 45, 60, 90, and 120 min. The area under of the curve for glucose was calculated using GraphPad Prism. Plasma samples were collected from 5-hr fasted mice via a retroorbital bleed and were used for the insulin assay. Plasma insulin was measured using the Crystal Chem Ultrasensitive Mouse Insulin ELISA Kit (catalog # 90080).

Plasma lipid and lipoprotein analysis. Plasma was collected, via a retroorbital bleed or cardiac puncture, from 5-hr fasted mice and 5-hr fasted mice that had undergone an OGTT (see Supplemental Table 1). For males and a portion of the female samples: plasma TG and cholesterol were measured using colorimetric kits (Inifinty, Thermo Scientific, TG catalog #TR22421, chol catalog #TR13421) and plasma FFAs were measured using Abcam's Free Fatty Acid Assay Kit-Quantification (ab65341). For the rest of the females: plasma samples were measured by the Vanderbilt Hormone Assay and Analytical Services Core, where plasma cholesterol and TG were measured by standard enzymatic assays, and plasma FFAs were analyzed with an enzymatic kit (Fujifilm Healthcare Solutions, catalog #999-34691). Lipoproteins were separated using FPLC on a Superose6 column (GE Healthcare) from 150 µl plasma (single mouse or pooled) and the TG and cholesterol content were measured using

colorimetric kits (Inifinity, Thermo Scientific, TG catalog #TR22421, chol catalog #TR13421). AUC was calculated using GraphPad Prism.

Plasma lipidomics. Plasma was collected, via a retroorbital bleed or cardiac puncture, from 5-hr fasted mice and some samples are pooled plasma (see Supplemental Table 1). Lipid metabolites were extracted from 100 µL plasma by methyl methyltert-butyl ether (MTBE) extraction. The lipid metabolites were then analyzed by HPLC-IM-MS/MS on an Agilent 6560 mass spectrometer using a ZORBAX Extend-C18 RPLC column (Phase A: 0.1% formic acid and 10 mM NH_4CHOO in water, Phase B: 0.1% formic acid and 10 mM NH_4CHOO in 60:36:4 isopropanol:acetonitrile: H_2O) [121]. Data alignment and biostatical analysis was performed using Progenesis QI (Waters). Tentative compound identifications were assigned using accurate mass databases and a previously described ion mobility-based filtering method [122].

RNA Sequencing. VF was flash frozen in liquid nitrogen and then kept at -80^{o}C until thawed at -20^{o}C in RNA*later* (ThermoFisher, catalog # AM7030). The tissue was then homogenized in QIAzol Lysis Reagent (Qiagen, catalog #79306) using a Bullet Blender (Next Advance, BT24M). The RNA layer acquired after the QIAzol Lysis protocol was cleaned up using the RNeasy Lipid Tissue Mini Kit (Qiagen, catalog #NC9036170). Quality control measurements and Next Generation Sequencing (NGS) was performed on 20 uL of RNA (>10 ng) by Vanderbilt Technologies for Advanced Genomics (VANTAGE); briefly, NEBNext Ultra II Directional RNA kit (Cat no: E7760L) was used and for the sequencing; NovaSeq 6000 and PE150 read lengths were used.Analysis of NGS data was performed by Vanderbilt Technologies for Advanced Genomics Analysis and Research Design (VANGARD).

Cell cultures and treatment. Human Umbilical Vein Endothelial Cells (HUVEC) were from Lonza (Walkersville, MD; cat. #C2519A, lot #21TL347550) and were cultured in EGM^{TM}-2 medium (Lonza, Walkersville, MD) at 37 ^{o}C with 5% CO_2. SVEC4-10 cells from mouse lymph node endothelium were purchased from ATCC (Manassas, VA) and maintained in DMEM with 10% FBS and 1%

penicillin/streptomycin (Life Technologies, Gaithersburg, MD). Cells from passage 2 to 9 were used in this study. For silencing experiments, cells were transfected for 48 h with non-silencing siRNA (50 nM, transfection control) or ATP10A siRNA (combined 25 nM each ATP10A sequences #1 and #2) using Lipofectamine RNAiMAX (Invitrogen by Thermo Fisher Scientific) according to manufacturer's instructions. Silencer Select pre-designed ATP10A siRNAs (human sequence #1 (5'-3'): CAACGACCUGAGUAGGUUUtt; human sequence #2 (5'-3'): CCAAUUUCCUUAUACGUUUtt; mouse sequence #1 (5'-3'): CCUUAUAUGUUUCCAUUGAtt; mouse sequence #2 (5'-3'): CAAUGACCUGAGUAGGUUUtt) and Silencer Select Negative control #1 siRNA were bought from Ambion by Life Technologies™. For treatment with insulin, human recombinant zinc solution of insulin was used (Gibco™ by Thermo Fisher Scientific). Cells were treated with either growth medium (control) or with 100 nM insulin (diluted in growth medium) for 0-60 min.

Immunoblot analysis. HUVEC or SVEC4-10 were harvested at the indicated times of respective treatment. Total protein extraction was performed using M-PER (Pierce, Rockford, IL) with phosphatase and protease inhibitors (Sigma). For tissue samples, T-PER (Pierce, Rockford, IL) with phosphatase and protease inhibitors (Sigma) were used. Protein concentration was quantified using BCA Reagent (Pierce, Rockford, IL). Protein extracts (40 µg for cells; 100 µg for tissues) were subjected to Western immunoblot analysis. The following primary antibodies were used for detection of: ATP10A (Vanderbilt Antibody and Protein Resource, Vanderbilt University, see below), DGAT1 (sc-32861, Santa Cruz Biotech), DGAT2 (sc-66859, Santa Cruz Biotech), phospho-AMPKα^{T172} (#2535, Cell Signaling), AMPKα (#2532, Cell Signaling), phospho-ACC^{S79} (#3661, Cell Signaling), ACC (#3676, Cell Signaling) , phospho- IGF-IRβ^{Y1131}/IRβ^{Y1146} (#3021, Cell Signaling), phospho-IGF-IRβ$^{Y1135/1136}$/IRβ$^{Y1150/1151}$(#3024, Cell Signaling), IRβ (#3025, Cell Signaling), phospho-IRS-1^{S612} (#3203, Cell Signaling), IRS-1 (#3407, Cell Signaling), phospho-Akt$^{T308/S473}$ (#13038/#4060, Cell Signaling), Akt (#9272, Cell signaling), phospho-GSK-3β^{S9} (#5558, Cell Signaling), GSK-3β (#9315, Cell Signaling), phospho-cPLA$_2$α^{S505}(#53044, Cell Signaling), cPLA$_2$α (#5249, Cell Signaling), phospho-eNOS^{S1177} (ab215717,

Abcam), eNOS (#32027, Cell signaling). Antibody to actin (#4970, Cell Signaling) was used to evaluate protein loading in each lane. Immunoblots were developed using the Western Lightning Chemiluminescence Plus detection system (PerkinElmer, Wellesley, MA) according to the manufacturer's protocol. Intensity of the immunoblot bands was measured using AI600 CCD Imager for chemiluminescent assays (Amersham). Densitometry was performed using ImageJ. For quantification, OD of bands for phosphoprotein was normalized to total protein and β-actin; otherwise, OD of bands for total protein was normalized to β-actin.

Generation of ATP10A antibodies. Anti-ATP10A antibody were produced by Vanderbilt Antibody and Protein Resource. ATP10A peptides 1 (27 RTRTVRSNLLPPC 38), 3 (498 HKTQSIKSHRRTC 510) and 5 (1280 QTLLGDPLFYLTC 1292) for antibody production were chosen based on conservation between mouse and human ATP10A orthologs, lack of conservation with ATP10B and ATP10D paralogs, and predicted water solubility (https://pepcalc.com) (Supplemental Figure 6A). Peptide epitopes were synthesized (GenScript, USA, Inc.) with a C-terminal Cys residue and conjugated to Imject™ Maleimide-Activated mcKLH, Imject™ Maleimide-Activated BSA, and SulfoLink™ Coupling Resin following the manufacturer's recommended protocol (ThermoFisher Scientific) by the Vanderbilt Antibody and Protein Resource (VAPR) group. The three peptide-Keyhole Limpet Hemocyanin (KLH) conjugates were used for antibody production in a single rabbit (VU579, Cocalico, Stevens, PA). Antibodies recognizing the peptide epitopes were purified from the rabbit by differential affinity chromatography using the peptide conjugated resin. Briefly, 5 ml of antisera was passed over the peptide 1 column (2 ml) and the material that failed to bind was then applied sequentially to the peptide 3 and 5 columns. After washing with 40-50 ml PBS, bound antibodies were eluted from each column with 8.5 ml of 100 mM glycine, pH 2.5 and collected in tubes containing 1.5 M Tris-HCl, pH 8. Finally, to ensure peptide specificity, antibodies eluted from one peptide column were applied sequentially to the other two columns and the flow-through was retained. Affinity purifications were performed in duplicate to generate anti-peptide 1A and 1B, anti-peptide 3A and 3B, and antipeptide 5A and 5B antibodies. The

specificity of the affinity purified antibodies was then assessed by dot blot analysis using the peptide-BSA conjugates. The rabbit produced antibodies to all three peptides but only anti-peptide 1 recognized full-length ATP10A (Supplementary Figure 6B).

Immunofluorescent staining of mouse tissues. Tissue was fixed in 10% neutral buffered formalin and further processing and paraffin embedding was done by the Vanderbilt Translation Pathology Shared Resource (TPSR). Tissue sections are 5 μm thick. To stain paraffin embedded sections, the sections underwent re-hydration, antigen retrieval, blocking, and antibody treatment [123]. The slides were treated with anti-ATP10A (1:20) followed by goat anti-rabbit Alexa-Fluor 647 secondary antibody (1:1,000, Abcam, #150083) and ProLong Gold Antifade Mountant with DAPI (Thermo Fisher, catalog # P36931). Images of tissues were acquired using a confocal microscope (Zeiss LSM 880 with AiryScan) with a Zeiss C Plan Apochromat ×40/1.40 Plan-Apochromat Oil using the ZEN black software. Confocal images were taken of vas deferens, liver, VF, and heart. Laser irradiation at 633 nm was used to excite the Alexa-Fluor 647, and at 405 nm to excite DAPI. Detector gain and laser intensity were constant for all experimental groups. Images were false colored green and edited using ImageJ (images from the same tissues were edited using the same scripts).

Immunofluorescent staining of cells. Routinely grown HUVEC or SVEC4-10 cells were plated on Nunc™ Lab-Tek™ Chamber Slides (Thermo Fisher Scientific, #177399). For silencing experiments, cells were transfected for 48 h with non-silencing or ATP10A siRNA as described previously. Cells were fixed, washed, permeabilized, blocked and treated with anti-ATP10A antibody (1:20) followed by goat anti-rabbit Alexa-Fluor 488 secondary antibody (1:1,000, Invitrogen by Thermo Fisher Scientific, #A11008) and ProLong Gold Antifade Mountant with DAPI. Images of cells were acquired using a confocal microscope (Zeiss LSM 880 with AiryScan) with a Zeiss C Plan Apochromat ×63/1.40 Plan-Apochromat Oil using the ZEN black software. Laser irradiation at 488 nm was used to excite the Alexa-Fluor 488, and at 405 nm to excite DAPI. Detector gain and laser intensity were constant for all

experimental groups. Images were edited using ImageJ (images from experimental groups were edited via the exact same parameters).

Immunohistochemistry (Tissues). Tissue was fixed in 10% neutral buffered formalin and further processing and paraffin embedding was done by the Vanderbilt Translation Pathology Shared Resource (TPSR). Tissue sections are 5 μm thick. Slides were placed on the Leica Bond Max IHC stainer. All steps besides dehydration, clearing and cover slipping are performed on the Bond Max. Slides are deparaffinized. Heat induced antigen retrieval was performed on the Bond Max using their Epitope Retrieval 2 solution for 20 minutes. Slides were incubated with anti-CD31 (Dianova, catalog # DIA-310) for one hour at a 1:75 dilution and followed by a biotinylated anti-rat (Vector Laboratories, Inc., Burlingame, catalog # BA-4000) for 15 minutes at a 1:2000 dilution. The Bond Refine (catalog # DS9800) detection system was used for visualization. Slides were then dehydrated, cleared and cover slipped. Images of tissues were acquired using light microscopy (Zeiss AxioPlan, Upright Fluorescence Microscope, Germany) with a x63/1.0 Oil using the Zeiss Axio Color Camera (Axiocam 208c) and the ZEN 3.1 software (blue edition). Microscope settings were held constant for all experimental groups.

Promethion System*.* Indirect calorimetry and additional measures of food intake and physical activity were performed in open-circuit indirect calorimetry cages (Promethion System, Sable Systems International) at Vanderbilt Mouse Metabolic Phenotyping Center (MMPC). One week prior to the experiment start date, mice were singly housed for acclimation. On the day of the experiment start date, mice were weighed and body composition was assessed. The mice were placed in the cages of the Promethion system, one mouse per cage. The cages were housed in a light and temperature-controlled chamber. The light cycle was set on a 12:12h cycle (6am-6pm). Mice were left undisturbed for 5 days during which all the measurements were made. The system periodically measured rates of O2 consumption (VO2) and CO2 production (VCO2) for each cage, as well as food intake and physical activity (infrared beam array). Data were processed in time segments (daily 24-hour, and 12-hour

dark/12-hour light), and averages calculated for each as well as for the 24-hour period. After 5 days, the mice were removed from the cages, and body composition and weight were measured again.

Measuring liver lipids. Liver FFA, total cholesterol, cholesterol ester, unesterified cholesterol, TG, PLs, and ceramides were measured by the Vanderbilt Hormone Assay and Analytical Services Core using methods described in [124-126].

Oil Red O. Livers were placed in frozen section medium (Epredia, Neg-50, catalog #22-110-617) and then placed on dry ice. When the frozen section medium was solidified, the livers were placed at -20^{o}C until further processing. Further processing was done by the Vanderbilt Translation Pathology Shared Resource (TPSR): Slides were brought to room temperature and placed in 10% NBF solution for 10 minutes. The Newcomer Supply Tech Oil Red O, Propylene Glycol staining kit (Newcomer Supply, catalog # 12772B) was used for visualization. Slides were then cover slipped with aqueous mounting medium. In regard to Oil Red O scoring: Dr. Katherine Gibson Corley, a board-certified veterinary pathologist at the Vanderbilt TPSR, created the scoring system used to score the Oil Red O stained liver sections. The scoring system is characterized by: 0= no Oil Red O staining, 1=rare and scattered Oil Red O staining, 2=multi-focal and coalescing Oil Red O staining, 3=diffuse Oil Red O staining (in whole tissue). To score the slides, the scorer was blinded to the slide IDs and then scored the slides twice, on two separate days. Then the scores from both days were compared and if they did not match, the scorer viewed the slide again and decided on a final score. The diameter of the Oil Red O positive lipid droplets was measured from slides with a score of 2, using ImageJ.

Statistics. All statistical analysis was done using GraphPad Prism, version 9.5.0 (GraphPad Software). Error bars indicate mean with standard error of the mean (SEM). When more than 2 groups were compared, a 2-way ANOVA was used with Dunnett's correction for multiple comparisons with a control group. Šidák's correction was used for comparison of groups of means. Differences between group

mean values were tested using a 2-tailed Student's *t* test or a Mann-Whitney *U* test for nonparametric data. A *P* value of less than 0.05 was considered statistically significant.

Study approval. The animal protocol was approved by Vanderbilt University Medical Center and IACUC.

Data Availability. The untargeted lipidomics data is available at the NIH Common Fund's National Metabolomics Data Repository (NMDR) website, the Metabolomics Workbench, https://www.metabolomicsworkbench.org where it has been assigned DataTrack ID 3874.The reads from the RNASeq data can be found at NCBI (https://www.ncbi.nlm.nih.gov/genbank/samplerecord/) using these accession numbers: SRR24233646 (*Atp10A* WT reads) and SRR24233645 (*Atp10A* KO reads).

RESULTS

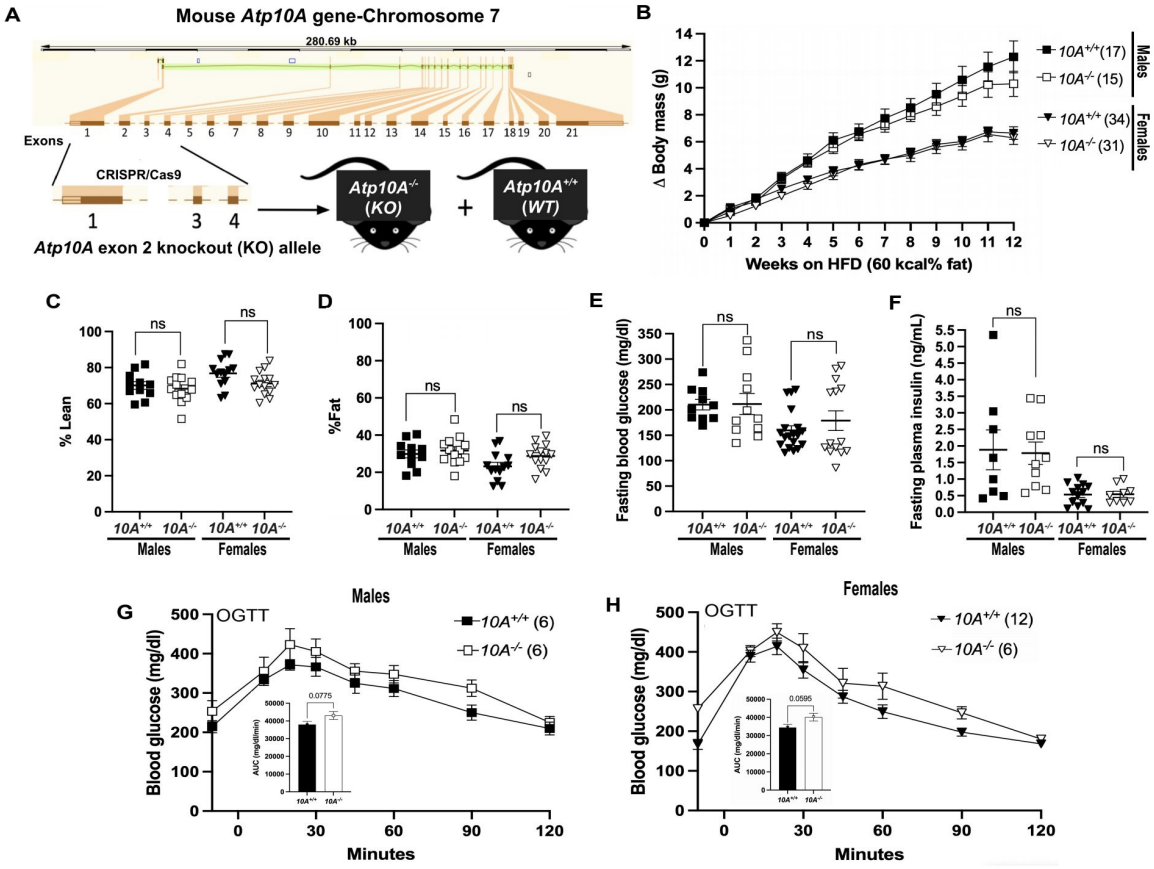

Figure 3. *Atp10A* deletion leads to sex-specific perturbations to body composition in female mice after 12 weeks on a HFD. (A) Graphic illustrating how CRISPR/cas9 was used to delete exon 2 in the mouse *Atp10A* to create the *Atp10A*$^{-/-}$ (KO) mouse line. (B) Weight gain of male and female *Atp10A*$^{+/+}$ (*10A*$^{+/+}$) and *Atp10A*$^{-/-}$ (*10A*$^{-/-}$) mice over the course of 12 weeks on a HFD (60 kcal% fat, Ad lib feeding), P value by 2-way ANOVA with Sidak's multiple comparison. (**Male:** *10A*$^{+/+}$ n=17, *10A*$^{-/-}$ n=15; **Female:** *10A*$^{+/+}$ n=34, *10A*$^{-/-}$ n=31) (C) Lean and (D) fat body mass were normalized to body mass to calculate % Lean and % Fat mass, P value by unpaired t-test. (**Male**: *10A*$^{+/+}$ n=11,*10A*$^{-/-}$ n=13; **Female**:*10A*$^{+/+}$ n=13,*10A*$^{-/-}$ n=14). (E) Fasting blood glucose was measured from tail blood after a 5 hour fast, via a glucometer, P value by unpaired t-test **(Male:** *10A*$^{+/+}$ n=10, *10A*$^{-/-}$ n=11; **Female**: *10A*$^{+/+}$ n=19, *10A*$^{-/-}$ n=14). (F) Fasting plasma insulin was measured after a 5 hour fast, P value by unpaired t-test (**Male:** *10A*$^{+/+}$ n=8, *10A*$^{-/-}$ n=10; **Female:** *10A*$^{+/+}$ n=13,*10A*$^{-/-}$ n=9). (G) Male and (H) female mice were gavaged with 20% dextrose after a 5-hour fast, then an oral glucose tolerance test (OGTT) was performed, the inset shows the area under the curve (AUC) normalized to time 0 blood glucose. OGTT, P value by 2-way ANOVA with Sidak's multiple comparison, AUC, P value by unpaired t-test (**Male:** *10A*$^{+/+}$ n=6,*10A*$^{-/-}$ n=6; **Female**: *10A*$^{+/+}$ n=12, *10A*$^{-/-}$ n=6).

To develop the *Atp10A*$^{-/-}$ mice, we created a gene-specific knockout allele of *Atp10A* in the C57BL/6J background using CRISPR/Cas9 guide RNA sequences targeted to regions flanking exon 2 (Figure 2A). To test the potential impact of *Atp10A* on weight gain, we placed male and female WT (*Atp10A*$^{+/+}$) and KO (*Atp10A*$^{-/-}$) mice on a HFD for 12 weeks. We found that there was no significant difference in weight gain in male or females based on genotype (Figure 3B). We next examined body composition and size and found that male and female mice did not display a difference in % lean mass (Figure 3C) (normalized to body mass) or % fat mass (Figure 3D). The male mice did not exhibit a different in body length based on genotype, but the female *Atp10A*$^{-/-}$ had smaller body lengths compared to *Atp10A*$^{+/+}$ controls (Supplemental Figure 1A). Additionally, we did not observe any changes in tissue mass (Supplemental Figure 1B) or food intake and energy expenditure (Supplemental Figure 2) based on genotype. To distinguish between the metabolic effects of *Atp10A* deficiency versus HFD feeding, we measured weight gain, body composition, and body length in female mice on normal chow; and found no significant differences based on genotype (Supplemental Figure 3A-D). Altogether, these results indicate that *Atp10A* deficiency does not cause diet-induced obesity under the conditions tested.

To assess the influence of *Atp10A* on glucose homeostasis, we fasted mice for 5 hours and measured their fasting blood glucose, insulin levels, and performed an oral glucose tolerance test (OGTT). We found no significant difference in fasting blood glucose (Figure 3E), insulin levels (Figure 3F), or in the kinetics of glucose clearance following a glucose challenge (Figure 3G, H, inset: AUC), in males or females based on genotype. However, the area under the curve (AUC) from the OGTT shows a trend toward the *Atp10A*$^{-/-}$ female mice having greater glucose excursion compared to *Atp10A*$^{+/+}$ controls. We also found no significant difference in fasting blood glucose and insulin levels between WT and KO females on a normal chow diet (Supplemental Figure 3E,F). Therefore, *Atp10A* deficiency does not appear to perturb whole-body glucose homeostasis.

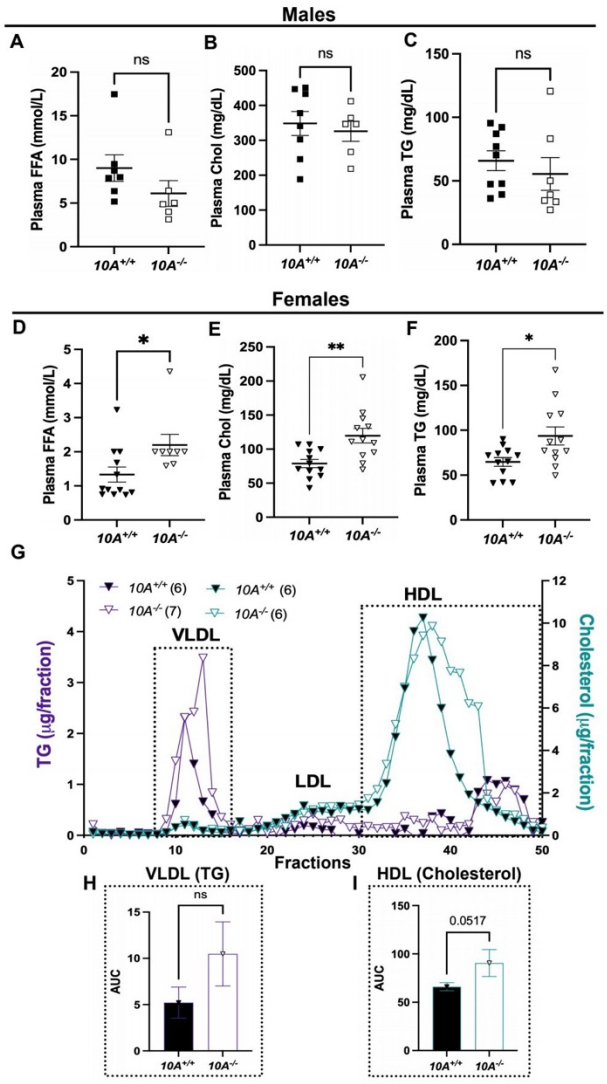

Figure 4. *Atp10A* deletion causes diet-induced dyslipidemia in female mice. (A-F) Free fatty acids (FFA), cholesterol (chol), and triglycerides (TG) were measured in plasma from males (A-C) or females (D-F) after a 5 hour fast or after a 5 hour fast followed by an OGTT. P value by unpaired t-test. (A, $10A^{+/+}$ n=7, $10A^{-/-}$ n=6; B, $10A^{+/+}$ n=8, $10A^{-/-}$ n=6; C, $10A^{+/+}$ n=9, $10A^{-/-}$ n=7; D, $10A^{+/+}$ n=12, $10A^{-/-}$ n=9,*P=0.0320; E, $10A^{+/+}$ n=12, $10A^{-/-}$ n=9, **P=0.0030; F, $10A^{+/+}$ n=12, $10A^{-/-}$ n=9, *P=0.0165.) (G-I) Lipoproteins in pooled plasma from females, collected after a 5-hour fast or 5-hour fast and OGTT, were separated via FPLC (G). Plasma TG (purple) and cholesterol (blue) content were measured from the separated lipoproteins, LDL=low density lipoprotein. AUC of fractions 10-18 of VLDL (H) and fractions 30-50 of HDL (I) are from panel G. P value by unpaired t-test (**TG:** $10A^{+/+}$ n=6, $10A^{-/-}$ n=7, **Chol:** $10A^{+/+}$ n=6, $10A^{-/-}$ n=6).

To further probe the influence of *Atp10A* on whole-body metabolism, we measured the concentration of free fatty acids (FFA), cholesterol (chol), and triglycerides (TG) in the mouse plasma. While the male mice showed no difference in plasma lipids based on genotype (Figure 4A-C), the female $Atp10A^{-/-}$ mice display substantially elevated plasma concentrations of FFA (Figure 4D), chol (Figure 4E), and TG (Figure 4F) compared to $Atp10A^{+/+}$ controls. To further explore this female-specific dyslipidemia phenotype, we performed fast performance liquid chromatography (FPLC) on plasma to

assess the relative size and lipid content of the different lipoprotein fractions (Figure 4G). We found that the *Atp10A*$^{-/-}$ mice carry most of their TG and cholesterol in smaller sized very low-density lipoprotein (VLDL) and high-density lipoprotein (HDL) particles, respectively (indicated by a shift to the right in the chromatograms). We also compared the AUC of the VLDL (Figure 4H) and HDL (Figure 4I) fractions and found that the *Atp10A*$^{-/-}$ mice trend toward having more lipids in these fractions compared to controls. Together, these results show that *Atp10A* deficiency causes female-specific dyslipidemia and changes to lipoprotein metabolism after HFD feeding.

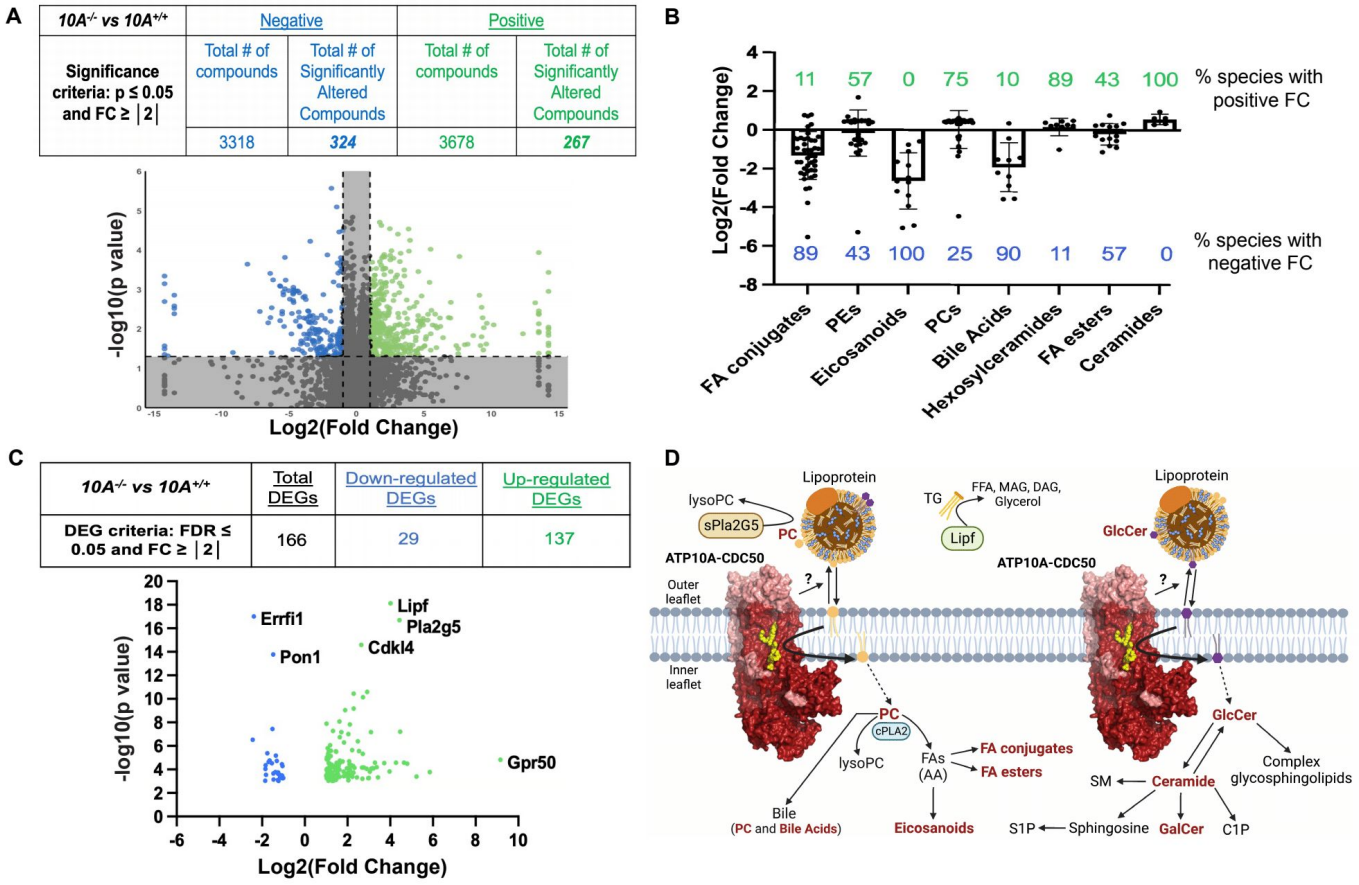

Figure 5. *Atp10A* deletion leads to substantial perturbations in the plasma lipidome and VF transcriptome in female mice on a HFD. (A) Lipid metabolites from fasting plasma were measured by HPLC-IM-MS/MS and the data was processed via Progenesis QI. The table indicates the number of total and significantly changed lipid metabolites (compounds) observed from each ionization mode (Negative and Positive); the volcano plot illustrates the fold changes (FC) of compounds between *10A*$^{-/-}$ vs. *10A*$^{+/+}$ mice, the grey shading indicates changes that did not meet the significance criteria. P-values by ANOVA. (*10A*$^{+/+}$ n=5 samples (8 mice), *10A*$^{-/-}$ n=5 samples (8 mice). (B) The log2(FoldChange) of lipid metabolites compared between *10A*$^{-/-}$ vs. *10A*$^{+/+}$ mice are grouped by indicated categories (green and blue indicate the % of lipid species with positive and negative fold change, respectively, between *10A*$^{-/-}$ vs. *10A*$^{+/+}$ mice; P values ≤ 0.1 by ANOVA). (C) Sequencing of VF mRNA was performed using the Illumina NovaSeq 6000. The table provides the criteria used to calculate the number of differentially expressed genes (DEGs) and how many DEGs were measured; the volcano plot illustrates the DEGs (*10A*$^{+/+}$ n=3,*10A*$^{-/-}$ n=3). (D) Schematic illustrating the metabolic pathways linking ATP10A substrates to observed changes in the plasma lipidome and VF transcriptome. Lipid metabolites with significant changes due to *10A* deletion from panel B are in bold red, the hexosylceramide category includes both GalCer and GlcCer. The protein products from two mRNA transcripts that were significantly upregulated in the VF from *10A*$^{-/-}$ mice (panel C), Pla2G5 and Lipf, are highlighted to show their role in lipid metabolism. Schematic created using Biorender.com. See Supplemental Table 2 for RNASeq KEGG pathway analysis. PC= phosphatidylcholine, AA=arachidonic acid, TG= triglyceride, FA=fatty acids, FFA=free fatty acids, DAG=diacylglycerol, MAG=monoacylglycerol, SM=sphingomyelin, S1P= sphingosine 1-phosphate, C1P= ceramide 1-phosphate, GalCer= galactosylceramide, GlcCer= glucosylceramide.

To get a broader view of the dyslipidemia we observed in the plasma of female *Atp10A*$^{-/-}$ mice, we performed mass spectrometry-based untargeted lipidomics on plasma from female *Atp10A*$^{-/-}$ and *Atp10A*$^{+/+}$ mice after 12 weeks on HFD. We found that *Atp10A* deficiency resulted in statistically significant changes to the abundance of a large number of plasma lipid species; 591 in total, with 324 of these observed from positive ion mode and 267 from negative ion mode lipidomics (Figure 5A, NMDR Data ID:3874). To highlight how *Atp10A* deficiency altered specific classes of lipid species, we plotted the log2(FoldChange) of lipid species that were significantly changed and calculated the % of the lipid species in each group that had a positive fold change (increase in abundance, green values) versus a negative fold change (decrease in abundance, blue values) (Figure 5B). Interestingly we saw modest increases in the abundance of ATP10A's lipid substrates, PC and hexosylceramides (this includes GlcCer and galactosylceramide (GalCer)). We observed that plasma eicosanoid, bile acid and fatty acid (FA) conjugate species were dramatically depleted in *Atp10A*$^{-/-}$ mice compared to *Atp10A*$^{+/+}$ controls. We further probed the influence of *Atp10A* on metabolism by performing RNAseq on VF (Figure 5C, NCBI GenBank accession numbers: SRR24233646, SRR24233645). We found that 166 genes were differentially expressed in *Atp10A*$^{-/-}$ compared to *Atp10A*$^{+/+}$ mice, where 29 were downregulated and 137 were upregulated. Some notable differences were substantial increases in expression of *Lipf* and *Pla2g5,* encoding a TG lipase and a secreted phospholipase, respectively*,* in *Atp10A*$^{-/-}$ mice (Figure 5C, Supplemental Table 2). These studies show that *Atp10A* deficiency results in changes to the abundance of a large number of circulating lipid species as well as expression of mRNA transcripts in VF. Taken together, these results indicate that ATP10A has a substantial role in lipid metabolism in female mice fed a HFD. The potential mechanistic links between the lipid transport activity of ATP10A and whole-body lipid metabolism are shown in Figure 5D. By translocating phospholipids (PLs) from the outer leaflet to the inner leaflet of the plasma membrane, ATP10A provides substrates to intracellular lipid metabolism enzymes for production of bioactive lipid signaling molecules while decreasing the availability of PC and GlcCer to molecules in circulation (i.e. lipoproteins, lipases) (Figure 5D). Thus,

this flipping could affect levels of lipid species in the intracellular space and in circulation (Figure 4B) as well as change the expression levels of lipid handling enzymes (Figure 5C).

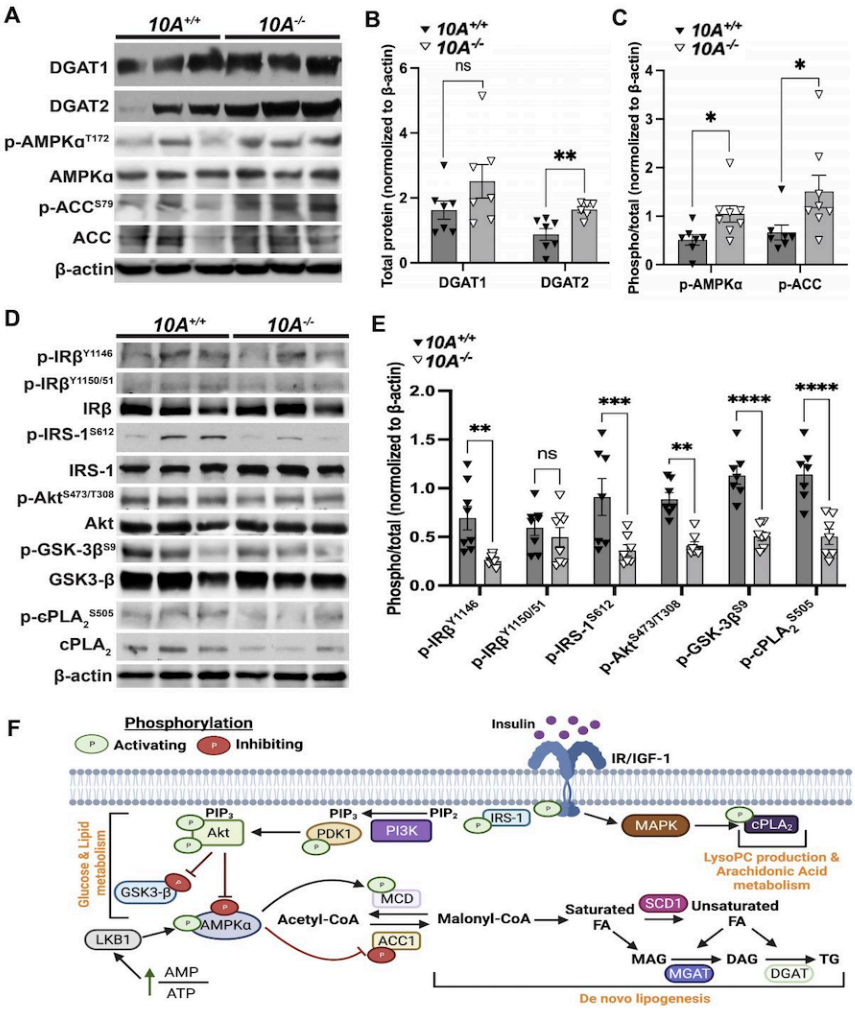

Figure 6. *Atp10A* deletion perturbs liver insulin signaling in female mice fed a HFD. (A, D) Representative blots for total and/or phosphorylated (A) DGAT1, DGAT2, AMPKα, ACC, and (D) IRβ, IRS-1, Akt, GSK-3β, and cPLA$_2$. (B) For DGAT1 and DGAT2 quantitation, total protein was normalized to β-actin levels. (C, E) The phosphoproteins were normalized to their respective total protein and β-actin levels. Mean measurements of 4-6 independent experiments are shown. P value by (B, C) unpaired t-test or (E) 2-way ANOVA with Sidak's multiple comparison test. (A-C, *10A*$^{+/+}$ n=7, *10A*$^{-/-}$ n=7, B: **P=0.0050; C: *P=0.0229, *P=0.0481; D, E, *10A*$^{+/+}$ n=8, *10A*$^{-/-}$ n=8, **P=0.0044, ***P=0.0007, **P=0.0038, ****P=<0.0001,). (F) Schematic adapted from (141) and created using Biorender.com. The illustration shows insulin binding to the insulin receptor and the resulting downstream signaling events that stimulate lysoPC production, AA metabolism, changes to glucose and lipid metabolism; including the promotion of lipogenesis. MAPK= mitogen-activated protein kinase, cPLA$_2$= cytosolic phospholipase 2, IRS-1= insulin receptor substrate 1, PI3K= phosphoinositide 3-kinase, PIP2=phosphatidylinositol 4,5-bisphosphate, PIP3= phosphatidylinositol 3,4,5-triphosphate, PDK1= pyruvate dehydrogenase kinase 1, GSK-3β= glycogen synthase kinase-3 beta, LKB1= liver kinase B1, AMPKα= AMP-activated protein kinase alpha, MCD= malonyl-CoA decarboxylase, ACC1=acetyl-CoA carboxylase, SCD1= stearoyl-CoA desaturase 1, MGAT=monoglycerol acyltransferase, DGAT= diglyceride acyltransferase.

Next, we evaluated potential hepatic mechanisms responsible for the metabolic phenotypes observed in the female mice after HFD, by examining key regulators of energy and lipid metabolism in the liver (Figure 6F). Diacylglycerol acyltransferases (DGATs) catalyze the final step in TG synthesis (Figure 6F) and we found that DGAT2 was significantly elevated in HFD-fed *Atp10A*$^{-/-}$ females (Figure 6A,B). AMP kinase (AMPK) is a central regulator of energy metabolism that inhibits acetyl-CoA carboxylase (ACC) by phosphorylating it at S79; and thus inhibits the lipogenesis pathway (Figure 6F). We showed the liver kinase B1 (LKB1)-dependent stimulatory phosphorylation of AMPK at T172 and inhibitory phosphorylation of ACC were significantly increased in *Atp10A*$^{-/-}$ females (Figure 6A,C); suggesting downregulation of *de novo* lipogenesis in liver. Indeed, we found that *Atp10A*$^{-/-}$ mice have less liver FFA (Supplemental Figure 5A). Thus, excess TG in *Atp10A*$^{-/-}$ plasma is likely driven by FFA from adipose tissue that is converted to TG and secreted by the liver. We also measured levels of several other liver lipid species and found no changes in total cholesterol, cholesterol esters (CE), unesterified cholesterol, TG, PL, or ceramides based on genotype (Supplemental Figure 5B-G). We did find that there was an increase in the abundance of unsaturated vs. saturated species of several TG and PL species and one CE species (Supplemental Figure 5H, I). Even though the amount of cholesterol and TG in the liver was not different based on genotype, Oil Red O stained lipid droplets from the *Atp10A*$^{-/-}$ mice were larger on average compared to *Atp10A*$^{+/+}$ (Supplemental Figure 5J-L). Therefore, *Atp10A* deficiency results in changes to the levels and phosphorylation state of several proteins involved in lipid metabolism as well as changes to the amount of and saturation state of several lipid species in the liver.

Next, we probed the phosphorylation state of proteins in the insulin signaling pathway that are upstream of DGAT 1/2, ACC, and AMPK within the liver (Figure 6F). We found a decrease in the activating phosphorylation of the insulin receptor β subunit (IRβ) at Y1146, insulin receptor substrate-1 (IRS-1) at S612, and Akt at S473/T308. Lastly, we observed a decrease in the inhibitory phosphorylation at GSK-3B at S9 in *Atp10A*$^{-/-}$ females (Figure 6D,E). Interestingly, we also observed a decrease in the activating phosphorylation of cytosolic phospholipase 2 ($cPLA_2$) at S505 in the *Atp10A*$^{-/-}$

mice (Figure 6D,E). $cPLA_2$ is an enzyme that catalyzes the hydrolysis of PLs, such as PC, to lysoPLs and AA, and this fatty acid species can be oxidized to form eicosanoids. These results are indicative of impaired insulin signaling in the liver in *Atp10A*$^{-/-}$ mice, as plasma insulin levels did not differ based on genotype (Figure 3F). Altogether, these studies reveal that *Atp10A* deficiency in females fed a HFD results in several alterations to the liver, including in lipid metabolism and handling as well as in insulin signaling.

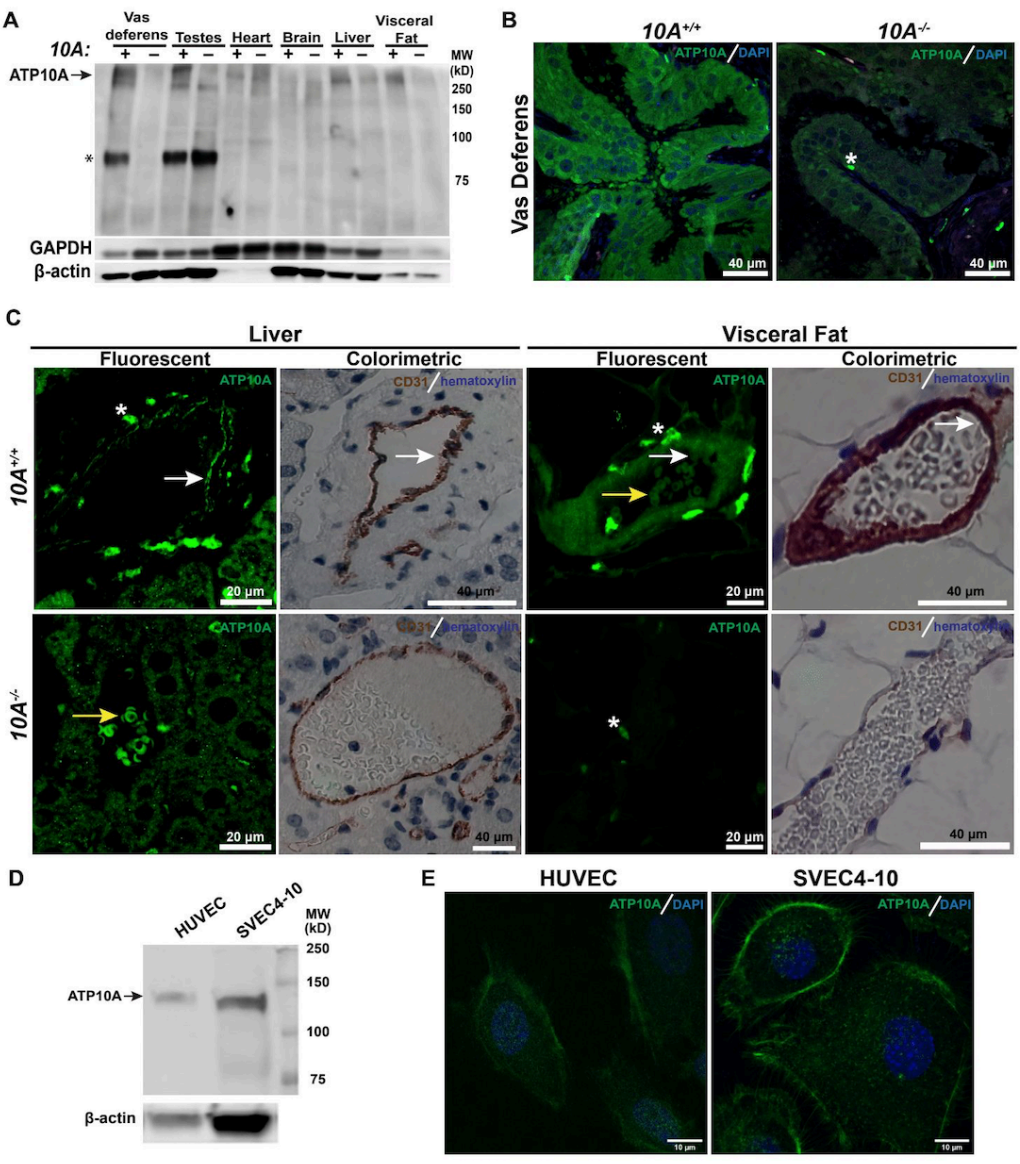

Figure 7. **ATP10A is expressed in endothelial cells.** (A) Total tissue lysates from the *10A*$^{+/+}$ and *10A*$^{-/-}$ mice (vas deferens,testes, heart - males; brain, liver, VF - females) were subjected to Western immunoblot analysis for expression of ATP10A (100 μg total protein). ATP10A migrates as a high-molecular-weight smear in the tissue samples. β-actin and GAPDH served as loading controls. The asterisk indicates a nonspecific band that appears in some tissues. (B) Representative immunofluorescent images of vas deferens showing expression of ATP10A and DAPI. Scale bar= 40 μm. The white asterisk indicates background staining (*10A*$^{+/+}$ n=1, *10A*$^{-/-}$ n=1). (C) Representative immunofluorescent and colorimetric images of livers and VF from females showing expression of ATP10A (fluorescence), CD31, and hematoxylin (colorimetric). Scale bar: fluorescent images=20 μm; colorimetric images= 40 μm. The white asterisk indicates background staining, the white arrows indicate locations that are positive for ATP10A expression (fluorescent) and CD31 expression (colorimetric) in sequential sections, the yellow arrows indicate auto fluorescent red blood cells (Liver: *10A*$^{+/+}$ n=3, *10A*$^{-/-}$ n=1; VF: *10A*$^{+/+}$ n=3, *10A*$^{-/-}$ n=2). (D) Total lysates from routinely grown HUVEC and SVEC4-10 were subjected to Western immunoblot analysis for expression of ATP10A (50 μg total protein). β-actin served as loading control. (E) Representative immunofluorescent images of routinely grown HUVEC and SVEC4-10 showing expression of ATP10A and DAPI. Scale bar=10 μm.

Next, we wanted to determine where ATP10A is expressed in mice to better understand the potential mechanisms behind its effects on metabolism. To do this, we produced an anti-ATP10A antibody and tested its specificity in HeLa cells overexpressing an HA-tagged ATP10A (Supplemental Figure 7A, B). ATP10A is large, integral membrane protein that often aggregates when subjected to SDS-PAGE and migrates as a high-molecular weight smear above 250 kDa (Supplemental Figure 6B). We then probed several mouse tissues with the anti-ATP10A antibody via immunoblotting and found a band specific for ATP10A above 250 kD in vas deferens, testes, liver, and VF from *Atp10A*$^{+/+}$ mice, that was absent in the *Atp10A*$^{-/-}$ tissues (Figure 7A). We did not observe ATP10A via immunoblotting in the heart or brain (Figure 7A), however using immunofluorescence imaging, we observed weak ATP10A staining in the heart that appeared to be in vessels based on morphological assessment (Supplemental Figure 6C). We applied this method to vas deferens samples and observed robust ATP10A-positive staining of most cells in *Atp10A*$^{+/+}$ mice that was not present in the *Atp10A*$^{-/-}$ mice, further confirming the specificity of the anti-ATP10A antibody (Figure 7B). Additionally, for liver and VF, we observed specific staining for ATP10A that appeared to be in ECs (Figure 7C). To confirm endothelial expression, we used immunohistochemistry to examine CD31, a vascular EC marker, on sequential tissue slides (to examine the same vessels seen via immunofluorescence). We found that cells that were positive for ATP10A staining were also positive for CD31 staining in *Atp10A*$^{+/+}$ liver and VF, and that the ATP10A signal was absent in ECs from *Atp10A*$^{-/-}$ mice (Figure 7C). Next, we detected endogenous expression of ATP10A in human umbilical vein ECs (HUVECs) and ECs from mouse auxiliary lymph nodes (SVEC4-10) via immunoblot analysis (Figure 7D). Note that the ATP10A band migrated just below 150 kD, instead of at the top of the gel (Figure 7A), presumably because the decreased complexity of the cell culture lysates, compared to tissues, helped improve solubilization and denaturation of the protein. Additionally, we observed ATP10A staining, primarily at the plasma membrane, via immunofluorescence imaging in both HUVEC and SVEC4-10 (Figure 7E). These experiments show that ATP10A is expressed in mouse vas deferens, as well as ECs in heart, liver and VF, as well as human vascular ECs (HUVECs) and mouse auxiliary lymph nodes (SVEC4-10).

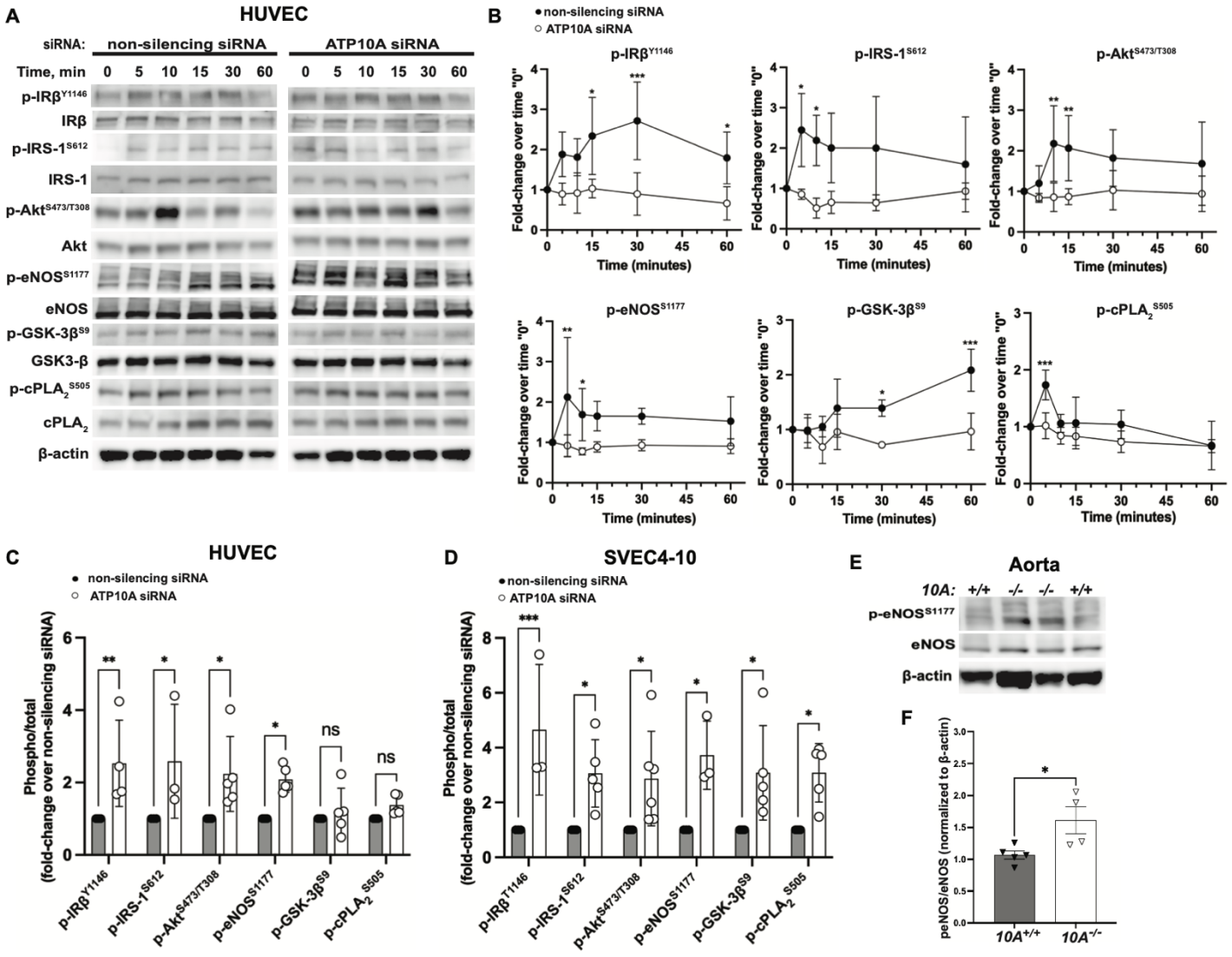

Figure 8. **ATP10A expression regulates insulin signaling pathways in cultured endothelial cells and mouse aorta**. (A) Representative blots and (B) quantitative analysis from immunoblots of phosphorylated and total IRβ, IRS-1, Akt, eNOS, GSK-3β, and cPLA2 from HUVEC transfected with non-silencing siRNA or ATP10A siRNA and then treated with insulin for 0-60 mins. (C,D) Quantitative analysis of immunoblots at time 0 from (C) HUVEC or (D) SVEC4-10. (E) Representative blots and (F) quantitative analysis from immunoblots of phosphorylated and total eNOS from total aorta lysates from female mice (10A+/+ n=5, 10A-/- n=4, *P=0.0290). Mean measurements of 3-6 independent experiments are shown. (B-D) *p≤0.05; **p≤0.005; ***p≤0.0005 between cells transfected with non-silencing or ATP10A siRNA by 2-way ANOVA with Sidak's multiple comparison test, (F) P value by unpaired t-test.

We next determined the impact of ATP10A expression on insulin signaling *in vitro* with the HUVEC and SVEC4-10 ECs. To do this, we first used an siRNA approach to knockdown ATP10A and

confirmed the reduction of this protein by immunoblot (Supplemental Figure 7A,D HUVEC knockdown: ~50%, SVEC4-10 knockdown: ~70%) and immunofluorescence (Supplemental Figure 7B,E). The ATP10A siRNA-treated or control cells (non-silencing siRNA) were stimulated with insulin and samples were collected over a 60-minute time course (Figure 8A,B, Supplemental Figure 8A,B). The control cells responded with a rapid increase in IR phosphorylation accompanied by increased phosphorylation of IRS-1, Akt and eNOS. Akt directly phosphorylates eNOS on S1177 and GSK-3β on S9, thus confirming the insulin-dependent activation of Akt in these cells. $cPLA_2$ phosphorylation, which is downstream of the Ras/ERK arm of this pathway, was also stimulated by insulin. By striking contrast, the ATP10A siRNA-treated cells failed to respond to insulin stimulation and no significant change in phosphorylation was observed for any downstream component of the insulin-dependent pathway. However, we noticed that the level of phosphorylation for each tested protein appeared elevated in the knockdown cells relative to the control cells at time 0, for which no insulin was added. Therefore, we re-examined the time 0 samples from control and knockdown cells side-by-side on the same immunoblot for quantitation (Figure 8C,D, Supplemental figure 7C,F). Indeed, the basal levels of IRβ, IRS-1, Akt and eNOS phosphorylation were elevated two to four-fold in ATP10A siRNA-treated cells. GSK-3β and $cPLA_2$ were also significantly hyperphosphorylated in ATP10A knockdown SVEC4-10 cells but were not significantly different in the HUVECs. Altogether, basal insulin signaling, observed at time 0, in cultured ECs was substantially elevated in ATP10A siRNA-treated cells compared to control.

Next, we sought to determine if basal signaling through Akt is elevated in ECs of the *Atp10A*$^{-/-}$ mouse. To do this, we measured the extent of eNOS phosphorylation by Akt in aorta, a tissue rich in ECs. eNOS is almost exclusively expressed in ECs, therefore p-eNOS^{S1177} levels provide a readout of Akt activity in these cells. We found that *Atp10A*$^{-/-}$ mice exhibit elevated basal phosphorylation of eNOS in aorta compared to *Atp10A*$^{+/+}$ mice (Females: Figure 8E,F; Males: Supplemental 8C,D). Taken together, these results reveal a role for ATP10A in regulating insulin signaling in ECs (HUVEC, SVEC4-10, aorta). Decreasing ATP10A expression in ECs results in elevated phosphorylation of proteins in the

insulin signaling pathway during basal conditions, which ablates the ability of the cells to respond to additional insulin stimulus (added insulin).

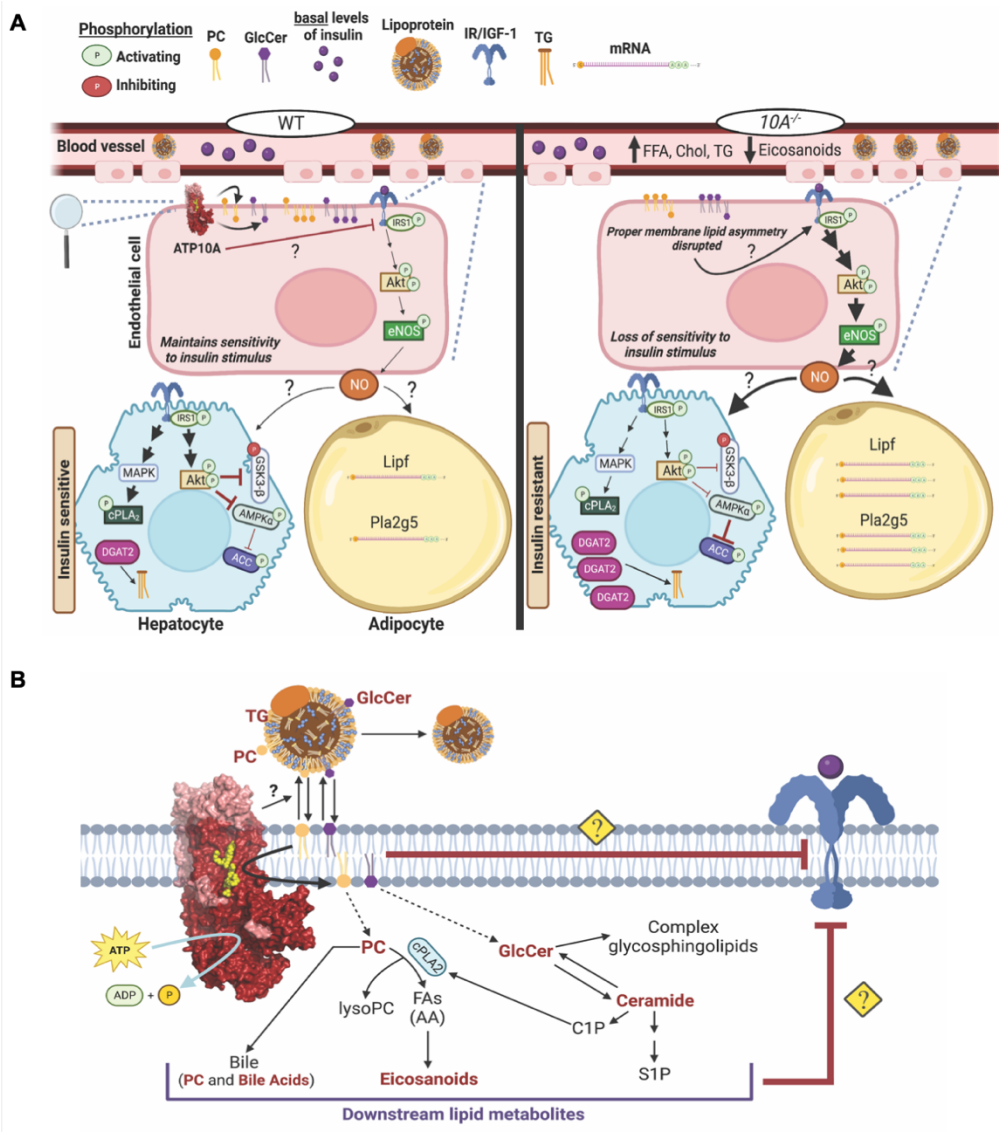

Figure 9. Model of ATP10A's role in metabolism. (A) Schematic illustrating ATP10A maintaining insulin sensitivity in ECs. Left panel: WT ATP10A in ECs blocks IR/IGF1R signaling, via an unknown mechanism, during basal levels of insulin and downstream of this; the tissues associated with the ECs (hepatocytes and adipocytes) also maintain their sensitivity to insulin. Right panel: When ATP10A is knocked out/down; ECs lose their sensitivity to insulin stimulus due to IR/IGF1R inappropriately responding to basal levels of insulin, downstream of this the tissues associated with the ECs also lose their sensitivity to insulin stimulus (become insulin resistant). (B) Schematic illustrating ATP10A's function specifically at the plasma membrane (what is being magnified by magnifying glass in (A)). ATP10A translocates PC and GlcCer from the outer leaflet to the inner leaflet, this could potentially affect how lipoproteins interact with the plasma membrane, the lipid platforms where proteins reside (insulin receptor), and the abundance of bioactive lipid species in the cytosolic space (that could also potentially affect IR/IGFR1 signaling). Schematics created using Biorender.com.

DISCUSSION AND CONCLUSIONS

This study reveals a requirement for ATP10A in protecting female mice from HFD-induced dyslipidemia and endothelial dysfunction. *Atp10A*$^{-/-}$ mice fed a HFD do not gain more weight or exhibit perturbed glucose metabolism compared to controls (Figure 3). Despite the normal weight gain, female *Atp10A*$^{-/-}$ mice display elevated plasma levels of cholesterol, TGs and FFAs, and these parameters are unchanged in male *Atp10A*$^{-/-}$ mice relative to controls (Figure 4). The plasma lipidome and adipose transcriptome are also substantially perturbed in the knockout female mice (Figure 5), and basal insulin signaling in the liver is depressed although the plasma insulin levels are comparable to wild-type littermates (Figure 6). We also show that ATP10A is expressed in ECs (Figure 7). In contrast to the liver, *Atp10A* deficiency in ECs causes hyperactive basal signaling through IRS-1, Akt, $cPLA_2$, and eNOS as well as a failure to respond to additional insulin (Figure 8). Our results suggest that dysregulation of IR-dependent signaling within ECs results in impaired insulin signaling in hepatocytes and alterations to transcription in adipocytes (Figure 9A). Additionally, we propose that ATP10A-dependent translocation of PC and GlcCer from the outer leaflet to the inner leaflet of the plasma membrane promotes desensitization of the insulin receptor by modulating the lipid environment or through the production of bioactive lipids in the cell (Figure 9B).

Prior studies analyzing mice with an overlapping series of radiation-induced deletions encompassing the *p* locus on chromosome 7 implicated *Atp10A* deficiency in diet-induced obesity, insulin resistance, and hyperlipidemia [59, 60]. These phenotypes were observed in heterozygous mice that inherited the chromosomal deletion maternally, suggesting that the paternal *Atp10A* allele was silenced. However, we found no evidence for obesity or metabolic defects in *Atp10A*$^{+/-}$ heterozygous mice inheriting the KO allele paternally or maternally (Supplemental Figure 4), nor did the *Atp10A*$^{-/-}$ homozygous mice display diet-induced obesity (Figure 3). These results are in contrast to previous reports, most likely because the mice used in those studies had a large chromosomal deletion that, in addition to *Atp10A*, removed several other genes, some of which are known to be imprinted [127]. It is

also possible that differences in the strain background or rearing environment alter the susceptibility of *Atp10A*$^{-/-}$ mice to diet-induced obesity and glucose metabolism perturbations.

The molecular basis for female-specific dyslipidemia we observe in *Atp10A*$^{-/-}$ mice is unclear. There are established differences in disease severity and prevalence between men and women [128]. Premenopausal women tend to have lower cardiovascular risks compared to men which could be due to the effects that estrogen exerts on the endothelium [129]. The *Atp10A* promoter is predicted to have a transcription factor binding site for estrogen receptor alpha (Genecards.org, QIAGEN), so it is possible that differences in expression due to sex contribute to the consequences of *Atp10A* deletion. However, the effect of sex on the phenotypes caused by *Atp10A* deficiency in ECs is not apparent because we observe similar signaling perturbations in HUVECs, cells from male and/or female humans, SVEC4-10 cells from male mice, and aorta from female and male mice (Figure 8E,F, Supplemental Figure 8C,D). Thus, endothelial dysfunction in *Atp10A* deficient mice occurs in both sexes, however, the dyslipidemia is female-specific, suggesting that this phenotype is either promoted by estrogen or suppressed by testosterone. Further studies are needed to define the basis of the observed sex-specific dyslipidemia.

Atp10A deficient female mice exhibit dyslipidemia characterized by elevated plasma FFA, cholesterol, TG, and alterations in the size and lipid content of both VLDL and HDL (Figure 4D-G). We suggest that the increased release of FFA from adipose (Figure 6F) drives an increase in TG synthesis in the liver and its secretion in VLDL [130-132]. Dysregulation in adipose could also be responsible for the excess circulating cholesterol [133]. Another potential source of TGs is *de novo* lipogenesis in the liver; however, *Atp10A* deficient mice exhibit an increase in activating phosphorylation of hepatic AMPK (Figure 6A,C), a master regulator of lipid metabolism, that increases fatty acid oxidation and decreases *de novo* lipogenesis [134], as well as decreased total liver FFAs (Supplemental Figure 5A). Thus, it is unlikely that FA production in the liver is driving the excess plasma TG. Mice naturally lack the cholesterol ester transfer protein (CETP) and have increased cholesterol in HDL relative to humans. As

expected, *Atp10A* deficient mice carry most of their circulating cholesterol in HDL but unexpectedly, this cholesterol is mostly carried in smaller HDL particles compared to controls. This observation may suggest a potential issue with the quality of HDL in these mice [135]. Additionally, *Atp10A* deficient mice show reduced circulating levels of bile acids (Figure 5A,B), which are important signaling lipids with implications in cholesterol metabolism and cardiovascular health [136]. Further research is needed to understand the mechanisms underlying dyslipidemia observed in *Atp10A* deficient mice and if this defect is caused by endothelial dysfunction.

The response of ECs to insulin is mediated by IRs and can affect the systemic response to insulin by inducing vasodilation via activation of eNOS, thereby affecting glucose disposal [137, 138]. Therefore, the endothelium itself is a target of insulin and insulin resistance can exist at the level of ECs. We discovered that ATP10A is expressed in ECs (Figure 7), *Atp10A* deficiency in ECs results in hyperactive signaling at basal levels of insulin (Figure 8), and *Atp10A* deficient mice display impaired insulin signaling in the liver (Figure 6). A model of excess insulin signaling in ECs resulting in hepatic insulin resistance/impaired insulin signaling has been previously described [139]. The authors showed that mice carrying an EC-specific knockout of all three FoxO isoforms display hyperactive insulin signaling in ECs and hepatic insulin resistance, which was attributed to excessive eNOS activity and nitrosylation of hepatic IRs. Further studies are needed to determine if hyperphosphorylation of eNOS observed in *Atp10A* deficient ECs (Figure 8E) leads to excess nitrosylation of IRs in underlying tissues. Interestingly, a vascular EC-specific deletion of the IR perturbs the kinetics of insulin action on peripheral tissues and accelerates the development of systemic insulin resistance in HFD-fed mice, implying either an important role for the IR in insulin transport across the vascular endothelium or insulin-dependent signaling in ECs [140]. Moreover, HFD-induced insulin resistance appears to develop first in the vasculature, accompanied by changes in the production of nitric oxide, before it develops in muscle, liver or adipose tissue [141, 142]. These findings support the idea that *Atp10A* deficiency modulates the endothelial response to insulin first, and then, impaired insulin signaling in the liver occurs subsequently. Our ability to detect ATP10A protein in liver ECs but not in the hepatocytes

(Figure 7C) adds further support to this model. However, it is still a possibility that ATP10A is expressed in hepatocytes, but our methods might not be sensitive enough to detect the signal.

Hyperactive signaling in ATP10A deficient ECs appears to originate at the level of the IR; however, due to a lack of antibodies that can distinguish between phosphorylated IR and IGF1R, the p-IRβ labeled in our western blots could also represent p-IGF1R (Figure 8, Supplemental Figure 7&8). This is a common problem given the high homology between IR and IGF1R [143]. Therefore, the specific receptor(s) responsible for the hyperactive basal signaling observed in ATP10A knockdown ECs is still an open question. We have focused our studies on the IR, but it is also possible that other receptor tyrosine kinases that activate the PI3K/Akt and Ras/MAPK pathways are also hyperactivated in ATP10A-deficient ECs.

Our studies indicate that *Atp10A* deficiency may disrupt the phosphoregulation of $cPLA_2$ and the production of eicosanoids, which may further exacerbate endothelial dysfunction. We found a reduction of activating phosphorylation of cPLA2 in the liver and an increase in ECs (Figure 6D,E, Figure 8) as well as a depletion of circulating levels of eicosanoids (Figure 5A,B) due to *Atp10A* deficiency. $cPLA_2$ can hydrolyze PC to release AA which can be oxidized to form eicosanoids, bioactive lipids with roles in inflammation and vasculature maintenance [108, 109]. $cPLA_2$ can only act on lipids in the cytosolic leaflet and ATP10A could potentially provide additional PC substrate to this enzyme, derived from the extracellular leaflet or an external source, such as lipoproteins. We hypothesize that ATP10A can modulate $cPLA_2$ activity by modulating signaling pathways that activate $cPLA_2$ (Figure 9A) as well as by increasing substrate availability in ECs (Figure 9B). Interestingly ATP10A could also translocate GlcCer to potentially promote synthesis of ceramide 1-phosphate (C1P), another activator of $cPLA_2$ [144] (Figure 9B). $cPLA_2$ hydrolysis of PC also produces lysoPC, a bioactive lipid that may link saturated FAs to insulin resistance [145]. Despite the reduction of eicosanoids in the plasma, there was no substantial difference in the levels of circulating lysoPC based on genotype. It is possible that the increased expression of *Pla2g5* (Figure 5C), a secreted phospholipase, may have compensated for the perturbations in $cPLA_2$ signaling and normalized lysoPC levels in the plasma. Altogether, the

modulation of $cPLA_2$ activity due to *Atp10A* deficiency could alter the levels of vasoactive compounds, and further work is needed to better define the specific influence of ATP10A on eicosanoid production.

HUVECs and ECs in mouse aorta are macrovascular cells, and we have not studied the influence of ATP10A on microvessels. This is an important distinction to make because macrovessels and microvessels exhibit distinct characteristics and respond to stimuli differently; indeed, eNOS has been shown to mediate differential effects in macro- and microvessels [146]. We observed similar, but distinct, signaling defects in ATP10A knockdown HUVECs and SVEC4-10, mouse lymphatic ECs. Upon knockdown of ATP10A, both cell types exhibited insulin resistance characterized by hyperactive basal signaling; however, unlike in HUVECs, SVEC4-10 displayed a significant increase in activating phosphorylation of GSK3- and $cPLA_2$ at basal insulin levels (Figure 8C,D). Therefore, ATP10A could have distinct effects in lymphatic vascular ECs compared to blood vascular ECs and this also requires further study. Insulin resistance may develop in the vasculature before it develops in other tissues, therefore, therapeutics directed at improving insulin sensitivity in ECs, such as an ATP10A agonist, could potentially halt further disease progression.

Chapter 3: ATP10A deficiency results in male-specific infertility in mice

INTRODUCTION

Infertility remains a significant health problem that affects 8-12% of couples worldwide and 40-50% of cases are due to male-specific factors [148]. Male factor infertility is often due to poor semen quality; including low sperm count, reduced motility, and altered morphology. There are several potential causes of male infertility, such as hormonal imbalances, physical abnormalities, sexually transmitted diseases, lifestyle factors, and genetic factors [149]. However, the cause of male factor infertility remains unknown in about 40% of patients [150, 151]. Therefore, the discovery of new genetic factors that result in male-specific infertility could help elucidate the molecular basis of this type of reproductive defect.

One potential genetic factor is *ATP10A*, a gene that encodes for a lipid translocating P4-ATPase. ATP10A translocates phosphatidylcholine (PC) and glucosylceramide (GlcCer) [90] across the plasma membrane and transcripts from this gene are expressed in several human [152, 153] and mouse tissues [154, 155] including reproductive organs. While the involvement of ATP10A in metabolism has been previously described [59, 60] (ATP10A was previously called ATP10C), its role in fertility remains largely unexplored. However, there is evidence that type 2 diabetic patients exhibit differential DNA methylation patterns of *ATP10A* in human spermatozoa, compared to healthy individuals [156]. Additionally, the lipid substrates of ATP10A have established roles in fertility. PC is a major component of membranes in all cells and levels of this phospholipid and its acyl chain composition can substantially affect the function of the male reproductive tract [157-160]. Furthermore, PC is an important component of the sperm plasma membrane and levels of this phospholipid can act as an indicator of sperm fertilization potential [161, 162]. Additionally, supplementing growth medium with PC expedites the *in vitro* development of human sperm; assessed by the molecular response of the sperm acrosome to progesterone (acrosomal responsiveness) [163]. GlcCer metabolism has also been implicated in fertility; mice deficient for the non-lysosomal glucosylceramidase (*Gba2*), an enzyme

that cleaves GlcCer into glucose and ceramide, exhibit GlcCer accumulation in the testes and impaired fertility associated with abnormal acrosomes and defective sperm mobility [164].

The mouse genome contains 15 P4-ATPase genes annotated *Atp8A1* to *Atp11C* and a few members of this protein family have been implicated in male fertility. *Atp8A3* is highly expressed in the acrosome region of sperm and disruption of this gene causes a modest reduction in male fertility; where morphologically normal and fully motile sperm are produced by the mutant males but the acrosome reaction *in vitro* is abrogated [165]. The similar *Atp8B3* gene is also highly expressed during spermatogenesis although its impact on fertility is unknown [30]. The *Atp10B* and *Atp10D* genes are highly homologous to *Atp10A* and encode PC/GlcCer (*Atp10B*) [166] and GlcCer (*Atp10D*) [90] translocases. Interestingly, the C57Bl/6J inbred mouse line carries a naturally occurring nonsense mutation in the middle of the *Atp10D* open reading frame [92]. The truncated ATP10D protein in C57Bl/6J mice lacks structurally essential components of the transporter and should be nonfunctional. The extent of functional redundancy, if any, between the *Atp10A* and *Atp10D* genes is unknown.

Given the transcription of *ATP10A* in male reproductive organs and its involvement in the translocation of bioactive lipids with roles in fertility; we examined fertility parameters in C57Bl/6J mice lacking *Atp10A*. We also corrected the *Atp10D* nonsense codon in C57Bl/6J mice to the wild-type glutamine codon to determine if *Atp10A* deficiency alone is sufficient to cause male-specific infertility.

MATERIALS AND METHODS

Animals. All mouse experiments were approved under the Vanderbilt University Institutional Animal Care and Use Committee. Mice were housed in 12 h light/dark cycles in temperature and humidity-controlled facilities with ad-libitum access to diet and water (in the Barrier facility). Mice in this study were sacrificed via CO_2 euthanasia systems, operating at the recommended flow rates, followed by cervical dislocation; this method is an acceptable euthanasia method according to the American

Veterinary Medical Association (AVMA) guidelines. The mouse studies described in this manuscript are reported in accordance with the ARRIVE guidelines (https://arriveguidelines.org/).

Randomization. Experimental mice were generated using het x het breeding schemes. WT and KO mice were assigned to studies as they became available from the breeding process.

Creating mouse models. The *Atp10A* mouse model (*Atp10Aem1(Vtrg))* and the *Atp10D* mouse model (*Atp10Dem1 (Vtrg))* were created via CRISPR-Cas9 in collaboration with the Vanderbilt Genome Editing Resource. **For the *Atp10A* mouse model**: Guide RNAs (crRNA) were created to target *Atp10A* on chromosome 7, exon 2 (note that exon 2 encodes a structurally essential part of the protein and there are no functional transcripts detected that skip exon 2): Target Intron 1-2: TGACTGCTTAATGATTCGAGG, GAGTGACTGCTAATGATCG, Target Intron 2-3: GGAAAAAGCCCAATTCCACAC, AGCCCAATCCACACAGGAAC. Approximately 608 bp were deleted using this method: nucleotides 58389679-58390287 (NCBI reference sequence: NC_000073). More details about the creation and validation of the *Atp10A* mouse model can be found in [167]. **For the *Atp10D* mouse model**: The purpose of the mouse model was to correct the premature stop codon in the *Atp10D* allele in C57BL/6J mice with a glutamine seen in other mouse models (X817Q). A guide RNA (crRNA) was created to target *Atp10D* on chromosome 5 (nucleotides 72203329-72298771 bp, + strand): cRNA: AGTCAAAGGGCAGAATGTGT. The donor DNA sequence was: TATGCCGCCAGAGCTTACCGTTGCACTTTACAGTCTCGGACCCCAGAGCAGGTCATGGTGGACTT TGCTG CTTTGGGCTCATTAACATTT C[1]AG[2]CTG[3]CTT[4]CACATTCTGCCCTTTGACTCTGTAAGGAAAAGAATGTCGGTCGTGGTCAGGCATC CTCTTTCCAAACAAGTCGTGGTGTAT. The superscript numbers next to the nucleotides indicate the following mutations: **1**. T to C introduces the desired STOP to Q correction. **2**. A to G is a silent mutation (CAA to CAG) that along with mutation 1 and 3 introduces a PvuII restriction site for screening and genotyping purposes. **3**. C to G is a silent mutation (CTC to CTG = L) that along with mutation 1 and 2 introduces a PvuII restriction site and mutates the PAM in the guide RNA. **4.** A to T is a silent

mutation (CTA to CTT = L) that serves as a second mismatch, that along with the PAM mutation, ensures inhibition of Cas9 retargeting. The underlined sequence indicates the crRNA location. **For both mouse models**: CRISPR editing reagents were delivered into the pronuclei of one-cell fertilized mouse zygotes (C57BL/6J). The resulting pups were biopsied and screened by PCR and Sanger sequencing. The predicted founders were bred to WT C57BL/6J animals and the offspring were genotyped (N1 generation). The offspring with the appropriate genotype were then backcrossed two more times.

Genotyping. Mice were genotyped using tail DNA. The *Atp10A* DNA products were detected via PCR (Q5 DNA Polymerase, NEB) followed by gel electrophoresis; *Atp10A-F* (GTGCACTGTATTTGTCTGCCTGTTCC), *Atp10A-R (*GGTCCTTTGAAGAGATAATGTTCCCAAC). For *Atp10D* mice: *Atp10D* DNA products were detected via PCR (Q5 High-Fidelity Polymerase, NEB, catalog #M0491S) followed by gel electrophoresis; *Atp10D*-F (CAAAACTGTCACCTCCTATGGA), *Atp10D*-R (GTATACACCACGACTTGTTTGG) for visualization (expected band size: 567 bp). After confirming amplification of the expected target via gel electrophoresis, PCR samples were purified (QIAquick spin column (lot No. 166028242)) and sent to Genewiz (https://www.genewiz.com/) for sequencing or a restriction digest reaction was done (PvuII-HF enzyme (NEB, catalog # R3151S), followed by gel electrophoresis and visualization. PCR products from *Atp10D* mice without the X817Q allele were not cut during the restriction digest (1 band on the gel (567 bp)) and those with the X817Q allele were cut (2 bands on the gel (567 bp, ~400 bp)).

Generation of ATP10A antibodies. Anti-ATP10A antibodies were produced by Vanderbilt Antibody and Protein Resource. ATP10A peptides 1 (27 RTRTVRSNLLPPC 38), 3 (498 HKTQSIKSHRRTC 510) and 5 (1280 QTLLGDPLFYLTC 1292) for antibody production were chosen based on conservation between mouse and human ATP10A orthologs, lack of conservation with ATP10B and ATP10D paralogs, and predicted water solubility (https://pepcalc.com) (Supplemental Figure 9A,B). Peptide epitopes were synthesized (GenScript, USA, Inc.) with a C-terminal Cys residue and conjugated to

Imject™ Maleimide-Activated mcKLH, Imject™ Maleimide-Activated BSA, and SulfoLink™ Coupling Resin following the manufacturer's recommended protocol (ThermoFisher Scientific) by the Vanderbilt Antibody and Protein Resource (VAPR) group. The three peptide-Keyhole Limpet Hemocyanin (KLH) conjugates were used for antibody production in a single rabbit (VU579, Cocalico, Stevens, PA). Antibodies recognizing the peptide epitopes were purified from the rabbit by differential affinity chromatography using the peptide conjugated resin. Briefly, 5 ml of antisera was passed over the peptide 1 column (2 ml) and the material that failed to bind was then applied sequentially to the peptide 3 and 5 columns. After washing with 40-50 ml PBS, bound antibodies were eluted from each column with 8.5 ml of 100 mM glycine, pH 2.5 and collected in tubes containing 1.5 M Tris-HCl, pH 8. Finally, to ensure peptide specificity, antibodies eluted from one peptide column were applied sequentially to the other two columns and the flow-through was retained. Affinity purifications were performed in duplicate to generate anti-peptide 1A and 1B, anti-peptide 3A and 3B, and anti-peptide 5A and 5B antibodies (only 1 replicate is shown in Supplemental Figure 9C).

Cell cultures and immunoblot analysis for assessment of specificity of anti-ATP10A antibodies. WT HeLa cells (WT) or HeLa cells that were transfected with an HA-tagged ATP10A overexpression vector (HA-ATP10A-OE; a generous gift from Dr. Hye-Won Shin) were used to assess the specificity of the affinity purified anti-ATP10A antibodies. Briefly, WT and HA-ATP10A-OE HeLa cells were maintained in growth medium, DMEM with 10% FBS and 1% penicillin/streptomycin (Life Technologies, Gaithersburg, MD), at 37 ^{o}C with 5% CO_2. For immunoblot analysis, cells were cultured in growth medium in 100 mm cell culture plates to 90-100% confluency. Cells were washed with PBS and total protein extraction was performed using M-PER reagent (Thermo Scientific, Waltham, MA, USA) with phosphatase and phosphatase inhibitor cocktails 1 and 2 (Sigma-Aldrich, P5726 and P0044, respectively). Protein concentration was quantified using BCA Reagent (Pierce, Rockford, IL). Protein extracts (40 µg) were subjected to Western immunoblot analysis using anti-ATP10A peptides 1, 2 and 3 antibodies (1:200 dilution). Anti-HA antibody (catalog #3274S, Cell Signaling) were used as a positive

control. Immunoblots were developed using the Western Lightning Chemiluminescence Plus detection system (PerkinElmer, Wellesley, MA) according to the manufacturer's protocol. Images of the immunoblot bands was obtained using AI600 CCD Imager for chemiluminescent assays (Amersham). Only anti-peptide 1 recognized full-length ATP10A (Supplemental Figure 9C). Anti-peptide 1 antibodies were used in this study.

Tissue collection and immunoblot analysis. Western immunoblots were initially performed and quantified blinded to the genotype. After unblinding, samples were grouped by genotype and re-run for presentation of the data. Testes and vas deferens tissues were collected from mice after CO_2 sacrifice and cervical dislocation and were flash frozen in liquid nitrogen and then kept at -80^{o}C until further processing. For immunoblot analysis, tissues were then weighed and lysed in T-PER reagent (Thermo Scientific, Waltham, MA, USA) with protease inhibitors (Sigma-Aldrich, P8340, St. Louis, MO, USA) and phosphatase inhibitor cocktails 1 and 2 (Sigma-Aldrich, P5726 and P0044, respectively), using a Polytron homogenizer. Protein concentration was quantified using BCA Reagent (Pierce, Rockford, IL). Protein extracts (100 µg) were subjected to Western immunoblot analysis. The following primary antibodies were used for detection of: ATP10A (Vanderbilt Antibody and Protein Resource, Vanderbilt University; 1:200), FSHR (LS-C331489/121448, LSBio; 1:1,000), LHCGR/LHR (LS-C334599/229916, LSBio; 1:1,000), phospho-ERK1/2$^{T202/Y204}$ (#4370, Cell Signaling; 1:10,000), ERK1/2 (#4695, Cell Signaling; 1:5,000), phospho-p38$^{T180/Y182}$ (#4511, Cell signaling, 1:5,000), p38 (#9212, Cell Signaling; 1:5,000), phospho-Akt$^{T308/S473}$(#13038/#4060, Cell Signaling; 1:1,000), Akt (#9272, Cell Signaling; 1:1,000), phospho-cPLA$_2$α^{S505} (#53044, Cell Signaling; 1:1,000), cPLA$_2$α (#5249, Cell Signaling; 1:1,000). Antibody to β-actin (#3700, Cell Signaling; 1:10,000) was used to evaluate protein loading in each lane. Immunoblots were developed using the Western Lightning Chemiluminescence Plus detection system (PerkinElmer, Wellesley, MA) according to the manufacturer's protocol. Images of the immunoblot bands were obtained using AI600 CCD Imager for chemiluminescent assays (Amersham). Densitometry of the immunoblot bands was performed using ImageJ. For quantification, OD of bands

for phosphoprotein was normalized to total protein after normalization to β-actin; otherwise, OD of bands for total protein was normalized to β-actin. Fold-change over mean value of *10A*$^{+/+}$ samples was calculated for graphs.

Immunofluorescent staining of mouse tissues. Testes and vas deferens were collected from mice after CO_2 sacrifice and cervical dislocation. Vas deferens samples were fixed in 10% neutral buffered formalin and testes samples were fixed in Modified Davidson's fixative (Polysciences, catalog #24355-500) and further processing and paraffin embedding was done by the Vanderbilt Translation Pathology Shared Resource (TPSR). Tissue sections are 5 μm thick. To stain paraffin embedded sections, the sections underwent re-hydration, antigen retrieval, blocking, and antibody treatment. The slides were treated with anti-ATP10A (1:20) followed by goat anti- rabbit Alexa-Fluor 647 secondary antibody (1:500, Abcam, #150083) and DAPI Fluoromount-G (Southern Biotech, catalog # 0100-20). Images of tissues were acquired using a confocal microscope (Zeiss LSM 880 with AiryScan) with a Zeiss C Plan Apochromat ×40/1.40 Plan-Apochromat Oil using the ZEN black software. Laser irradiation at 633 nm was used to excite the Alexa-Fluor 647, and at 405 nm to excite DAPI. Detector gain and laser intensity were constant for all experimental groups. Images were false colored green and edited using ImageJ (images from the same tissues were edited using the same scripts).

Mating studies. Monogamous mating pairs (1 male and 1 female) with the reported genotypes were housed together for 6-21 weeks and the frequency of litters and number of pups born in each litter were recorded (see **Supplemental Table 3** for details). Various mating times were employed to obtain an average number of litters produced while minimizing the need for sacrificing a large number of pups.

Weighing testes. Researchers were blind to the genotype of the mice during the following procedure: mice were sacrificed using CO_2 euthanasia systems followed by cervical dislocation and testes were removed from mice and the wet mass was weighed (both testes together) using an analytical scale.

Evaluation of epididymal sperm. Mice were housed alone for 1 week prior to sperm counts to avoid any social subordination effects. Researchers were blind to the genotype of the mice during the following procedure: mice were sacrificed using CO_2 euthanasia systems followed by cervical dislocation and the caput epididymis was removed from mice and cut into several pieces (to release the sperm) and then incubated in 1X PBS at 37°C for 10 minutes. After the incubation; 10 µL of the sperm solution was added to a hemocytometer (Petroff-Hausser Counter, Hausser Scientific, Catalog #3900) and the sperm cells were viewed and counted using the Inverted Tissue Culture Microscope with 5MP Digital Camera (AmScope, catalog # IN200TB-5MA). The percent of motile sperm was calculated by dividing the sperm that were moving by all the sperm cells counted.

Histopathologic assessment of testes and vas deferens. Testes and vas deferens were collected from mice after euthanasia via CO_2 followed by cervical dislocation. The tissues were fixed in 10% neutral buffered formalin for 48 hours before undergoing further processing, paraffin embedding, and sectioning done by the Vanderbilt Translation Pathology Shared Resource (TPSR). Tissue sections are 5 µm thick, and stained with hematoxylin and eosin (H&E). A board-certified veterinary pathologist (TSY) was blind to the genotype of the mice and scores were assigned to each pair of testes according to a modified scoring system (**Table 1**) established based on the presence and extent of pathologic features [168, 169]. Vas deferens were examined separately and not scored.

Measurement of circulating hormones. Mice were sacrificed using CO_2 euthanasia systems followed by cervical dislocation and blood was collected via cardiac puncture and put into a tube with 5 µL of 0.5M EDTA. After 20 min of centrifugation at 1000 *x g* at 4°C the plasma was collected and stored at -20 °C before analysis. Total testosterone, LH, FSH, and Inhibin B levels were measured using ELISA kits (Testosterone: CrystalChem, catalog #80552, LH: MyBioSource, catalog # MBS2514287, FSH: MyBioSource, catalog # MBS2700327, Inhibin B: MyBioSource, catalog # MBS2088142). Ratios were calculated by dividing the total levels of the hormones measured from the same mouse.

Statistics. All statistical analysis was done using GraphPad Prism, version 9.5.0 (GraphPad Software). Error bars indicate mean with standard error of the mean (SEM). When more than 2 groups were compared, a 2-way ANOVA was used with Dunnett's correction for multiple comparisons with a control group. Šidák's correction was used for comparison of groups of means. Differences between group mean values were tested using a 2-tailed Student's *t* test. A *P* value of less than 0.05 was considered statistically significant.

Study approval. The animal protocol was approved by Vanderbilt University Medical Center and IACUC and all methods were performed in accordance with the relevant guidelines and regulations.

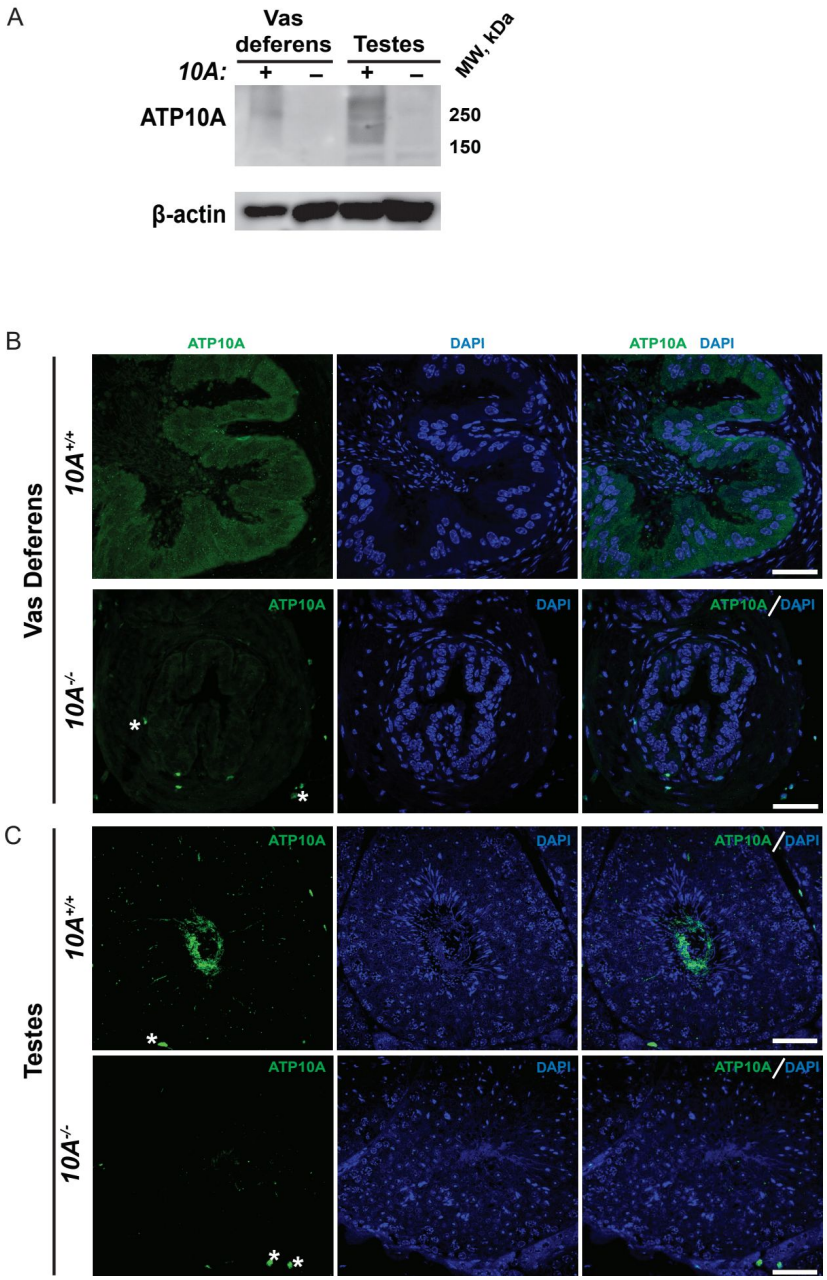

Figure 10. ATP10A is expressed in vas deferens and testes. (A) Total tissue lysates from vas deferens and testes from the *Atp10A*$^{+/+}$ (*10A* +) and *Atp10A*$^{-/-}$ (*10A* -) mice were subjected to Western immunoblot analysis for expression of ATP10A (100 µg total protein) using the anti-ATP10A antibody described in Supplemental Figure 1. β-actin served as a loading control. Note that ATP10A migrates as a high-molecular-weight smear. Representative immunofluorescent images of (B) vas deferens and (C) testes showing expression of ATP10A (green) and DAPI (blue). Scale bar= 40 µm. White asterisks indicate background staining. (Vas deferens: *10A*$^{+/+}$ n=1, *10A*$^{-/-}$ n=2, Testes: *10A*$^{+/+}$ n=2, *10A*$^{-/-}$ n=2).

To begin to explore the potential role ATP10A in fertility we first tested if ATP10A protein is expressed in male reproductive organs. To do this, we produced anti-ATP10A antibodies to three different peptide sequences conserved between human and mouse ATP10A but not present in other P4-ATPases (Supplemental Figure 9A,B). We then tested the specificity of these different antibodies toward human ATP10A in HeLa cells overexpressing an HA-tagged ATP10A and found that the affinity purified antibody targeting amino acids 27-38 (labeled peptide 1) was specific for ATP10A (Supplemental Figure 9C,D). ATP10A is a large, integral membrane protein that often aggregates when subjected to SDS-PAGE and migrates as a high molecular weight smear above 250 kDa. We then used immunoblot analysis to probe two male reproductive organs, the vas deferens, a muscular tube that transports sperm from the epididymis to the urethra during ejaculation, and the testes, for ATP10A expression. We observed a high molecular weight smear above 250 kDa, specific for ATP10A, in the vas deferens and testes that was absent in *Atp10A* deficient mice (Figure 10A). Additionally, we observed a specific ATP10A-positive signal via immunofluorescence (IF) in WT mice that was absent in knockout (KO) mice in the vas deferens (Figure 10B) and in the testes, specifically in the seminiferous tubules (the functional unit of the testes) and spermatocytes predominately towards the tubular lumen (Figure 10C). Therefore, ATP10A is expressed in the vas deferens and testes.

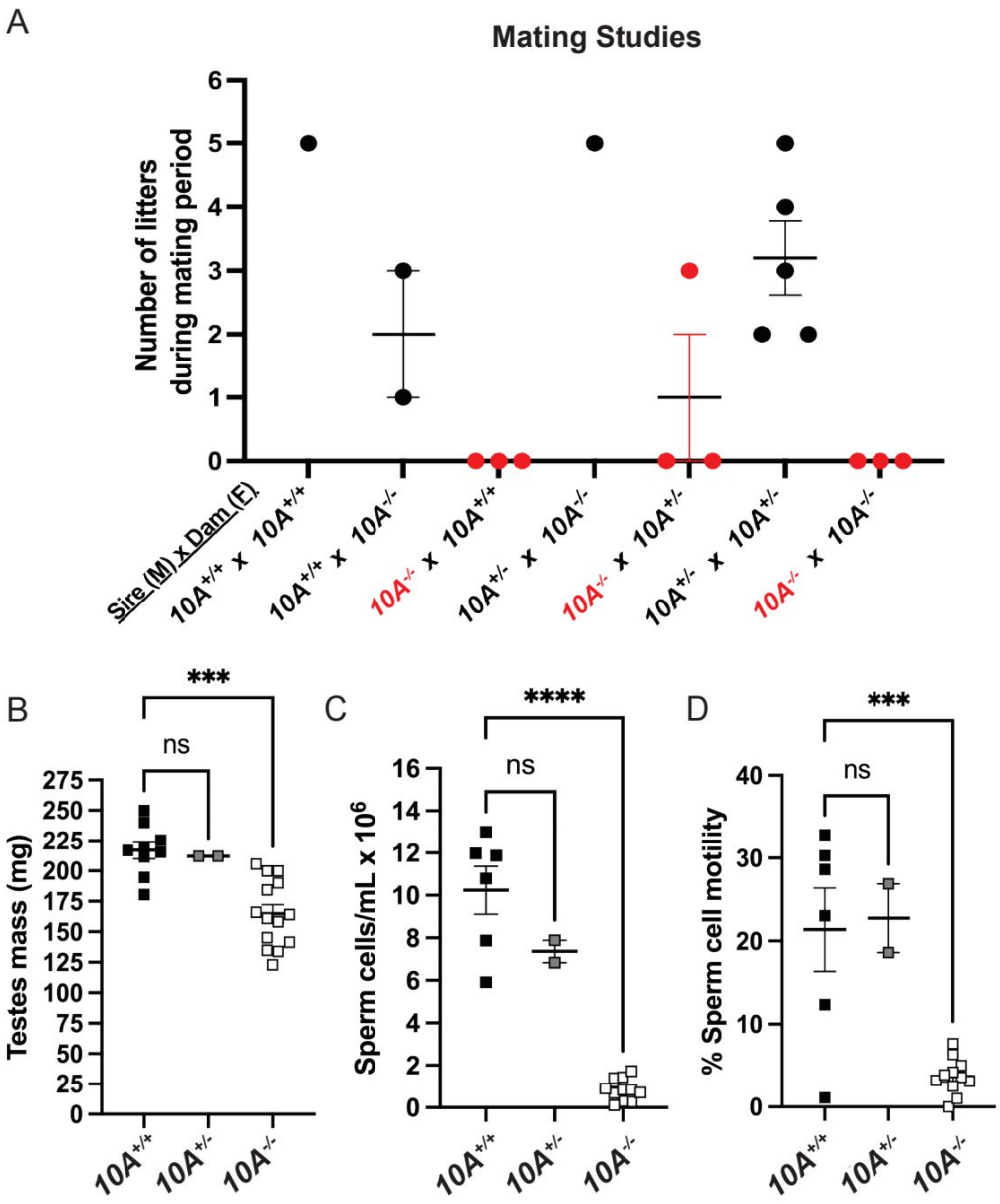

Figure 11. *Atp10A* deficiency results in male-specific infertility, smaller testes and reduced sperm count and motility. (A) Mating studies were done by housing pairs of mice together (without separating) for 6-21 weeks and recording the number of litters produced. (See Supplemental Table 1 for more details) (B) The wet mass of testes was measured in 8-19-week-old mice, ***P=0.0002. (C) Sperm cells collected from the caput epididymis were counted using a hemocytometer, ****P<0.0001. (D)% Sperm cell motility was measured using the equation: motile sperm/total sperm counted, ***P=0.0003. P-value by ordinary one-way ANOVA with Dunnett's multiple comparison test (B-D: *10A*$^{+/+}$ n=9, *10A*$^{+/-}$ n=2, *10A*$^{-/-}$ n=14).

Given the expression of ATP10A in male reproductive organs, we next investigated whether the loss of *Atp10A* in mice would perturb fertility. To explore this, we housed male and female mice together for at most 21 weeks and recorded the number of litters they produced (Figure 11A) as well as calculated the average number of pups born in each litter (Supplemental Table 3). We observed that the majority of pairs with *10A*$^{-/-}$ sires (a total of 9 *10A*$^{-/-}$ sires were examined) were unable to produce litters, with a single exception (see cross: *10A*$^{-/-}$ *(M) x 10A*$^{+/-}$ *(F),* Figure 11A*)*, while pairs with *10A*$^{-/-}$ dams were able to produce litters. Additionally, the heterozygous mice (*10A*$^{+/-}$) that are used to breed the *10A*$^{+/+}$ and *10A*$^{-/-}$ experimental mice had an average of 3 litters during the mating period of approximately 12 weeks. Taken together, *Atp10A* deficiency results in a male-specific reduction in fertility. We next measured the mass of testes and found that *10A*$^{-/-}$ mice exhibited 1.3-fold lower average testes mass compared to *10A*$^{+/+}$ and *10A*$^{+/-}$ mice (Figure 11B). To further probe the effects of *Atp10A* deficiency on male fertility we measured the number of sperm/mL in the caput epididymis as well as the motility of these cells. We found that *10A*$^{-/-}$ mice have 12.2-fold and 8.7-fold fewer sperm/mL compared to *10A*$^{+/+}$ and *10A*$^{+/-}$ littermates, respectively (Figure 11C). We also found that the percent of motile sperm from *10A*$^{-/-}$ mice was 5.8-fold and 6.2-fold lower compared to *10A*$^{+/+}$ and *10A*$^{+/-}$ mice, respectively (Figure 11D). Altogether, *Atp10A* deficiency results in small testes, oligozoospermia, and asthenozoospermia.

C57BL/6J mice have a naturally occurring premature stop codon in *Atp10D* (*10D*), a closely-related homolog of *Atp10A*. Therefore, the genotypes of the mice used in this study are *10A*$^{+/+}$*10D*$^{-/-}$ (WT) and *10A*$^{-/-}$*10D*$^{-/-}$ (KO) and it was formally possible that the male infertility observed in the *10A*$^{-/-}$ *10D*$^{-/-}$ (KO) mice was caused by loss of both *Atp10A* and *Atp10D*. To determine if *Atp10A* deficiency was sufficient to cause this phenotype, we generated *10D*$^{+/+}$ mice via CRISPR-mediated repair of the nonsense mutation back to the wild-type glutamine codon and confirmed the genotype of the mice via sequencing (Supplemental Figure 10A). We found that male *10A*$^{-/-}$ *10D*$^{+/+}$ mice, were unable to produce litters (Supplemental Figure 10B), had significantly smaller testes (Supplemental Figure 10C) as well as

16.2-fold fewer sperm/ml (Supplemental Figure 10D) and 4.1-fold less motile sperm (Supplemental Figure 2E), compared to *10A*$^{+/+}$ *10D*$^{+/+}$ mice. Therefore, ATP10A deficiency alone is sufficient to cause the male-specific infertility phenotypes.

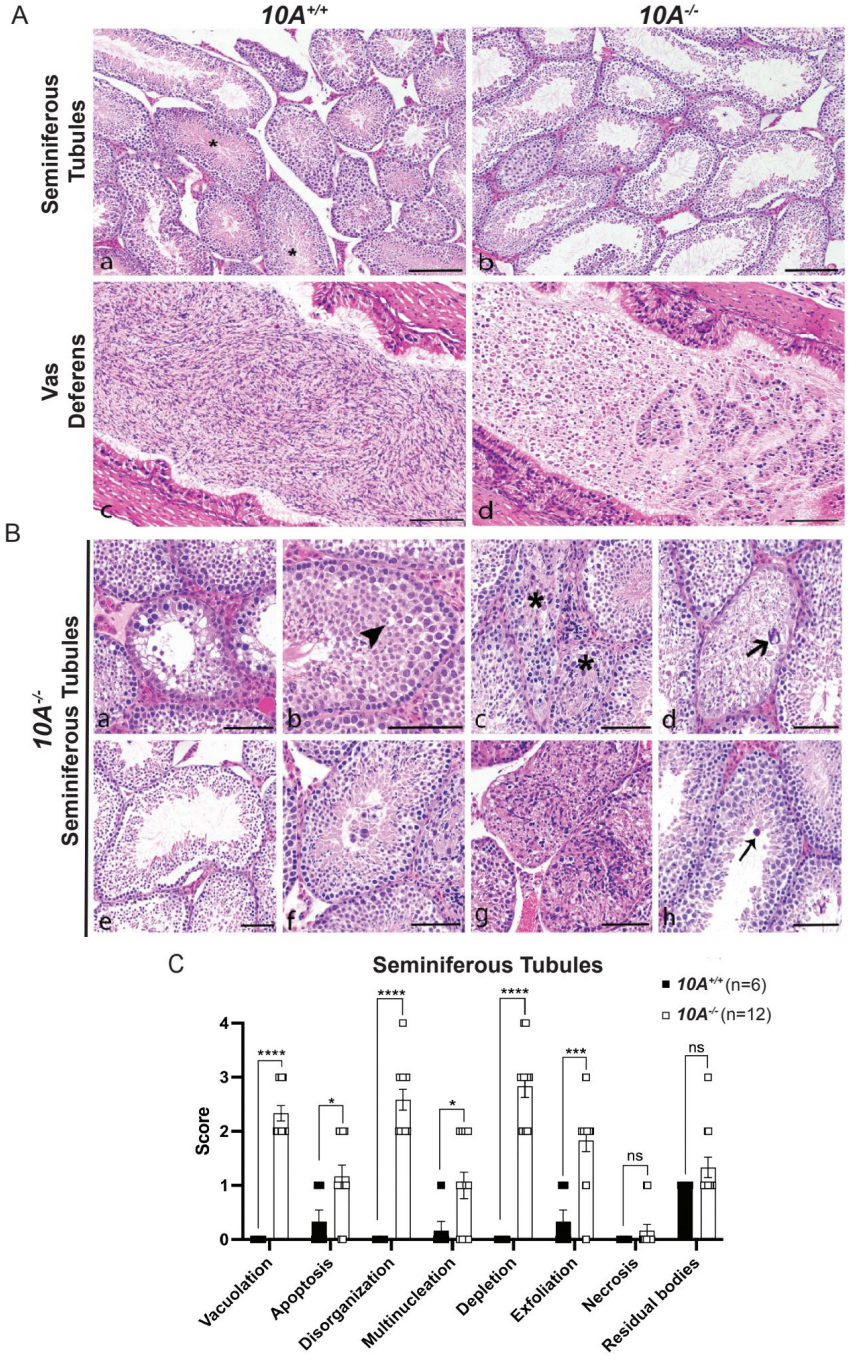

Figure 12. Testes and vas deferens from *Atp10A* deficient mice display several pathologic features. Effects of knocking out *Atp10A* on testicular and vas deferens morphology were determined from H&E stained tissues from 8-19-week-old mice. (A) Seminiferous tubules from *10A*$^{+/+}$ mice displayed various stages of spermatogenesis with presence of elongated spermatids at the center of the tubules (asterisk). Seminiferous tubules from *10A*$^{-/-}$ mice displayed marked germ cell depletion and lacked elongated spermatids. Vas deferens from *10A*$^{+/+}$ mice contained a large number of morphologically normal sperm. Vas deferens from *10A*$^{-/-}$ mice displayed sloughed immature germ and epithelial cells and cell debris. Bar, 100 µm. (B) Representative H&E images of pathologic features in seminiferous tubules from *10A*$^{-/-}$ mice. **a.** Vacuolation **b.** Apoptosis (arrowhead) **c.** Disorganization (asterisk) **d.** Multinucleation (thick arrow) **e.** Depletion **f.** Exfoliation **g.** Necrosis **h.** Residual body (thin arrow). Bar, 100 µm. (C) Quantitative assessment of pathologic features shown in (B) (*10A*$^{+/+}$, n= 6 mice; *10A*$^{-/-}$, n= 12 mice). P-value by unpaired t-test (****P<0.0001, *P=0.0228, *P=0.0394, ***P=0.0003).

Table 1. Histopathologic scoring of seminiferous tubules

Pathologic features of germ cells in seminiferous tubules
Vacuolation, apoptosis, disorganization, multinucleation, depletion, exfoliation, necrosis, and residual bodies

Score	Approximate portion of seminiferous tubules affected
0	0%
1 (minimal)	< 5%
2 (mild)	5 – 25%
3 (moderate)	25 – 50%
4 (severe)	> 50%

Table 1. Histopathologic scoring of seminiferous tubules. A scoring system was developed to assess the severity of several different germ cell pathologies in the seminiferous tubules. The scoring system is based on the percentage of affected seminiferous tubules, with 0 representing no observable pathology and 4 indicating a severe pathologic feature observed in over 50% of the seminiferous tubules. Details about the establishment of the scoring system are outlined in Materials and Methods.

To further explore the effect of *Atp10A* deficiency on male fertility, the morphology of the seminiferous tubules and the vas deferens were examined by a board-certified veterinary pathologist (TSY). The seminiferous tubules from *10A*$^{-/-}$ mice exhibited marked germ cell depletion and fewer elongated spermatids at the center of the tubules compared to *10A*$^{+/+}$ littermates (Figure 12A, inset b vs a). Additionally, the vas deferens from *10A*$^{-/-}$ mice displayed sloughed off immature germ and epithelial cells as well as cell debris in the tubular lumen, which were absent in *10A*$^{+/+}$ mice (Figure 12A, inset d vs c). We next scored pathologic features in the seminiferous tubules using the scoring system described in Table 1. We found seminiferous tubules from *10A*$^{-/-}$ mice displayed a significantly greater amount of vacuolation, apoptosis, disorganization, multinucleation, depletion, and exfoliation, compared to *10A*$^{+/+}$ mice (Figure 12B,C). However, there was no difference in the amount of necrosis or residual bodies based on genotype. Taken together, *Atp10A* deficiency results in marked seminiferous tubule and vas deferens pathologies.

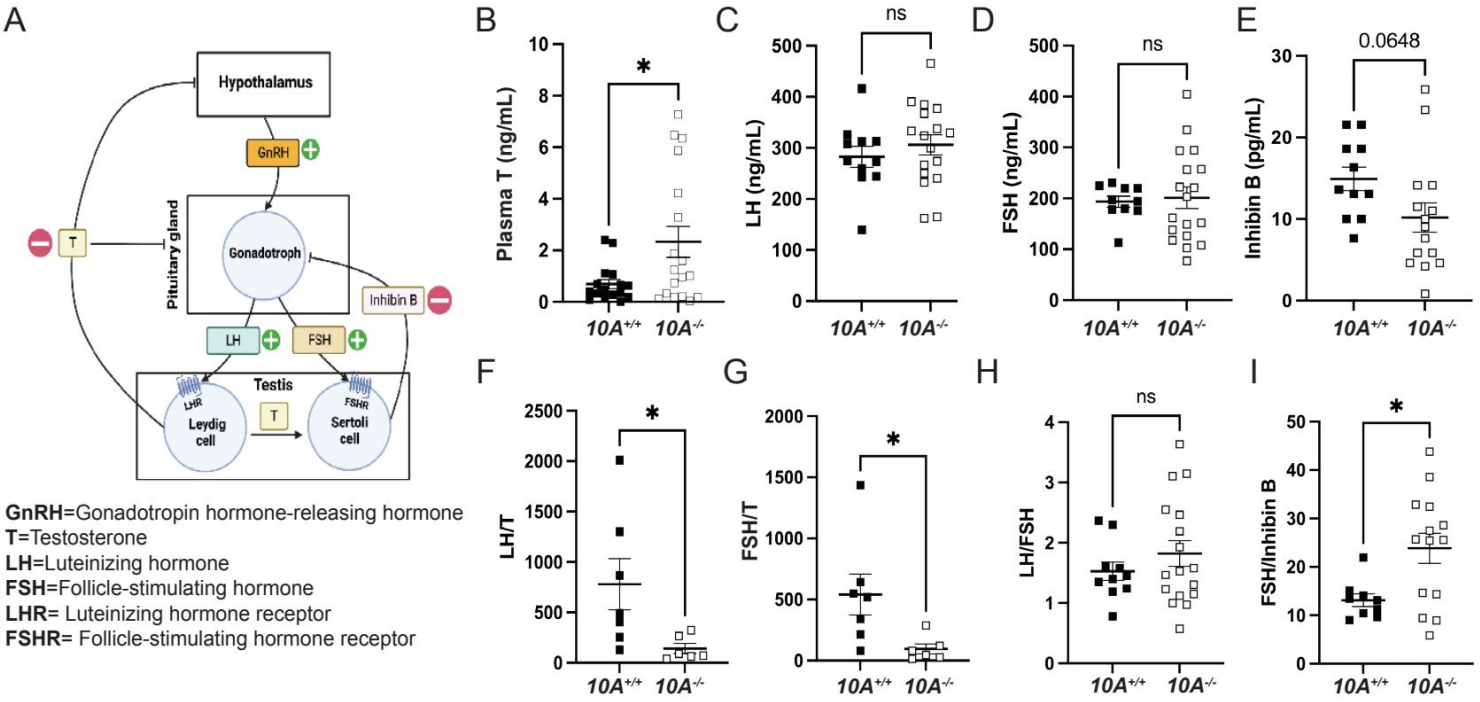

Figure 13. *Atp10A* deficient male mice exhibit reduced levels of circulating testosterone and altered ratios of HPG-axis-regulated hormones.

(A) Schematic representation of the HPG-axis. Schematic created using Biorender.com. ELISA analysis of circulating (B) testosterone (T), *P=0.0187, (C) luteinizing hormone (LH), (D) follicle stimulating hormone (FSH), and (E) Inhibin B from 8-20-week-old mice. Ratio of ELISA analysis of circulating (F) LH to T, *P=0.0437, (G) FSH to T, *P=0.0354, (H) LH to FSH, and (I) FSH to inhibin B. *P=0.0146. P-value by unpaired t-test.

To further understand the mechanism of how *Atp10A* deficiency causes male infertility, we measured hormones regulated by the HPG-axis, which regulates the production and release of hormones involved in male reproductive function (Figure 13A). We found that *Atp10A* deficient males have significantly higher levels of circulating testosterone (T) compared to WT littermates (Figure 13B). We did not find any significant differences in the level of circulating luteinizing hormone (LH) (Figure 13C), follicle stimulating hormone (FSH) (Figure 13D), or Inhibin B (Figure 13E), although the *Atp10A* deficient mice trended toward having lower circulating levels of Inhibin B compared to WT littermates. We also found that *Atp10A* deficient mice exhibit lower LH/T (Figure 13F) and FSH/T (Figure 13G) ratios, driven by the elevated testosterone, compared to WT mice. Additionally, *Atp10A* deficient mice exhibited no difference in their ratio of LH/FSH (Figure 13H) but did display an elevated FSH/Inhibin B

ratio compared to WT mice (Figure 13I). Altogether, *Atp10A* deficiency perturbs the total levels and relative amounts of hormones regulated by the HPG-axis.

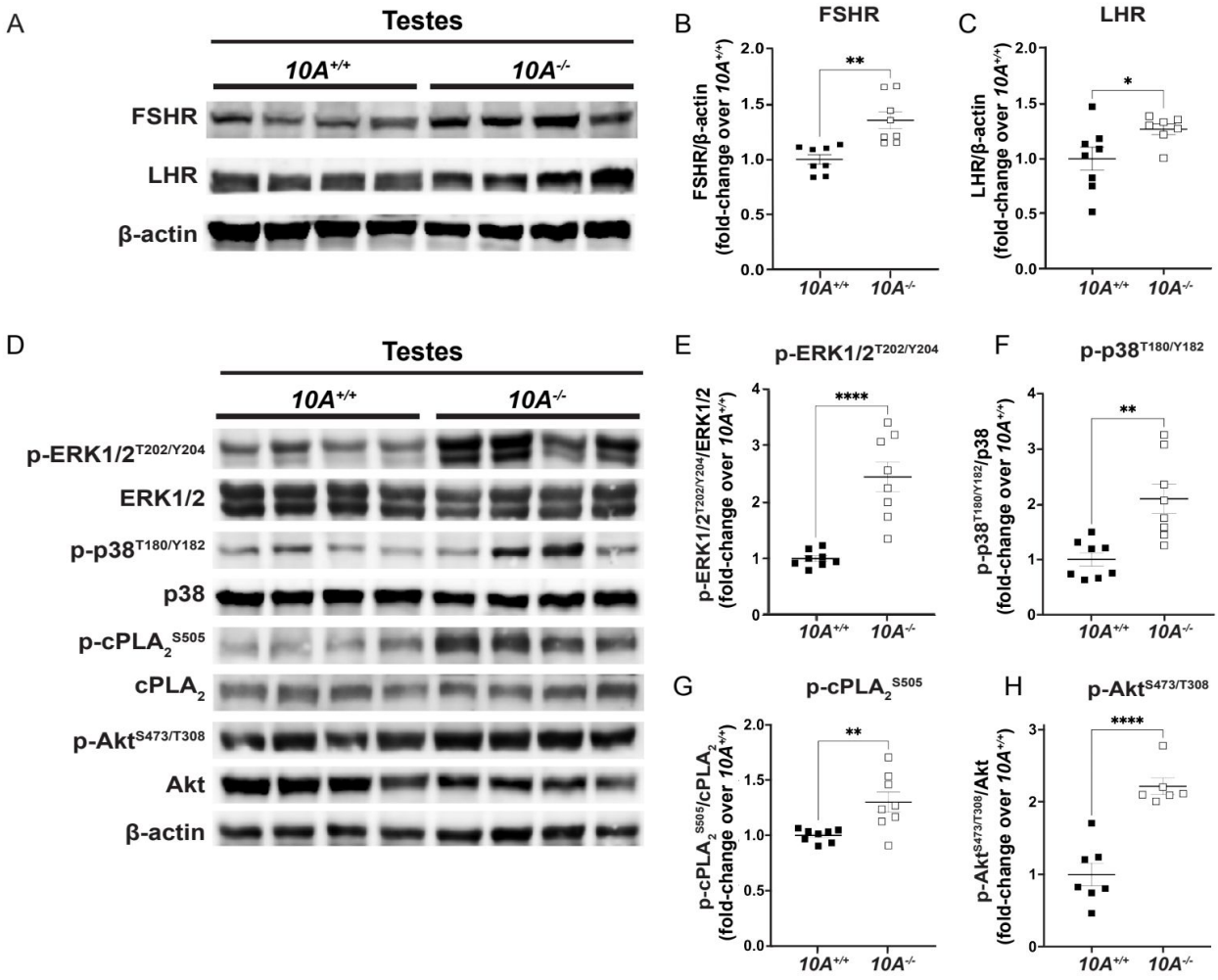

Figure 14. *Atp10A* deficiency results in changes to signaling in the testes. Total tissue lysates from testes from the *10A*$^{+/+}$ and *10A*$^{-/-}$ mice were subjected to Western immunoblot analysis. Representative blots for total and/or phosphorylated (A) FSHR, LHR, (D) ERK1/2, p38, cPLA$_2$, and Akt. (B, C) For FSHR and LHR quantitation, total protein was normalized to β-actin levels and total protein from *10A*$^{+/+}$ samples. (E, F, G,H) The phosphoproteins were normalized to their respective total protein, β-actin levels, and total protein from *10A*$^{+/+}$ samples. Mean measurements of 4-6 independent experiments are shown. P value by unpaired t-test. (B, *10A*$^{+/+}$ n=8, *10A*$^{-/-}$ n=8, **P= 0.0012; C, *10A*$^{+/+}$ n=8, *10A*$^{-/-}$ n=7, *P=0.0448; E,F,G, *10A*$^{+/+}$ n=8, *10A*$^{-/-}$ n=8, E: ****P<0.0001, F:**P=0.0020, G:**P=0.0058; H, *10A*$^{+/+}$ n=7, *10A*$^{-/-}$ n=6,H: ****P<0.0001).

To explore the molecular mechanisms underlying *Atp10A* deficiency-induced infertility, we examined the levels and phosphorylation status of key proteins involved in gonadotropin signaling within the testes. First, we probed the amount of the FSH receptor (FSHR) [170] and LH receptor (LHR) [171] and found that the *Atp10A* deficient mice exhibit elevated levels of both FSHR and LHR in their testes (Figure 14A-C). We next measured the total amounts and phosphorylation status of several proteins that have critical roles in the growth, development, and maintenance of testes, including ERK, p38 MAPK (p38) and Akt. We found an increase in the activating phosphorylation of ERK1/2 at T202/Y204 (Figure 14D,E), p38 at T180/Y182 (Figure 14D, F), and Akt at S473 and T308 (Figure 14D, H) in the testes of *Atp10A*$^{-/-}$ mice. We also observed an increase in activating phosphorylation of $cPLA_2$, an enzyme that has been previously implicated in fertility [166], at S505 in the *Atp10A* deficient mice (Figure 14D, G). This enzyme catalyzes the hydrolysis of phospholipids, such as PC, to lysoPLs and arachidonic acid and this fatty acid species can be oxidized to form eicosanoids [173]. We next examined the phosphorylation status and total levels of these proteins in the vas deferens and found that *Atp10A* deficient mice exhibit reduced activating phosphorylation of ERK1/2 at T202/Y204 (Supplemental Figure 11A,B) and p38 at T180/Y182 (Supplemental Figure 11A,C). We also found that the KO mice had increased activating phosphorylation of Akt at S473 and T308 (Supplemental Figure 11A,D) and $cPLA_2$ at S505 (Supplemental Figure 11A,E), similar to what was observed in the testes. Taken together, *Atp10A* deficiency leads to alterations in the total amount and phosphorylation status of proteins implicated in signaling that effects the response to gonadotropins as well as growth, development, and maintenance of the testes and vas deferens.

DISCUSSION AND CONCLUSIONS

In this study, we show that ATP10A protein is expressed in the vas deferens and testes of mice (Figure 11) and that *Atp10A* deficiency results in male-specific infertility characterized by small testes, oligozoospermia, and asthenozoospermia (Figure 12). Male *Atp10A* deficient mice also exhibit vas

deferens and testes pathologies (Figure 13), alterations to total levels and relative amounts of HPG-axis controlled hormones (Figure 14), and changes to signaling in the testes (Figure 6) and vas deferens (Supplemental Figure 11).

We found that ATP10A is expressed in murine vas deferens and testes (Figure 10). There is ubiquitous ATP10A-positive signal in the vas deferens (Figure 10D) and in several different locations within the seminiferous tubules of the testes, especially the lumen (Figure 10E). The Mouse Cell Atlas [155] reports *Atp10A* mRNA expression in Leydig cells, Sertoli cells, peritubular cells, fibroblast, macrophages, elongated spermatid, round spermatid, spermatocytes, and differentiated spermatogonia in the testes. Further work is needed to determine the precise cell type(s) in which ATP10A protein is expressed within the vas deferens and testes and if ATP10A is expressed in other components of the male reproductive system, such as the epididymis. Additionally, according to the Mouse Cell Atlas [155], *Atp10A* is also expressed in chondrocytes, macrophages, and several other cell types. Therefore, further investigation is required to determine whether the male infertility resulting from loss of *Atp10A* is solely due to its absence in reproductive tissues or if this phenotype is also influenced by its absence in other cell types where it is expressed.

Interestingly, several members of the P-type ATPase family have roles in fertility [38]. Two Type II P-type ATPases, Ca^{2+}-ATPase isoform 4 (ATP2B4) and -4 isoform of the Na^{+}/K^{+}-ATPase are responsible for sperm motility [174, 175]. ATP8B3 has been implicated in sperm cell acrosome formation and capacitation [165] and ATP8B5 (also known as FetA) has potential roles in spermatogenesis and acrosome biogenesis based on expression patterns [30]. In this study, we show that another member of the P-type ATPase family, ATP10A, which translocates PC and GlcCer [90], has a role in the maintenance of male-specific fertility. A closely-related homolog of ATP10A, ATP10D, also translocates GlcCer [90], is transcriptionally expressed in murine [155] and human testes [152, 153], and has been implicated as being a transcript in human spermatozoa necessary for successful intrauterine insemination [176]. Interestingly, C57BL/6J mice exhibit a stop codon in exon 12 in the *Atp10d* gene [92], therefore the genotypes of the mice used in this study, unless otherwise noted, are $10A^{+/+}10D^{-/-}$ (WT) and $10A^{-/-}$

10D$^{-/-}$ (KO). To determine any potential functional redundancy between ATP10A and ATP10D we generated *10D*$^{+/+}$ mice via CRISPR-mediated repair of the nonsense mutation back to the wild-type glutamine codon (Supplemental Figure 10A). We found that reintroduction of WT *Atp10D* did not rescue the infertility phenotypes in *Atp10A* deficient mice (Supplemental Figure 10B-E). Therefore, ATP10A deficiency alone is sufficient to cause the male-specific infertility phenotypes in mice and this suggests that the specific ATP10A substrate critical for male fertility is PC and not GlcCer. However, it is possible that ATP10D (and GlcCer) have a role in human fertility and this needs to be investigated.

We found that male *Atp10A* deficient mice have small testes (Figure 11B), oligozoospermia (Figure 11C), a trend of decreased circulating levels of Inhibin B, a marker for spermatogenesis [177], and elevated circulating levels of testosterone (Figure 13B). The combination of small testes, oligozoospermia, and elevated testosterone levels appears paradoxical, as testosterone is a critical factor in facilitating testes growth and supporting spermatogenesis [178]. However, it is possible that the low sperm count could lead to a compensatory increase in testosterone production. Interestingly, transgenic male mice overexpressing human chorionic gonadotropin (hCG), a hormone that is structurally similar to LH that signals through the LH receptor (LHR), also exhibit small testes with elevated circulating levels of testosterone [179]. Although these disparate phenotypes co-occurring has been previously observed, the specific mechanisms remain unexplored. Reduced testicular size could persist despite elevated testosterone levels if the excessive testosterone fails to evoke the intended effects on its target tissues, including Sertoli cells, or induce the negative feedback loop in the HPG-axis (Figure 13A). These possibilities should be further explored.

We focused our efforts on exploring the cause of the elevated testosterone levels in the *Atp10A* deficient mice. Elevated testosterone levels could arise from hyperactivation of LHR-mediated signaling in Leydig cells. We found that *Atp10A* deficient mice have increased levels of FSHR and LHR in the testes (Figure 14A-C). Cellular levels of FSHR and LHR are regulated through receptor endocytosis, facilitating their desensitization, or degradation of their mRNA transcripts [180, 181]. The elevated levels of FSHR and LHR detected in the testes of *Atp10A* deficient mice warrants further investigation into

whether these changes arise from reduced endocytosis or modifications in mRNA transcript processing. Additionally, changes to aromatase activity, the enzyme that converts testosterone to estrogen [182], could also affect levels of circulating testosterone, and this possibility should be tested.

We investigated various signaling events within the testes and found increased activating phosphorylation of proteins involved in growth and control of gene expression, including p-ERK, p-38 (MAPK), and Akt (Figure 14E,F,H). We also found an increase in activating phosphorylation of an enzyme that has been previously implicated in female fertility (27), $cPLA_2$ (Figure 14G). Additionally, in the testes, Akt-dependent signaling results in multiple downstream effects [183]; including facilitating proliferation and anti-apoptosis of immature Sertoli cells [184-186]. Interestingly, there is evidence that a potent toxin produced by cyanobacteria, Microcystin-LR, which has adverse effects on reproduction; initiates Akt-dependent signaling pathways, disrupts the blood-testis barrier, and induces apoptosis in Sertoli cells [187-190]. Interestingly, the testes from *Atp10A* deficient mice exhibit increased apoptosis and a marker of abnormal proliferation (multinucleation) as well as damage and disruption to the normal architecture of the tissue (vacuolation, disorganization, depletion, and exfoliation) (Figure 12). Whether these pathologies are caused by elevated Akt-dependent signaling in the testes or defects in other processes requires further study. Furthermore, activation of LHR and FSHR in the testes can trigger phosphorylation of ERK and p38 (MAPK) [170, 191, 192], as well as Akt [185, 186, 193, 194]. Notably, activation of MAPKs and Akt signaling pathways in distinct cell types in testes result in specific outcomes. Activation of LH-LHR-MAPKs/Akt in Leydig cells leads to testosterone production and FSH-FSHR-MAPKs/Akt pathways in Sertoli cells potentiate this process. At the same time, in Sertoli cells, the binding of testosterone to androgen receptors (classical testosterone signaling pathway) or to Epidermal Growth Factor (EGF) receptor (non-classical kinase activation pathway) also induces activating phosphorylation of ERK and Akt, which is critical for successful spermatogenesis [178]. Interestingly, in the non-classical Ca^{2+} influx pathway, testosterone interacts with a receptor in the plasma membrane that has characteristics of a Gq coupled G-protein coupled receptor (GPCR) leading to changes in membrane lipid composition and membrane depolarization [195]. Understanding the relationship between the

observed infertility phenotypes and cell type- and ligand/receptor-specific activation of the MAPKs and Akt, the elevated levels of FSHR and LHR in the testes, and the elevated circulating testosterone levels in *Atp10A* deficient mice requires further study.

The testes and vas deferens are functionally interdependent components of the male reproductive system; the testes produce sperm and the vas deferens is a muscular tube that serves as passageway for the sperm cells. ATP10A is expressed in both the testes and vas deferens (Figure 10) and these tissues exhibit similar but distinct pathologies (Figure 12) and disruptions to signaling (Figure 14, Supplemental Figure 11) in *Atp10A* deficient mice. The specific functions ATP10A has in the testes and vas deferens remains a topic for speculation, as it is yet to be determined whether the protein exerts primary influences on the testes that subsequently impact the vas deferens or vice versa, or if the two organs are independently affected, leading to a synergistic negative effect on fertility.

Altogether, this study has demonstrated the importance of ATP10A in male reproductive health and its expression in both the testes and vas deferens underscores its important role in male fertility. The phenotypes caused by *Atp10A* deficiency, such as reduced testes size, oligozoospermia, asthenozoospermia, and the observed histopathological changes in the testes and vas deferens, emphasize its importance in the maintenance of male-specific fertility. Furthermore, the elevated circulating testosterone levels and changes to signaling within the testes in *Atp10A* deficient mice highlight the impact ATP10A has on hormonal regulation and intracellular pathways essential for reproductive function. ATP10A translocates PC and GlcCer from the outer to the inner leaflet of the plasma membrane and we show here that *Atp10A* deficiency in the testes results in enhanced activating phosphorylation of $cPLA_2$, potentially leading to changes in eicosanoid levels within the testes. Further research is needed to understand how ATP10A's influence on lipid levels in the intracellular space intersects with its role in male fertility. There is also a need to determine if mutations in *ATP10A* could be potential risk factors for male-specific infertility in humans.

Chapter 4: Studies of lipoprotein lipase activity and localization in *Atp10A* knockout mice.

INTRODUCTION

As described in Chapter 2 ATP10A is expressed in endothelial cells and *Atp10A* deficient female mice exhibit dyslipidemia characterized by elevated levels of plasma FFA, cholesterol, TG, and alterations in the size and lipid content of both VLDL and HDL (Figure 4). The mechanistic link between *Atp10A* deficiency and dyslipidemia remains unknown. One possibility is that the asymmetrical distribution of PC and GlcCer set by ATP10A modulates the membrane lipid environment and effects the activity and/or localization of membrane resident enzymes that regulate lipid metabolism [196]. One such enzyme is lipoprotein lipase (LPL). LPL is responsible for the hydrolysis of TG in capillaries and transforms chylomicrons and VLDL to smaller lipoprotein particles, and this process is under several levels of regulation; including post-translational mechanisms and binding to different proteins including GPIHBP1 and apolipoproteins. Post-translational mechanisms involve phosphorylation and glycosylation events, where enzymes modify LPL to modulate its activity. Additionally, the interaction between LPL and GPIHBP1, a glycosylphosphatidylinositol-anchored protein, plays a crucial role in the translocation of LPL to the capillary endothelial surface. Moreover, LPL activity is influenced by apolipoproteins, such as ApoC-II, which acts as a cofactor, and ApoC-III, which inhibits its function. These complex regulatory processes ensure precise control over lipid metabolism, allowing LPL to efficiently participate in the breakdown of triglycerides and the subsequent distribution of fatty acids for energy utilization or storage. [197]. Importantly, a reduction in the activity of LPL can reduce the clearance of TG from the plasma and result in hypertriglyceridemia [198, 199].

Because ATP10A is expressed in endothelial cells and its deficiency leads to elevated TGs in lipoproteins, we tested whether perturbation of LPL activity underlined the mechanistic link between ATP10A deficiency and hypertriglyceridemia. To explore this, we measured LPL

activity, localization, and TG production and clearance in the female WT and KO mice after high fat diet feeding.

MATERIALS AND METHODS

Animals. All mouse experiments were approved under the Vanderbilt University Institutional Animal Care and Use Committee. Mice were housed in 12 h light/dark cycles in temperature and humidity-controlled facilities with ad-libitum access to diet and water (in the Barrier facility). Mice in this study were sacrificed via CO_2 euthanasia systems, operating at the recommended flow rates, followed by cervical dislocation; this method is an acceptable euthanasia method according to the American Veterinary Medical Association (AVMA) guidelines. The mouse studies described in this manuscript are reported in accordance with the ARRIVE guidelines (https://arriveguidelines.org/).

Creating the mouse model. The *Atp10A* mouse model (knockout allele name: *Atp10Aem1(Vtrg)*) was created via CRISPR-Cas9 in collaboration with the Vanderbilt Genome Editing Resource. Guide RNAs (crRNA) were created to target *Atp10A* on chromosome 7: Target Intron 1-2: TGACTGCTTAATGATTCGAGG, GAGTGACTGCTAATGATCG, Target Intron 2-3: GGAAAAAGCCCAATTCCACAC, AGCCCAATCCACACAGGAAC. CRISPR editing reagents were delivered into the pronuclei of one-cell fertilized mouse zygotes (C57BL/6J). Approximately 608 bp were deleted using this method: nucleotides 58389679-58390287 (NCBI reference sequence: NC_000073). The resulting pups were biopsied and screened by PCR and Sanger sequencing. The predicted founders were bred to WT C57BL/6J animals and the offspring were genotyped (N1 generation). The offspring with the appropriate genotype were then backcrossed two more times.

Genotyping. Mice were genotyped using tail DNA. *Atp10A* DNA products were detected via PCR (Q5 DNA Polymerase, NEB) followed by gel electrophoresis; *Atp10A-F* (

GTGCACTGTATTTGTCTGCCTGTTCC), *Atp10A-R (*GGTCCTTTGAAGAGATAATGTTCCCAAC). PCR samples were purified (QIAquick spin column (lot No. 166028242)) and sent to Genewiz (https://www.genewiz.com/) for sequencing.

LPL Activity. Muscle and adipose tissue depots were collected from mice after CO_2 sacrifice and cervical dislocation and were flash frozen in liquid nitrogen and then kept at -80^{o}C until further processing. The lipoprotein lipase (LPL) activity was measured via a commercial LPL assay kit (STA-610, Cell BioLabs, Inc., San Diego). Briefly, after homogenizing frozen mouse adipose and muscle tissue in a buffer containing protease inhibitors followed by centrifugation; the tissue lysates were used for LPL activity assays. After incubation with reagents in the assay kit according to the manufacturer's instructions, the fluorescence signal (excitation in 480–485 nm and emission in the 515–525 nm) was read and recorded with a fluorescence microplate reader (Biotek Synergy Ht Plate Reader). The activity of LPL was then calculated following the kit instructions and was normalized to protein amount that was calculated using a BCA reagent (Pierce, Rockford, IL).

Immunofluorescent staining of visceral fat. Visceral fat was collected from mice after CO_2 sacrifice and cervical dislocation Samples were fixed in 10% neutral buffered formalin and further processing and paraffin embedding was done by the Vanderbilt Translation Pathology Shared Resource (TPSR). Tissue sections are 5 μm thick. To stain paraffin embedded sections, the sections underwent re-hydration, antigen retrieval, blocking, and antibody treatment. The slides were treated with anti-LPL (1:100, Santa Cruz Biotechnology Inc., sc-373759), anti-ATP10A (1:20) followed by goat anti- rabbit Alexa-Fluor 488 secondary antibody (1:50000, Invitrogen, A-11008), and rat anti-mouse Alexa Fluor 594 secondary antibody (1:10000, Invitrogen, A-11005). ProLong Gold antifade reagent with DAPI (Invitrogen, P36931) was used to mount the slides. Images of tissues were acquired using a confocal microscope (Zeiss LSM 880 with AiryScan) with a Zeiss C Plan Apochromat ×40/1.40 Plan-Apochromat Oil using the ZEN black software. Laser irradiation at: 488 nm was used to excite the Alexa-Fluor 488,

at 561 nm to excite the Alexa-Fluor 594, and at 405 nm to excite DAPI. Detector gain and laser intensity were constant for all experimental groups. Images were edited using ImageJ (images from the same tissues were edited using the same scripts).

***In vivo* TG production and clearance.** TG production and clearance were measured as described in [200]. Briefly; to measure TG production, 3-h fasted mice were given 200 µl intraperitoneal Poloxamer-407 (500 or 300 mg/kg; Sigma), an inhibitor of lipolysis [201], and plasma TG was measured over 2 h. To measure TG clearance (lipid tolerance test), 12-h fasted mice were orally gavaged with olive oil (200 µl/mouse) and plasma TG was measured from tail blood sampling over 6 h, using a colorimetric kit (Infinity, Thermo Scientific, catalog #TR22421).

Statistics. All statistical analysis was done using GraphPad Prism, version 9.5.0 (GraphPad Software). Error bars indicate mean with standard error of the mean (SEM). When more than 2 groups were compared, a 2-way ANOVA was used with Dunnett's correction for multiple comparisons with a control group. Šidák's correction was used for comparison of groups of means. Differences between group mean values were tested using a 2-tailed Student's *t* test or a Mann-Whitney *U* test for nonparametric data. A *P* value of less than 0.05 was considered statistically significant.

Study approval. The animal protocol was approved by Vanderbilt University Medical Center and IACUC and all methods were performed in accordance with the relevant guidelines and regulations.

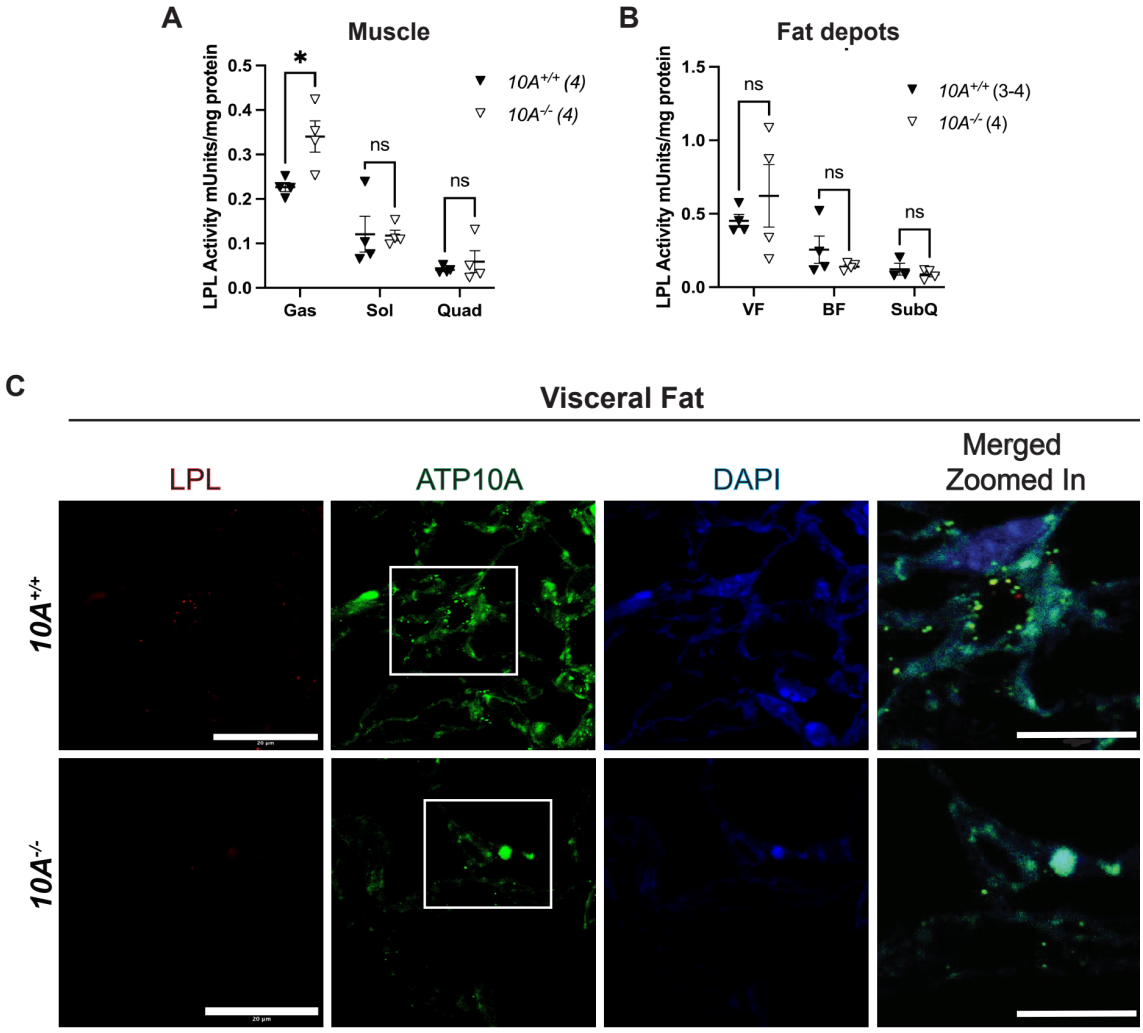

Figure 15. ATP10A and LPL: Protein activity and localization. (A, B) LPL activity was measured from total tissue lysates from (A) gastrocnemius (gas), soleus (sol), quadricep (quad), (B) visceral fat (VF), brown fat (BF), and subcutaneous fat (SubQ) from *Atp10A*$^{+/+}$ and *Atp10A*$^{-/-}$ female mice after 12 weeks of high fat diet feeding. (C) Representative immunofluorescent images of visceral fat showing expression of LPL (red), ATP10A (green), and DAPI (blue). Scale bar= 20 μm. The white box indicates the area that was zoomed in on for the merged and zoomed in images (*10A*$^{+/+}$ n=1, *10A*$^{-/-}$ n=1).

To explore the effect ATP10A has on LPL activity, we first measured LPL activity in muscle and fat depots from females after 12 weeks of high fat diet feeding (Figure 15A,B). We found that *Atp10A* KO mice exhibited more LPL activity in gastrocnemius muscle compared to WT mice (Figure 15A). We next wanted to determine the localization of ATP10A and LPL in the different muscle and fat depots. Due to difficulties with background autofluorescence in several of the tissues; only the visceral fat images were of good enough quality to be shown. We found that in visceral fat from *10A*$^{+/+}$ mice; there was puncta specific for LPL and puncta specific for ATP10A that appeared to exhibit staining patterns that were consistent with colocalization (Figure 15C). The visceral fat from the *10A*$^{-/-}$ mice exhibited no puncta specific for LPL but displayed some background puncta with the ATP10A antibodies (Figure 15C). Taken together, ATP10A effects LPL activity in gastrocnemius muscle and exhibits staining patterns consistent with colocalization with LPL in visceral fat. However, the relatively high nonspecific staining of *10A*$^{-/-}$ tissue with the anti-ATP10A antibodies clouds the interpretation of the IF analyses.

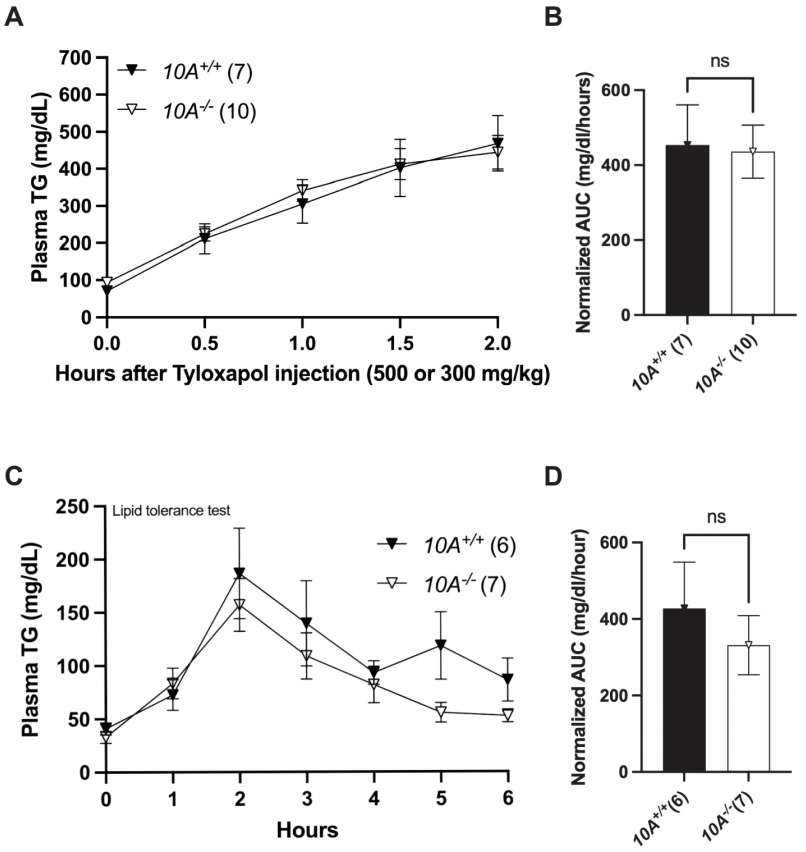

Figure 16. *Atp10A* deficiency does not affect the kinetics of lipid production or clearance in females. After HFD feeding, *10A*$^{+/+}$ and *10A*$^{-/-}$ female mice were: (A) fasted for 3 hours and retro-orbitally injected with poloxamer 407 (Tyloxapol) and plasma TG was measured over 2 hours (AUC in (B)) or (C) fasted for 12 hours overnight and gavaged with olive oil (200 ul/mouse) and postprandial plasma TGs were measured over 6 hours (AUC in (D)). (A,C) P values by 2-way ANOVA with Sidak's multiple comparison or (B,D) unpaired t-test.

We next wanted to determine if *Atp10A* deficiency would affect the kinetics of TG production or clearance in female mice. TG production rate is determined by measuring increases in plasma TG over time; in conditions in which TG hydrolysis by LPL is inhibited (after Poloxamer 407 (Tyloxapol) treatment [202]. We found no difference in the kinetics of TG production, after Poloxamer 407 treatment, based on genotype (Figure 16A,B). We also performed a lipid tolerance test in fasted mice that were gavaged with olive oil and also found no significant difference in the kinetics of TG clearance overtime based on genotype (Figure 16C,D). Therefore, under the conditions tested, ATP10A does not affect the kinetics of TG production or clearance in female mice after high fat diet feeding.

DISCUSSION & CONCLUSIONS

We found that high fat diet fed *Atp10A* deficient female mice exhibit increased LPL activity in their gastrocnemius muscle compared to their WT counterparts (Figure 15A,B). Additionally, via immunofluorescent staining of visceral fat, we found that puncta that stained for ATP10A and LPL appear to colocalize and that tissue from *Atp10A* deficient mice did not show puncta specific for LPL (Figure 15C). Despite these findings; we did not find a difference in TG production or clearance in high fat diet fed female mice based on genotype (Figure 16).

High fat diet fed *Atp10A* deficient female mice exhibit greater LPL activity in gastrocnemius muscle compared to WT mice (Figure 15A). However there was no difference in LPL activity, based on genotype, in the other muscle depots (soleus, quadricep) or any of the fat depots we examined (VF, BF,subQ) (Figure 15A,B). ATP10A is expressed in vascular endothelial cells (Figure 7) and one reason that ATP10A could affect LPL activity in the gastrocnemius muscle but not the other muscle depots could be because muscle depots exhibit different resident endothelial cell phenotypes [203]. Arteries perfusing soleus muscle (slow-twitch muscle fibers) and those perfusing gastrocnemius muscle (fast-twitch muscle fibers) exhibit differential responses to obesity. Indeed, arteries to soleus muscle exhibit protection from endothelial dysfunction compared with the arteries to the gastrocnemius muscle that

are vulnerable to obesity induced endothelial dysfunction [203]. More work is needed to determine if endothelial heterogeneity underlies *Atp10A* deficiency resulting in changes to LPL activity in some tissues and not in others. One way to begin to determine this would be to measure ATP10A expression in the different muscle and fat depot resident endothelial cells. However, the LPL activity studies presented here lack sufficient statistical power and necessitate a larger sample size to ascertain the robustness of the observed alterations in LPL activity within the gastrocnemius muscle of *Atp10A* deficient mice and to confirm the findings in the other tissues.

High fat diet fed *Atp10A* deficient female mice exhibit elevated circulating levels of TG and alterations to the size and lipid content of VLDL (Figure 4). Therefore, we hypothesized that *Atp10A* deficiency might result in reduced LPL activity, however we observed greater LPL activity in gastrocnemius muscle from *Atp10A* deficient mice (Figure 15A). It is important to note that the LPL activity assay shown here does not provide any insight into the localization of LPL in the tissues; because the tissues are homogenized before the activity assay is performed. Therefore, despite there being greater activity of LPL in the gastrocnemius muscle from the *Atp10A* deficient mice, it is unclear where the LPL was localized in the tissue (intracellular versus extracellular). To measure activity of LPL at the luminal side of the capillary endothelium (extracellular), one could treat mice with heparin to release bound LPL and then measure LPL activity in the plasma [204].

ATP10A and LPL appear to colocalize in some locations in visceral fat (Figure 15C). Additionally, there is a lack of LPL positive staining in *Atp10A* deficient mice and whether this is due to LPL localization changes due to *Atp10A* deficiency or due to experimental error needs to be determined. LPL localization and expression levels are tightly regulated [205], however, to the knowledge of this author, there are no publications about LPL localization or activity being regulated by flippases or membrane composition. Therefore, exploring the potential ATP10A-dependent regulation of LPL would be a new and exciting avenue of research. The potential colocalization of ATP10A and LPL needs to be by determined by obtaining better quality IF images (with less autofluorescence) and

using colocalization software to determine the extent, if any, of their colocalization. Additionally, FRET, proximity ligation assays, and co-immunoprecipitation experiments with antibodies towards LPL and ATP10A could be done. It would also be interesting to perform the *in vivo* heparin experiment on *Atp10A* WT and KO mice to determine if the amount of LPL localized to the lumen of the vasculature is different based on genotype.

Although high fat diet fed *Atp10A* deficient female mice exhibit elevated circulating levels of TG and alterations to the size and lipid content of VLDL (Figure 4) we did not observe a difference in TG production or clearance in the female mice based on genotype (Figure 16). This was a surprising finding and the explanation for this is not completely clear to us. One idea is that the fasting times for the mice are too different between the various measurements to directly compare them. Indeed, fasting lengths regulate several parameters in mice, including cardiovascular measurements, hormone balance, liver metabolism, and body temperature [206]. The fast length for measuring total TG amount is 5 hours (Figure 4), 3 hours for the TG production assay (Figure 16A,B), and 12 hours for the TG clearance assay (Figure 16C,D). Perhaps ATP10A's regulation of circulating TGs and lipid metabolism changes based on the length of fasts and this possibility needs to be further explored.

Chapter 5: Metabolic phenotyping of the *Atp10D corrected mice*.

INTRODUCTION

We discovered that both human ATP10A and one of its homologs, ATP10D, are glucosylceramide (GlcCer) transporters [90]. GlcCer is a central player in sphingolipid metabolism and sphingolipids are integral components of membranes. Sphingolipids also have roles in vascular biology [207] and the pathophysiology of cardiovascular diseases, such as hypertension, coronary artery disease, heart failure, arrhythmias, and stroke [208]. Alterations in circulating levels of GlcCer have been shown to be associated with risk of myocardial infarction [209] and serum ceramides strongly correlate with markers of heart disease and are an emerging new biomarker for detection of cardiovascular dysfunction [210]. Therefore, we wanted to determine the role of both ATP10A and ATP10D in metabolism. In a previous chapter we reported on the role of ATP10A and in this chapter we will discuss ATP10D.

Interestingly, *ATP10D* single nucleotide polymorphisms (SNPs) prevalent in the population have been directly correlated with an increased risk of myocardial infarction and elevated GlcCer concentrations in plasma [88]. Additionally, the C57BL/6 mouse strain that is widely used in metabolic studies, harbors a spontaneous nonsense mutation in the middle of the *Atp10d* coding sequence [92]. A previous attempt to complement "wild-type" C57BL/6J mice with an integrated *Atp10d*+ clone led to insights into diet-induced obesity, insulin resistance, and dyslipidemic phenotypes, but the authors did not definitively establish whether the transgene was expressed at normal levels and in the relevant tissues [93]. Additionally, the phenotypic analyses in this study lacked proper controls because the authors were not able to generate a control strain and therefore were unable to includes littermates to control for maternal effects. Consequently, existing mouse models have left questions unanswered regarding the precise influence of *Atp10D* on metabolic phenotypes.

To address this, in collaboration with the Vanderbilt Gene Editing Resource, we generated a "corrected" *Atp10d* allele in C57BL/6J mice. Briefly, CRISPR/Cas9 guide RNA sequences were designed to target the premature stop codon (TAA) in exon 12 and repair the sequence to the CAA (Gln) codon found in other strains of WT mice and the human *ATP10D* gene. To determine the role of *Atp10D* in metabolism, we placed the 'corrected' mice ($10A^{+/+}10D^{+/+}$) and the original C57BL/6J mice ($10A^{+/+}10D^{-/-}$) on a HFD for 12 or 16 weeks and measured different metabolic parameters. We hypothesize that correcting the *Atp10D* gene could be metabolically protective and protect the susceptible C57BL/6J mice from metabolic perturbations after high fat diet feeding. It's important to note that the results presented herein are based on pilot studies with limited sample sizes in each group, making them underpowered. Therefore, these preliminary findings underscore the necessity for further validation with a more extensive mouse studies.

MATERIALS AND METHODS

Animals. All mouse experiments were approved under the Vanderbilt University Institutional Animal Care and Use Committee. Mice were housed in 12 h light/dark cycles in temperature and humidity-controlled facilities with ad-libitum access to diet and water (in the Barrier Facility). Mice in this study were sacrificed via CO_2 euthanasia systems, operating at the recommended flow rates, followed by cervical dislocation; this method is an acceptable euthanasia method according to the American Veterinary Medical Association (AVMA) guidelines. The mouse studies described in this manuscript are reported in accordance with the ARRIVE guidelines (https://arriveguidelines.org/).

Creating mouse models. The *Atp10D* mouse model (*Atp10Dem1 (Vtrg))* was created via CRISPR-Cas9 in collaboration with the Vanderbilt Genome Editing Resource. The purpose of the mouse model was to correct the premature stop codon in the *Atp10D* allele in C57BL/6J mice with a glutamine seen in other mouse models (X817Q). A guide RNA (crRNA) was created to target *Atp10D* on chromosome 5 (nucleotides 72203329-72298771 bp, + strand): cRNA: AGTCAAAGGGCAGAATGTGT. The donor DNA

sequence was:

TATGCCGCCAGAGCTTACCGTTGCACTTTACAGTCTCGGACCCCAGAGCAGGTCATGGTGGACTTT GCTG CTTTGGGCTCATTAACATTT

C[1]AG[2]CTG[3]CTT[4]CACATTCTGCCCTTTGACTCTGTAAGGAAAAGAATGTCGGTCGTGGTCAGGCATC CTCTTTCCAAACAAGTCGTGGTGTAT. The superscript numbers next to the nucleotides indicate the following mutations: **1**. T to C introduces the desired STOP to Q correction. **2**. A to G is a silent mutation (CAA to CAG) that along with mutation 1 and 3 introduces a PvuII restriction site for screening and genotyping purposes. **3**. C to G is a silent mutation (CTC to CTG = L) that along with mutation 1 and 2 introduces a PvuII restriction site and mutates the PAM in the guide RNA. **4.** A to T is a silent mutation (CTA to CTT = L) that serves as a second mismatch, that along with the PAM mutation, ensures inhibition of Cas9 retargeting. The underlined sequence indicates the crRNA location. CRISPR editing reagents were delivered into the pronuclei of one-cell fertilized mouse zygotes (C57BL/6J). The resulting pups were biopsied and screened by PCR and Sanger sequencing. The predicted founders were bred to WT C57BL/6J animals and the offspring were genotyped (N1 generation). The offspring with the appropriate genotype were then backcrossed two more times.

Genotyping. Mice were genotyped using tail DNA. *Atp10D* DNA products were detected via PCR (Q5 High-Fidelity Polymerase, NEB, catalog #M0491S) followed by gel electrophoresis; *Atp10D*-F (CAAAACTGTCACCTCCTATGGA), *Atp10D*-R (GTATACACCACGACTTGTTTGG) for visualization (expected band size: 567 bp). After confirming amplification of the expected target via gel electrophoresis, PCR samples were purified (QIAquick spin column (lot No. 166028242)) and sent to Genewiz (https://www.genewiz.com/) for sequencing or a restriction digest reaction was done (PvuII-HF enzyme (NEB, catalog # R3151S), followed by gel electrophoresis and visualization. PCR products from *Atp10D* mice without the X817Q allele were not cut during the restriction digest (1 band on the gel (567 bp)) and those with the X817Q allele were cut (2 bands on the gel (567 bp, ~400 bp)).

Body composition. WT and experimental mice were 60% HFD (D12492, Research Diets) ad libitum at 6-9 weeks old. Mice were weighed once per week to measure body weight gain over time. On the 12th week on the HFD, body composition was assessed via NMR (LF50 Body Composition Mice Analyzer, Bruker, stock # E140000501).

Blood collection. Blood was taken from tail-veins, retroorbital bleeds, or cardiac punctures (for each method described here, the blood collection method is reported). Mice were awake and being monitored for signs of stress when tail blood was taken. Tail blood was collected using EDTA tubes (Sarstedt, Microvette CB 300 K2E, order # 16.444.100) and spun down at 4°C at full speed for 2 minutes. Before retroorbital bleeds were taken, mice were anesthetized for 1 minute via inhalation of Isoflurane via the SomnoFlo Low-Flow Electronic Vaporizer (Kent Scientific Corporation) operating at the settings approved by the IACUC protocol and mice were closely monitored during this procedure. For cardiac punctures, mice were first sacrificed using CO2 euthanasia systems followed by cervical dislocation. Retroorbital blood and cardiac puncture blood were placed into tubes containing 5 uL of 0.5M EDTA and centrifuged at 4°C at 2000 rcf for 15 minutes.

Oral glucose tolerance tests (OGTT) and fasting blood glucose/insulin measurements. Researchers were blind to the genotype of the mice during the OGTT. Mice were fasted for 5 hours (7AM-12PM) and then fasting blood was collected via retroorbital bleeds and mice were allowed to wake up and fully recover before the start of the OGTT. The mice were then gavaged with 20% w/v dextrose (final 2g/kg body weight), and a tail-vein blood glucose was measured via a glucometer (Accu-Chek, Accu-Chek Aviva Plus Meter) at baseline, 15, 30, 45, 60, 90, and 120 min. The area under of the curve for glucose was calculated using GraphPad Prism. Insulin from plasma samples collected from 5-hr fasted mice via the retroorbital bleed were measured using the Crystal Chem Ultrasensitive Mouse Insulin ELISA Kit (catalog # 90080).

Plasma lipid and lipoprotein analysis. Plasma was collected, via a cardiac puncture, in 5-hr fasted mice that had undergone an OGTT. Plasma samples were measured by the Vanderbilt Hormone Assay and Analytical Services Core, where plasma cholesterol and TG were measured by standard enzymatic assays, and plasma FFAs were analyzed with an enzymatic kit (Fujifilm Healthcare Solutions, catalog #999-34691).

Measuring liver lipids. Liver was collected from mice after CO2 sacrifice and cervical dislocation and was flash frozen in liquid nitrogen and then kept at -80^{o}C until further processing. Total liver lipids and lipid species were measured by the Vanderbilt Hormone Assay and Analytical Services Core. Briefly; lipids were extracted using the method of Folch-Lees [124]. The extracts were filtered and lipids recovered in the chloroform phase. Individual lipid classes were separated by thin layer chromatography using Silica Gel 60 A plates developed in petroleum ether, ethyl ether, acetic acid (80:20:1) and visualized by rhodamine 6G. Phospholipids, triglycerides and cholesteryl esters were scraped from the plates and methylated using BF_3 /methanol as described by Morrison and Smith [125]. The methylated fatty acids were extracted and analyzed by gas chromatography. Gas chromatographic analyses were carried out on an Agilent 7890A gas chromatograph equipped with flame ionization detectors and a capillary column (SP2380, 0.25 mm x 30 m, 0.20 μm film, Supelco, Bellefonte, PA). Helium was used as the carrier gas. The oven temperature was programmed from 160 °C to 230 °C at 4 °C/min. Fatty acid methyl esters are identified by comparing the retention times to those of known standards. Inclusion of lipid standards with odd chain fatty acids permits quantitation of the amount of lipid in the sample. Dipentadecanoyl phosphatidylcholine (C15:0), diheptadecanoin (C17:0), trieicosenoin (C20:1), and cholesteryl eicosenoate (C20:1) were used as standards.

Oil Red O. Liver was collected from mice after CO2 sacrifice and cervical dislocation and then placed in frozen section medium (Epredia, Neg-50, catalog #22-110-617) and then on dry ice. When the frozen section medium was solidified, the livers were placed at -20^{o}C until further processing. Further processing was done by the Vanderbilt Translation Pathology Shared Resource (TPSR): Slides were

brought to room temperature and placed in 10% NBF solution for 10 minutes. The Newcomer Supply Tech Oil Red O, Propylene Glycol staining kit (Newcomer Supply, catalog # 12772B) was used for visualization. Slides were then cover slipped with aqueous mounting medium. In regard to Oil Red O scoring: Dr. Katherine Gibson Corley, a board-certified veterinary pathologist at the Vanderbilt TPSR, created the scoring system used to score the Oil Red O stained liver sections. The scoring system is characterized by: 0= no Oil Red O staining, 1=rare and scattered Oil Red O staining, 2=multi-focal and coalescing Oil Red O staining, 3=diffuse Oil Red O staining (in whole tissue). To score the slides, the scorer was blinded to the slide IDs and then scored the slides twice, on two separate days. Then the scores from both days were compared and if they did not match, the scorer viewed the slide again and decided on a final score.

Statistics. All statistical analysis was done using GraphPad Prism, version 9.5.0 (GraphPad Software). Error bars indicate mean with standard error of the mean (SEM). When more than 2 groups were compared, a 2-way ANOVA was used with Dunnett's correction for multiple comparisons with a control group. Šidák's correction was used for comparison of groups of means. Differences between group mean values were tested using a 2-tailed Student's *t* test or a Mann-Whitney *U* test for nonparametric data. A *P* value of less than 0.05 was considered statistically significant.

Study approval. The animal protocol was approved by Vanderbilt University Medical Center and IACUC and all methods were performed in accordance with the relevant guidelines and regulations.

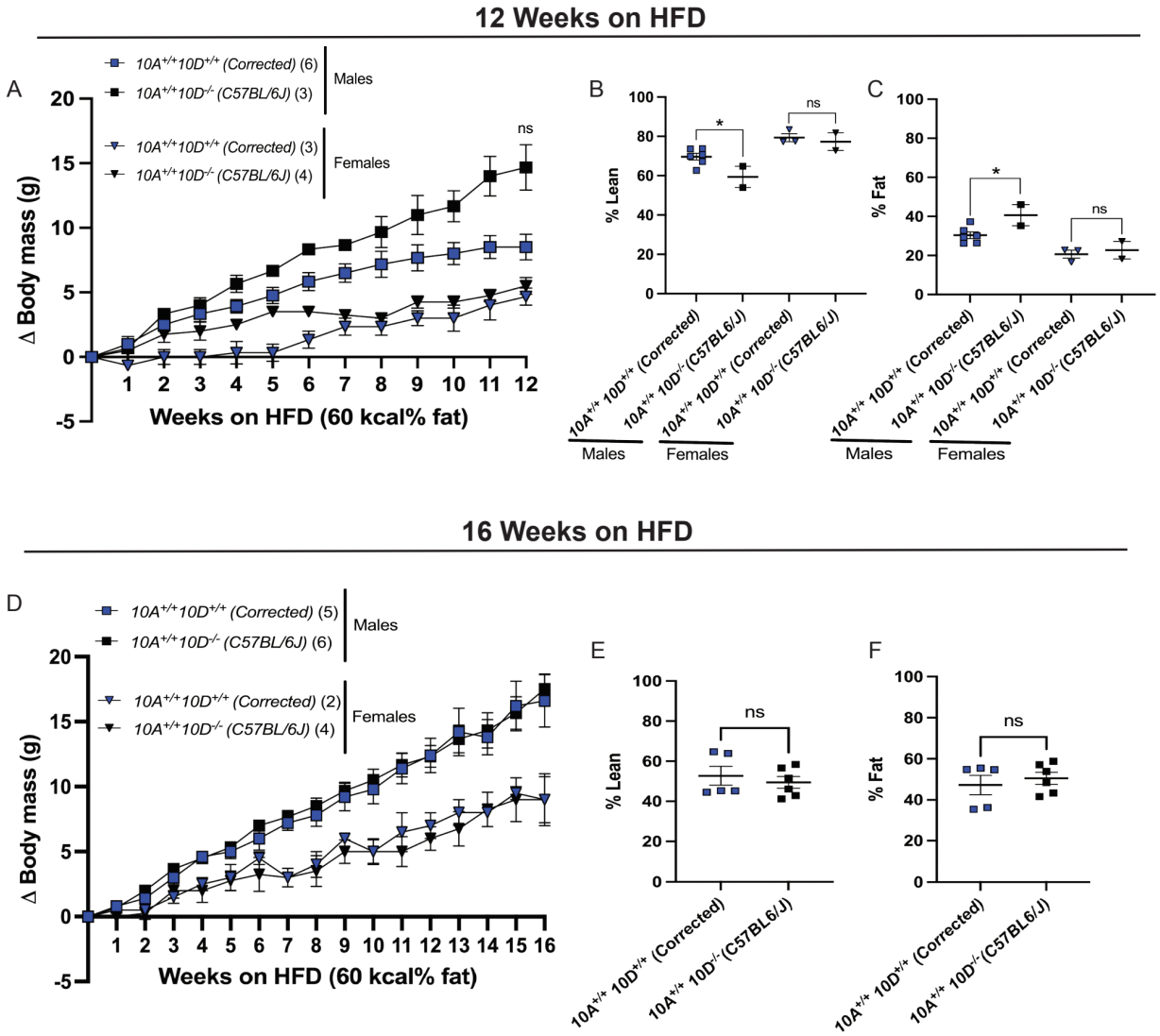

Figure 17. Body mass changes and body composition in *10D* corrected mice. (A,D) Weight gain of *10A$^{+/+}$10D$^{+/+}$ (Corrected)* and *10A$^{+/+}$10D$^{-/-}$* (*C57BL/6J)* mice over the course of (A) 12 weeks on a HFD (60 kcal% fat, Ad lib feeding) (male and female) or (D) 16 weeks on a HFD (males). P value by 2-way ANOVA with Sidak's multiple comparison. (B,C,E,F) Lean and fat mass were normalized to the combined sum of lean and fat mass to calculate % Lean and % Fat mass after (B,C) 12 weeks on a HFD (male and female) or (E,F) 16 weeks on a HFD (male) . P value by unpaired t-test. *P=0.0434 (**12 weeks on HFD**: **Male:** *10D$^{+/+}$* n=6, *10D$^{-/-}$* n=2; **Female:** *10D$^{+/+}$* n=3, *10D$^{-/-}$* n=2, **16 weeks on HFD**: **Male:** *10D$^{+/+}$* n=5, *10D$^{-/-}$* n=6).Average body mass (g) at end of HFD: **12 weeks**: Males: *10A$^{+/+}$10D$^{+/+}$*: 30.2 g, *10A$^{+/+}$10D$^{-/-}$*: 37.7 g, Females: *10A$^{+/+}$10D$^{+/+}$*: 24.3 g, *10A$^{+/+}$10D$^{-/-}$*: 24.5 g, **16 weeks**: Males: *10A$^{+/+}$10D$^{+/+}$*: 39.8 g, *10A$^{+/+}$10D$^{-/-}$*: 40.5 g, Females: *10A$^{+/+}$10D$^{+/+}$*: 28.5 g, *10A$^{+/+}$10D$^{-/-}$*: 28 g.

To test the effect of correcting ATP10D expression on weight gain, we placed *10A$^{+/+}$10D$^{+/+}$ (Corrected)* and *10A$^{+/+}$10D$^{-/-}$* (C57BL6/J) mice on a high fat diet and measured weight gain over time. Note that experimental mice were produced by the following breeding scheme: *10A$^{+/+}$10D$^{+/-}$* x *10A$^{+/+}$10D$^{+/-}$*. We measured weight gain over 12 weeks on a HFD and found no significant difference in weight gain based on genotype (Figure 17A). However, the male corrected mice appeared to have a trend toward gaining less weight over the course of the high fat diet; therefore, we placed the mice on a high fat diet for a longer period of time to determine if this would lead to a significant difference. However, we found no significant difference or trend toward a difference in weight gain over time, after 16 weeks on HFD, in male or female mice based on genotype (Figure 17D). We also measured body composition after 12 weeks of HFD feeding and found no significant difference in females based on genotype (Figure 17B, C). However, we did find that the male corrected mice exhibited significantly more % lean mass (Figure 17B) and less % fat mass (Figure 17C) compared to the original C57BL6/J mice. However, after adding more mice and extending the high fat diet to 16 weeks, we did not observe a significant difference in body composition in males based on genotype (Figure 17E, F). These results, though informative, arise from a pilot study with a limited number of mice in each group, resulting in underpowered analyses. To establish robust conclusions, further substantiation with a more extensive mouse population is warranted.

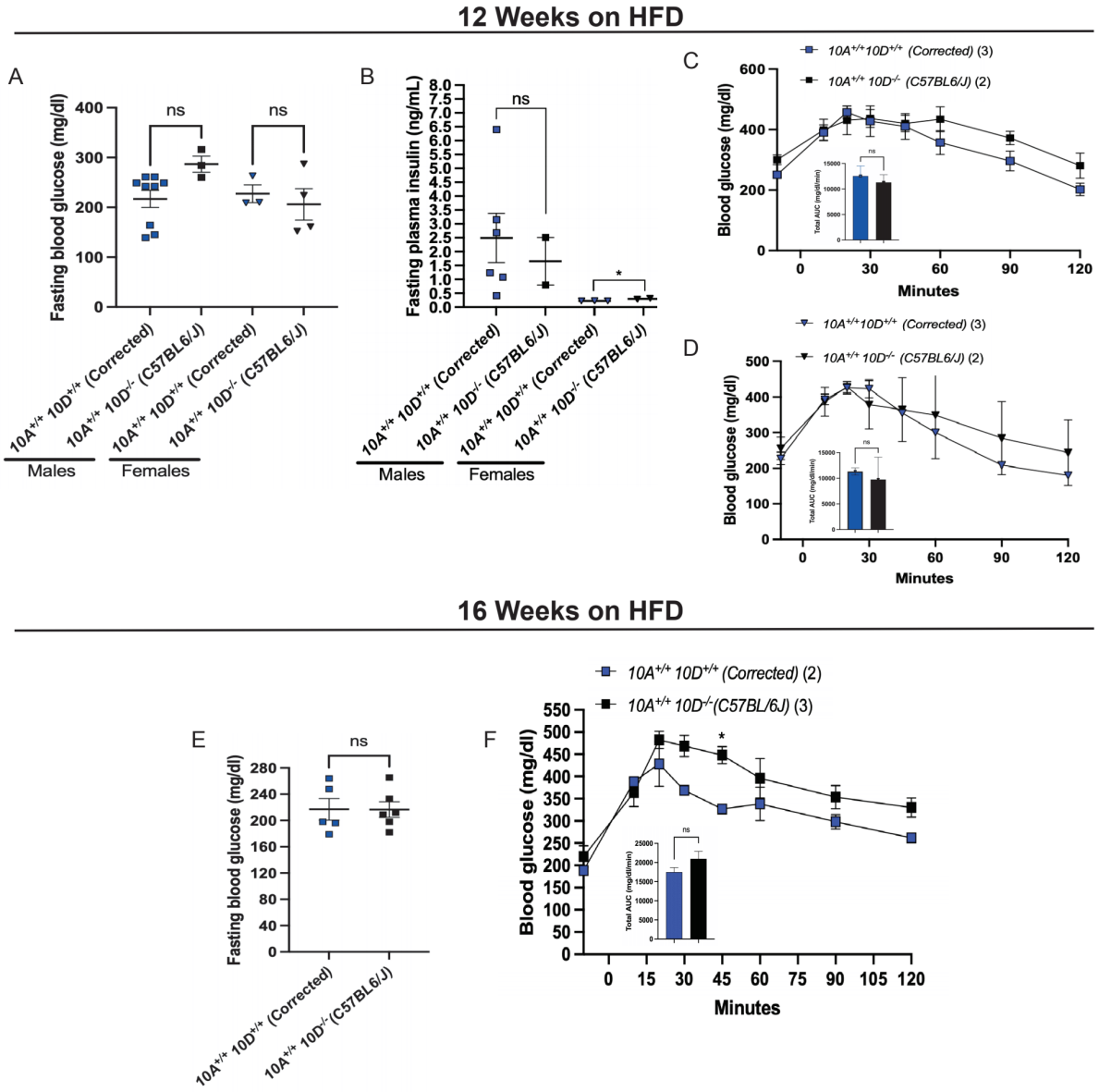

Figure 18. Glucose homeostasis in *10D* corrected mice. (A, E) Fasting blood glucose was measured from tail blood after a 5 hour fast, via a glucometer, after (A) 12 weeks on a HFD (males and females) or (E) 16 weeks on a HFD (males). P value by unpaired t-test **(12 weeks on HFD: Male:** *10D*$^{+/+}$ n=9, *10D*$^{-/-}$ n=3; **Female**: *10D*$^{+/+}$ n=3, *10D*$^{-/-}$ n=4, **16 weeks on HFD: Male:** *10D*$^{+/+}$ n=5, *10D*$^{-/-}$ n=6). (B) Fasting plasma insulin was measured after a 5 hour fast. P value by unpaired t-test, *P=0.0100 (**Male:** *10D*$^{+/+}$ n=6, *10D*$^{-/-}$ n=2; **Female:** *10D*$^{+/+}$ n=3,*10D*$^{-/-}$ n=2). (C,D,F) Mice were gavaged with 20% dextrose after a 5-hour fast, then an oral glucose tolerance test (OGTT) was performed after (C,D) 12 weeks on a HFD (males and females) or (E) 16 weeks on a HFD (males); the insets show the area under the curve (AUC) normalized to time 0 blood glucose. OGTT: P value by 2-way ANOVA with Sidak's multiple comparison, *P= 0.0436. AUC: P value by unpaired t-test.

We next measured glucose homeostasis in the *10A$^{+/+}$10D$^{+/+}$ (Corrected)* and *10A$^{+/+}$10D$^{-/-}$* (C57BL6/J) mice after 12 weeks or 16 weeks of high fat diet feeding (Figure 18). We found no significant difference in fasting blood glucose levels in males or females based on genotype after 12 weeks on HFD (Figure 18A) or in males, after 16 weeks on HFD (Figure 18E). We next determined fasting plasma insulin levels and found that after 12 weeks on HFD, male mice showed no significant difference based on genotype, but the female *10A$^{+/+}$10D$^{-/-}$* (C57BL6/J) mice exhibited higher fasting insulin levels compared to *10A$^{+/+}$10D$^{+/+}$ (Corrected)* mice (Figure 18B). However, the number of mice analyzed were too small to draw a conclusion. We also performed OGTT and found that after 12 weeks on HFD, there was no significant difference in glucose excursion following a glucose bolus in males or females based on genotype (Figure 18C, D). After 16 weeks on HFD, male *10A$^{+/+}$10D$^{-/-}$* (C57BL6/J) mice exhibited elevated glucose levels 45 minutes after the glucose bolus, compared to *10A$^{+/+}$10D$^{+/+}$ (Corrected)* mice, however the AUC from the OGTT did not show a significant difference based on genotype (Figure 18F). We also measured body weight gain, body composition, and fasting blood glucose after 12 weeks of HFD feeding in a model of 10A deficiency paired with 10D correction (*10A$^{+/+}$10D$^{+/+}$* vs. *10A$^{-/-}$10D$^{+/+}$*) and found no differences based on genotype (Supplemental Figure 12).

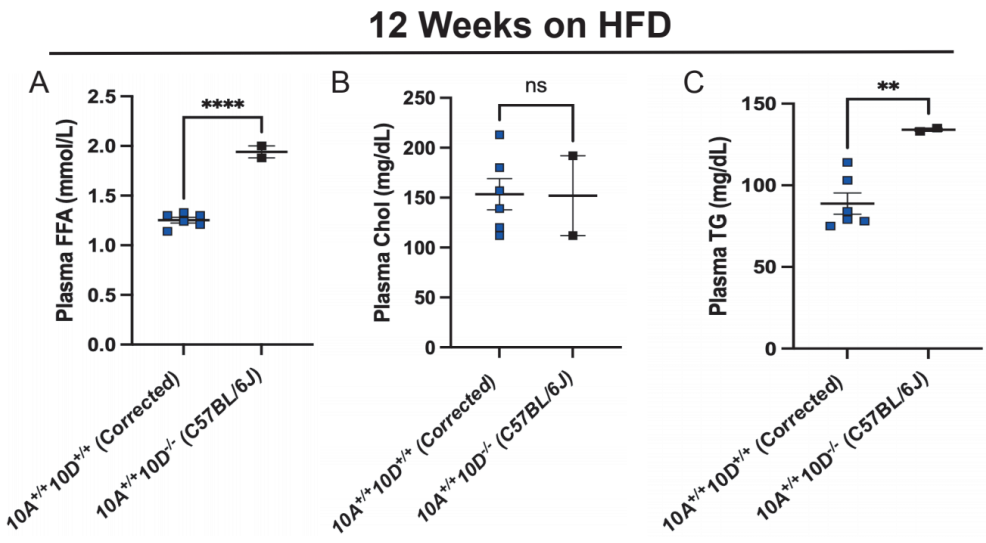

Figure 19. Plasma lipid measurements in male *10D corrected* mice after 12 weeks on HFD. (A) Free fatty acids (FFA), (B) cholesterol (chol), and (C) triglycerides (TG) were measured in plasma from males after a 5 hour fast followed by an OGTT. P value by unpaired t-test (*10D$^{+/+}$* n=6, *10D$^{-/-}$* n=2, ****P<0.0001, **P=0.0089).

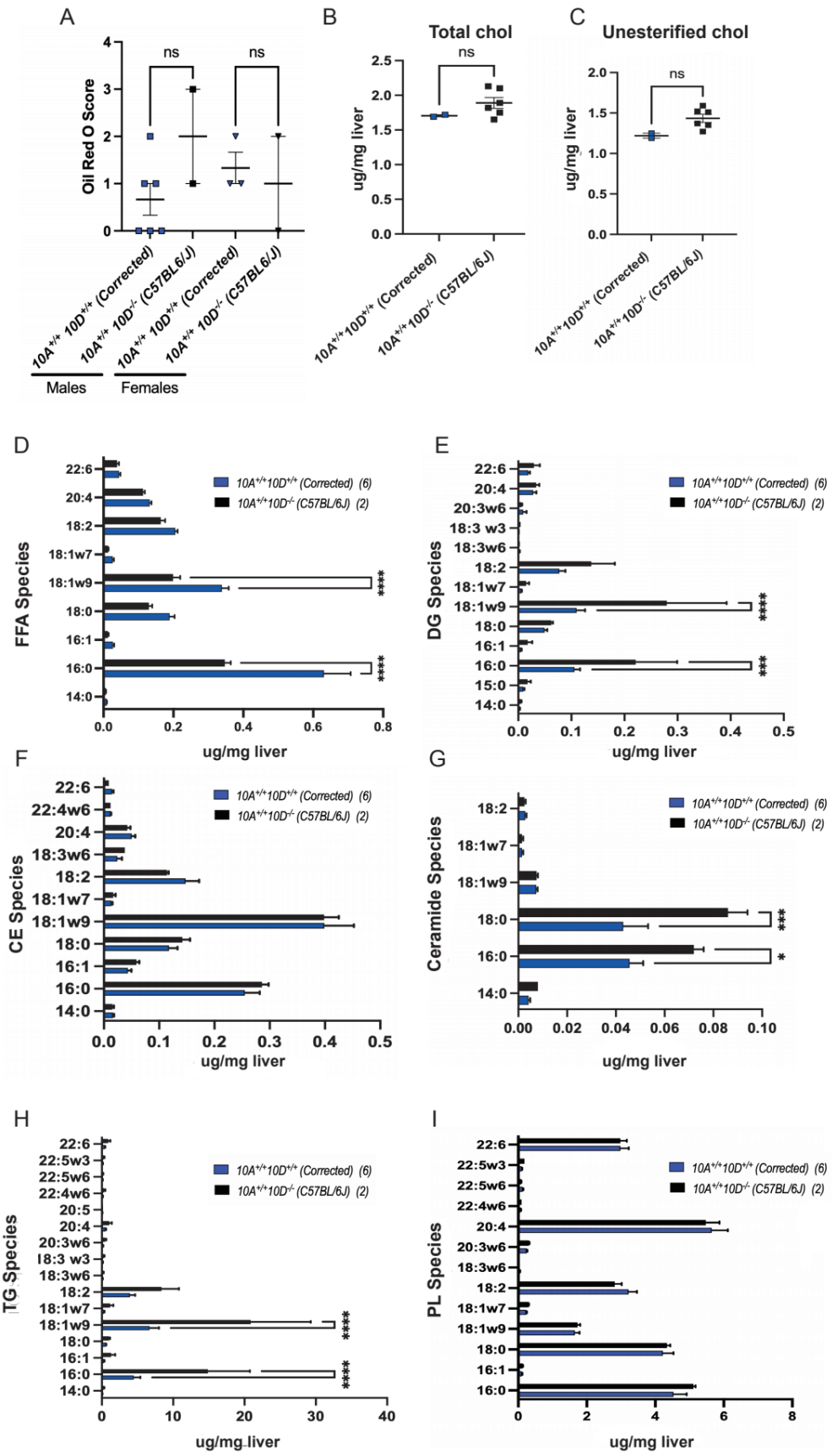

Figure 20. Liver lipid measurements after 12 weeks on HFD. (A) Liver sections were scored using the Oil Red O Score described in the Materials and Methods. P value by unpaired t-test (Males: *10D*$^{+/+}$ n=6, *10D*$^{-/-}$ n=2, Females: *10D*$^{+/+}$ n=3, *10D*$^{-/-}$ n=2). (B) Total cholesterol and (C) unesterified cholesterol were measured from flash frozen livers from male mice via gas chromatography. Livers were collected after a 5 hour fast followed by an OGTT test (Males: *10D*$^{+/+}$ n=2, *10D*$^{-/-}$ n=6). (D-I) The total amount of several different (D) FFA, (E) diacylglycerol (DG), (F) cholesterol ester (CE), (G) ceramide, (H) TG, and (I) PL were measured from flash frozen livers from males, via gas chromatography. Livers were collected after a 5 hour fast followed by an OGTT. P values by 2-way ANOVA with Sidak's multiple comparisons test, *P=0.0316, ***P= 0.0002, ****P=<0.0001.

To determine if correcting ATP10D expression resulted in changes to the levels of circulating lipids; we measured plasma free fatty acids (FFA), cholesterol (chol), and triglycerides in male *10A$^{+/+}$10D$^{+/+}$ (Corrected)* and *10A$^{+/+}$10D$^{-/-}$* (C57BL6/J) mice after 12 weeks of HFD feeding (Figure 19), note that the n for these studies is very small and we do not have enough statistical power to draw any conclusions. We found no difference in circulating levels of cholesterol based on genotype (Figure 19B). Interestingly, we did find that the *10A$^{+/+}$10D$^{-/-}$* (C57BL6/J) mice exhibited elevated levels of plasma FFA (Figure 19A) and TG (Figure 19C) compared to the *10A$^{+/+}$10D$^{+/+}$ (Corrected)* mice. To further probe the impact of correcting *Atp10D* on lipid metabolism, we measured levels of various lipid species in the liver. First, we determined the level of Oil Red O staining, a stain that binds to neutral lipids, in livers from *10A$^{+/+}$10D$^{+/+}$ (Corrected)* and *10A$^{+/+}$10D$^{-/-}$* (C57BL6/J) male and female mice after 12 weeks of HFD feeding and found no significant difference based on genotype (Figure 20A). As expected from the Oil Red O results, we also did not find a significant difference in total levels of cholesterol (Figure 20B) or unesterified cholesterol (Figure 20C) in livers from male mice based on genotype. Additionally, we measured several different FFA, diacylglycerol (DG), cholesterol esters (CE), ceramide, TG, and phospholipid (PL) ceramide species from the livers of male mice, differing in carbon chain lengths and saturation levels (Figure 20D-I). We found that *10A$^{+/+}$10D$^{+/+}$ (Corrected)* mice had elevated levels of FFA 16:0 and 18:1w9 compared to *10A$^{+/+}$10D$^{-/-}$* (C57BL6/J) mice (Figure 20D) while the *10A$^{+/+}$10D$^{-/-}$* (C57BL6/J) mice exhibited elevated levels of DG 16:0 and 18:1w9 (Figure 20E), ceramide 16:0 and 18:0 (Figure 20G), and TG 16:0 and 18:1w9 (Figure 20H). We found no significant differences in the levels of any of the CE (Figure 20F) or PL species (Figure 20I) measured, based on genotype.

DISCUSSION & CONCLUSIONS

We conducted pilot studies, that require more mice and statistical power, to investigate the impact of correcting ATP10D expression on weight gain and other metabolic parameters in mice after high fat diet feeding. From these preliminary results, we found no difference in weight gain in males or

females based on genotype (Figure 17. We also found that, after 12 weeks on a HFD, female *10A$^{+/+}$10D$^{+/+}$ (Corrected)* mice exhibited less fasting plasma insulin compared to *10A$^{+/+}$10D$^{-/-}$* (C57BL6/J) mice (Figure 18C) and that after 16 weeks on a HFD, male *10A$^{+/+}$10D$^{+/+}$ (Corrected)* mice exhibited lower glucose levels compared to *10A$^{+/+}$10D$^{-/-}$* (C57BL6/J) mice, 45 minutes after a glucose bolus (Figure 18F). Additionally, we found that after 12 weeks on a HFD, *10A$^{+/+}$10D$^{+/+}$ (Corrected)* mice had significantly less circulating levels of FFA (Figure 19A) and TG (Figure 19C) compared to *10A$^{+/+}$10D$^{-/-}$* (C57BL6/J) mice. Male *10A$^{+/+}$10D$^{+/+}$ (Corrected)* and *10A$^{+/+}$10D$^{-/-}$* (C57BL6/J) mice also exhibited differences in the amount of several different liver lipid species after 12 weeks on a HFD (Figure 20D-I). However, given the preliminary nature of the results presented in this chapter, it is essential to conduct further studies with a larger sample size. Therefore, the findings presented here serve as a foundation for future investigations but should not be construed as conclusive evidence regarding *Atp10D*'s role in metabolism.

Previously, there was a mouse model of *Atp10D* correction created by integrating a BAC-derived WT *Atp10D* into an undefined chromosomal position in the C57BL/6J background [93]. In this study, the control and experimental mice were fed a high-fat diet to induce metabolic defects and they reported improvements in body weight gain and composition, glucose tolerance, and lipid factors in the mice with the BAC-derived WT *Atp10D.* However, the study mice were all males and were hemizygous for the transgene and homozygous for *Atp10d$^{-/-}$* and the authors were not able to generate a control strain and did not study littermates to control for maternal effects, therefore, existing mouse models of *Atp10D* correction fail to clearly define the influence of this gene on metabolism. Our model of *Atp10D* correction provides an endogenous model of correcting this gene; where we are able to compare littermate controls. In opposition to the previous study [93]; we did not find any differences in body weight gain over time (Figure 17), fasting blood glucose (Figure 18A,E), or fasting insulin levels in males (Figure 18B). Interestingly the previous study reported a decrease in hepatic FFA 18:1w9 levels in the corrected mice compared to controls, and we found the opposite (Figure 20D). They also

reported no difference in hepatic FFA 16:0 levels based on genotype, however we found an increase in this lipid species in the corrected mice compared to controls (Figure 20D). Somewhat in line with the previous study [93]; we found an increase in % lean mass (Figure 17B) and reduced % fat mass (Figure 17C) in the *Atp10D* correction mice after HFD feeding, however this observation was lost when more mice were added and the HFD regimen was extended (Figure 17E, D). Additionally, we did find an improvement in glucose tolerance 45 minutes after a glucose bolus in the *Atp10D* correction mice compared to controls (Figure 18F) (note that the other study found a difference 90 minutes after the bolus). Similar to the Sigruener et al. paper, we did find that after HFD feeding, *Atp10D* correction mice had reduced circulating levels of TG (Figure 19C). However, as the investigations detailed in this chapter are preliminary and underpowered, there remains a need to compare the 'corrected mice' from the previous report with our more appropriate and more rigorously controlled *Atp10D* correction model.

We found that *Atp10A* has a sex specific role in dyslipidemia and endothelial cell insulin sensitivity, in C57BL6J mice that are naturally *Atp10D* deficient. Because we hypothesize that *Atp10D* also has a role in metabolism, it is necessary to determine the functional redundancy, if any, between these two genes. Therefore, we put $10A^{+/+}10D^{+/+}$ and $10A^{-/-}10D^{+/+}$ on a HFD for 12 weeks and measured weight gain in males and females, as well as body composition and fasting blood glucose in females. We found no significant differences in any of the metabolic parameters measured (Supplemental Figure 12). However, this study was preliminary and necessitates the addition of more mice, and this is currently being done in the lab.

In summary, different models of *Atp10d* correction could yield different outcomes and it is therefore important to use a model of endogenous expression where appropriate controls can be used. Furthermore, it is essential to incorporate both male and female subjects in mouse studies to avoid overlooking sex-specific differences. However, it is important to note that the studies discussed in this chapter are preliminary, and most results require a larger sample size, replication in both sexes, and examination at 12 and 16 weeks after a high-fat diet. Consequently, drawing conclusions from these

findings would be premature. Nevertheless, these initial results serve as a valuable starting point for further investigations into *Atp10d*'s role in metabolism, and this is still being studied in our lab.

Chapter 6: Metabolic profiling of the *Atp10A* deficient mouse model: Feces Lipid Content, Gene Expression, and Blood Pressure Analysis

INTRODUCTION

We previously determined that *Atp10A* deficient female mice exhibit diet-induced dyslipidemia, characterized by elevated circulating levels of cholesterol, TG, and FFAs as well as changes to lipoprotein (Figure 4) and liver lipid metabolism (Supplemental Figure 5). We also discovered that ATP10A is expressed in endothelial cells (Figure 7) and maintains insulin sensitivity in this cell type, including regulating the phosphorylation status of eNOS (Figure 8). To further characterize these phenotypes, we measured fecal cholesterol content as a measure of nutrient absorption, expression levels of several genes involved in metabolism in the liver and visceral fat, and blood pressure as a readout of vascular function in *Atp10A* deficient mice.

ATP10A transports PC [45] and we have previously shown that *Atp10A* deficient female mice exhibit alterations to cholesterol metabolism, including an increase in the levels of circulating cholesterol and alterations in HDL size and lipid content (Figure 4). Interestingly, mutations in the *ATP8B1* gene, which encodes a flippase that also transports PC [46] leads to cholestasis in humans, causing impaired bile flow and liver damage [47] and *Atp8b1*-deficient mice also demonstrate disrupted cholesterol handling, contributing to cholestasis [48]. In addition, *Atp10A* deficient mice exhibit a depletion of circulating bile acids compared to controls (Figure 5). Building on this context and considering the relationship between bile acid metabolism and cholesterol absorption [211], we measured fecal cholesterol content in *Atp10A* deficient mice, as a readout of cholesterol absorption. Indeed, fecal cholesterol represents the portion of ingested cholesterol that is not absorbed by the intestines and an increase in fecal cholesterol could indicate malabsorption or impaired cholesterol processing in the digestive system.

Female mice lacking *Atp10A* exhibit several changes in the transcriptome of visceral fat (VF), specifically impacting mRNA associated with glycerolipid metabolism and bile secretion (Figure 5, Supplemental Table 2). Additionally, hepatic proteins involved in glucose and lipid metabolism show alterations in both quantity and phosphorylation status in these mice (Figure 6). To further explore metabolic transcriptome changes in the liver and visceral fat of HFD fed *Atp10A*-deficient mice, we utilized qPCR to measure the mRNA levels of several genes. The panel of genes examined in the visceral fat include: *Pla2g5* and *Pla2g6*, members of the phospholipase A2 family that are involved in phospholipid hydrolysis, contributing to the release of bioactive lipids [212], *SCD1*, responsible for synthesizing monounsaturated fatty acids [213],*LPL*, which facilitates the hydrolysis of triglycerides in lipoproteins [214], *FAS*, involved in *de novo* lipogenesis, specifically the synthesis of long-chain fatty acids [215], *DGAT1* and *DGAT2*, enzymes involved in triglyceride synthesis [216], and *CGI58*, which participates in lipid droplet lipolysis [217]. Additionally, we examined the expression of multiple transcription factors, including *PPAR* and *PPARγ*, master regulators of lipid metabolism and storage as well as adipocyte differentiation [218], *LXR*, a transcription factor involved in cholesterol homeostasis [219], and *SREBP-1c*, which controls lipid and cholesterol synthesis [220]. In the liver, we also measured the mRNA expression of *PPARγ*, *FAS*, *SCD1*, and *LPL*, in addition to *Cyp7a1* and *Cyp8b1*, enzymes involved in bile acid synthesis [221].

We found that *Atp10A* deficient endothelial cells and aorta from female mice exhibit hyperphosphorylation of eNOS (Figure 8), a central cellular regulator involved in maintaining endothelial homeostasis, including vascular tone [222]. Alterations to the phosphorylation state of eNOS have been reported in a number of diseases, including hypertension and atherosclerosis, emphasizing the importance of regulation of eNOS activity [223]. Additionally, when the NO produced by eNOS reaches the blood, it can mediate NO bioactivities in the blood or vasculature, including regulating blood pressure [222, 224, 225]. Therefore, to determine if the hyperactivation of eNOS in the

aorta of the *Atp10A* deficient mice could alter systemic hemodynamics we measured blood pressure in the mice.

Due to the preliminary nature of the results presented in this chapter, it is essential to conduct further studies with a larger sample size. Therefore, the findings presented here serve as a foundation for future investigations but should not be construed as conclusive evidence regarding *Atp10A*'s role in cholesterol metabolism, gene expression, or blood pressure.

MATERIALS AND METHODS

Animals. All mouse experiments were approved under the Vanderbilt University Institutional Animal Care and Use Committee. Mice were housed in 12 h light/dark cycles in temperature and humidity-controlled facilities with ad-libitum access to diet and water (in the Barrier Facility). Mice in this study were sacrificed via CO2 euthanasia systems, operating at the recommended flow rates, followed by cervical dislocation; this method is an acceptable euthanasia method according to the American Veterinary Medical Association (AVMA) guidelines. The mouse studies described in this manuscript are reported in accordance with the ARRIVE guidelines (https://arriveguidelines.org/).

Creating the mouse model*.* The *Atp10A* mouse model (knockout allele name: *Atp10Aem1(Vtrg)*) was created via CRISPR-Cas9 in collaboration with the Vanderbilt Genome Editing Resource. Guide RNAs (crRNA) were created to target *Atp10A* on chromosome 7: Target Intron 1-2: TGACTGCTTAATGATTCGAGG, GAGTGACTGCTAATGATCG, Target Intron 2-3: GGAAAAAGCCCAATTCCACAC, AGCCCAATCCACACAGGAAC. CRISPR editing reagents were delivered into the pronuclei of one-cell fertilized mouse zygotes (C57BL/6J). Approximately 608 bp were deleted using this method: nucleotides 58389679-58390287 (NCBI reference sequence: NC_000073). The resulting pups were biopsied and screened by PCR and Sanger sequencing. The predicted founders were bred to WT C57BL/6J animals and the offspring were genotyped (N1 generation). The offspring with the appropriate genotype were then backcrossed two more times.

Genotyping. Mice were genotyped using tail DNA. *Atp10A* DNA products were detected via PCR (Q5 DNA Polymerase, NEB) followed by gel electrophoresis; *Atp10A-F* (GTGCACTGTATTTGTCTGCCTGTTCC), *Atp10A-R (*GGTCCTTTGAAGAGATAATGTTCCCAAC). PCR samples were purified (QIAquick spin column (lot No. 166028242)) and sent to Genewiz (https://www.genewiz.com/) for sequencing.

Feces sampling. Mice were housed alone for 72 hours and then feces were collected from the cage and the total amount collected was weighed. Feces were then flash frozen in liquid nitrogen and stored at -80^{0}C until further processing.

Measuring cholesterol in feces samples. Frozen feces were homogenized in cold 1x PBS using the OMNI INTERNATIONAL Homogenizer (Grainger) for 3-5 minutes and homogenate was stored at 4^{o}C until further processing (the amount of PBS used (mL) and the amount of feces added (mg) was recorded to determine concentration). Lipid was extracted from feces using a lipid extraction kit (catalog #STA-612, Cell BioLabs, Inc.). Cholesterol was measured from the extracted lipid using a total cholesterol assay kit (catalog # STA-384 Cell BioLabs, Inc.).

RNA extraction. After removal from mice; tissues were flash frozen in liquid nitrogen and stored at -80^{0}C until further processing. Tissues were thawed using RNA*later*-ICE **(**catalog # AM7030, Invitrogen) and then homogenized in QIAzol lysis reagent (catalog # 79306, QIAGEN) using the Bullet Blender (Next Advance). RNA was extracted from the homogenate using the RNeasy Lipid Tissue Mini Kit (catalog # 74804, QIAGEN). RNA purity and quality was assessed via spectrophotometry and gel electrophoresis, respectively.

RT-PCR and qPCR. cDNA was generated from RNA samples using iScript Reverse Transcription SuperMix (catalog # 1708840, Bio-Rad). The qPCR master mix consisted of cDNA (1:5), primers (4 uM)

(Primer sequences for each of the targets can be found in Supplemental Table 4), and the iQ SYBR Green Supermix (catalog # 1708880, Bio-Rad).qPCR was performed using the CFX96 Touch Real-Time PCR Detection System (Bio-Rad) with the following cycle sequence: 1: 95.0°C for 3:00, 2: 95.0°C for 0:15, 3: 56.0°C for 0:30 Increment temperature by 0.1°C per cycle, 4: 72.0°C for 0:30, Plate Read,5: GOTO 2, 40 more times, 6: Melt Curve 55.0°C to 95.0°C: Increment 0.5°C 0:05, Plate Read. qPCR data was processed using the CFX Maestro Software for CFX Real-Time PCR Instruments (Bio-Rad). The delta-delta Ct method ($2^{-\Delta\Delta Ct}$) was used to quantify the qPCR data, briefly, the difference between the target gene's cycle threshold (Ct) values and the reference gene's Ct values (Hprt1) were normalized to the average of the Ct values from the control samples.

Blood pressure measurements. Conscious mice were subjected to blood pressure measurements using the tail cuff method, employing the MC4000 Multi Channel Blood Pressure Analysis System (Hatteras Instruments) and corresponding software. The assessment spanned three days, with the initial day serving as a training session, during which each mouse underwent a single reading (comprising up to 10 blood pressure measurements). On days 2 and 3, mice underwent a total of three readings each (up to 30 measurements in total). Subsequent to data collection, a comprehensive analysis was conducted, involving outlier tests that compared the training data (day 1 measurements) with those from days 2 and 3. Inclusion or exclusion of the training data in the final blood pressure calculation was determined based on the absence of outliers in this comparison.

Statistics. All statistical analysis was done using GraphPad Prism, version 9.5.0 (GraphPad Software). Error bars indicate mean with standard error of the mean (SEM). When more than 2 groups were compared, a 2-way ANOVA was used with Dunnett's correction for multiple comparisons with a control group. Šidák's correction was used for comparison of groups of means. Differences between group

mean values were tested using a 2-tailed Student's *t* test or a Mann-Whitney *U* test for nonparametric data. A *P* value of less than 0.05 was considered statistically significant.

Study approval. The animal protocol was approved by Vanderbilt University Medical Center and IACUC and all methods were performed in accordance with the relevant guidelines and regulations

RESULTS

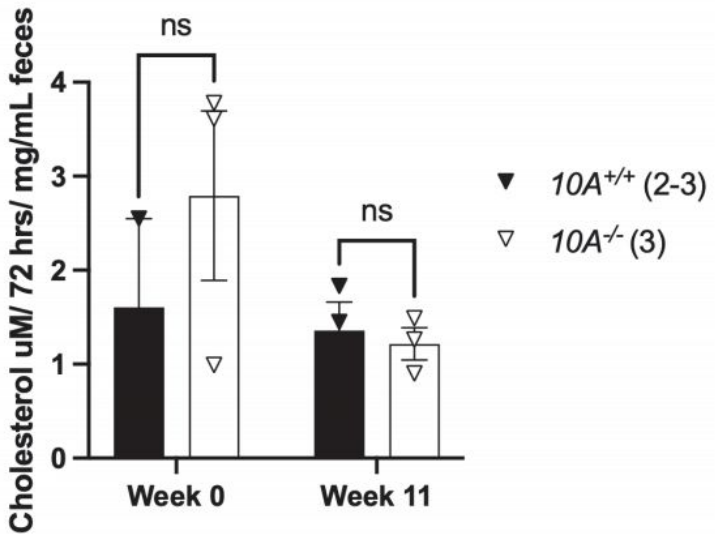

Figure 21. Fecal cholesterol measurements from *10A* deficient mice. Analysis of the cholesterol content in feces from *10A*$^{+/+}$ and *10A*$^{-/-}$ female mice, housed alone for 72 hours, after 0 (week 0) or 11 (week 11) weeks of HFD feeding (60 kcal% fat, Ad lib feeding). P value by unpaired t-test.

After high fat diet feeding, *Atp10A* deficient female mice exhibit elevated circulating levels of cholesterol and smaller HDL particles that trend toward having more cholesterol content compared to WT mice (Figure 4). To determine if these changes to cholesterol metabolism were due to alterations in cholesterol absorption and were also diet-induced; we measured cholesterol content in the feces from the mice before HFD feeding (week 0) and 11 weeks after HFD feeding (week 11). We found no significant difference in the amount of cholesterol in the fecal content before HFD feeding (week 0) or 11 weeks after HFD feeding based on genotype (Figure 21).

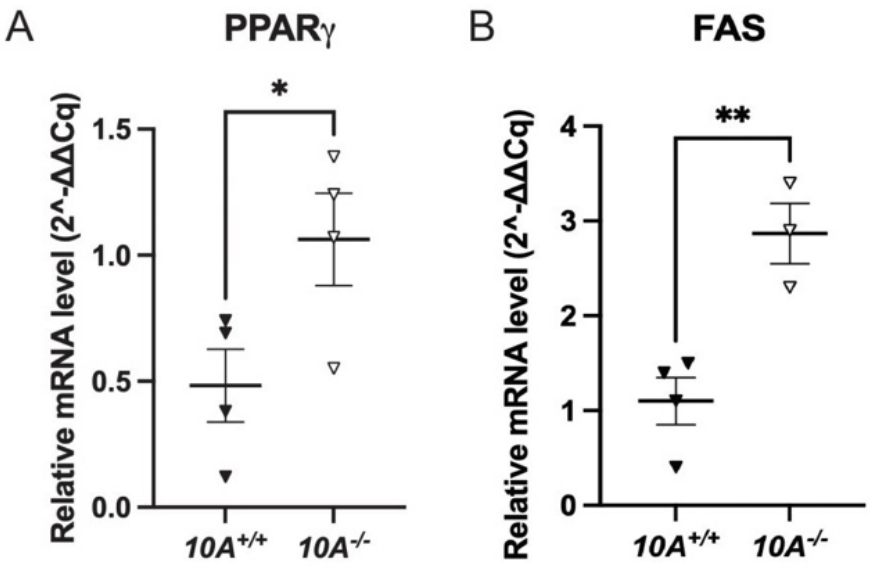

Figure 22. *10A* deficient female mice display increased mRNA levels of Peroxisome proliferators–activated receptor γ (PPARγ) and fatty acid synthase (FAS) in liver. (A,B) mRNA expression of (A) PPARγ and (B) FAS were measured via RT-PCR followed by qPCR, in livers from *10A*$^{+/+}$ and *10A*$^{-/-}$ female mice after 12 weeks of HFD feeding (60 kcal% fat, Ad lib feeding). mRNA levels were normalized using the 2–ΔΔCt method with Hrpt1 as the housekeeping gene. P value by unpaired t-test. *P=0.0474, **P=0.0067 ((A) *10A*$^{+/+}$ n=4, *10A*$^{-/-}$ n=4, (B) *10A*$^{+/+}$ n=4, *10A*$^{-/-}$ n=3).

Atp10A deficient female mice exhibit changes to the visceral fat (VF) transcriptome (Figure 5), including expression of mRNA with roles in glycerolipid metabolism and bile secretion (Supplemental Table 2). *Atp10A* deficient female mice also display several alterations to the total amount and phosphorylation status of several proteins in the liver that have roles in glucose and lipid metabolism (Figure 6). We next examined the expression, via qPCR, of various transcripts found from the RNA sequencing data as well as others not found in the dataset. We did not find any significant differences in the expression levels of any of the transcripts we measured in the visceral fat, based on genotype (Supplemental Table 5). We also measured the expression level of several transcripts involved in

metabolism in the liver and found significantly elevated mRNA levels of PPARγ and FAS in the *Atp10A* deficient females, compared to controls (Figure 22A,B).

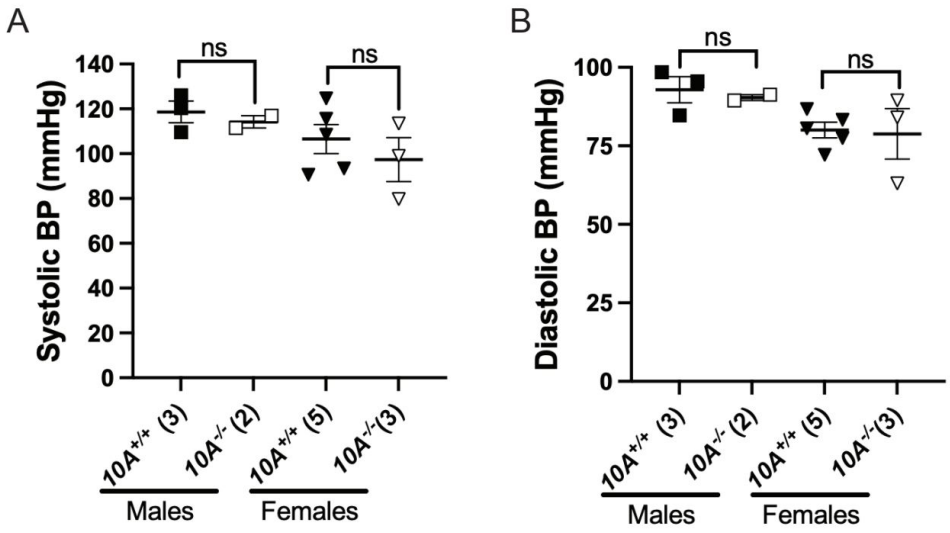

Figure 23. Blood Pressure (BP) measurements from *10A* deficient mice. (A) Systolic and (B) diastolic BP were measured using the tail cuff method in conscious 10-week old *10A*$^{+/+}$ and *10A*$^{-/}$ male and female on normal chow diets (4.5 kcal% fat, Ad lib feeding). P value by unpaired t-test.

We have previously shown that ATP10A is expressed in endothelial cells (Figure 7) and has a role in maintaining insulin sensitivity in this cell type (Figure 8). We also found that *Atp10A* deficiency leads to hyperphosphorylation of eNOS in HUVEC and SVEC as well as aorta from female mice (Figure 8). Because eNOS is a major regulator of vascular tone; we next wanted to determine if *Atp10A* deficiency would affect vasculature function in mice. To begin to explore this, we measured blood pressure (BP). However, we observed no significant differences in systolic BP (the pressure exerted on artery walls during heartbeats) or diastolic BP (the pressure in the arteries between heartbeats) between males or females based on genotype. (Figure 23A,B).

DISCUSSION & CONCLUSIONS

We found that *Atp10A* deficient mice do not display differences in cholesterol content in their feces (Figure 21) (females) or differences in blood pressure (males and females) (Figure 23), based on genotype. However, we did find that female *Atp10A* deficient mice exhibit elevated mRNA expression of PPARγ and FAS in their livers, compared to WT mice (Figure 22). However, these observations are from underpowered studies and require more study.

We have previously shown that after high fat diet feeding, *Atp10A* deficient female mice exhibit elevated circulating levels of cholesterol and smaller HDL particles that trend toward having more cholesterol content compared to WT mice (Figure 4). Changes in levels of circulating cholesterol and lipoprotein metabolism suggest abnormalities in multiple levels of cholesterol processing, including nutrient absorption [226, 227]. Interestingly, human ATP10A is expressed in the proximal digestive tract and gastrointestinal tract (protein data, [228]) and the stomach (RNA data, [153]). Additionally, murine *Atp10A* is expressed in the intestine (RNA data, [155]). Therefore, we measured cholesterol content of feces, a readout of ingested cholesterol that is not absorbed by the intestines, in our mouse model to determine if *Atp10A* deficiency effects cholesterol absorption. We also wanted to determine if this observation would be affected by high fat diet feeding and we found no difference in fecal cholesterol content before HFD feeding or 11 weeks after HFD feeding in female mice, based on genotype (Figure 21). However, the n for these experiments is small and necessitates the inclusion of more mice as well as measurements taken at more time points over the course of the HFD.

We found elevated mRNA expression of PPARγ (Figure 22A) and FAS (Figure 22B) in the liver of female *Atp10A* deficient mice after HFD feeding, compared to controls. The PPAR of proteins are master regulators of metabolism that are expressed in multiple tissues, including the liver [218]. These proteins are activated by multiple ligands and interestingly, PPARγ is activated by arachidonic acid metabolites [229, 230] and ATP10A effects the activation of $cPLA_2$, an enzyme that produces

arachidonic acid (Figure 6,8). Under normal conditions, PPARγ is highly expressed in adipose tissue and macrophages [231] and exhibits much lower expression in the liver. However, a significant increase in hepatic PPARγ is a common phenotype of steatotic animals associated with obesity [232, 233]. Additionally, when PPARγ is ectopically overexpressed in hepatocytes, lipid droplets accumulate [234]. Indeed, PPARγ up-regulates several proteins associated with lipid uptake, TG storage, and formation of lipid droplets, such as CD36, SCD1, MOGAT1, and PLIN2. Female *Atp10A* deficient mice exhibit higher levels of unsaturated versus saturated lipid species (a readout of elevated SCD1 activity) (Supplemental Figure 5H,I) larger liver lipid droplets (Supplemental Figure 5L), and elevated protein expression of DGAT 2 in the liver (Figure 6). The potential contribution of elevated PPARγ expression to the alterations in liver lipid metabolism observed in the *Atp10A* deficient female mice needs to be further investigated and the expression of genes that are transcriptionally regulated by PPARγ needs to be examined in these mice. *Atp10A* deficient female mice also exhibit elevated mRNA expression of hepatic FAS (Figure 22B). FAS (also known as FASN) catalyzes the last step in FA synthesis and is the major determinant of the maximal hepatic capacity to generate FA via *de novo* lipogenesis [235, 236] and there is a correlation between FAS expression and hepatic steatosis [237]. The effect ATP10A has on FA metabolism in the liver is complex because *Atp10A* deficient mice exhibit elevated activating phosphorylation of hepatic AMPK (Figure 6), a protein that inhibits FA production [238], and *Atp10A* deficient mice have lower liver FFA compared to controls (Supplemental Figure 5A), despite exhibiting elevated mRNA expression of FAS in the liver (Figure 22B). One potential explanation is that elevated FAS mRNA expression may indicate that the liver is responding to the lower FFA levels by upregulating FAS mRNA expression, but the hyperactivation of AMPK could be limiting the actual synthesis of FAs due to inhibition of the protein FAS and this needs to be investigated.

In our prior research, we demonstrated the expression of ATP10A in endothelial cells (Figure 7) and its involvement in preserving insulin sensitivity within this cell type (Figure 8). Additionally, we observed that the absence of *Atp10A* results in hyperphosphorylation of eNOS in HUVEC and SVEC as well as in aorta from female mice (Figure 8). Given the important role of eNOS in regulating vascular

tone, we investigated whether *Atp10A* deficiency could impact vascular function in mice by measuring blood pressure. We found no difference in blood pressure measurements in male or female mice (Figure 23). However, this was a pilot study with a small number of mice that were on a normal chow diet and therefore did not capture any diet-induced changes and we also used the tail cuff method which is a less accurate measure of blood pressure compared to other procedures such as implanted telemetry systems [239]. In the future, we will run well powered studies using the implanted telemetry systems as well as wire myographs to evaluate vasoconstrictor and vasodilator properties of isolated mouse arteries [240] in response to molecules such as insulin in male and female *Atp10A* deficient and WT mice after normal chow diet or HFD feeding.

It is crucial to emphasize that the investigations presented in this chapter are in their preliminary stages, and the majority of outcomes necessitate a larger sample size. As a result, making definitive conclusions based on these findings would be premature. Nevertheless, these initial findings provide a valuable foundation for ongoing research into the role of ATP10A in metabolism and vasculature function.

Chapter 7: Conclusions and Future Directions

The journey embarked upon in this dissertation has been both exciting and productive, marked by numerous discoveries that have significantly advanced our understanding of ATP10A's function. Notably, we achieved the first gene-specific knockout of *Atp10A* and unveiled its important role in lipid homeostasis in females. Additionally, our research revealed a novel connection between ATP10A and insulin receptor signaling in endothelial cells and the liver, shedding light on previously unexplored aspects of this important signaling cascade. Furthermore, we described the first-ever demonstration of male-specific infertility in *Atp10A* knockout mice. We also performed one of the first comprehensive analyses of ATP10A protein expression in various tissues and cells and this helped us understand more about the potential physiological implications of *Atp10A* deficiency. Moreover, we created the first genetic correction of *Atp10d* in the C57Bl/6J background, paving the way for future investigations as well as providing much needed context for all of the metabolic studies done with this mouse strain. Collectively, our findings underscore the significance of ATP10A in lipid homeostasis in females, endothelial cell insulin sensitivity, and the maintenance of fertility in males.

The role of ATP10A in maintaining endothelial cell and hepatic insulin sensitivity

We have shown that ATP10A is expressed in endothelial cells (ECs) (Figure 7) and inhibits the insulin signaling pathway during basal levels of insulin to maintain EC insulin sensitivity. *Atp10A* deficiency results in EC insulin resistance, characterized by hypersignaling during basal conditions of insulin. This hypersignaling includes hyperphosphorylation of endothelial nitric oxide synthase (eNOS), an enzyme involved in vasodilation (Figure 8). We propose that downstream of EC insulin resistance, hepatocytes, and possibly adipocytes, exhibit impaired insulin signaling via an unknown mechanism (Figure 9A). Additionally, we hypothesize that ATP10A is inhibiting insulin signaling by translocating PC and GlcCer from the outer leaflet to the inner leaflet of the plasma membrane (PM) and thus modulating the lipid environment and affecting the activity of membrane-resident receptors and enzymes, altering the levels of bioactive lipids in the cell, and/or inducing endocytosis of the insulin receptor (Figure 9B).

EC's response to insulin, mediated by insulin receptors, can affect the systemic response to insulin in several ways; by controlling the transendothelial transport of insulin and thus the kinetics of target tissue's response to insulin [241-244], by inducing vasodilation via activation of eNOS and affecting glucose disposal [245], and by inducing production of molecules such as nitric oxide (NO), a potent vasodilator, that can increase glucose uptake in target tissues [137,138]. Therefore, the endothelium itself is a target tissue of insulin, not only for transendothelial transport, but also to undergo insulin signaling upon insulin binding the insulin receptor, therefore, insulin resistance can exist at the level of ECs. We discovered that *Atp10A* deficient ECs hypersignal during basal levels of insulin and cannot further respond to insulin stimulus**.** We also observed hepatic IR in *Atp10A* deficient mice (Figure 6) and we propose that hypersignaling in ECs could cause downstream insulin resistance in tissues associated with the endothelium, such as the liver. A model of excessive insulin signaling in ECs resulting in hepatic insulin resistance has been previously proposed [139]. The authors created mice that lack FoxO isoforms, a family of transcription factors that are inhibited by insulin signaling [246], specifically in ECs. They found that the mice developed hepatic insulin resistance due to constitutively active eNOS in the ECs resulting in excessive generation of NO that impaired insulin action in hepatocytes via tyrosine nitration of the insulin receptors. Classically, NO has been described as exerting metabolically protective effects, however, whether NO has beneficial or harmful effects depends on the bioavailability of NO (balance between NO production and removal), how much is produced, and the genetic background of the animal where NO levels are being modulated [247]. Altogether, these findings can inform our model of how *Atp10A* deficiency in ECs could result in insulin resistance in hepatocytes (Figure 9); perhaps the constitutive activation of eNOS we observed in *Atp10A* deficient ECs results in excessive NO production and tyrosine nitration of insulin receptors in the hepatocytes. To test this, *Atp10A* deficient HUVECs could be co-cultured with hepatocytes and NO production from HUVECs and tyrosine nitration of insulin receptors in hepatocytes could be measured and compared to control cells. Insulin has been shown to stimulate NO production in HUVECs [248] by

binding the insulin receptor and signaling through PI3K and Akt [249], therefore the EC cell model we used in this report would be suitable for these purposes.

Atp10A deficiency in female mice on HFD results in impaired insulin signaling in the liver. Insulin resistance can be defined as a condition in which elevated levels of insulin are needed to elicit an appropriate metabolic response or normal insulin concentrations do not achieve a metabolic response [250]. In the case of *Atp10A* deficiency, we hypothesize that we are observing impaired insulin signaling in the liver characterized by the latter because we did not observe elevated fasting insulin in the mice (Figure 3F) and we found that *Atp10A* deficient ECs cannot respond to insulin treatment. Although the *Atp10A* deficient mice exhibit impaired insulin signaling in the liver, we did not detect changes to whole-body glucose homeostasis (Figure 3E-H). Indeed, insulin resistance can occur without resulting in systemic changes to glucose homeostasis if some tissues remain insulin sensitive [251]. We hypothesize that the adipose tissue in *Atp10A* deficient mice is undergoing some sort of metabolic dysfunction because we observed ATP10A expression in ECs in visceral fat (Figure 7C), alterations to the transcriptome in this tissue in *Atp10A* deficient mice (Figure 5C), as well as elevated levels of plasma FFA (Figure 4D), that might be due to insulin resistance in the adipose tissue resulting in an increase in hormone sensitive lipase (HSL) activity and thus an increase in intracellular lipolysis of TG stored in lipid droplets. However, we did not specifically measure the phosphorylation state of proteins downstream of insulin binding the insulin receptor in adipose tissue. Additionally, we did not measure if *Atp10A* deficiency alters insulin signaling in the muscle, therefore the adipose tissue and muscle in *Atp10A* deficient mice could still be insulin sensitive and therefore compensating for impaired insulin signaling in the liver and thus able to maintain systemic glucose homeostasis.

The temporal sequence of metabolic perturbation in *Atp10A* KO mice

The temporal sequence of the metabolic perturbations in the *Atp10A* deficient mice is not yet defined. We propose that *Atp10A* deficiency results in insulin resistance at the level of the ECs and downstream of this whole-body metabolic perturbation occur. Indeed, during obesity induced by HFD-

feeding, insulin resistance develops in the vasculature, due to changes in the production of the potent vasodilator, NO, before it develops in muscle, liver or adipose tissue [141, 142]. This supports the idea that *Atp10A* deficiency results in changes to the endothelium first and that impaired insulin signaling in the liver occurs subsequently. *Atp10A* deficient female mice exhibit dyslipidemia characterized by elevated levels of plasma FFA (Figure 4D), cholesterol (Figure 4E), TG (Figure 4F), and alterations in the size and lipid content of both VLDL and HDL (Figure 4G,H). Dyslipidemia and IR are tightly linked [252, 253] therefore, the observed dyslipidemia could originate due to insulin resistance in ECs. Indeed, eNOS has been shown to regulate lipid metabolism; *eNOS*$^{-/-}$ mice display liver lipid accumulation [254], hypertension [255], dyslipidemia characterized by elevated plasma levels of cholesterol, TGs, and FFAs [256], as well as defective mitochondrial biogenesis and lower mitochondrial beta-oxidative activity [257, 258]. Another way insulin resistance originating at the endothelium could result in dyslipidemia is via modulation of the expression of lipoprotein lipase (LPL), an enzyme expressed on the endothelium that degrades circulating TGs, and is regulated by insulin [259-262]. A reduction in LPL activity can reduce the clearance of TG from the plasma and result in hypertriglyceridemia [198, 199]. In Chapter 4, we showed evidence of ATP10A and LPL colocalizing in visceral fat and elevated LPL activity in gastrocnemius muscle in *Atp10A* deficient mice (Figure 15). More work is needed to determine the potential relationship between ATP10A and LPL, including colocalization studies such as FRET, proximity ligation assays, and co-immunoprecipitation experiments with antibodies towards LPL and ATP10A. It would also be interesting to perform an *in vivo* heparin experiment on *Atp10A* WT and KO mice to determine if the amount of extracellularly localized LPL is different based on genotype.

Perhaps EC insulin resistance results in adipose tissue insulin resistance and downstream of this dyslipidemia occurs. Insulin resistant adipocytes with increased activity of HSL can increase FFA in plasma and thus FFA flux to the liver, which is substrate for VLDL TG synthesis [130-132]. Another potential option is that EC insulin resistance results in impaired insulin signaling in the liver and downstream of this dyslipidemia occurs. Another source of TGs for assembly and secretion into VLDL is de novo lipogenesis (DNL) in the liver, and increased DNL has been shown to contribute to VLDL TG

synthesis in obese and IR humans [263-265]. However, *Atp10A* deficient mice exhibit an increase in activating phosphorylation of AMPK, a master regulator of lipid metabolism, that increases fatty acid oxidation and decreases DNL [134], as well as decreased total liver FFAs (Supplemental Figure 5A). However, these mice also exhibit elevated hepatic mRNA levels of FAS and one potential explanation is that elevated FAS mRNA expression may indicate that the liver is responding to the lower FFA levels by upregulating FAS mRNA expression, but the hyperactivation of AMPK could be limiting the actual synthesis of FAs due to inhibition of the protein FAS and this needs to be investigated. Taken together, it is likely that the trend toward *Atp10A* deficient mice having more TG in VLDL is born from eNOS dysfunction in ECs or insulin resistant adipocytes providing elevated levels of FFA to the liver to be used in VLDL TG synthesis. The temporal sequence of the metabolic perturbations observed in *Atp10A* deficient mice needs to be elucidated and will provide more mechanistic insight into ATP10A's role in metabolism. To explore this, a plausible approach involves subjecting female *Atp10A*-deficient mice and WT controls to a HFD for 12 weeks. Weekly assessments can be conducted to investigate the emergence of liver insulin resistance, adipose insulin resistance, and vascular insulin resistance. This entails examining the insulin signaling pathway status in these distinct tissues, aiming to discern any temporal variations in the onset of insulin resistance across different tissues.

ATP10A's role in Cholesterol Metabolism

Atp10A deficient mice exhibit more cholesterol in HDL and smaller HDL particles (Figure 4G). Mice naturally lack cholesterol ester transfer protein (CETP) [266] and therefore one would expect to see more cholesterol in HDL in mice. However, the smaller HDL particles caused by *Atp10A* deficiency is an unexpected and interesting finding and might be indicative of a quality versus quantity issue [135]. We also examined potential cholesterol absorption issues in the *Atp10A* deficient mice by measuring fecal cholesterol content, but found no difference based on genotype (Figure 20). However, this is still an open and interesting question that requires more well powered studies to determine if there is a difference. Additionally, *Atp10A* deficient mice display elevated levels of monounsaturated versus

saturated TG, PL, and cholesterol ester (CE) species in their livers (Supplemental Figure 5H,I). This could be due to an increase in activity of stearoyl-CoA desaturase–1 (SCD1), an enzyme that catalyzes the synthesis of monounsaturated FAs from saturated FAs. Interestingly, Scd1 activity has been suggested to be required for the onset of diet-induced hepatic insulin resistance [267]. *Atp10A* deficient mice also exhibit more Oil Red O staining, a stain that binds neutral lipids, compared to control mice (Supplemental Figure 5J,K), however we did not measure an increase in levels of liver cholesterol (Supplemental Figure 5B) or TG (Supplemental Figure 5E), therefore we propose that the increase in Oil Red O staining is due to staining of another neutral lipid. Additionally, the *Atp10A* deficient mice display larger liver lipid droplets compared to control mice (Supplemental Figure 5L), this could be another reason we observed more Oil Red O staining in these mice. The mechanisms behind the smaller HDL particles, the increase in monounsaturated lipid species, the potential alterations to cholesterol absorption, and the increase in Oil Red O staining in the *Atp10A* deficient mice needs to be further explored.

Investigating the Systemic Metabolic Consequences due to *Atp10A* Deficiency: A Tale with Endothelial Cell Origins?

We hypothesize that ATP10A could affect metabolism in ECs and then systemically by three different methods. The first is that ATP10A flips its lipid substrate to modulate the PM lipid environment where receptors, such as IR and IGF1, and enzymes, such as LPL, reside, and thus potentially modulate their activity [196]. The phenotypes observed due to *Atp10A* deficiency provide evidence that modulating the PM can have systemic effects on metabolism and caveolae provide another example of this. Caveolae are a kind of membrane microdomain that have implications in membrane organization, signaling, and protein trafficking [268]. *Atp10A* deficiency results in activating hyperphosphorylation of eNOS, therefore ATP10A most likely has a role in inhibiting eNOS, either directly or indirectly. Interestingly, caveolae are highly expressed in ECs [269] and cav-1, the main protein component in caveolae, has been found to also inhibit eNOS [270]. Additionally, global *cav-1* knockout mice display

endothelial dysfunction [271] and HFD induced obesity has been shown to increase Cav-1 expression in the vasculature and result in impaired NO-mediated vasodilation [272]. Insulin receptors and IGF-I receptors are also enriched in caveolae and insulin and IGF-I signaling result in cav-1 phosphorylation [273-277]. Taken together, these observations could be revealing a conserved regulatory mechanism in ECs that originates through modulation of PM organization, by lipid translocation (i.e. ATP10A) or by specialized PM domain formation (i.e. caveolae).

Another way ATP10A could affect metabolism in ECs and then systemically is by modulating the levels of bioactive lipids in the cell by translocating lipids from the outer leaflet to the inner leaflet of the PM, making them available to the cytosolic space to have a bioactive effect. ATP10A can translocate PC. Interestingly, increasing PC synthesis in mice without *mTORC1*, a major downstream mediator of insulin action on cellular anabolic processes [278], restores normal TG secretion [279]; therefore, PC has a role in whole body lipid homeostasis. Additionally, our studies indicate that *Atp10A* deficiency leads to a decrease in activating phosphorylation of cytosolic phospholipase 2 ($cPLA_2$) in the liver (Figure 6D,E), depletion of circulating levels of eicosanoids (Figure 5A,B), and activating hyperphosphorylation of $cPLA_2$ in ECs. $cPLA_2$, an enzyme with established roles in disease [280], catalyzes the hydrolysis of phospholipids, such as PC, to lysophospholipids and arachidonic acid (AA), and AA species can be oxidized to form eicosanoids. It is possible that ATP10A is providing substrate to $cPLA_2$ by translocating PC into the cytosolic space. Interestingly, we found that in testes and vas deferens, *Atp10A* deficiency also results in elevated activating phosphorylation of $cPLA_2$ (Figure 8) and $cPLA_2$ knockout mice exhibit reduced fertility [172]. The relationship between ATP10A flipping PC and $cPLA_2$ activity in the liver, ECs, and male reproductive organs needs to be further investigated.

$cPLA_2$ can hydrolyze PC into lysophosphatidylcholine (LPC), a bioactive lipid. LPC has been implicated as the lipid intermediate that links saturated FAs to IR [145] and in the liver; LPCs can upregulate genes involved in cholesterol biosynthesis, downregulate genes involved in hepatic FA oxidation, and induce mitochondrial dysfunction [281]. Additionally, there is evidence that LPC can bind to and activate PPARγ [282] and we found an increase in hepatic PPARγ mRNA expression in the

Atp10A deficient mice, compared to controls (Figure 22A). Levels of LPC in circulation are associated with the development of atherosclerotic plaques [283, 284], and some LPC species are diagnostic markers for myocardial infarction and coronary atherosclerosis [285, 286]. As made evident by the association between circulating LPC levels and cardiovascular dysfunction; LPC can affect the endothelium. Enhanced activity of PLA2 has been shown to increase the LPC content in LDL and oxidized LDL and result in endothelial dysfunction and affect the development of atherosclerotic plaques [287]. Interestingly, *Atp10A* deficient mice exhibit elevated mRNA expression of *Pla2g5,* a secreted phospholipase, in visceral fat (Figure 5C). Additionally, LPC induces overproduction of NO, which may increase oxidative stress on ECs [288] and it also has an inhibitory effect on the insulin signaling pathway at the point of IRS-1 in the vasculature [289]. $cPLA_2$ can also hydrolyze PC to form AA, which can be oxidized to form eicosanoids. Eicosanoids are bioactive lipids, with roles in inflammation and vasculature maintenance [108, 109], created by oxidation of either ω-3 or ω-6 20-carbon fatty acids and are grouped into several categories including leukotrienes, lipoxins, hydroxy-eicosatetraenoic acids, hydroxy-eicosapentaenoic acids, eoxins, isoprostanes, resolvins and prostanoids. AA and eicosanoids are potent bioactive molecules and are not normally stored in cells; instead they are stored as membrane phospholipids, such as PC. Therefore, the first step in AA biosynthesis is for membrane phospholipids to be made available to phospholipases in the cytosolic space, perhaps by flippases, such as ATP10A. ECs exhibit all the major eicosanoid production pathways [290] and therefore, ECs are a source of eicosanoids in the body. Eicosanoids can act in an autocrine fashion and affect ECs. Indeed, eicosanoids have been identified as contributors to atherogenesis [291] and there is crosstalk between eicosanoids and NO. NO can react with superoxide anions and become peroxynitrite, which directly regulates eicosanoid biosynthesis [292]. Altogether, the modulation of $cPLA_2$ activity due to *Atp10A* deficiency could alter the levels of bioactive lipids such as LPC, AA, and eicosanoids, and affect EC function as well as have downstream metabolic effects on hepatocytes. We hypothesize that ATP10A can modulate $cPLA_2$ activity at the level of controlling substrate availability, however, we could be observing changes in $cPLA_2$ activating phosphorylation due

to *Atp10A* deficiency resulting in insulin resistance. $cPLA_2$ is phosphorylated by MAPK [293] and the initiation of the MAPK signaling pathway is induced by insulin, therefore, the differences we see in the phosphorylation state of $cPLA_2$ could be a result of insulin resistance instead of alterations to substrate availability. *Atp10A* deficient mice also exhibit a depletion in circulating bile acid levels (Figure 5A,B). Bile acids are important signaling lipids and have implications in cholesterol metabolism and cardiovascular health [136]. We have measured the mRNA levels of two important enzymes involved in bile synthesis, Cyp7a1 and Cyp8b1, in liver from *Atp10A* deficient female mice, but found no difference compared to controls (Supplemental Table 5). However, this was a preliminary study and requires the need for the addition of more mice. Therefore, ATP10A's role in bile acid homeostasis is another open and interesting question.

ATP10A can also translocate GlcCer, a glycosphingolipid. *Atp10A* deficient mice have elevated levels of circulating hexosylceramides (GalCer and GlcCer) and ceramide (Figure 5A,B). Therefore, ATP10A could be a novel factor regulating circulating levels of sphingolipids. Sphingolipids are integral components of membranes and they also have roles in vascular biology [207] and the pathophysiology of cardiovascular diseases, such as hypertension, coronary artery disease, heart failure, arrhythmias, and stroke [208]. Alterations in circulating levels of GlcCer have been shown to be associated with risk of myocardial infarction [209] and serum ceramides strongly correlate with markers of heart disease and are an emerging new biomarker for detection of cardiovascular dysfunction [210]. Additionally, a phosphorylated sphingolipid, sphingosine 1-phosphate (S1P), has been shown to stimulate eNOS activity through Akt/phosphoinositide 3-kinase and calcium-dependent pathways [294, 295]. Altogether, ATP10A could be a factor involved in regulating circulating and intracellular levels of sphingolipids, molecules with established roles in EC function and cardiovascular health.

Another way ATP10A could affect metabolism in ECs and then systemically is by inducing endocytosis of receptors in the PM to effect signaling. *Atp10A* deficient ECs exhibit constitutive insulin signaling during basal levels of insulin, therefore we hypothesize that ATP10A has a role in inhibiting the insulin signaling pathway, perhaps by inducing endocytosis of the insulin receptor to

remove it from the PM. Indeed, ATP10A flipping PC has been shown to induce membrane curvature [296] and therefore might have a role in endocytosis. Additionally, endocytosis of the insulin receptor is an important mechanism to regulate the intensity and duration of the insulin signaling pathway [297]. ATP10A's potential effect on endocytosis of the insulin receptor in ECs is still an open question that needs to be tested. Interestingly, we have shown that *Atp10A* deficient male mice exhibit elevated protein levels of both FSHR and LHR as well as elevated levels of phosphorylation of proteins that are potentially downstream of these receptors (Figure 14) in the testes. This observation could potentially due to ATP10A having a role in the endocytosis of these GPCRs and without ATP10A expression, these receptors are 'stuck' at the plasma membrane and downstream of this, there is an inappropriate activation of downstream proteins. More studies are needed to determine if this is the case, including measuring the endocytosis of these receptors in testes derived cells with or without ATP10A expression, via imaging techniques, where FSHR and LHR trafficking can be tracked over time, or fractionation experiments, to compare LHR and FSHR levels in endosomes versus other membranes.

Exploring the sex-specific effects of *Atp10A* deficiency

There are established differences in disease severity and prevalence between males and females [128]. Premenopausal women tend to have lower cardiovascular risks compared to men and this has been suggested to be due to the effects that estrogen exerts on the endothelium [129]. Therefore, endothelial health and vascular maintenance is an important factor in establishing the cardiovascular protection observed in premenopausal women. Our studies reveal that *Atp10A* deficiency results in female-specific metabolic perturbations in mice (Figure 3, Figure 4) and the promoter of the *ATP10A* gene is predicted to have a transcription factor binding site for estrogen receptor alpha (Genecards.org, QIAGEN). ATP10A could be a novel factor involved in female-specific cardiovascular protection. However, the effect of sex on the phenotypes caused by *Atp10A* deficiency in ECs is not completely clear because we observe similar signaling perturbations in HUVECs, cells from female humans, SVEC4-10, cells from male mice, and aorta from male mice (Figure 8E,F), although the aorta results are preliminary.

Additionally, female *Atp10A* deficient fed a high fat diet exhibit dyslipidemia, but the male mice do not (Figure 4). It is possible that the elevated circulating testosterone levels in male *Atp10A* deficient mice (Figure 13) confers them protection against metabolic dysfunction that could result from *Atp10A* deficiency and high fat diet feeding. Indeed, testosterone deficiency in men is an independent cardiovascular risk which is associated with obesity, metabolic syndrome, and type 2 diabetes [298, 299] and testosterone treatment reverses metabolic defects in mice with low testosterone [300]. Therefore, male *Atp10A* deficient mice exhibit fertility issues accompanied by elevated testosterone levels, which paradoxically could confer protection against metabolic disorders. Altogether, the impact of sex on the phenotypes that arise from *Atp10A* deficiency is still an open and interesting question.

Caveats

We do not have an antibody that can distinguish between the insulin receptor and the IGF1 receptor (IGF1R), therefore the IR labeled in the western blots could also be IGF1R. This is not an uncommon problem because homology between IR and IGF1R is high, ranging from 45–65% in the ligand binding domains to 60–85% in the tyrosine kinase and substrate recruitment domains [143]. However, mutations in the insulin receptor in humans [301] or knockout in mice [302, 303] results in severe hyperglycemia and mutations in the IGF1R [304] or mice lacking IGF1R [305] show severe growth retardation, but no changes in glucose homoeostasis. Indeed, IGF1R has been shown to activate genes involved in proliferation, whereas the insulin receptor has been shown to result in more phosphorylation of IRS-1 and genes involved in metabolic pathways [306]. Therefore, there are distinct signaling effects exerted by the insulin receptor versus IGF1R. Future studies could be aimed at determining if *Atp10A* deficiency specifically has an effect on the insulin receptor, IGF1R, or both.

We observed hyperphosphorylation of eNOS in *Atp10A* deficient HUVECs and mouse aorta, which are both macrovascular, however we have not empirically measured expression of ATP10A in macrovessels versus microvessels. Macrovessels are responsible for distributing blood throughout the body and play a role in maintaining blood pressure and flow and microvessels are thin and permeable

and are responsible for the exchange of oxygen, nutrients, and waste products between blood and tissues [307]. Additionally, macrovessels and microvessels exhibit distinct characteristics and respond to stimuli differently. Interestingly, eNOS has been shown to mediate differential effects in macro- and microvessels [146]. Therefore, the potential role that ATP10A has in macrovessels versus microvessels needs to be elucidated.

We observed similar, but distinct, signaling defects in *Atp10A* deficient HUVECs, human vascular ECs, and SVEC4-10, mouse lymphatic ECs. Both cell types exhibited insulin resistance characterized by hypersignaling due to *Atp10A* deficiency, however, unlike the HUVECs, there was a significant increase in basal levels of GSK3- and cPLA2 in the SVEC4-10. Therefore, ATP10A could have distinct effects in lymphatic ECs compared to vascular ECs. Vascular ECs line blood vessels and have roles in maintenance of blood pressure and flow as well as nutrient and gas exchange. Lymphatic ECs line lymphatic vessels which transport lymph, drain the interstitial fluid that collects in tissues, and ultimately are involved in immune cell trafficking and fat absorption [308]. Therefore, the distinct role that ATP10A has in vascular versus lymphatic ECs needs to be elucidated.

The *Atp10A* deficient mice appear healthy and do not exhibit any visible adverse health outcomes, such as being lethargic or having physical deformities. This is most likely because *Atp10A* was knocked out from birth and the mice were probably able to partially compensate for knock out induced perturbations during development. Therefore, an inducible transgenic mouse model of *Atp10A* deficiency could be used to potentially precipitate more severe phenotypes. Additionally, we have created a mouse that has *Atp10A* exon 2 flanked by loxP sites so we can generate an EC-specific *Atp10A* knockout mouse in the future.

Exploring imprinting phenotypes in *Atp10A* deficient mice

We found no evidence for female-specific metabolic defects in *Atp10A*$^{+/-}$ heterozygous mice that inherited the KO allele paternally or maternally, however, we did observe changes in fasting blood glucose levels between male mice that inherited the KO allele paternally versus maternally (Supplemental Figure

4). Altogether our findings most likely reveal that *Atp10A* might be imprinted in a manner that is affected by the sex and genetic background of the mice, specifically, if *Atp10A* deficiency occurs via a specific knockout (model in this publication) or via a large chromosomal deletion [59]. Indeed, the idea that *Atp10A*'s imprinting pattern is complex and dependent on multiple factors is not novel [117]. This idea is supported by multiple conflicting publications about *ATP10A*'s expression patterns; in humans, it has been reported that *ATP10A* has an imprinted expression pattern and only exhibits maternal expression [309] and conversely, that it exhibits both monoallelic and biallelic expression that is dependent on gender and other genetic variations [118]. Biallelic expression of *Atp10A* in the mouse brain has also been reported [119]. Altogether, *ATP10A*'s expression pattern is different between mice and humans and is dependent on multiple factors; including gender, genetic background, and tissue type.

Navigating the Spectrum of ATP10A Functions and Open Questions

We show elevated activating phosphorylation of Akt in endothelial cells as a consequence of ATP10A deficiency (Figure 8). Building upon these findings, we found a similar phenomenon in the testes and vas deferens (Figure 14, Supplemental Figure 11). Based on these observations, we propose a broader hypothesis suggesting that ATP10A plays a regulatory role across multiple signaling pathways and tissues. In endothelial cells, ATP10A maintains cellular insulin sensitivity by inhibiting insulin signaling under basal insulin levels (Figure 8). In the testes, ATP10A might act to maintain sensitivity to LH and FSH by inhibiting signaling through LHR and FSHR, as evidenced by the increased amounts of LHR and FSHR in *Atp10A* deficient testes (Figure 14). Indeed, *Atp10A* deficient mice exhibit phenotypes that could result from elevated signaling through LHR and FSHR, such as elevated Akt phosphorylation and increased circulating levels of testosterone (Figure 13, Figure 14). Additionally, more work is needed to determine the regulation of ATP10A activity. Indeed, if this flippase has a role in inhibiting insulin signaling during basal levels of insulin in ECs, then there must be a mechanism of inhibiting ATP10A's function during conditions of elevated levels of insulin. The same is true for ATP10A in the testes; there must be a mechanism of inhibiting its function for LHR and FSHR signaling to occur. The potential mechanism of

regulation of ATP10A in different cell types and signaling contexts is an open question that requires more investigation.

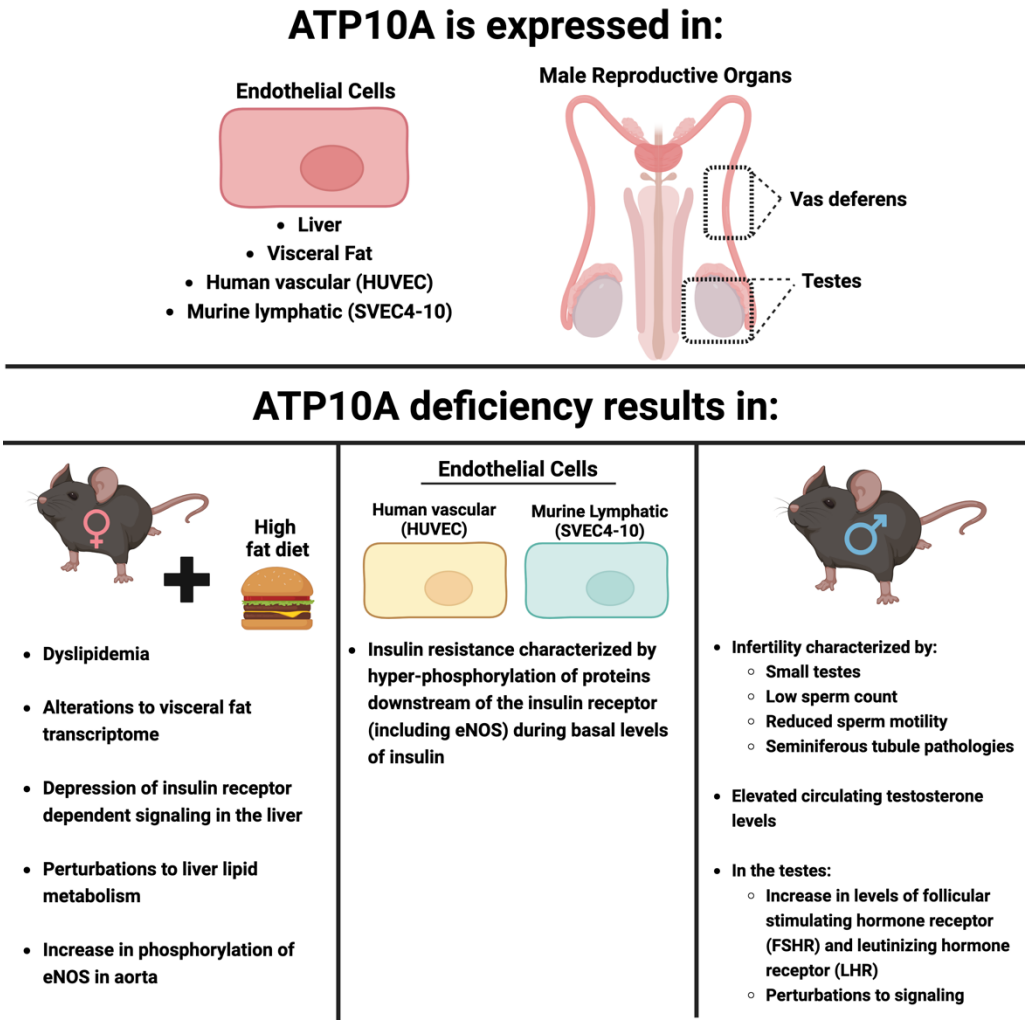

Figure 24. ATP10A has a role in metabolism, endothelial cell insulin sensitivity, and fertility. Schematic showing the conclusion from the different chapters in this thesis. Graphic created using Biorender.com

We made several discoveries, including showing expression of ATP10A in endothelial cells and male sexual organs and that ATP10A deficiency results in female-specific alterations to dyslipidemia and lipid metabolism, insulin resistance in endothelial cells, and male-specific infertility (Figure 24) and there are still many open questions about these findings. One major question is the molecular basis for

the sex specific phenotypes that arise due to ATP10A deficiency and one way to figure this out would be to do ovariectomies and/or gonadectomies on the mice and measure metabolic perturbations (after high fat diet feeding) as well as fertility parameters. Another important question is the connection between the dyslipidemia and the endothelial cell dysfunction observed in the *Atp10A* deficient mice. To begin to answer this question, an EC-specific *Atp10A* KO mouse should be created. The EC-specific KO mice should be placed on a high fat diet and metabolic parameters should be examined, including dyslipidemia. If the dyslipidemia still arises due to *Atp10A* deficiency specifically in ECs, this will provide us evidence that this phenotype is due to EC dysfunction. Additionally, fertility parameters of the EC-specific KO male mice should be examined to determine if EC expression of ATP10A is important for the maintenance of fertility. Additionally, the potential consequences to vascular health, including the development of atherosclerosis, that could arise from *Atp10A* deficiency in ECs is not known. One method to determine this would be to cross EC-specific *Atp10A* KO mice with $Ldlr^{-/-}$ mice and measure atherosclerotic plaque formation after Western diet feeding. Lastly, which lipid substrate(s) of ATP10A's, PC and/or GlcCer, are driving the observed metabolic phenotypes in the *Atp10A* KO mice is still an open question. To answer this question, the $Atp10A^{-/-}Atp10D^{+/+}$ mouse model should be used in high fat diet/metabolism studies (preliminary data in Supplemental Figure 12). In summary, ATP10A is as a key player in metabolism, endothelial cell function, and fertility (Figure 24). I posit that this flippase serves a regulatory function across diverse signaling pathways and tissues and it is evident that there still remains a considerable amount to be discovered about ATP10A.

REFERENCES

1. Watson, H., *Biological membranes.* Essays in Biochemistry, 2015. **59**: p. 43-69.
2. GM, C., *The Cell: A Molecular Approach. 2nd edition. Sunderland (MA): Sinauer Associates; 2000. Structure of the Plasma Membrane.*
3. Levental, I. and E. Lyman, *Regulation of membrane protein structure and function by their lipid nano-environment.* Nat Rev Mol Cell Biol, 2023. **24**(2): p. 107-122.
4. Harayama, T. and H. Riezman, *Understanding the diversity of membrane lipid composition.* Nature Reviews Molecular Cell Biology, 2018. **19**(5): p. 281-296.
5. Gorter, E. and F. Grendel, *On Bimolecular Layers of Lipoids on the Chromocytes of the Blood.* J Exp Med, 1925. **41**(4): p. 439-43.
6. Bretscher, M.S., *Phosphatidyl-ethanolamine: differential labelling in intact cells and cell ghosts of human erythrocytes by a membrane-impermeable reagent.* J Mol Biol, 1972. **71**(3): p. 523-8.
7. Bretscher, M.S., *Asymmetrical Lipid Bilayer Structure for Biological Membranes.* Nature New Biology, 1972. **236**(61): p. 11-12.
8. Verkleij, A.J., et al., *The asymmetric distribution of phospholipids in the human red cell membrane. A combined study using phospholipases and freeze-etch electron microscopy.* Biochimica et Biophysica Acta (BBA) - Biomembranes, 1973. **323**(2): p. 178-193.
9. Gordesky, S.E. and G.V. Marinetti, *The asymmetric arrangement of phospholipids in the human erythrocyte membrane.* Biochemical and Biophysical Research Communications, 1973. **50**(4): p. 1027-1031.
10. Sheetz, M.P. and S.J. Singer, *Biological membranes as bilayer couples. A molecular mechanism of drug-erythrocyte interactions.* Proc Natl Acad Sci U S A, 1974. **71**(11): p. 4457-61.

11. McConnell, H.M. and R.D. Kornberg, *Inside-outside transitions of phospholipids in vesicle membranes.* Biochemistry, 1971. **10**(7): p. 1111-1120.

12. Morrot, G., et al., *Aminophospholipid translocase of human erythrocytes: phospholipid substrate specificity and effect of cholesterol.* Biochemistry, 1989. **28**(8): p. 3456-3462.

13. Devaux, P.F., P. Fellmann, and P. Hervé, *Investigation on lipid asymmetry using lipid probes: comparison between spin-labeled lipids and fluorescent lipids.* Chemistry and physics of lipids, 2002. **116**(1-2): p. 115-134.

14. Maekawa, M. and G.D. Fairn, *Molecular probes to visualize the location, organization and dynamics of lipids.* Journal of cell science, 2014. **127**(22): p. 4801-4812.

15. Allhusen, J.S. and J.C. Conboy, *The Ins and Outs of Lipid Flip-Flop.* Accounts of Chemical Research, 2017. **50**(1): p. 58-65.

16. Daleke, D.L. and W.H. Huestis, *Incorporation and translocation of aminophospholipids in human erythrocytes.* Biochemistry, 1985. **24**(20): p. 5406-16.

17. Moriyama, Y. and N. Nelson, *Purification and properties of a vanadate- and N-ethylmaleimide-sensitive ATPase from chromaffin granule membranes.* Journal of Biological Chemistry, 1988. **263**(17): p. 8521-8527.

18. Zachowski, A., J.-P. Henry, and P.F. Devaux, *Control of transmembrane lipid asymmetry in chromaffin granules by an ATP-dependent protein.* Nature, 1989. **340**(6228): p. 75-76.

19. Seigneuret, M. and P.F. Devaux, *ATP-dependent asymmetric distribution of spin-labeled phospholipids in the erythrocyte membrane: relation to shape changes.* Proceedings of the National Academy of Sciences, 1984. **81**(12): p. 3751-3755.

20. Morrot, G., A. Zachowski, and P.F. Devaux, *Partial purification and characterization of the human erythrocyte Mg2+ -ATPase A candidate aminophospholipid translocase.* FEBS Letters, 1990. **266**(1): p. 29-32.

21. Auland, M.E., et al., *Reconstitution of ATP-dependent aminophospholipid translocation in proteoliposomes.* Proc Natl Acad Sci U S A, 1994. **91**(23): p. 10938-42.

22. Ripmaster, T.L., G.P. Vaughn, and J.L. Woolford, Jr., *DRS1 to DRS7, novel genes required for ribosome assembly and function in Saccharomyces cerevisiae.* Mol Cell Biol, 1993. **13**(12): p. 7901-12.

23. Tang, X., et al., *A subfamily of P-type ATPases with aminophospholipid transporting activity.* Science, 1996. **272**(5267): p. 1495-7.

24. Pomorski, T., et al., *Drs2p-related P-type ATPases Dnf1p and Dnf2p are required for phospholipid translocation across the yeast plasma membrane and serve a role in endocytosis.* Mol Biol Cell, 2003. **14**(3): p. 1240-54.

25. Natarajan, P., et al., *Drs2p-coupled aminophospholipid translocase activity in yeast Golgi membranes and relationship to in vivo function.* Proc Natl Acad Sci U S A, 2004. **101**(29): p. 10614-9.

26. Chen, S., et al., *Roles for the Drs2p-Cdc50p complex in protein transport and phosphatidylserine asymmetry of the yeast plasma membrane.* Traffic, 2006. **7**(11): p. 1503-17.

27. Poulsen, L.R., et al., *The Arabidopsis P4-ATPase ALA3 localizes to the golgi and requires a beta-subunit to function in lipid translocation and secretory vesicle formation.* Plant Cell, 2008. **20**(3): p. 658-76.

28. Xu, P., et al., *Identification of a novel mouse P4-ATPase family member highly expressed during spermatogenesis.* J Cell Sci, 2009. **122**(Pt 16): p. 2866-76.

29. Ujhazy, P., et al., *Familial intrahepatic cholestasis 1: studies of localization and function.* Hepatology, 2001. **34**(4 Pt 1): p. 768-75.

30. Palmgren, M.G. and K.B. Axelsen, *Evolution of P-type ATPases.* Biochim Biophys Acta, 1998. **1365**(1-2): p. 37-45.

31. Axelsen, K.B. and M.G. Palmgren, *Evolution of substrate specificities in the P-type ATPase superfamily.* J Mol Evol, 1998. **46**(1): p. 84-101.

32. Quazi, F. and R.S. Molday, *Lipid transport by mammalian ABC proteins.* Essays in Biochemistry, 2011. **50**: p. 265-290.

33. Bevers, E.M. and P.L. Williamson, *Phospholipid scramblase: An update.* FEBS Letters, 2010. **584**(13): p. 2724-2730.

34. Sebastian, T.T., et al., *Phospholipid flippases: building asymmetric membranes and transport vesicles.* Biochim Biophys Acta, 2012. **1821**(8): p. 1068-77.

35. Lopez-Marques, R.L., et al., *P4-ATPases: lipid flippases in cell membranes.* Pflügers Archiv - European Journal of Physiology, 2014. **466**(7): p. 1227-1240.

36. Best, J.T., P. Xu, and T.R. Graham, *Phospholipid flippases in membrane remodeling and transport carrier biogenesis.* Current Opinion in Cell Biology, 2019. **59**: p. 8-15.

37. Folmer, D.E., R.P.J.O. Elferink, and C.C. Paulusma, *P4 ATPases - Lipid flippases and their role in disease.* Biochimica et Biophysica Acta (BBA) - Molecular and Cell Biology of Lipids, 2009. **1791**(7): p. 628-635.

38. van der Mark, V.A., R.P. Elferink, and C.C. Paulusma, *P4 ATPases: flippases in health and disease.* Int J Mol Sci, 2013. **14**(4): p. 7897-922.

39. *Dyslipidemia.* Annals of Internal Medicine, 2017. **167**(11): p. ITC81-ITC96.

40. Ahmed, B., R. Sultana, and M.W. Greene, *Adipose tissue and insulin resistance in obese.* Biomedicine & Pharmacotherapy, 2021. **137**: p. 111315.

41. Schofield, J.D., et al., *Diabetes Dyslipidemia.* Diabetes Therapy, 2016. **7**(2): p. 203-219.

42. Saltiel, A.R. and J.E. Pessin, *Insulin signaling pathways in time and space.* Trends Cell Biol, 2002. **12**(2): p. 65-71.

43. Muniyappa, R., et al., *Cardiovascular Actions of Insulin.* Endocrine Reviews, 2007. **28**(5): p. 463-491.

44. Duan, Y., et al., *Regulation of cholesterol homeostasis in health and diseases: from mechanisms to targeted therapeutics.* Signal Transduct Target Ther, 2022. **7**(1): p. 265.

45. Naito, T., et al., *Phospholipid Flippase ATP10A Translocates Phosphatidylcholine and Is Involved in Plasma Membrane Dynamics *.* Journal of Biological Chemistry, 2015. **290**(24): p. 15004-15017.

46. Takatsu, H., et al., *Phospholipid Flippase Activities and Substrate Specificities of Human Type IV P-type ATPases Localized to the Plasma Membrane *.* Journal of Biological Chemistry, 2014. **289**(48): p. 33543-33556.

47. Bull, L.N., et al., *A gene encoding a P-type ATPase mutated in two forms of hereditary cholestasis.* Nature Genetics, 1998. **18**(3): p. 219-224.

48. Paulusma, C.C., et al., *Activity of the Bile Salt Export Pump (ABCB11) Is Critically Dependent on Canalicular Membrane Cholesterol Content.* Journal of Biological Chemistry, 2009. **284**(15): p. 9947-9954.

49. Henkel, S.A., et al., *Expanding etiology of progressive familial intrahepatic cholestasis.* World J Hepatol, 2019. **11**(5): p. 450-463.

50. Dieudonné, T., et al., *Autoinhibition and regulation by phosphoinositides of ATP8B1, a human lipid flippase associated with intrahepatic cholestatic disorders.* eLife, 2022. **11**: p. e75272.

51. Takikawa, Y., et al., *The bile acid activated phosphatidylinositol 3-kinase pathway inhibits Fas apoptosis upstream of bid in rodent hepatocytes.* Gastroenterology, 2001. **120**(7): p. 1810-1817.

52. Hohenester, S., et al., *Phosphatidylinositol-3-kinase p110γ contributes to bile salt-induced apoptosis in primary rat hepatocytes and human hepatoma cells.* Journal of Hepatology, 2010. **53**(5): p. 918-926.

53. Siggs, O.M., et al., *X-linked cholestasis in mouse due to mutations of the P4-ATPase ATP11C.* Proceedings of the National Academy of Sciences, 2011. **108**(19): p. 7890-7895.

54. Yusuke, M., H. Hisamitsu, and K. Hiroyuki, *Impaired Hepatic Uptake by Organic Anion-Transporting Polypeptides Is Associated with Hyperbilirubinemia and Hypercholanemia in Atp11c Mutant Mice.* Molecular Pharmacology, 2015. **88**(6): p. 1085.

55. de Waart, D.R., et al., *ATP11C targets basolateral bile salt transporter proteins in mouse central hepatocytes.* Hepatology, 2016. **64**(1).

56. Kishimoto, T., et al., *Phospholipid flippases and Sfk1 are essential for the retention of ergosterol in the plasma membrane.* Mol Biol Cell, 2021. **32**(15): p. 1374-1392.

57. Yang, Y., et al., *The phosphatidylserine flippase b-subunit Tmem30a is essential for normal insulin maturation and secretion.* Molecular Therapy, 2021. **29**(9): p. 2854-2872.

58. Irvin, M.R., et al., *Genome-wide detection of allele specific copy number variation associated with insulin resistance in African Americans from the HyperGEN study.* PLoS One, 2011. **6**(8): p. e24052.

59. Dhar, M.S., et al., *Mice Heterozygous for Atp10c, a Putative Amphipath, Represent a Novel Model of Obesity and Type 2 Diabetes.* The Journal of Nutrition, 2004. **134**(4): p. 799-805.

60. Dhar, M.S., et al., *A type IV P-type ATPase affects insulin-mediated glucose uptake in adipose tissue and skeletal muscle in mice.* The Journal of Nutritional Biochemistry, 2006. **17**(12): p. 811-820.

61. Cory, S., *Phosphatidylserine hide-and-seek.* Proc Natl Acad Sci U S A, 2018. **115**(48): p. 12092-12094.

62. Williamson, P., *Phospholipid Scramblases.* Lipid Insights, 2015. **8s1**: p. LPI.S31785.

63. Soupene, E. and F.A. Kuypers, *Identification of an erythroid ATP-dependent aminophospholipid transporter.* Br J Haematol, 2006. **133**(4): p. 436-8.

64. Levano, K., et al., *Atp8a1 deficiency is associated with phosphatidylserine externalization in hippocampus and delayed hippocampus-dependent learning.* Journal of Neurochemistry, 2012. **120**(2): p. 302-313.

65. Yabas, M., et al., *ATP11C is critical for the internalization of phosphatidylserine and differentiation of B lymphocytes.* Nature Immunology, 2011. **12**(5): p. 441-449.

66. Yabas, M., et al., *Mice Deficient in the Putative Phospholipid Flippase ATP11C Exhibit Altered Erythrocyte Shape, Anemia, and Reduced Erythrocyte Life Span.* Journal of Biological Chemistry, 2014. **289**(28): p. 19531-19537.

67. Manno, S., Y. Takakuwa, and N. Mohandas, *Identification of a functional role for lipid asymmetry in biological membranes: Phosphatidylserine-skeletal protein interactions modulate membrane stability.* Proc Natl Acad Sci U S A, 2002. **99**(4): p. 1943-8.

68. An, X., et al., *Phosphatidylserine Binding Sites in Erythroid Spectrin: Location and Implications for Membrane Stability.* Biochemistry, 2004. **43**(2): p. 310-315.

69. An, X., et al., *Human and murine erythropoiesis.* Current Opinion in Hematology, 2015. **22**(3).

70. Nobuto, A., et al., *ATP11C is a major flippase in human erythrocytes and its defect causes congenital hemolytic anemia.* Haematologica, 2016. **101**(5): p. 559-565.

71. Segawa, K., et al., *Caspase-mediated cleavage of phospholipid flippase for apoptotic phosphatidylserine exposure.* Science, 2014. **344**(6188): p. 1164-1168.

72. Jing, W., et al., *Calpain cleaves phospholipid flippase ATP8A1 during apoptosis in platelets.* Blood Advances, 2019. **3**(3): p. 219-229.

73. Seki, M., et al., *Reduction in flippase activity contributes to surface presentation of phosphatidylserine in human senescent erythrocytes.* Journal of Cellular and Molecular Medicine, 2020. **24**(23): p. 13991-14000.

74. Muhlberger, T., et al., *Inhibition of flippase-like activity by tubulin regulates phosphatidylserine exposure in erythrocytes from hypertensive and diabetic patients.* The Journal of Biochemistry, 2021. **169**(6): p. 731-745.

75. Barber, L.A., et al., *Activation of protein kinase C by phorbol ester increases red blood cell scramblase activity and external phosphatidylserine.* European Journal of Haematology, 2015. **95**(5): p. 405-410.

76. Robinson, J.M. and D.D. Vandré, *Stimulus-dependent alterations in macrophage microtubules: increased tubulin polymerization and detyrosination.* Journal of Cell Science, 1995. **108**(2): p. 645-655.

77. Takatsu, H., et al., *Phospholipid flippase ATP11C is endocytosed and downregulated following Ca2+-mediated protein kinase C activation.* Nature Communications, 2017. **8**(1): p. 1423.

78. Liou, A.Y., et al., *Identification and functional analyses of disease-associated P4-ATPase phospholipid flippase variants in red blood cells.* Journal of Biological Chemistry, 2019. **294**(17): p. 6809-6821.

79. Arashiki, N., et al., *ATP11C T418N, a gene mutation causing congenital hemolytic anemia, reduces flippase activity due to improper membrane trafficking.* Biochemical and Biophysical Research Communications, 2019. **516**(3): p. 705-712.

80. Segawa, K., et al., *Phospholipid flippases enable precursor B cells to flee engulfment by macrophages.* Proc Natl Acad Sci U S A, 2018. **115**(48): p. 12212-12217.

81. Li, N., et al., *Tmem30a Plays Critical Roles in Ensuring the Survival of Hematopoietic Cells and Leukemia Cells in Mice.* The American Journal of Pathology, 2018. **188**(6): p. 1457-1468.

82. Rivelli, J.F., et al., *High glucose levels induce inhibition of Na,K-ATPase via stimulation of aldose reductase, formation of microtubules and formation of an acetylated tubulin/Na,K-ATPase complex.* The International Journal of Biochemistry & Cell Biology, 2012. **44**(8): p. 1203-1213.

83. Rivelli, J.F., et al., *Regulation of aldose reductase activity by tubulin and phenolic acid derivates.* Archives of Biochemistry and Biophysics, 2018. **654**: p. 19-26.

84. Amaiden, M.R., et al., *Tubulin pools in human erythrocytes: altered distribution in hypertensive patients affects Na+, K+-ATPase activity.* Cellular and Molecular Life Sciences, 2011. **68**(10): p. 1755-1768.

85. Amaiden, M.R., et al., *Effects of detyrosinated tubulin on Na+,K+-ATPase activity and erythrocyte function in hypertensive subjects.* FEBS Letters, 2015. **589**(3): p. 364-373.

86. Thomas, M.C., et al., *Unrecognized Anemia in Patients With Diabetes: A cross-sectional survey.* Diabetes Care, 2003. **26**(4): p. 1164-1169.

87. Bazan, I.S. and W.H. Fares, *Hypercoagulability in Pulmonary Hypertension.* Clinics in Chest Medicine, 2018. **39**(3): p. 595-603.

88. Hicks, A.A., et al., *Genetic determinants of circulating sphingolipid concentrations in European populations.* PLoS Genet, 2009. **5**(10): p. e1000672.

89. Kengia, J.T., et al., *A gene variant in the Atp10d gene associates with atherosclerotic indices in Japanese elderly population.* Atherosclerosis, 2013. **231**(1): p. 158-162.

90. Roland, B.P., et al., *Yeast and human P4-ATPases transport glycosphingolipids using conserved structural motifs.* J Biol Chem, 2019. **294**(6): p. 1794-1806.

91. Surwit, R.S., et al., *Differential effects of fat and sucrose on the development of obesity and diabetes in C57BL/6J and A/J mice.* Metabolism, 1995. **44**(5): p. 645-51.

92. Flamant, S., et al., *Characterization of a putative type IV aminophospholipid transporter P-type ATPase.* Mammalian Genome, 2003. **14**(1): p. 21-30.

93. Sigruener, A., et al., *Lipidomic and metabolic changes in the P4-type ATPase ATP10D deficient C57BL/6J wild type mice upon rescue of ATP10D function.* PLoS One, 2017. **12**(5): p. e0178368.

94. Fahed, G., et al., *Metabolic Syndrome: Updates on Pathophysiology and Management in 2021.* International Journal of Molecular Sciences, 2022. **23**(2): p. 786.

95. Aguilar, M., et al., *Prevalence of the Metabolic Syndrome in the United States, 2003-2012.* JAMA, 2015. **313**(19): p. 1973-1974.

96. Chavez, J.A., et al., *Ceramides and Glucosylceramides Are Independent Antagonists of Insulin Signaling *.* Journal of Biological Chemistry, 2014. **289**(2): p. 723-734.

97. Zhao, H., et al., Inhibiting Glycosphingolipid Synthesis Improves Glycemic Control and Insulin Sensitivity in Animal Models of Type 2 Diabetes. Diabetes, 2007. **56**(5): p. 1210-1218.

98. Norris, A.C., et al., *Deficiency of the lipid flippase ATP10A causes diet-induced dyslipidemia in female mice*. Sci Rep 14**, 343** (2024). https://doi.org/10.1038/s41598-023-50360-5

99. Norris, A.C., et al., *ATP10A deficiency results in male-specific infertility in mice*. Front. Cell Dev. Biol. Sec. Molecular and Cellular Reproduction (2024). doi: 10.3389/fcell.2024.1310593.

100. Graupera, M. and M. Claret, Endothelial Cells: New Players in Obesity and Related Metabolic Disorders. Trends in Endocrinology & Metabolism, 2018. **29**(11): p. 781-794.

101. Andersen, J.P., et al., P4-ATPases as Phospholipid Flippases—Structure, Function, and Enigmas. Frontiers in Physiology, 2016. **7**.

102. Kook, S., et al., *AP-3-dependent targeting of flippase ATP8A1 to lamellar bodies suppresses activation of YAP in alveolar epithelial type 2 cells.* Proc Natl Acad Sci U S A, 2021. **118**(20).

103. Ristovski, M., et al., *Lipid Transporters Beam Signals from Cell Membranes.* Membranes, 2021. **11**(8): p. 562.

104. Ramos-Martín, F. and N. D'Amelio, *Biomembrane lipids: When physics and chemistry join to shape biological activity.* Biochimie, 2022. **203**: p. 118-138.

105. Testerink, N., et al., *Depletion of phosphatidylcholine affects endoplasmic reticulum morphology and protein traffic at the Golgi complex.* Journal of Lipid Research, 2009. **50**(11): p. 2182-2192.

106. Knuplez, E. and G. Marsche, *An Updated Review of Pro- and Anti-Inflammatory Properties of Plasma Lysophosphatidylcholines in the Vascular System.* International Journal of Molecular Sciences, 2020. **21**(12): p. 4501.

107. Liu, P., et al., *The mechanisms of lysophosphatidylcholine in the development of diseases.* Life Sciences, 2020. **247**: p. 117443.

108. Yamaguchi, A., E. Botta, and M. Holinstat, *Eicosanoids in inflammation in the blood and the vessel.* Front Pharmacol, 2022. **13**: p. 997403.

109. Mitchell, J.A. and N.S. Kirkby, *Eicosanoids, prostacyclin and cyclooxygenase in the cardiovascular system.* British Journal of Pharmacology, 2019. **176**(8): p. 1038-1050.

110. Ishibashi, Y., A. Kohyama-Koganeya, and Y. Hirabayashi, *New insights on glucosylated lipids: Metabolism and functions.* Biochimica et Biophysica Acta (BBA) - Molecular and Cell Biology of Lipids, 2013. **1831**(9): p. 1475-1485.

111. Mobarak, E., et al., *Glucosylceramide modifies the LPS-induced inflammatory response in macrophages and the orientation of the LPS/TLR4 complex in silico.* Scientific Reports, 2018. **8**(1): p. 13600.

112. Aerts, J.M., et al., *Pharmacological Inhibition of Glucosylceramide Synthase Enhances Insulin Sensitivity.* Diabetes, 2007. **56**(5): p. 1341-1349.

113. Baccam, G.C., et al., *Glucosylceramide synthase inhibition protects against cardiac hypertrophy in chronic kidney disease.* Scientific Reports, 2022. **12**(1): p. 9340.

114. Bikman, B.T. and S.A. Summers, *Ceramides as modulators of cellular and whole-body metabolism.* The Journal of Clinical Investigation, 2011. **121**(11): p. 4222-4230.

115. Turpin-Nolan, S.M. and J.C. Brüning, *The role of ceramides in metabolic disorders: when size and localization matters.* Nature Reviews Endocrinology, 2020. **16**(4): p. 224-233.

116. Sandhoff, R., H. Schulze, and K. Sandhoff, *Chapter One - Ganglioside Metabolism in Health and Disease*, in *Progress in Molecular Biology and Translational Science*, R.L. Schnaar and P.H.H. Lopez, Editors. 2018, Academic Press. p. 1-62.

117. Kayashima, T., et al., *On the conflicting reports of imprinting status of mouse ATP10a in the adult brain: strain-background-dependent imprinting?* Journal of Human Genetics, 2003. **48**(9): p. 492-493.

118. Hogart, A., K.A. Patzel, and J.M. LaSalle, *Gender influences monoallelic expression of ATP10A in human brain.* Human Genetics, 2008. **124**(3): p. 235-242.

119. DuBose, A.J., et al., *Atp10a, a gene adjacent to the PWS/AS gene cluster, is not imprinted in mouse and is insensitive to the PWS-IC.* neurogenetics, 2010. **11**(2): p. 145-151.

120. Hurst, S.E., et al., *Transient Silencing of a Type IV P-Type ATPase, Atp10c, Results in Decreased Glucose Uptake in C2C12 Myotubes.* Journal of Nutrition and Metabolism, 2012. **2012**: p. 152902.

121. May, J.C., et al., *Conformational Ordering of Biomolecules in the Gas Phase: Nitrogen Collision Cross Sections Measured on a Prototype High Resolution Drift Tube Ion Mobility-Mass Spectrometer.* Analytical Chemistry, 2014. **86**(4): p. 2107-2116.

122. Rose, B.S., et al., *Improving confidence in lipidomic annotations by incorporating empirical ion mobility regression analysis and chemical class prediction.* Bioinformatics, 2022. **38**(10): p. 2872-2879.

123. Yazlovitskaya, E.M., et al., *The laminin-binding integrins regulate nuclear factor κB-dependent epithelial cell polarity and inflammation.* Journal of Cell Science, 2021. **134**(24).

124. Folch, J., M. Lees, and G.H. Sloane Stanley, *A simple method for the isolation and purification of total lipides from animal tissues.* J Biol Chem, 1957. **226**(1): p. 497-509.

125. Morrison, W.R. and L.M. Smith, *Preparation of Fatty Acid Methyl Esters and Dimethylacetals from Lipids with Boron Fluoride--Methanol.* J Lipid Res, 1964. **5**: p. 600-8.

126. Rudel, L.L., et al., *Dietary monounsaturated fatty acids promote aortic atherosclerosis in LDL receptor-null, human ApoB100-overexpressing transgenic mice.* Arterioscler Thromb Vasc Biol, 1998. **18**(11): p. 1818-27.

127. Butler, M.G., *Imprinting disorders in humans: a review.* Current Opinion in Pediatrics, 2020. **32**(6).

128. Crimmins, E.M., et al., *Differences between Men and Women in Mortality and the Health Dimensions of the Morbidity Process.* Clinical Chemistry, 2019. **65**(1): p. 135-145.

129. CID, M.C., H.W. SCHNAPER, and H.K. KLEINMAN, *Estrogens and the Vascular Endothelium.* Annals of the New York Academy of Sciences, 2002. **966**(1): p. 143-157.

130. Barter, P.J. and P.J. Nestel, *Precursors of plasma triglyceride fatty acids in obesity.* Metabolism, 1973. **22**(6): p. 779-785.

131. Kissebah, A.H., et al., *Role of insulin resistance in adipose tissue and liver in the pathogenesis of endogenous hypertriglyceridaemia in man.* Diabetologia, 1976. **12**(6): p. 563-571.

132. Lewis, G.F., *Lipid metabolism.* Curr Opin Lipidol, 1999. **10**(5): p. 475-7.

133. Rose, A.M.I., V. Bazioti, and M. Westerterp, *Adipocyte Membrane Cholesterol Regulates Obesity.* Arteriosclerosis, Thrombosis, and Vascular Biology, 2018. **38**(4): p. 687-689.

134. Garcia, D. and R.J. Shaw, *AMPK: Mechanisms of Cellular Energy Sensing and Restoration of Metabolic Balance.* Molecular Cell, 2017. **66**(6): p. 789-800.

135. Asztalos, B.F., M. Tani, and E.J. Schaefer, *Metabolic and functional relevance of HDL subspecies.* Current Opinion in Lipidology, 2011. **22**(3): p. 176-185.

136. Hanafi, N.I., et al., *Overview of Bile Acids Signaling and Perspective on the Signal of Ursodeoxycholic Acid, the Most Hydrophilic Bile Acid, in the Heart.* Biomolecules, 2018. **8**(4): p. 159.

137. Young, M.E., G.K. Radda, and B. Leighton, *Nitric oxide stimulates glucose transport and metabolism in rat skeletal muscle in vitro.* Biochemical Journal, 1997. **322**(1): p. 223-228.

138. Etgen, G.J., Jr, D.A. Fryburg, and E.M. Gibbs, *Nitric Oxide Stimulates Skeletal Muscle Glucose Transport Through a Calcium/Contraction– and Phosphatidylinositol-3-Kinase–Independent Pathway.* Diabetes, 1997. **46**(11): p. 1915-1919.

139. Tsuchiya, K. and D. Accili, *Liver Sinusoidal Endothelial Cells Link Hyperinsulinemia to Hepatic Insulin Resistance.* Diabetes, 2013. **62**(5): p. 1478-1489.

140. Konishi, M., et al., *Endothelial insulin receptors differentially control insulin signaling kinetics in peripheral tissues and brain of mice.* Proc Natl Acad Sci U S A, 2017. **114**(40): p. E8478-E8487.

141. Kim, F., et al., *Vascular Inflammation, Insulin Resistance, and Reduced Nitric Oxide Production Precede the Onset of Peripheral Insulin Resistance.* Arteriosclerosis, Thrombosis, and Vascular Biology, 2008. **28**(11): p. 1982-1988.

142. Zhao, L., et al., *Inflammation-induced microvascular insulin resistance is an early event in diet-induced obesity.* Clinical Science, 2015. **129**(12): p. 1025-1036.

143. Belfiore, A., et al., *Insulin Receptor Isoforms and Insulin Receptor/Insulin-Like Growth Factor Receptor Hybrids in Physiology and Disease.* Endocrine Reviews, 2009. **30**(6): p. 586-623.

144. Chalfant, C.E. and S. Spiegel, *Sphingosine 1-phosphate and ceramide 1-phosphate: expanding roles in cell signaling.* Journal of Cell Science, 2005. **118**(20): p. 4605-4612.

145. Han, M.S., et al., *Lysophosphatidylcholine as an effector of fatty acid-induced insulin resistance [S].* Journal of Lipid Research, 2011. **52**(6): p. 1234-1246.

146. Mohan, S., et al., *Diabetic eNOS knockout mice develop distinct macro- and microvascular complications.* Laboratory Investigation, 2008. **88**(5): p. 515-528.

147. Zhang, B.B., G. Zhou, and C. Li, *AMPK: An Emerging Drug Target for Diabetes and the Metabolic Syndrome.* Cell Metabolism, 2009. **9**(5): p. 407-416.

148. Kumar, N. and A.K. Singh, *Trends of male factor infertility, an important cause of infertility: A review of literature.* J Hum Reprod Sci, 2015. **8**(4): p. 191-6.

149. Babakhanzadeh E, N.M., Ghasemifar S, Khodadadian A, *Some of the Factors Involved in Male Infertility: A Prospective Review.* Dovepress, 23 January 2020. **13**: p. 29-41.

150. Krausz, C. and A. Riera-Escamilla, *Genetics of male infertility.* Nat Rev Urol, 2018. **15**(6): p. 369-384.

151. Winters, B.R. and T.J. Walsh, *The epidemiology of male infertility.* Urol Clin North Am, 2014. **41**(1): p. 195-204.

152. Soraggi, S., et al., *Evaluating genetic causes of azoospermia: What can we learn from a complex cellular structure and single-cell transcriptomics of the human testis?* Hum Genet, 2021. **140**(1): p. 183-201.

153. Consortium, G.T., *The Genotype-Tissue Expression (GTEx) project.* Nat Genet, 2013. **45**(6): p. 580-5.

154. Wang, J., et al., *Proteomic Analysis and Functional Characterization of P4-ATPase Phospholipid Flippases from Murine Tissues.* Sci Rep, 2018. **8**(1): p. 10795.

155. Wang, R., et al., *Construction of a cross-species cell landscape at single-cell level.* Nucleic Acids Res, 2023. **51**(2): p. 501-516.

156. Chen, X., et al., *Whole genome bisulfite sequencing of human spermatozoa reveals differentially methylated patterns from type 2 diabetic patients.* J Diabetes Investig, 2020. **11**(4): p. 856-864.

157. Lenzi, A., et al., *Lipids of the sperm plasma membrane: from polyunsaturated fatty acids considered as markers of sperm function to possible scavenger therapy.* Hum Reprod Update, 1996. **2**(3): p. 246-56.

158. Pirie, N.W., *Biochemistry of semen and of the male reproductive tract. Second edition*. 1965.

159. Mann, T.a.L.-M., C. (eds) (1981) Male Reproductive Function and Semen. , *Male Reproductive Function and Semen.* 1981. **Springer-Verlag, Berlin, 495 pp.**

160. Lin, D.S., M. Neuringer, and W.E. Connor, *Selective changes of docosahexaenoic acid-containing phospholipid molecular species in monkey testis during puberty.* J Lipid Res, 2004. **45**(3): p. 529-35.

161. Shan, S., et al., *Sperm Lipid Markers of Male Fertility in Mammals.* Int J Mol Sci, 2021. **22**(16).

162. Evans, R.W., D.E. Weaver, and E.D. Clegg, *Diacyl, alkenyl, and alkyl ether phospholipids in ejaculated, in utero-, and in vitro-incubated porcine spermatozoa.* J Lipid Res, 1980. **21**(2): p. 223-8.

163. Cross, N.L., *Phosphatidylcholine enhances the acrosomal responsiveness of human sperm.* J Androl, 1994. **15**(5): p. 484-8.

164. Yildiz, Y., et al., *Mutation of beta-glucosidase 2 causes glycolipid storage disease and impaired male fertility.* J Clin Invest, 2006. **116**(11): p. 2985-94.

165. Wang, L., C. Beserra, and D.L. Garbers, *A novel aminophospholipid transporter exclusively expressed in spermatozoa is required for membrane lipid asymmetry and normal fertilization.* Dev Biol, 2004. **267**(1): p. 203-15.

166. Martin, S., et al., *Mutated ATP10B increases Parkinson's disease risk by compromising lysosomal glucosylceramide export.* Acta Neuropathol, 2020. **139**(6): p. 1001-1024.

167. Norris, A.C., et al., *Deficiency of the lipid flippase ATP10A causes diet-induced dyslipidemia in female mice.* bioRxiv, 2023.

168. Creasy, D., et al., *Proliferative and nonproliferative lesions of the rat and mouse male reproductive system.* Toxicol Pathol, 2012. **40**(6 Suppl): p. 40S-121S.

169. Lanning, L.L., et al., *Recommended approaches for the evaluation of testicular and epididymal toxicity.* Toxicol Pathol, 2002. **30**(4): p. 507-20.

170. Casarini, L. and P. Crepieux, *Molecular Mechanisms of Action of FSH.* Front Endocrinol (Lausanne), 2019. **10**: p. 305.

171. Johnson, G.P. and K.C. Jonas, *Mechanistic insight into how gonadotropin hormone receptor complexes direct signaling†.* Biology of Reproduction, 2019. **102**(4): p. 773-783.

172. Bonventre, J.V., et al., *Reduced fertility and postischaemic brain injury in mice deficient in cytosolic phospholipase A2.* Nature, 1997. **390**(6660): p. 622-5.

173. Niknami, M., et al., *Molecules in focus: cytosolic phospholipase A2-alpha.* Int J Biochem Cell Biol, 2009. **41**(5): p. 994-7.

174. Prasad, V., et al., *Phenotypes of SERCA and PMCA knockout mice.* Biochem Biophys Res Commun, 2004. **322**(4): p. 1192-203.

175. Woo, A.L., P.F. James, and J.B. Lingrel, *Sperm Motility Is Dependent on a Unique Isoform of the Na,K-ATPase *.* Journal of Biological Chemistry, 2000. **275**(27): p. 20693-20699.

176. Garcia-Herrero, S., et al., *The transcriptome of spermatozoa used in homologous intrauterine insemination varies considerably between samples that achieve pregnancy and those that do not.* Fertil Steril, 2010. **94**(4): p. 1360-1373.

177. Anderson, R.A. and R.M. Sharpe, *Regulation of inhibin production in the human male and its clinical applications.* Int J Androl, 2000. **23**(3): p. 136-44.

178. Kenneth P. Roberts, T.R.C., *Molecular mechanisms of testosterone action on the testis.* Current Opinion in Endocrine and Metabolic Research, 2019. **6**(2451-9650): p. 29-33.

179. Rulli, S.B., et al., *Elevated steroidogenesis, defective reproductive organs, and infertility in transgenic male mice overexpressing human chorionic gonadotropin.* Endocrinology, 2003. **144**(11): p. 4980-90.

180. Ulloa-Aguirre, A., E. Reiter, and P. Crepieux, *FSH Receptor Signaling: Complexity of Interactions and Signal Diversity.* Endocrinology, 2018. **159**(8): p. 3020-3035.

181. Krishnamurthy, H., et al., *Postendocytotic trafficking of the follicle-stimulating hormone (FSH)-FSH receptor complex.* Mol Endocrinol, 2003. **17**(11): p. 2162-76.

182. Chan, H.J., K. Petrossian, and S. Chen, *Structural and functional characterization of aromatase, estrogen receptor, and their genes in endocrine-responsive and -resistant breast cancer cells.* J Steroid Biochem Mol Biol, 2016. **161**: p. 73-83.

183. Chen, K.Q., et al., *The PI3K/AKT signaling pathway: How does it regulate development of Sertoli cells and spermatogenic cells?* Histol Histopathol, 2022. **37**(7): p. 621-636.

184. Riera, M.F., et al., *Signal transduction pathways in FSH regulation of rat Sertoli cell proliferation.* Am J Physiol Endocrinol Metab, 2012. **302**(8): p. E914-23.

185. Nascimento, A.R., et al., *Crosstalk between FSH and relaxin at the end of the proliferative stage of rat Sertoli cells.* Reproduction, 2016. **152**(6): p. 613-628.

186. Xi, H., et al., *FSH inhibits autophagy and lysosomal biogenesis to regulate protein degradation in cultured goat Sertoli cells.* Mol Cell Endocrinol, 2022. **540**: p. 111505.

187. Chen, Y., et al., *Microcystin-LR induces autophagy and apoptosis in rat Sertoli cells in vitro.* Toxicon, 2013. **76**: p. 84-93.

188. Zhou, Y., et al., *Essential roles of Akt/Snail pathway in microcystin-LR-induced tight junction toxicity in Sertoli cell.* Food Chem Toxicol, 2018. **112**: p. 290-298.

189. Zhou, Y., et al., *Icariin attenuate microcystin-LR-induced gap junction injury in Sertoli cells through suppression of Akt pathways.* Environ Pollut, 2019. **251**: p. 328-337.

190. Zhou, Y., et al., *Responses of the proteome in testis of mice exposed chronically to environmentally relevant concentrations of Microcystin-LR.* Ecotoxicol Environ Saf, 2020. **187**: p. 109824.

191. Manna, P.R., M.T. Dyson, and D.M. Stocco, *Regulation of the steroidogenic acute regulatory protein gene expression: present and future perspectives.* Mol Hum Reprod, 2009. **15**(6): p. 321-33.

192. Wang, J.M., et al., *Follicle-stimulating hormone signaling in Sertoli cells: a licence to the early stages of spermatogenesis.* Reprod Biol Endocrinol, 2022. **20**(1): p. 97.

193. Fukuda, S., et al., *Luteinizing hormone-induced Akt phosphorylation and androgen production are modulated by MAP Kinase in bovine theca cells.* J Ovarian Res, 2009. **2**(1): p. 17.

194. Carvalho, C.R., et al., *Novel signal transduction pathway for luteinizing hormone and its interaction with insulin: activation of Janus kinase/signal transducer and activator of transcription and phosphoinositol 3-kinase/Akt pathways.* Endocrinology, 2003. **144**(2): p. 638-47.

195. Walker, W.H., *Testosterone signaling and the regulation of spermatogenesis.* Spermatogenesis, 2011. **1**(2): p. 116-120.

196. Lee, A.G., *How lipids affect the activities of integral membrane proteins.* Biochimica et Biophysica Acta (BBA) - Biomembranes, 2004. **1666**(1): p. 62-87.

197. Kumari, A., et al., *The Importance of Lipoprotein Lipase Regulation in Atherosclerosis.* Biomedicines, 2021. **9**(7).

198. Brunxell, J.D., *Familial Lipoprotein Lipase Deficiency and other Causes of the Chylomicronemia Syndrome.* The Metabolic Bases of Inherited Disease, 1995: p. 1913-1932.

199. Bijvoet, S., et al., *Alterations in plasma lipoproteins and apolipoproteins before the age of 40 in heterozygotes for lipoprotein lipase deficiency.* J Lipid Res, 1996. **37**(3): p. 640-50.

200. Palmisano, B.T., et al., *Low-density lipoprotein receptor is required for cholesteryl ester transfer protein to regulate triglyceride metabolism in both male and female mice.* Physiol Rep, 2021. **9**(4): p. e14732.

201. Millar, J.S., et al., *Normal production rate of apolipoprotein B in LDL receptor-deficient mice.* Arterioscler Thromb Vasc Biol, 2002. **22**(6): p. 989-94.

202. Millar, J.S., et al., *Determining hepatic triglyceride production in mice: comparison of poloxamer 407 with Triton WR-1339.* J Lipid Res, 2005. **46**(9): p. 2023-8.

203. Bender, S.B. and M.H. Laughlin, *Modulation of endothelial cell phenotype by physical activity: impact on obesity-related endothelial dysfunction.* Am J Physiol Heart Circ Physiol, 2015. **309**(1): p. H1-8.

204. Dallinga-Thie, G.M., et al., *Appraisal of hepatic lipase and lipoprotein lipase activities in mice.* J Lipid Res, 2007. **48**(12): p. 2788-91.

205. Kersten, S., *Physiological regulation of lipoprotein lipase.* Biochimica et Biophysica Acta (BBA) - Molecular and Cell Biology of Lipids, 2014. **1841**(7): p. 919-933.

206. Jensen, T.L., et al., *Fasting of mice: a review.* Lab Anim, 2013. **47**(4): p. 225-40.

207. Chatterjee, S., *Sphingolipids in Atherosclerosis and Vascular Biology.* Arteriosclerosis, Thrombosis, and Vascular Biology, 1998. **18**(10): p. 1523-1533.

208. Borodzicz-Jazdzyk, S., et al., *Sphingolipid metabolism and signaling in cardiovascular diseases.* Front Cardiovasc Med, 2022. **9**: p. 915961.

209. Park, J.Y., et al., *Alteration in metabolic signature and lipid metabolism in patients with angina pectoris and myocardial infarction.* PLoS One, 2015. **10**(8): p. e0135228.

210. Tippetts, T.S., W.L. Holland, and S.A. Summers, *Cholesterol; the devil you know; ceramide the devil you don't.* Trends in Pharmacological Sciences, 2021. **42**(12): p. 1082-1095.

211. Staels, B. and V.A. Fonseca, *Bile acids and metabolic regulation: mechanisms and clinical responses to bile acid sequestration.* Diabetes Care, 2009. **32 Suppl 2**(Suppl 2): p. S237-45.

212. Turnaev, II, M.E. Bocharnikova, and D.A. Afonnikov, *Human phospholipases A2: a functional and evolutionary analysis.* Vavilovskii Zhurnal Genet Selektsii, 2022. **26**(8): p. 787-797.

213. Mauvoisin, D. and C. Mounier, *Hormonal and nutritional regulation of SCD1 gene expression.* Biochimie, 2011. **93**(1): p. 78-86.

214. Wang, H. and R.H. Eckel, *Lipoprotein lipase: from gene to obesity.* American Journal of Physiology-Endocrinology and Metabolism, 2009. **297**(2): p. E271-E288.

215. Jones, S.F. and J.R. Infante, *Molecular Pathways: Fatty Acid Synthase.* Clinical Cancer Research, 2015. **21**(24): p. 5434-5438.

216. Yen, C.-L.E., et al., *Thematic Review Series: Glycerolipids: DGAT enzymes and triacylglycerol biosynthesis.* Journal of Lipid Research, 2008. **49**(11): p. 2283-2301.

217. Yu, L., et al., *CGI-58: Versatile Regulator of Intracellular Lipid Droplet Homeostasis.* Adv Exp Med Biol, 2020. **1276**: p. 197-222.

218. Wang, Y., et al., *PPARs as Metabolic Regulators in the Liver: Lessons from Liver-Specific PPAR-Null Mice.* Int J Mol Sci, 2020. **21**(6).

219. Steffensen, K.R. and J.-A.k. Gustafsson, *Putative Metabolic Effects of the Liver X Receptor (LXR).* Diabetes, 2004. **53**(suppl_1): p. S36-S42.

220. Eberlé, D., et al., *SREBP transcription factors: master regulators of lipid homeostasis.* Biochimie, 2004. **86**(11): p. 839-848.

221. Ma, H. and M.E. Patti, *Bile acids, obesity, and the metabolic syndrome.* Best Practice & Research Clinical Gastroenterology, 2014. **28**(4): p. 573-583.

222. Heiss, C., A. Rodriguez-Mateos, and M. Kelm, *Central role of eNOS in the maintenance of endothelial homeostasis.* Antioxid Redox Signal, 2015. **22**(14): p. 1230-42.

223. Kolluru, G.K., J.H. Siamwala, and S. Chatterjee, *eNOS phosphorylation in health and disease.* Biochimie, 2010. **92**(9): p. 1186-1198.

224. Rassaf, T., et al., *Plasma nitrosothiols contribute to the systemic vasodilator effects of intravenously applied NO: experimental and clinical Study on the fate of NO in human blood.* Circ Res, 2002. **91**(6): p. 470-7.

225. Rassaf, T., et al., *Evidence for in vivo transport of bioactive nitric oxide in human plasma.* J Clin Invest, 2002. **109**(9): p. 1241-8.

226. Kruit, J.K., et al., *Emerging roles of the intestine in control of cholesterol metabolism.* World J Gastroenterol, 2006. **12**(40): p. 6429-39.

227. Cohen, D.E., *Balancing cholesterol synthesis and absorption in the gastrointestinal tract.* J Clin Lipidol, 2008. **2**(2): p. S1-3.

228. Ponten, F., K. Jirstrom, and M. Uhlen, *The Human Protein Atlas--a tool for pathology.* J Pathol, 2008. **216**(4): p. 387-93.

229. O'Flaherty, J.T., et al., *5-Oxo-ETE analogs and the proliferation of cancer cells.* Biochim Biophys Acta, 2005. **1736**(3): p. 228-36.

230. Altmann, R., et al., *13-Oxo-ODE is an endogenous ligand for PPARgamma in human colonic epithelial cells.* Biochem Pharmacol, 2007. **74**(4): p. 612-22.

231. Ahmadian, M., et al., *PPARγ signaling and metabolism: the good, the bad and the future.* Nat Med, 2013. **19**(5): p. 557-66.

232. Matsusue, K., et al., *Liver-specific disruption of PPARgamma in leptin-deficient mice improves fatty liver but aggravates diabetic phenotypes.* J Clin Invest, 2003. **111**(5): p. 737-47.

233. Matsusue, K., et al., *Hepatic steatosis in leptin-deficient mice is promoted by the PPARgamma target gene Fsp27.* Cell Metab, 2008. **7**(4): p. 302-11.

234. Lee, Y.J., et al., *Nuclear receptor PPARgamma-regulated monoacylglycerol O-acyltransferase 1 (MGAT1) expression is responsible for the lipid accumulation in diet-induced hepatic steatosis.* Proc Natl Acad Sci U S A, 2012. **109**(34): p. 13656-61.

235. Asturias, F.J., et al., *Structure and molecular organization of mammalian fatty acid synthase.* Nat Struct Mol Biol, 2005. **12**(3): p. 225-32.

236. Chirala, S.S. and S.J. Wakil, *Structure and function of animal fatty acid synthase.* Lipids, 2004. **39**(11): p. 1045-53.

237. Dorn, C., et al., *Expression of fatty acid synthase in nonalcoholic fatty liver disease.* Int J Clin Exp Pathol, 2010. **3**(5): p. 505-14.

238. Srivastava, R.A.K., et al., *AMP-activated protein kinase: an emerging drug target to regulate imbalances in lipid and carbohydrate metabolism to treat cardio-metabolic diseases: Thematic Review Series: New Lipid and Lipoprotein Targets for the Treatment of Cardiometabolic Diseases.* Journal of Lipid Research, 2012. **53**(12): p. 2490-2514.

239. Zhao, X., et al., *Arterial Pressure Monitoring in Mice.* Curr Protoc Mouse Biol, 2011. **1**: p. 105-122.

240. del Campo, L. and M. Ferrer, *Wire Myography to Study Vascular Tone and Vascular Structure of Isolated Mouse Arteries.* Methods Mol Biol, 2015. **1339**: p. 255-76.

241. Yang, Y.J., et al., *Insulin transport across capillaries is rate limiting for insulin action in dogs.* J Clin Invest, 1989. **84**(5): p. 1620-8.

242. King, G.L. and S.M. Johnson, *Receptor-mediated transport of insulin across endothelial cells.* Science, 1985. **227**(4694): p. 1583-6.

243. Wang, H., et al., *The vascular endothelial cell mediates insulin transport into skeletal muscle.* Am J Physiol Endocrinol Metab, 2006. **291**(2): p. E323-32.

244. Wang, H., et al., *Insulin signaling stimulates insulin transport by bovine aortic endothelial cells.* Diabetes, 2008. **57**(3): p. 540-7.

245. Baron, A.D., *Hemodynamic actions of insulin.* Am J Physiol, 1994. **267**(2 Pt 1): p. E187-202.

246. Carter, M.E. and A. Brunet, *FOXO transcription factors.* Curr Biol, 2007. **17**(4): p. R113-4.

247. Luiking, Y.C., M.P.K.J. Engelen, and N.E.P. Deutz, *Regulation of nitric oxide production in health and disease.* Current Opinion in Clinical Nutrition & Metabolic Care, 2010. **13**(1).

248. Zeng, G. and M.J. Quon, *Insulin-stimulated production of nitric oxide is inhibited by wortmannin. Direct measurement in vascular endothelial cells.* The Journal of Clinical Investigation, 1996. **98**(4): p. 894-898.

249. Zeng, G., et al., *Roles for Insulin Receptor, PI3-Kinase, and Akt in Insulin-Signaling Pathways Related to Production of Nitric Oxide in Human Vascular Endothelial Cells.* Circulation, 2000. **101**(13): p. 1539-1545.

250. Bugianesi, E., A.J. McCullough, and G. Marchesini, *Insulin resistance: A metabolic pathway to chronic liver disease.* Hepatology, 2005. **42**(5): p. 987-1000.

251. Accili, D., *Lilly lecture 2003: the struggle for mastery in insulin action: from triumvirate to republic.* Diabetes, 2004. **53**(7): p. 1633-42.

252. Stern, M.P., *Diabetes and cardiovascular disease. The "common soil" hypothesis.* Diabetes, 1995. **44**(4): p. 369-74.

253. Ginsberg, H.N., *Insulin resistance and cardiovascular disease.* The Journal of Clinical Investigation, 2000. **106**(4): p. 453-458.

254. Nozaki, Y., et al., *Deficiency of eNOS exacerbates early-stage NAFLD pathogenesis by changing the fat distribution.* BMC Gastroenterol, 2015. **15**: p. 177.

255. Huang, P.L., et al., *Hypertension in mice lacking the gene for endothelial nitric oxide synthase.* Nature, 1995. **377**(6546): p. 239-242.

256. Duplain, H., et al., *Insulin resistance, hyperlipidemia, and hypertension in mice lacking endothelial nitric oxide synthase.* Circulation, 2001. **104**(3): p. 342-5.

257. Gouill, E.L., et al. *eNOS knock-out mice have defective mitochondrial beta-oxidation*. 2007.

258. Nisoli, E., et al., *Mitochondrial Biogenesis in Mammals: The Role of Endogenous Nitric Oxide.* Science, 2003. **299**(5608): p. 896-899.

259. Pradines-Figueres, A., C. Vannier, and G. Ailhaud, *Short-term stimulation by insulin of lipoprotein lipase secretion in adipose cells.* Biochem Biophys Res Commun, 1988. **154**(3): p. 982-90.

260. Spooner, P.M., et al., *Insulin regulation of lipoprotein lipase activity and release in 3T3-L1 adipocytes. Separation and dependence of hormonal effects on hexose metabolism and synthesis of RNA and protein.* J Biol Chem, 1979. **254**(20): p. 10021-9.

261. Semenkovich, C.F., et al., *Insulin regulation of lipoprotein lipase activity in 3T3-L1 adipocytes is mediated at posttranscriptional and posttranslational levels.* J Biol Chem, 1989. **264**(15): p. 9030-8.

262. Sadur, C.N. and R.H. Eckel, *Insulin stimulation of adipose tissue lipoprotein lipase. Use of the euglycemic clamp technique.* The Journal of Clinical Investigation, 1982. **69**(5): p. 1119-1125.

263. Diraison, F., P. Moulin, and M. Beylot, *Contribution of hepatic de novo lipogenesis and reesterification of plasma non-esterified fatty acids to plasma triglyceride synthesis during non-alcoholic fatty liver disease.* Diabetes Metab, 2003. **29**(5): p. 478-85.

264. Schwarz, J.M., et al., *Hepatic de novo lipogenesis in normoinsulinemic and hyperinsulinemic subjects consuming high-fat, low-carbohydrate and low-fat, high-carbohydrate isoenergetic diets.* Am J Clin Nutr, 2003. **77**(1): p. 43-50.

265. Hellerstein, M.K., *De novo lipogenesis in humans: metabolic and regulatory aspects.* Eur J Clin Nutr, 1999. **53 Suppl 1**: p. S53-65.

266. Hogarth, C.A., A. Roy, and D.L. Ebert, *Genomic evidence for the absence of a functional cholesteryl ester transfer protein gene in mice and rats.* Comp Biochem Physiol B Biochem Mol Biol, 2003. **135**(2): p. 219-29.

267. Gutiérrez-Juárez, R., et al., *Critical role of stearoyl-CoA desaturase–1 (SCD1) in the onset of diet-induced hepatic insulin resistance.* The Journal of Clinical Investigation, 2006. **116**(6): p. 1686-1695.

268. Parton, R.G. and M.A. del Pozo, *Caveolae as plasma membrane sensors, protectors and organizers.* Nature Reviews Molecular Cell Biology, 2013. **14**(2): p. 98-112.

269. Predescu, D. and G.E. Palade, *Plasmalemmal vesicles represent the large pore system of continuous microvascular endothelium.* American Journal of Physiology-Heart and Circulatory Physiology, 1993. **265**(2): p. H725-H733.

270. Schubert, W., et al., *Microvascular Hyperpermeability in Caveolin-1 Knock-out Mice: TREATMENT WITH A SPECIFIC NITRIC-OXIDE SYNTHASE INHIBITOR NAME, RESTORES NORMAL MICROVASCULAR PERMEABILITY IN Cav-1 NULL MICE *.* Journal of Biological Chemistry, 2002. **277**(42): p. 40091-40098.

271. Drab, M., et al., *Loss of Caveolae, Vascular Dysfunction, and Pulmonary Defects in Caveolin-1 Gene-Disrupted Mice.* Science, 2001. **293**(5539): p. 2449-2452.

272. Grayson, T.H., et al., *Increased caveolae density and caveolin-1 expression accompany impaired NO-mediated vasorelaxation in diet-induced obesity.* Histochemistry and Cell Biology, 2013. **139**(2): p. 309-321.

273. Mastick, C.C., M.J. Brady, and A.R. Saltiel, *Insulin stimulates the tyrosine phosphorylation of caveolin.* Journal of Cell Biology, 1995. **129**(6): p. 1523-1531.

274. Kimura, A., et al., *The Insulin Receptor Catalyzes the Tyrosine Phosphorylation of Caveolin-1 *.* Journal of Biological Chemistry, 2002. **277**(33): p. 30153-30158.

275. Maggi, D., et al., *IGF-I induces caveolin 1 tyrosine phosphorylation and translocation in the lipid rafts.* Biochemical and Biophysical Research Communications, 2002. **295**(5): p. 1085-1089.

276. Podar, K., et al., *Essential role of caveolae in interleukin-6-and insulin-like growth factor I-triggered Akt-1-mediated survival of multiple myeloma cells.* Journal of Biological Chemistry, 2003. **278**(8): p. 5794-5801.

277. Huo, H., et al., *Lipid rafts/caveolae are essential for insulin-like growth factor-1 receptor signaling during 3T3-L1 preadipocyte differentiation induction.* Journal of Biological Chemistry, 2003. **278**(13): p. 11561-11569.

278. Laplante, M. and D.M. Sabatini, *mTOR signaling in growth control and disease.* Cell, 2012. **149**(2): p. 274-93.

279. Quinn, W.J., 3rd, et al., *mTORC1 stimulates phosphatidylcholine synthesis to promote triglyceride secretion.* J Clin Invest, 2017. **127**(11): p. 4207-4215.

280. Leslie, C.C., *Cytosolic phospholipase A2: physiological function and role in disease.* Journal of Lipid Research, 2015. **56**(8): p. 1386-1402.

281. Hollie, N.I., et al., *Micromolar changes in lysophosphatidylcholine concentration cause minor effects on mitochondrial permeability but major alterations in function.* Biochim Biophys Acta, 2014. **1841**(6): p. 888-95.

282. Wang, J., B. Wang, and Y. Zhang, *Agonism activities of lyso-phosphatidylcholines (LPC) Ligands binding to peroxisome proliferator-activated receptor gamma (PPARγ).* J Biomol Struct Dyn, 2020. **38**(2): p. 398-409.

283. Lavi, S., et al., *Local production of lipoprotein-associated phospholipase A2 and lysophosphatidylcholine in the coronary circulation: association with early coronary atherosclerosis and endothelial dysfunction in humans.* Circulation, 2007. **115**(21): p. 2715-21.

284. Mannheim, D., et al., *Enhanced expression of Lp-PLA2 and lysophosphatidylcholine in symptomatic carotid atherosclerotic plaques.* Stroke, 2008. **39**(5): p. 1448-55.

285. Ward-Caviness, C.K., et al., *Improvement of myocardial infarction risk prediction via inflammation-associated metabolite biomarkers.* Heart, 2017. **103**(16): p. 1278-1285.

286. Shiomi, M., et al., *Identification of novel serum markers for the progression of coronary atherosclerosis in WHHLMI rabbits, an animal model of familial hypercholesterolemia.* Atherosclerosis, 2019. **284**: p. 18-23.

287. Law, S.-H., et al., *An Updated Review of Lysophosphatidylcholine Metabolism in Human Diseases.* International Journal of Molecular Sciences, 2019. **20**(5): p. 1149.

288. Kim, E.A., et al., *Lysophosphatidylcholine induces endothelial cell injury by nitric oxide production through oxidative stress.* The Journal of Maternal-Fetal & Neonatal Medicine, 2009. **22**(4): p. 325-331.

289. Motley, E.D., et al., *Lysophosphatidylcholine inhibits insulin-induced Akt activation through protein kinase C-alpha in vascular smooth muscle cells.* Hypertension, 2002. **39**(2 Pt 2): p. 508-12.

290. Schrör, K., *Prostaglandins, other eicosanoids and endothelial cells.* Basic Research in Cardiology, 1985. **80**(5): p. 502-514.

291. Praticò, D. and J.-M. Dogné, *Vascular biology of eicosanoids and atherogenesis.* Expert Review of Cardiovascular Therapy, 2009. **7**(9): p. 1079-1089.

292. Schildknecht, S. and V. Ullrich, *Peroxynitrite as regulator of vascular prostanoid synthesis.* Arch Biochem Biophys, 2009. **484**(2): p. 183-9.

293. Lin, L.L., et al., *cPLA2 is phosphorylated and activated by MAP kinase.* Cell, 1993. **72**(2): p. 269-78.

294. Levine, Y.C., G.K. Li, and T. Michel, *Agonist-modulated Regulation of AMP-activated Protein Kinase (AMPK) in Endothelial Cells: EVIDENCE FOR AN AMPK → Rac1 → Akt*

→ *ENDOTHELIAL NITRIC-OXIDE SYNTHASE PATHWAY *.* Journal of Biological Chemistry, 2007. **282**(28): p. 20351-20364.

295. Igarashi, J., S.G. Bernier, and T. Michel, *Sphingosine 1-phosphate and activation of endothelial nitric-oxide synthase: differential regulation of Akt and MAP kinase pathways by EDG and bradykinin receptors in vascular endothelial cells.* Journal of Biological Chemistry, 2001. **276**(15): p. 12420-12426.

296. Takada, N., et al., *Phospholipid-flipping activity of P4-ATPase drives membrane curvature.* Embo j, 2018. **37**(9).

297. Hall, C., H. Yu, and E. Choi, *Insulin receptor endocytosis in the pathophysiology of insulin resistance.* Experimental & Molecular Medicine, 2020. **52**(6): p. 911-920.

298. Jones, T.H., *Testosterone deficiency: a risk factor for cardiovascular disease?* Trends Endocrinol Metab, 2010. **21**(8): p. 496-503.

299. Kelly, D.M. and T.H. Jones, *Testosterone: a metabolic hormone in health and disease.* J Endocrinol, 2013. **217**(3): p. R25-45.

300. Kelly, D.M., et al., *Testosterone differentially regulates targets of lipid and glucose metabolism in liver, muscle and adipose tissues of the testicular feminised mouse.* Endocrine, 2016. **54**(2): p. 504-515.

301. Kadowaki, T., et al., *Five mutant alleles of the insulin receptor gene in patients with genetic forms of insulin resistance.* The Journal of clinical investigation, 1990. **86**(1): p. 254-264.

302. Accili, D., et al., *Early neonatal death in mice homozygous for a null allele of the insulin receptor gene.* Nature genetics, 1996. **12**(1): p. 106-109.

303. Joshi, R.L., et al., *Targeted disruption of the insulin receptor gene in the mouse results in neonatal lethality.* The EMBO journal, 1996. **15**(7): p. 1542-1547.

304. Abuzzahab, M.J., et al., *IGF-I receptor mutations resulting in intrauterine and postnatal growth retardation.* New England Journal of Medicine, 2003. **349**(23): p. 2211-2222.

305. Liu, J.P., et al., *Mice carrying null mutations of the genes encoding insulin-like growth factor I (Igf-1) and type 1 IGF receptor (Igf1r).* Cell, 1993. **75**(1): p. 59-72.

306. Cai, W., et al., *Domain-dependent effects of insulin and IGF-1 receptors on signalling and gene expression.* Nature Communications, 2017. **8**(1): p. 14892.

307. Rizzoni, D., et al., *Vascular remodeling, macro- and microvessels: Therapeutic implications.* Blood Pressure, 2009. **18**(5): p. 242-246.

308. Bautch, V.L. and K.M. Caron, *Blood and lymphatic vessel formation.* Cold Spring Harb Perspect Biol, 2015. **7**(3): p. a008268.

309. Herzing, L.B.K., et al., *The Human Aminophospholipid-Transporting ATPase Gene ATP10C Maps Adjacent to UBE3Aand Exhibits Similar Imprinted Expression.* The American Journal of Human Genetics, 2001. **68**(6): p. 1501-1505.

Appendix A: Supplemental Figures for Chapter 2

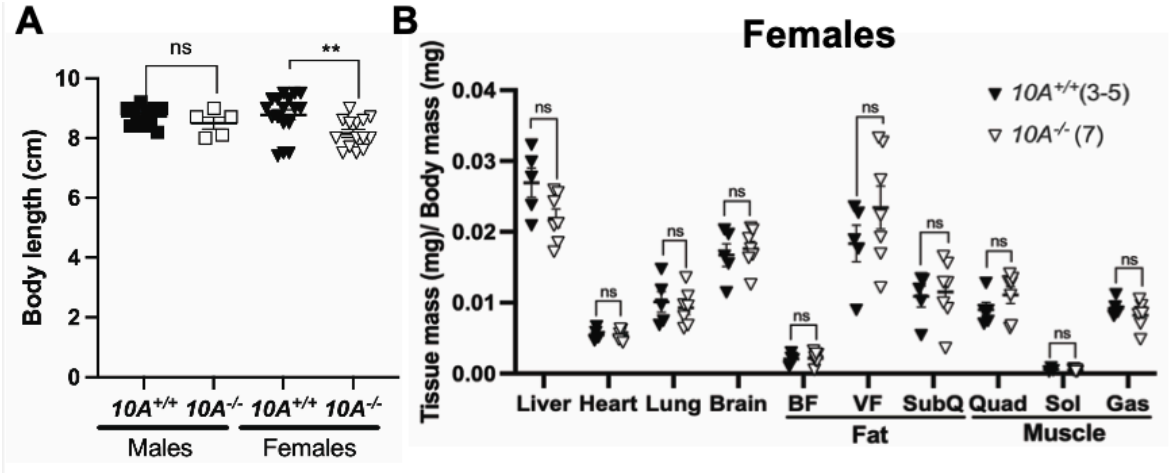

Supplemental Figure 1. *Atp10A* KO female mice have smaller bodies on the 12th week of the HFD. (A) Body length of mice was measured after CO_2 sacrifice. P value by unpaired t-test, **P=0.0094. (**Male:** *10A*$^{+/+}$ n=11, *10A*$^{-/-}$ n=5; **Female**: *10A*$^{+/+}$ n=17, *10A*$^{-/-}$ n=14). (B)The wet mass of tissue was measured after removal from female mice on the 12th week on the HFD. Tissue mass is normalized to body mass. P value by unpaired t-tests. (*10A*$^{+/+}$ n=3-5,*10A*$^{-/-}$ n=7).

Females	10A+/+ (WT) Average (n=7)			10A-/- (KO) Average (n=13)			P-value (t-test, WT vs KO)		
	Light	Dark	Full day	Light	Dark	Full day	Light	Dark	Full day
Avg. Daily Food intake (kcal/period)	6.5	9.5	14.4	5.4	9.5	13.5	***0.0353 (*)***	*0.9515 (ns)*	*0.4425 (ns)*
Avg. Daily Energy Expenditure (kcal/period)	17.3	28.9	46.1	17.4	28.4	45.7	*0.9596 (ns)*	*0.5622 (ns)*	*0.7033 (ns)*
Total Food (kcal)	47.3	57.5	57.5	43.7	54.1	54.1	*0.2807 (ns)*	*0.4428 (ns)*	*0.4428 (ns)*
O2 Consumption (ml/hr)	102.9	125	115.5	103.3	123.1	114.6	*0.8895 (ns)*	*0.5891 (ns)*	*0.7477 (ns)*
CO2 Production (ml/hr)	81	98.1	90.8	80.3	95.9	89.2	*0.7319 (ns)*	*0.4586 (ns)*	*0.5217 (ns)*
Energy balance (kcal)	2.1	9.3	11.5	-1.2	9.6	8.5	***0.0345 (*)***	*0.9394 (ns)*	*0.4886 (ns)*
Resipiratory Exchange Ratio	0.8	0.8	0.8	0.8	0.8	0.8	*0.0839 (ns)*	*0.3642 (ns)*	*0.1761 (ns)*
Locomotor Activity (beam breaks/hr)	121.5	269.9	206.3	100.9	266.1	195.3	*0.2581 (ns)*	*0.8697 (ns)*	*0.5679 (ns)*
Pedestrian Locomotion (m)	146.9	880.8	1027.7	141.1	843	984	*0.8056 (ns)*	*0.7245 (ns)*	*0.7222 (ns)*
Distances in cage Locomotion (m)	199.6	1017.4	1217	185.5	980.6	1166	*0.5972 (ns)*	*0.7443 (ns*	*0.6956 (ns)*

Supplemental Figure 2. *Atp10A* deletion causes alterations to average daily food intake and energy balance during the light hours in female mice fed a HFD for 13 weeks. The table indicates the parameters measured in the Sable System's Promethion Indirect Calorimetry System where the mice were single-housed. The values are an average measurement from 5 days in the system with ad libitum feeding. P value by unpaired t-test (*10A*$^{+/+}$ n=7, *10A*$^{-/-}$ n=13).

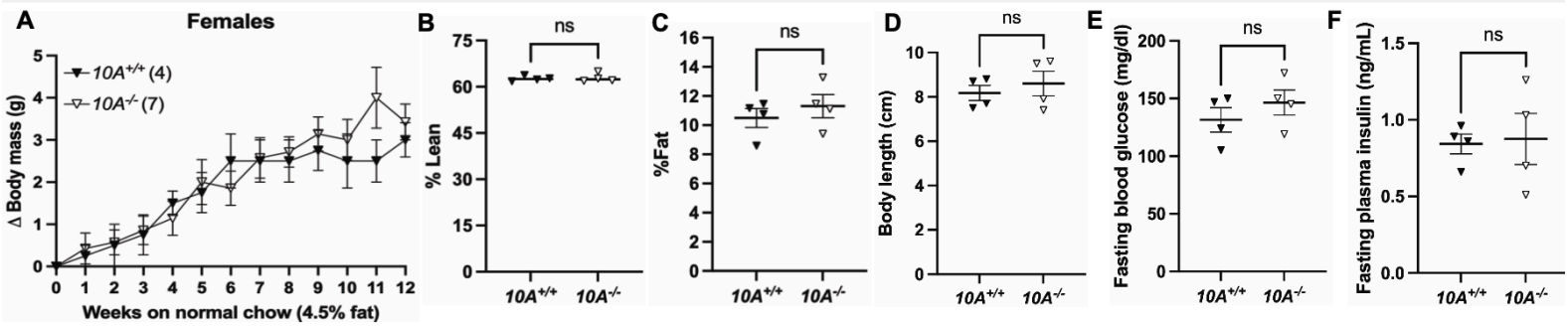

Supplemental Figure 3. *Atp10A* deletion does not affect weight gain, body composition, or glucose homeostasis in female mice after 12 weeks on normal chow. (A) Weight gain of $10A^{+/+}$ and $10A^{-/-}$ female mice over the course of 12 weeks on normal chow (4.5 kcal% fat, Ad lib feeding), P value by 2-way ANOVA with Sidak's multiple comparison. ($10A^{+/+}$ n=4, $10A^{-/-}$ n=7). (B) Lean and (C) fat body mass was normalized to total body mass to calculate % Lean and % Fat mass. P value by unpaired t-test ($10A^{+/+}$ n=4, $10A^{-/-}$ n=4). (D) Body length of mice was measured after CO_2 sacrifice. P value by unpaired t-test ($10A^{+/+}$ n=4, $10A^{-/-}$ n=4). (E) Fasting blood glucose was measured a 5 hour fast, via a glucometer. P value by unpaired t-test ($10A^{+/+}$ n=4, $10A^{-/-}$ n=4). (F) Fasting plasma insulin was measured aftr a 5 hour fast. P-value by unpaired t test ($10A^{+/+}$ n=4, $10A^{-/-}$ n=4).

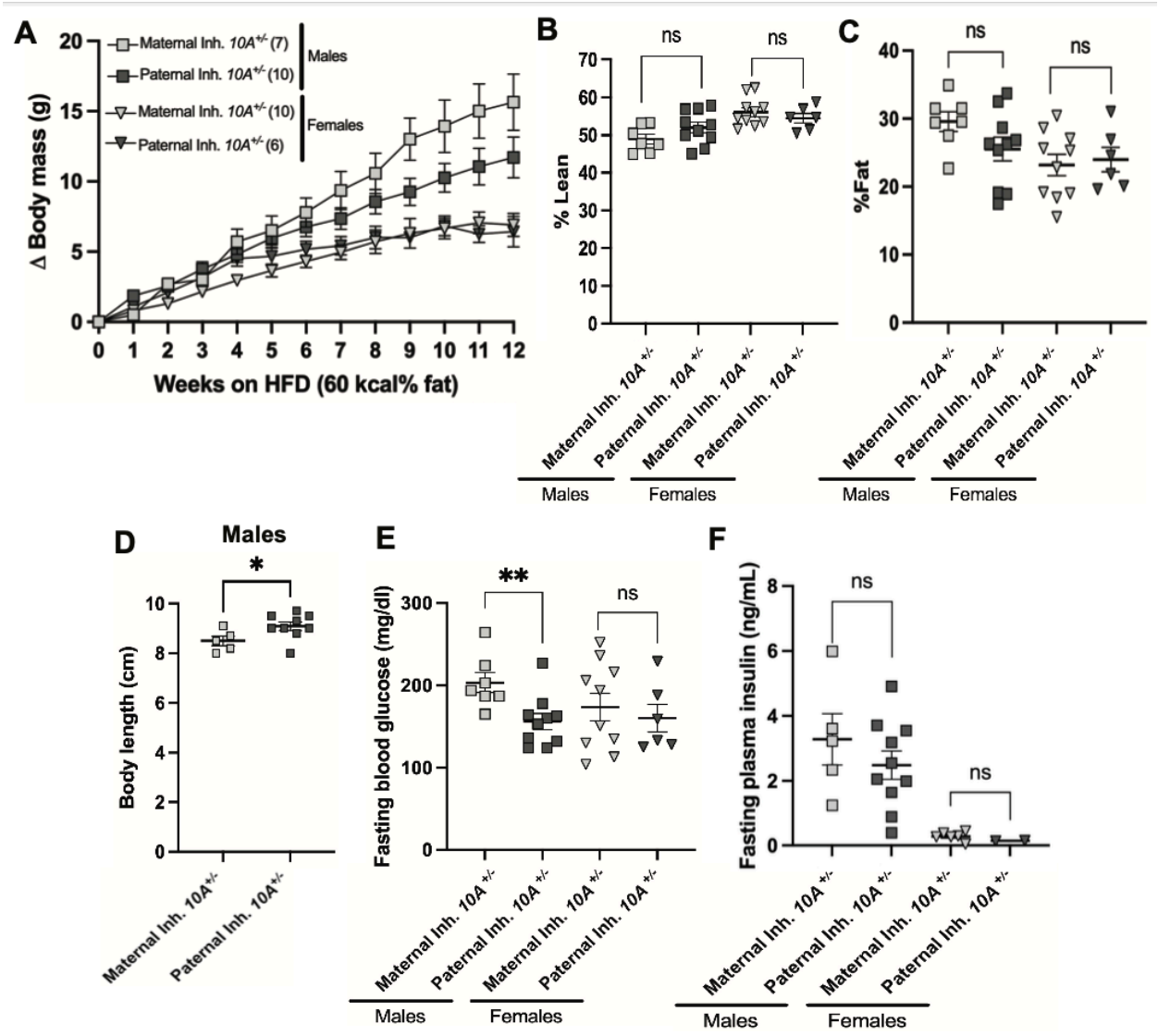

Supplemental Figure 4. Maternally inherited *Atp10A* deletion leads to smaller bodies and elevated fasting blood glucose in male mice on the 12th week on the HFD. (A) Weight gain of heterozygous males and females inheriting the KO allele maternally (Maternal Inheritance (Inh.), *10A*$^{+/-}$ dam X *10A*$^{+/+}$ sire) or paternally (Paternal Inh, *10A*$^{+/+}$ dam x *10A*$^{+/-}$ sire) over the course of 12 weeks on a HFD (60 kcal% fat, Ad lib feeding). P value by 2-way ANOVA with Sidak's multiple comparison. (**Males**: Maternal Inh.*10A*$^{+/-}$ n=7, Paternal Inh.*10A*$^{+/-}$ n=10; **Females**: Maternal Inh.*10A*$^{+/-}$ n=10, Paternal Inh.*10A*$^{+/-}$ n=6). (B) Lean and (C) fat body mass were normalized to body mass to calculate % Lean and % Fat mass. P value by unpaired t-test (**Male**: Maternal Inh.*10A*$^{+/-}$ n=7, Paternal Inh.*10A*$^{+/-}$ n=10; **Female**: Maternal Inh.*10A*$^{+/-}$ n=10, Paternal Inh.*10A*$^{+/-}$ n=6). (D) Body length of male mice was measured after CO_2 sacrifice. P value by unpaired t-test, *P=0.0490. (Maternal Inh.*10A*$^{+/-}$ n=4, Paternal Inh.*10A*$^{+/-}$ n=9). (E) Fasting blood glucose was measured after a 5 hour fast, via a glucometer. P value by unpaired t-test, **P=0.0081. (**Male**: Maternal Inh.*10A*$^{+/-}$ n=7, Paternal Inh.*10A*$^{+/-}$ n=10; **Female**: Maternal Inh.*10A*$^{+/-}$ n=10, Paternal Inh.*10A*$^{+/-}$ n=6). (F) Fasting plasma insulin was measured after a 5 hour fast, P value by unpaired t-test. (**Male**: Maternal Inh.*10A*$^{+/-}$ n=6, Paternal Inh.*10A*$^{+/-}$ n=10; **Female**: Maternal Inh.*10A*$^{+/-}$ n=5, Paternal Inh.*10A*$^{+/-}$ n=2).

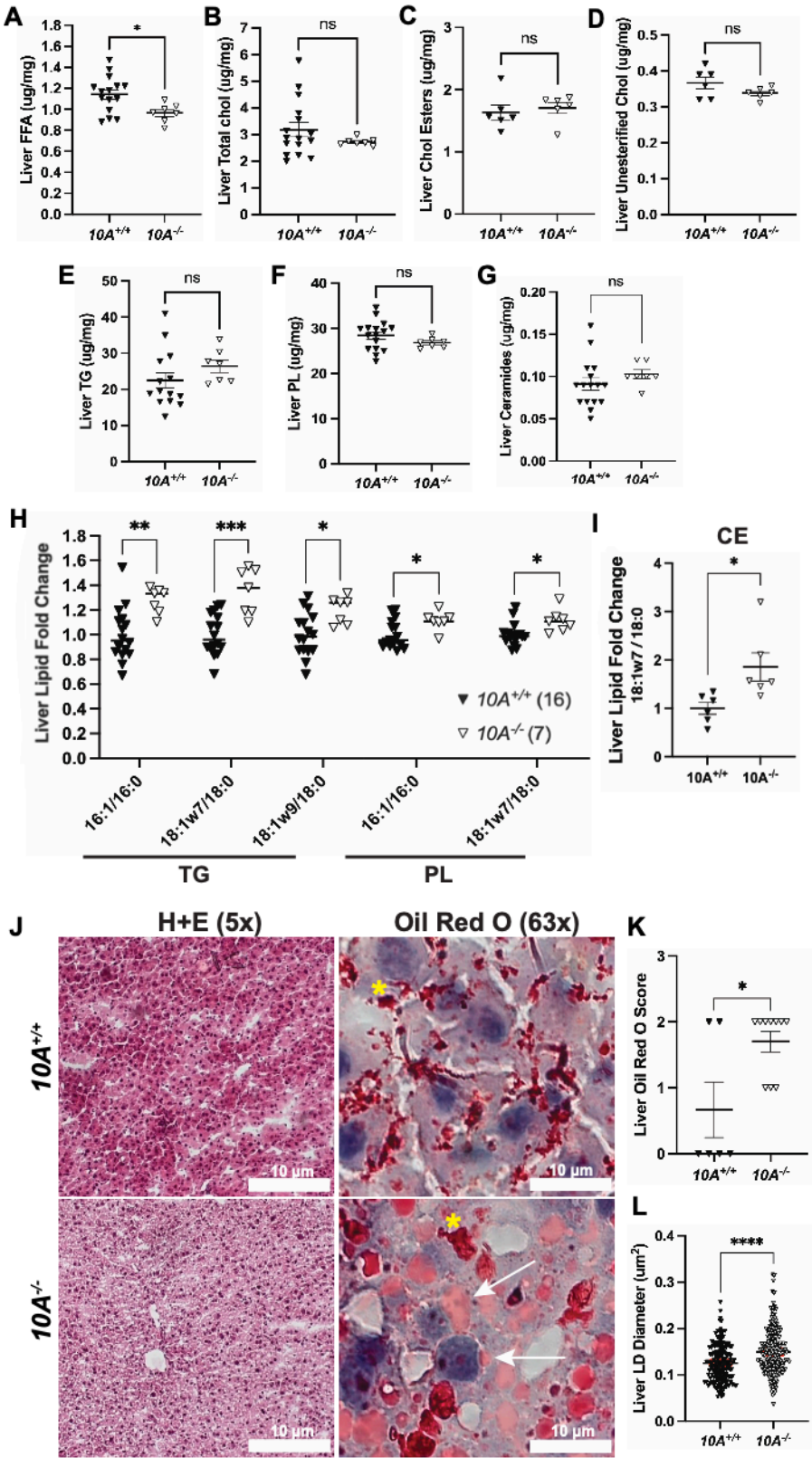

Supplemental Figure 5. *Atp10A* deletion causes changes to liver lipid metabolism in female mice after 12 weeks on a HFD. (A-G) FFAs, Total cholesterol, cholesterol esters, unesterifed cholesterol, TGs, PLs, and ceramides were measured from flash frozen livers via gas chromatography. Livers were collected after a 5 hour fast or after a 5 hour fast followed by an OGTT. P value by unpaired t-test (FFA: *10A*$^{+/+}$ n=15,*10A*$^{-/-}$ n=7, *P=0.0201; Total cholesterol: *10A*$^{+/+}$ n=16, *10A*$^{-/-}$ n=7; Cholesterol esters: *10A*$^{+/+}$ n=6,*10A*$^{-/-}$ n=6; Unesterified cholesterol: *10A*$^{+/+}$ n=6,*10A*$^{-/-}$ n=6; TG: *10A*$^{+/+}$ n=14, *10A*$^{-/-}$ n=7; PLs: *10A*$^{+/+}$ n=16, *10A*$^{-/-}$ n=7; Ceramides: *10A*$^{+/+}$ n=16, *10A*$^{-/-}$ n=7). The saturation of liver (H) TG, PL, and (I) CE species was determined by gas chromatography. The fold change of unsaturated vs saturated TG, PL, CE is shown. P value by 2-way ANOVA with Sidak's multiple comparison, **TG**: **P=0.0025, ***P=0.0001, *P=0.0443, **PL**: *P=0.0297, *P=0.0281 (*10A*$^{+/+}$ n=16, *10A*$^{-/-}$ n=7). **CE:** P value by unpaired t-test, *P=0.0223 (*10A*$^{+/+}$ n=6, *10A*$^{-/-}$ n=6). (J) Representative images of livers stained with H+E (5x) or Oil Red O (63x). The coalescence of the Oil Red O stain is indicated by yellow asterisks (artifact) and the arrows point to neutral lipids stained by Oil Red O. Scale bars = 10 µM. (K) Liver sections were scored using the Oil Red O Score described in the Materials and Methods. P value by nonparametric t-test (Mann-Whitney U), *P=0.0327 (*10A*$^{+/+}$ n=6, *10A*$^{-/-}$ n=10). (L) The diameters of Oil Red O positive lipid droplets (LD) in the liver sections with a score of 2 were measured using ImageJ. The red line in the graph represents the SEM. P value by unpaired t-test, ****P=<0.0001 (*10A*$^{+/+}$,120 LDs measured, n=2, *10A*$^{-/-}$, 203 LDs measured, n=3).

A

Peptides	1A, 1B	3A,3B	5A,5B
Amino acid number	27-38	41-53	498-509
Amino acid sequence	RTRTVRSNLLPP	TEDSTIGAPKGER	HKTQSIKSHRRT

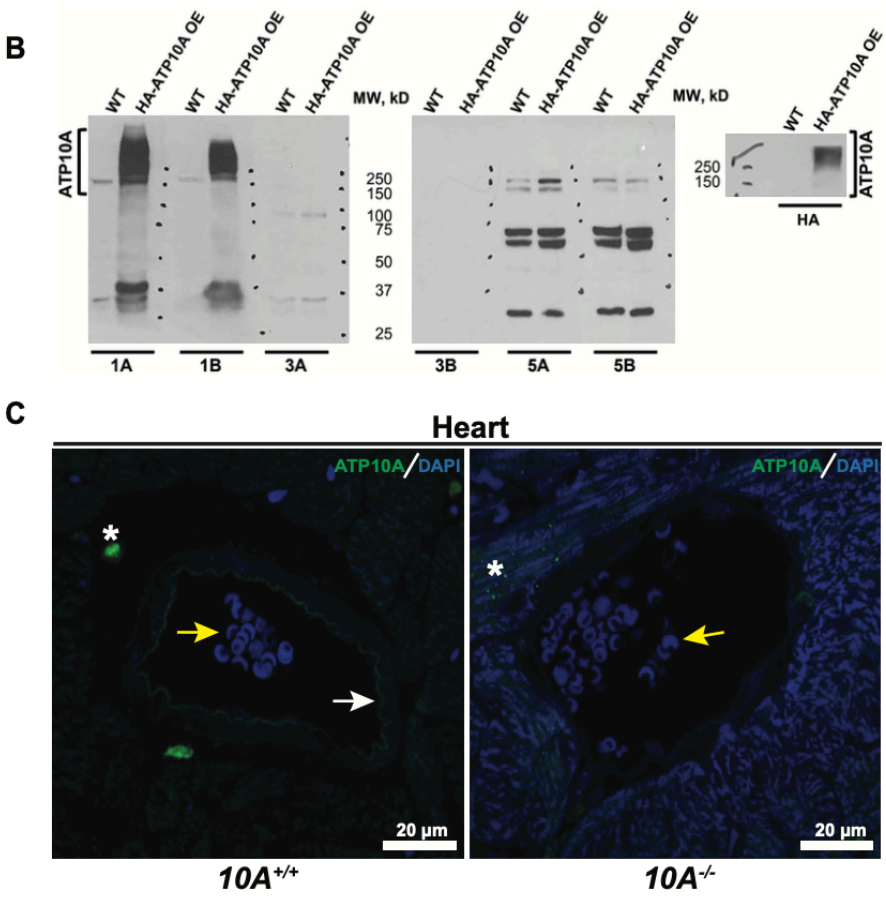

Supplemental Figure 6. Validation of anti-ATP10A antibody: expression of ATP10A in HeLa cells with over-expressed HA-ATP10A and in mouse heart. (A) Table indicating the sequences of the ATP10A peptides that were injected into rabbits to produce antibodies. (B) Representative images of total cell lysates from HeLa cells with over-expressed HA-ATP10A (40 µg total protein) that were subjected to Western immunoblot analyses for expression of ATP10A using antibody produced against ATP10A peptides (left and central panels) and HA (right panel). (C) Representative immunofluorescent images of hearts from female mice showing expression of ATP10A (green) and DAPI (blue). Scale bar = 20 µm. The white asterisk indicates background staining, the white arrow indicates ATP10A positive staining, the yellow arrow indicates auto fluorescent red blood cells (*10A*$^{+/+}$ n=1, *10A*$^{-/-}$ n=1).

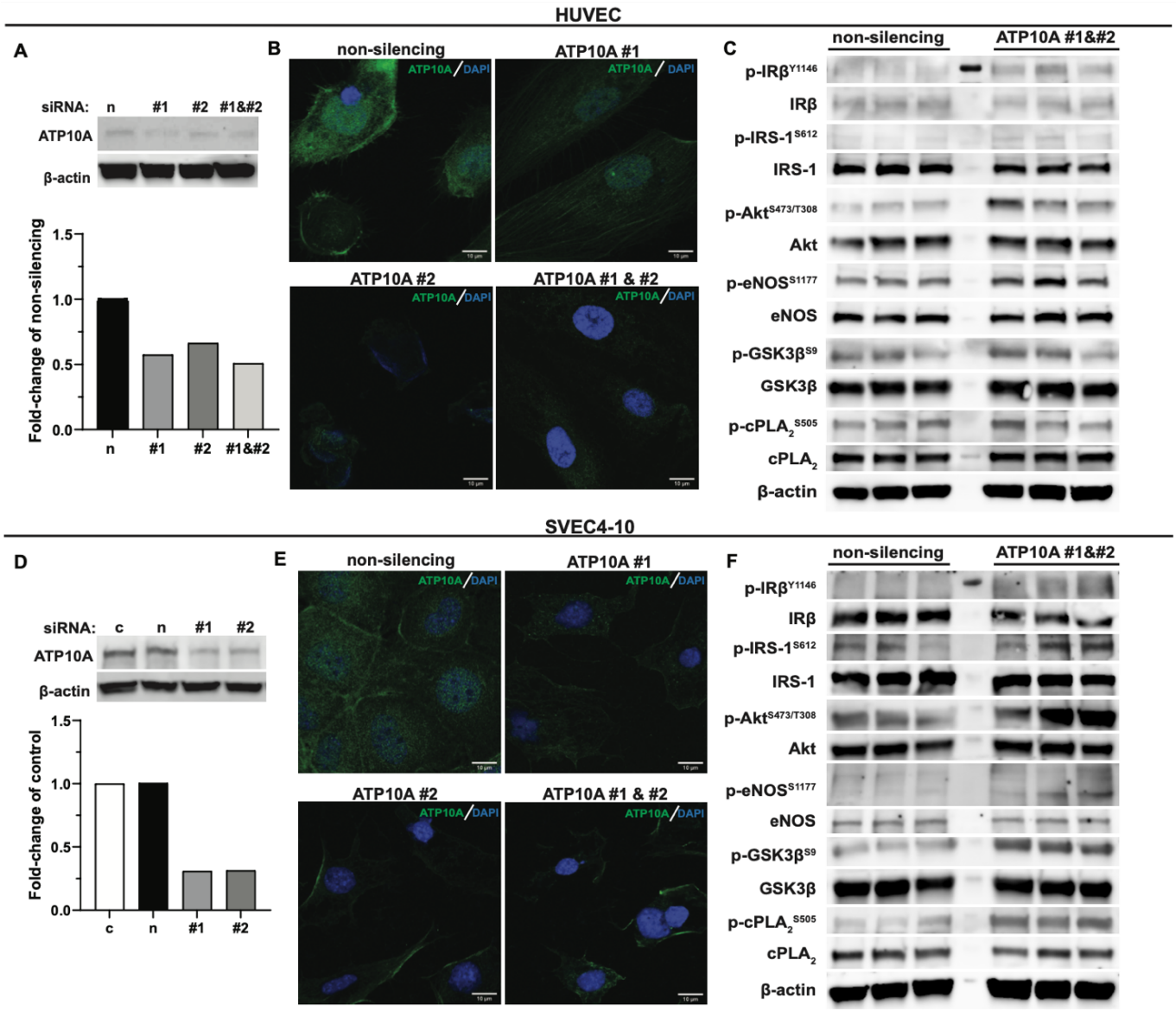

Supplemental Figure 7. ATP10A expression level regulates basal activity of insulin signaling pathways in endothelial cells. (A,D) Representative images and quantitative analysis of ATP10A from immunoblots of HUVEC (A) and SVEC4-10 (D) untreated (c), transfected with non-silencing siRNA or ATP10A siRNA constructs (#1, #2, #1&#2). (B, E) Representative immunofluorescent images showing expression of ATP10A and DAPI in HUVEC (B) and SVEC4-10 (E) transfected with non-silencing siRNA (n) or ATP10A siRNA constructs (ATP10A#1, ATP10A#2, ATP10A#1&#2). Scale bar=10 μm. (C, F) Representative images of basal phosphorylated and total IRβ, IRS-1, Akt, eNOS, GSK-3β, and cPLA2 from immunoblots of HUVEC (C) and SVEC4-10 (F) transfected with non-silencing siRNA or ATP10A#1&#2 siRNA constructs. Note th the lane between the non-silencing and ATP10A#1&#2 treated lanes contains the molecular weight marker.

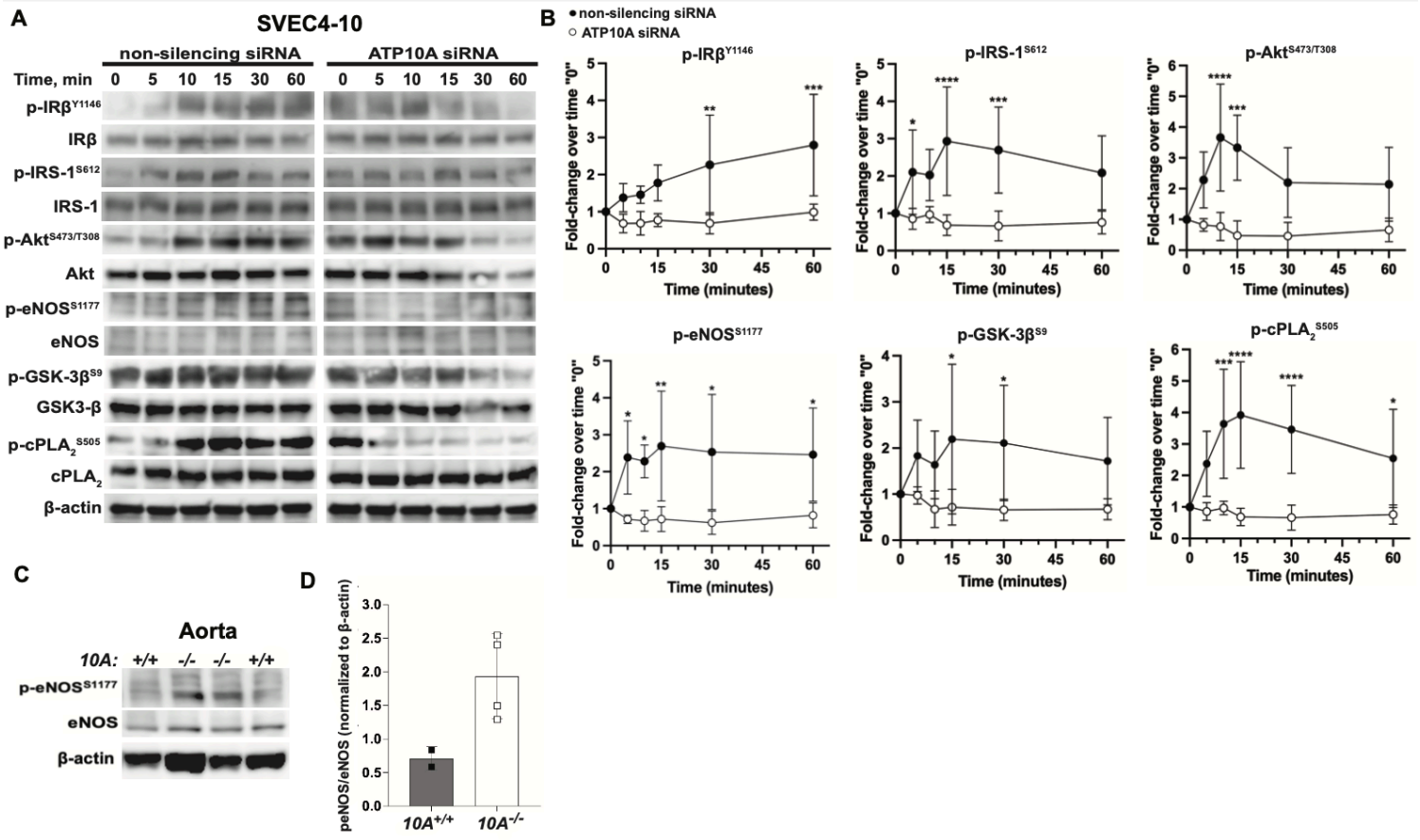

Supplemental Figure 8. ATP10A expression regulates insulin signaling pathway in SVEC4-10 cells and mouse aorta. (A) Representative images and (B) quantitative analysis from immunoblots of phosphorylated and total IRβ, IRS-1, Akt, eNOS, GSK-3β, and $cPLA_2$ from SVEC4-10 cells transfected with non-silencing siRNA or ATP10A siRNA constructs and then treated with insulin for 0-60 mins. Mean measurements of 3-6 independent experiments are shown. *p≤0.05; **p≤0.005; ***p≤0.0005; ***p≤0.0001 between cells transfected with non-silencing or ATP10A siRNA by 2-way ANOVA with Sidak's multiple comparison test. (C) Representative blots and (D) quantitative analysis from immunoblots of phosphorylated and total eNOS from total aorta lysates from male mice ($10A^{+/+}$ n=2, $10A^{-/-}$ n=4, statistics were not done due to low n). Mean measurements of 3-6 independent experiments are shown.

Appendix B. Supplemental Tables for Chapter 2

Supplemental Table 1

Figure 2	10A+/+ (WT)		10A-/- (KO)	10A+/+ (WT)		10A-/- (KO)	
(B) Weight gain	Males			Females			
n	17		15	34		31	
Avg. body mass on 12th week of HFD (g)	34		33.9	23.6		25.1	
t-test (p-value) from body mass at 12th week on HFD		0.7672 (ns)			0.0498 (*)		
Avg. Age on 12th week of HFD (weeks)	18		19.4	17.8		19.2	
Outliers removed by ROUT analysis	0		0	0		0	
(C-D) Body comp.	Males			Females			
n	11		13	13		14	
Avg. body mass on 12th week of HFD (g)	35.6		33.8	24.2		26.5	
t-test (p-value) from body mass at 12th week on HFD		0.3636 (ns)			0.0799 (ns)		
Avg. Age on 12th week of HFD (weeks)	17.4		19.5	16.5		19.2	
Outliers removed by ROUT analysis	0		0	0		0	
(E) Fastina blood glucose	Males			Females			
n	10		11	19		14	
Avg. body mass on 12th week of HFD (g)	36.3		34.2	23.1		26.4	
t-test (p-value) from body mass at 12th week on HFD		0.3410 (ns)			0.0049 (**)		
Avg. Age on 12th week of HFD (weeks)	17.2		19.5	16.7		19.2	
Outliers removed by ROUT analysis	0		0	0		0	
(F) Fastina plasma insulin	Males			Females			
n	8		10	13		9	
Avg. body mass on 12th week of HFD (g)	36.5		34.7	23		28.4	
t-test (p-value) from body mass at 12th week on HFD		0.4579 (ns)			0.0009 (***)		
Avg. Age on 12th week of HFD (weeks)	17.1		19.5	16.3		19.3	
Outliers removed by ROUT analysis	0		0	0		0	
(G-H) OGTT (retroorbital blood taken prior to gic administration)	Males			Females			
n	6		6	12		6	
Avg. body mass on 12th week of HFD (g)	36.5		35.7	23.7		27.8	
t-test (p-value) from body mass at 12th week on HFD		0.7215 (ns)			0.0169 (*)		
Avg. Age on 12th week of HFD (weeks)	17.5		19.3	16.3		19.5	
Outliers removed by ROUT analysis	0		0	0		0	

Figure 3: Plasma lipid and lipoproteins	10A+/+ (WT)		10A-/- (KO)	10A+/+ (WT)		10A-/- (KO)	
(A-D) Plasma FFA	Males			Females			
n	7 (all done by lab kit)		6 (all done by lab kit)	12 (11 done by Core, 1 done by lab kit)		8 (7 done by Core, 1 done by lab kit)	
Avg. body mass on 12th week of HFD (g)	34.2		37.2	23.1		27.2	
t-test (p-value) from body mass at 12th week on HFD		0.2427 (ns)			0.0014(**)		
Avg. Age on 12th week of HFD (weeks)	17.4		19.2	16.6		19.5	
Outliers removed by ROUT analysis	0		0	0		4	
(E-H) Plasma DGal	Males			Females			
n	8 (all done by lab kit)		6 (all done by lab kit)	12 (11 done by Core, 1 done by lab kit)		12 (7 done by Core, 5 done by lab kit)	
Avg. body mass on 12th week of HFD (g)	34.6		35.5	23.1		28.3	
t-test (p-value) from body mass at 12th week on HFD		0.5880 (ns)			0.0243 (*)		
Avg. Age on 12th week of HFD (weeks)	17.5		19.2	16.6		19.3	
Outliers removed by ROUT analysis	0		0	0		0	
(I-J) Plasma TG	Males			Females			
n	9 (all done by lab kit)		7 (all done by lab kit)	12 (11 done by Core, 1 done by lab kit)		12 (7 done by Core, 5 done by lab kit)	
Avg. body mass on 12th week of HFD (g)	34.9		37	23.1		28.3	
t-test (p-value) from body mass at 12th week on HFD		0.2130 (ns)			0.0243 (*)		
Avg. Age on 12th week of HFD (weeks)	17.6		19.1	16.6		19.3	
Outliers removed by ROUT analysis	0		0	0		0	
(G-I) Lipoprotein fractionation	Males			Females, chol			
n	N/A		N/A	6		6	
Avg. body mass on 12th week of HFD (g)	N/A		N/A	23.8		29.2	
t-test (p-value) from body mass at 12th week on HFD		N/A			0.0274 (*)		
Avg. Age on 12th week of HFD (weeks)	N/A		N/A	16.3		19.3	
Outliers removed by ROUT analysis	N/A		N/A	N/A		N/A	
	Males			Females, TG			
n	N/A		N/A	6		7	
Avg. body mass on 12th week of HFD (g)	N/A		N/A	23.8		28.6	
t-test (p-value) from body mass at 12th week on HFD		N/A			0.0272 (*)		
Avg. Age on 12th week of HFD (weeks)	N/A		N/A	16.3		19.3	
Outliers removed by ROUT analysis	N/A		N/A	N/A		N/A	

Figure 4: Plasma lipidomics and VF RNASeq	10A+/+ (WT)		10A-/- (KO)	10A+/+ (WT)		10A-/- (KO)	
(A-B) Plasma lipidomics	Males			Females			
n	N/A		N/A	ique mice (4 unpooled samples, 1 pooled sample		ique mice (3 unpooled samples, 2 pooled samples)	
Avg. body mass on 12th week of HFD (g)	N/A		N/A	22.9		28.4	
t-test (p-value) from body mass at 12th week on HFD		N/A			0.0068 (**)		
Avg. Age on 12th week of HFD (weeks)	N/A		N/A	16.5		19.4	
Outliers removed by ROUT analysis	N/A		N/A	N/A		N/A	
(C) VF RNASeq	Males			Females			
n	N/A		N/A	3		3	
Avg. body mass on 12th week of HFD (g)	N/A		N/A	23.3		31.8	
t-test (p-value) from body mass at 12th week on HFD		N/A			0.0261 (*)		
Avg. Age on 12th week of HFD (weeks)	N/A		N/A	17.3		19.3	
Outliers removed by ROUT analysis	N/A		N/A	N/A		N/A	

Figure 5: Liver signaling (WB analysis)	10A+/+ (WT)		10A-/- (KO)	10A+/+ (WT)		10A-/- (KO)	
(A,B,C) PGAT and AMPK	Males			Females			
n	N/A		N/A	7		7	
Avg. body mass on 12th week of HFD (g)	N/A		N/A	22.9		27.6	
t-test (p-value) from body mass at 12th week on HFD		N/A			0.0142 (*)		
Avg. Age on 12th week of HFD (weeks)	N/A		N/A	16.7		19.1	
Outliers removed by ROUT analysis	N/A		N/A	0		0	
(D,E) IRB, IRS1, Akt, etc...	Males			Females			
n	N/A		N/A	8		8	
Avg. body mass on 12th week of HFD (g)	N/A		N/A	23		27.3	
t-test (p-value) from body mass at 12th week on HFD		N/A			0.0118 (*)		
Avg. Age on 12th week of HFD (weeks)	N/A		N/A	16.9		19.1	
Outliers removed by ROUT analysis	N/A		N/A	0		0	

Figure 6: 10A Expression (WB & IF)	10A+/+ (WT)		10A-/- (KO)	10A+/+ (WT)		10A-/- (KO)	
(A) 10A Expression in Mouse tissues (WB)	Males			Females (fed HFD for 12 weeks)			
n	2 (vas def, heart,1 testes: 1)		2 (vas def, heart:1, testes: 1)	1 (brain, liver, VF)		1 (brain, liver, VF)	
Body mass at sacrifice (g)	N/A		N/A	27		25	
Age (weeks)	7.5		8	19		19	
Outliers removed by ROUT analysis	N/A		N/A	N/A		N/A	
(B) 10A Expression in Testes & Vas deferens (IF)	Males			Females			
n	1		1	N/A		N/A	
Body mass at sacrifice (g)	26		25	N/A		N/A	
t-test (p-value) from body mass at 12th week on HFD		N/A			N/A		
Age (weeks)	11		11	N/A		N/A	
Outliers removed by ROUT analysis	N/A		N/A	N/A		N/A	
(C) 10A Expression in Liver	Males			Females (Liver)			
n	N/A		N/A	3		1	
Avg. body mass on 12th week of HFD (g)	N/A		N/A	24		22	
t-test (p-value) from body mass at 12th week on HFD		N/A			N/A		
Avg. Age on 12th week of HFD (weeks)	N/A		N/A	18.7		21	
Outliers removed by ROUT analysis	N/A		N/A	N/A		N/A	
(D) 10A Expression in VF	Males			Females (VF)			
n	N/A		N/A	3		2	
Avg. body mass on 12th week of HFD (g)	N/A		N/A	24		23	
t-test (p-value) from body mass at 12th week on HFD		N/A			0.7445 (ns)		
Avg. Age on 12th week of HFD (weeks)	N/A		N/A	18.7		19.5	
Outliers removed by ROUT analysis	N/A		N/A	N/A		N/A	

Figure 7: EC signaling	10A+/+ (WT)		10A-/- (KO)	10A+/+ (WT)		10A-/- (KO)	
(E,F) Mouse Aorta	Males			Females (fed normal chow)			
n	N/A		N/A	5		4	
Avg. Body mass at sacrifice (g)	N/A		N/A	23.8		22.8	
t-test (p-value) from body mass at 12th week on HFD		N/A			0.5499 (ns)		
Avg. Age (weeks)	N/A		N/A	20.4		17.8	
Outliers removed by ROUT analysis	N/A		N/A	0		0	

Supp. Figure 1: Body length & tissue mass	10A+/+ (WT)		10A-/- (KO)	10A+/+ (WT)		10A-/- (KO)	
(A) Body length	Males			Females			
n	11		5	17		14	
Avg. body mass on 12th week of HFD (g)	34.7		36	23.7		27.3	
t-test (p-value) from body mass at 12th week on HFD		0.6672 (ns)			0.0666 (ns)		
Avg. Age on 12th week of HFD (weeks)	17.9		19.4	16.7		19.6	
Outliers removed by ROUT analysis	0		0	0		0	
(B) Tissue mass	Males			Females (12 weeks of HFD)			
n	N/A		N/A	3-5		7	
Avg. body mass on 12th week of HFD (g)	N/A		N/A	23.8		23.1	
t-test (p-value) from body mass at 12th week on HFD		N/A			0.7344 (ns)		
Avg. Age on 12th week of HFD (weeks)	N/A		N/A	18.4		19.1	
Outliers removed by ROUT analysis	N/A		N/A	0		0	
(C) T30 Serum Insulin	Males			Females			
n	4		4	8		6	
Avg. body mass on 12th week of HFD (g)	37.3		28.1	22.9		27.8	
t-test (p-value) from body mass at 12th week on HFD		0.5431 (ns)			0.0099 (**)		
Avg. Age on 12th week of HFD (weeks)	17.3		15.4	15.9		19.5	
Outliers removed by ROUT analysis	0		0	0		0	
(D) T60 Serum Insulin	Males			Females			
n	6		5	8		6	
Avg. body mass on 12th week of HFD (g)	36.5		35.1	20.7		27.8	
t-test (p-value) from body mass at 12th week on HFD		0.5726 (ns)			0.0270 (*)		
Avg. Age on 12th week of HFD (weeks)	17.5		19.2	14.1		19.5	
Outliers removed by ROUT analysis	0		0	0		0	

Supp. Figure 2: Table data	10A+/+ (WT)		10A-/- (KO)	10A+/+ (WT)		10A-/- (KO)	
(A) Body length	Males			Females			
n	N/A		N/A	7		13	
Avg. body mass on 12th week of HFD (g)	N/A		N/A	24.4		25.6	
t-test (p-value) from body mass at 12th week on HFD		N/A			0.5296 (ns)		
Avg. Age on 12th week of HFD (weeks)	N/A		N/A	19.7		19.1	
Outliers removed	N/A		N/A	1		0	

Supp. Figure 3 Normal chow studies	10A+/+ (WT)		10A-/- (KO)	10A+/+ (WT)		10A-/- (KO)	
(A) Weight gain	Males			Females			
n	N/A		N/A	4		7	
Avg. body mass on 12th week of HFD (g)	N/A		N/A	20.8		21.6	
t-test (p-value) from body mass at 12th week on HFD		N/A			0.2543 (ns)		
Avg. Age on 12th week of HFD (weeks)	N/A		N/A	20		19.7	
Outliers removed by ROUT analysis	N/A		N/A	0		0	
B, C, D, E F) % Lean, % Fat, Body length, FBG, Fasting plasma insulin	Males			Females			
n	N/A		N/A	4		4	
Avg. body mass on 12th week of HFD (g)	N/A		N/A	20		21.5	
t-test (p-value) from body mass at 12th week on HFD		N/A			0.4772 (ns)		
Avg. Age on 12th week of HFD (weeks)	N/A		N/A	20		20	
Outliers removed by ROUT analysis	N/A		N/A	0		0	

Supp. Figure 4: Inheritance pattern studies	Maternal inh. 10a +/-		Paternal inh. 10a +/-	Maternal inh. 10a +/-		Paternal inh. 10a +/-	
(A, B, C, E) Weight gain, %Lean, %Fat, FBG	Males			Females			
n	7		10	10		6	
Avg. body mass on 12th week of HFD (g)	35.9		32.5	25.4		25.6	
t-test (p-value) from body mass at 12th week on HFD		0.1405 (ns)			0.9195 (ns)		
Avg. Age on 12th week of HFD (weeks)	17.1		17.8	16.8		17.7	
Outliers removed by ROUT analysis	0		0	0		0	
(D) Body length	Males			Females			
n	4		11	N/A		N/A	
Avg. body mass on 12th week of HFD (g)	33		32.3	N/A		N/A	
t-test (p-value) from body mass at 12th week on HFD		0.7165 (ns)			N/A		
Avg. Age on 12th week of HFD (weeks)	17.6		17.8	N/A		N/A	
Outliers removed by ROUT analysis	0		0	N/A		N/A	
(F) Fastina plasma insulin	Males			Females			
n	6		10	5		2	
Avg. body mass on 12th week of HFD (g)	33		32.5	26		27.3	
t-test (p-value) from body mass at 12th week on HFD		0.7744 (ns)			0.7049 (ns)		
Avg. Age on 12th week of HFD (weeks)	17.6		17.8	16		17	
Outliers removed by ROUT analysis	0		0	0		0	

Supp. Figure 5: Liver lipidomics	10A+/+ (WT)		10A-/- (KO)	10A+/+ (WT)		10A-/- (KO)	
(A, B, E, F, G, H*) Liver FFA, T Chol, TG, Cer, PL, Lipid fold change*	Males			Females			
n	N/A		N/A	14-16		7	
Avg. body mass on 12th week of HFD (g)	N/A		N/A	23.1		28.5	
t-test (p-value) from body mass at 12th week on HFD		N/A			0.0096 (***)		
Avg. Age on 12th week of HFD (weeks)	N/A		N/A	16.3		19.6	
Outliers removed by ROUT analysis	N/A		N/A	FFA: 1, TG:2		0	
(C,D, I*) Liver Chol Est, Chol un-est, Lipid fold change*	Males			Females			
n	N/A		N/A	6		6	
Avg. body mass on 12th week of HFD (g)	N/A		N/A	23.8		27.8	
t-test (p-value) from body mass at 12th week on HFD		N/A			0.0091 (ns)		
Avg. Age on 12th week of HFD (weeks)	N/A		N/A	17		19.2	
Outliers removed by ROUT analysis	N/A		N/A	0		0	
J, K) Liver Oil Red O	Males			Females			
n	N/A		N/A	6		10	
Avg. body mass on 12th week of HFD (g)	N/A		N/A	22.7		28.1	
t-test (p-value) from body mass at 12th week on HFD		N/A			0.0059 (**)		
Avg. Age on 12th week of HFD (weeks)	N/A		N/A	17		19.4	
Outliers removed by ROUT analysis	N/A		N/A	N/A		N/A	
(N) Lipid droplet size	Males			Females			
n	N/A		N/A	2		3	
Avg. body mass on 12th week of HFD (g)	N/A		N/A	25.5		24.9	
t-test (p-value) from body mass at 12th week on HFD		N/A			0.5093 (ns)		
Avg. Age on 12th week of HFD (weeks)	N/A		N/A	19		19.3	
Outliers removed by ROUT analysis	N/A		N/A	3		1	

Supp. Figure 6: 10A Expression (WB, IF)	10A+/+ (WT)		10A-/- (KO)	10A+/+ (WT)		10A-/- (KO)	
(B) 10A Expression in heart IHC	Males			Females			
n	N/A		N/A	1		1	
Body mass on 12th week of HFD (g)	N/A		N/A	22		24	
t-test (p-value) from body mass at 12th week on HFD		N/A			N/A		
Avg. Age on 12th week of HFD (weeks)	N/A		N/A	19		19	
Outliers removed by ROUT analysis	N/A		N/A	N/A		N/A	

Supp. Figure 8: Aorta eNOS (WB)	10A+/+ (WT)		10A-/- (KO)	10A+/+ (WT)		10A-/- (KO)	
(C,D) 10A Expression in Mouse Aorta	Males			Females			
n	2 (both on HFD)		4 (1 on HFD)	N/A		N/A	
Body mass on 12th week of HFD (g)	30		27.8	N/A		N/A	
t-test (p-value) from body mass at 12th week on HFD		0.3177 (ns)			N/A		
Age on 12th week of HFD (weeks)	19		13	N/A		N/A	
Outliers removed by ROUT analysis	0		0	N/A		N/A	

Females

10A+/+ (WT): 11 fast + OGTT, 1: fast only (92% fast + OGTT, 8% fast only)
10A-/- (KO), FFA: 4: fast + OGTT, 4: fast only (50% fast + OGTT, 50% fast only)
10A-/- (KO): TG, chol: 4: fast + OGTT, 6: fast only (33% fast + OGTT, 67% fast only)

10A+/+ (WT): 2: fast + OGTT, 1: fast only (67% fast + OGTT, 33% fast only)
10A-/- (KO): 1: fast + OGTT, 2: fast only (33% fast + OGTT, 67% fast only)

10A+/+ (WT): 2: fast + OGTT, : 5 fast only (29% fast + OGTT, 71 % fast only)
10A-/- (KO): : 4 fast + OGTT, : 3 fast only (57% fast + OGTT,43% fast only)

10A+/+ (WT): 2: fast + OGTT, : 6 fast only (25% fast + OGTT, 75% fast only)
10A-/- (KO): : 4 fast + OGTT, : 4 fast only (50% fast + OGTT,50 % fast only)

IHC: n=tissues from different mice imaged in the same session where the representative image was imag

n=tissues from different mice imaged in the same session where the representative image was imaged

* TG: (16:1/16:0), (18:w7/18:0), (18:1w9/19:0), PL: (16:1/16:0), (18:1w7/18:0)

*CE: (18:1w7/18:0)

Supplemental Table 2

Pathway Kegg

geneSet	description	size	overlap	expect	enrichmentRatio	pValue	FDR
g.jp/kegg-bin/show_pathway? mmu04972+13487+1878	Pancreatic secretion	103	5	0.809063	6.179985	0.0012387	0.393894
tp://www.kegg.jp/kegg-bin/show_pathway? mmu00730+	Thiamine metabolism	15	2	0.117825	16.974359	0.0059725	0.566786
g-bin/show_pathway? mmu04080+110902+11555+126	Neuroactive ligand-receptor interaction	289	7	2.270091	3.083577	0.0072516	0.566786
ww.kegg.jp/kegg-bin/show_pathway? mmu05150+1351	Staphylococcus aureus infection	56	3	0.439879	6.820055	0.0095348	0.566786
ww.kegg.jp/kegg-bin/show_pathway? mmu00561+2355	Glycerolipid metabolism	61	3	0.479154	6.261034	0.0120409	0.566786
tp://www.kegg.jp/kegg-bin/show_pathway? mmu04964+	Proximal tubule bicarbonate reclamation	22	2	0.17281	11.573427	0.0126837	0.566786
g.jp/kegg-bin/show_pathway? mmu04145+12845+1499	Phagosome	181	5	1.421752	3.516787	0.0135801	0.566786
p://www.kegg.jp/kegg-bin/show_pathway? mmu00790+1	Folate biosynthesis	26	2	0.20423	9.792899	0.0174897	0.566786
ww.kegg.jp/kegg-bin/show_pathway? mmu04976+1384	Bile secretion	71	3	0.557704	5.379198	0.018093	0.566786
://www.kegg.jp/kegg-bin/show_pathway? mmu00650+2	Butanoate metabolism	27	2	0.212085	9.430199	0.0187942	0.566786

Significantly differential expressed genes in Pancreatic secretion

Stable IDs	Feature_gene_name	baseMean	pvalue	padj	FoldChange
ENSMUSG00000041193.15	Pla2g5	327.6929	0	0	21.6047666
ENSMUSG00000007107.6	Atp1a4	258.5906	0	0.000001	4.8748642
ENSMUSG00000071553.10	Cpa2	196.022	0	1.2E-06	3.7086972
ENSMUSG00000020431.5	Adcy1	104.9107	0.00022	0.020501	0.3598145
ENSMUSG00000001225.12	Slc26a3	29.11604	0.00024	0.021209	3.9715976

Significantly differential expressed genes in Thiamine metabolism

Stable IDs	Feature_gene_name	baseMean	pvalue	padj	FoldChange
ENSMUSG00000026817.14	Ak1	1358.032	0.000292	0.023143	2.018769
ENSMUSG00000028766.10	Alpl	237.0382	0.000518	0.034247	2.843773

Significantly differential expressed genes in Neuroactive ligand-receptor interaction

Stable IDs	Feature_gene_name	baseMean	pvalue	padj	FoldChange
ENSMUSG00000056380.13	Gpr50	56.43242	1.47E-05	0.003859	571.2601672
ENSMUSG00000040495.4	Chrm4	14.01271	2.69E-05	0.005626	25.0694979
ENSMUSG00000043017.9	Ptgir	400.5867	5.13E-05	0.008149	2.345606
ENSMUSG00000044338.9	Aplnr	803.3216	0.00076	0.04297	2.7616563
ENSMUSG00000021478.6	Drd1	52.58807	0.0009	0.048217	0.2768258
ENSMUSG00000022041.10	Chrna2	169.0929	0.000918	0.048854	2.1544465
ENSMUSG00000045730.4	Adrb2	637.536	0.000944	0.049661	0.4256661

Significantly differential expressed genes in Staphylococcus aureus infection

Stable IDs	Feature_gene_name	baseMean	pvalue	padj	FoldChange
ENSMUSG00000069441.3	Dsg1a	61.66929	4E-07	0.000233	5.596025
ENSMUSG00000061928.6	Dsg1b	20.82076	2.61E-05	0.00562	19.302742
ENSMUSG00000026580.16	Selp	210.5568	0.00073	0.04214	2.465355

Significantly differential expressed genes in Glycerolipid metabolism

Stable IDs	Feature_gene_name	baseMean	pvalue	padj	FoldChange
ENSMUSG00000024768.5	Lipf	231.5996	0	0	16.1785033
ENSMUSG00000012187.13	Mogat1	674.7383	0.000242	0.021213	0.4207309
ENSMUSG00000020258.16	Glyctk	130.4926	0.000281	0.022637	2.285067

Significantly differential expressed genes in Proximal tubule bicarbonate reclamation

Stable IDs	Feature_gene_name	baseMean	pvalue	padj	FoldChange
ENSMUSG00000007107.6	Atp1a4	258.5906	0	0.000001	4.874864
ENSMUSG00000010064.15	Slc38a3	708.3462	0.000883	0.048032	2.559326

Significantly differential expressed genes in Phagosome

Stable IDs	Feature_gene_name	baseMean	pvalue	padj	FoldChange
ENSMUSG00000031849.9	Comp	138.805	0.000068	0.009699	2.5941413
ENSMUSG00000020695.14	Mrc2	2506.892	0.00012	0.013829	2.7056454
ENSMUSG00000067201.11	H2-M9	240.8505	0.000181	0.017773	0.4219105
ENSMUSG00000028238.6	Atp6v0d2	208.2672	0.000195	0.018484	4.0684324
ENSMUSG00000026390.7	Marco	155.7569	0.000613	0.037129	2.3528541

Significantly differential expressed genes in Folate biosynthesis

Stable IDs	Feature_gene_name	baseMean	pvalue	padj	FoldChange
ENSMUSG00000006764.8	Tph2	959.1933	1E-07	5.16E-05	22.049261
ENSMUSG00000028766.10	Alpl	237.0382	0.000518	0.034247	2.843773

Significantly differential expressed genes in Bile secretion

Stable IDs	Feature_gene_name	baseMean	pvalue	padj	FoldChange
ENSMUSG00000007107.6	Atp1a4	258.5906	0	0.000001	4.8748642
ENSMUSG00000038776.13	Ephx1	4746.016	9.4E-06	0.002761	2.0548225

Significantly differential expressed genes in Butanoate metabolism

Stable IDs	Feature_gene_name	baseMean	pvalue	padj	FoldChange
ENSMUSG00000057880.12	Abat	3895.093	1E-07	4.84E-05	2.4992921
ENSMUSG00000030972.6	Acsm5	1971.103	0.000482	0.032604	0.4485598

Appendix C: Supplemental Figures for Chapter 3

A

```
                    ATP10A Peptide 1   ATP10A Peptide 3
hATP10A ---RRRRREGRTR---T-VRSNLLP--PPGAEDPAAGAAKGERR----------RRRGC   55
rATP10A -----AGRAGRAR-----CAPNCCR--PPGAEDSAAGAAKGERRPRR--------RLRGC   47
mATP10A RRPRRRRWEGRTR---T-VRSNLLP--PLGTEDSTIGAPKGER---L--------LMRGC   59
hATP10B HRWQWRVRDGFPH-----CPSETTPLLS--PEKGRQSYNLTQQRVVFPNNSIFHQDWEEV   62
mATP10B LRWKWRTQDGFSQ-----SPSETTPLLS--PETDRQSHNTAEQRVVYPNNSMCHQDWKKV   62
mATP10D ARHHWRRLSHGRAQGEDERPYNYASLLACGGKSSRTPRPAGKHRVVIPHLQCFKDEYERF   120
hATP10D ARYHWRRLIRGATRDDDSGPYNYSSLLACGRKSSQTPKLSGRHRIVVPHIQPFKDEYEKF   67
                                ATP10A Peptide 5
hATP10A G-SVSQRGS-------------IGSHQSVRVVHRTQSTKSHRRTGSRAEAKRASMLSKH   520
rATP10A N-TVSQRGS-------------IGSHQSIRIMSRSQSTRSHRRTGSRAEARRASILSKH   512
mATP10A G-TISHRGS-------------TGSHQSIWMTHKTQSIKSHRRTGSRAEAKRASMLSKH   524
hATP10B CLSFSARWAQDPATMRSQKGAQPLRRSQSARVP-----IQGH--YRQRSMGHR-ESSQPP   533
mATP10B CLSFPPRWAQGSTTMRSQGGAQPLRRCHSARVP-----IQSH--CRQRSVGRW-ETSQPP   533
mATP10D GGSLSNMARPRAQGCRT-VPSGPLGK-PSAQLS-----GSTS--AVGNGEGSGEVPHSRQ   590
hATP10D SGSLSNMAKPRAPSCRT-VHNGPLGNKPSNHLA-----GSSF--TLGSGEGASEVPHSRQ   538
```

B

ATP10A Peptides	1	3	5
Amino acid number	27-38	41-53	498-509
Amino acid sequence	RTRTVRSNLLPP	TEDSTIGAPKGER	HKTQSIKSHRRT

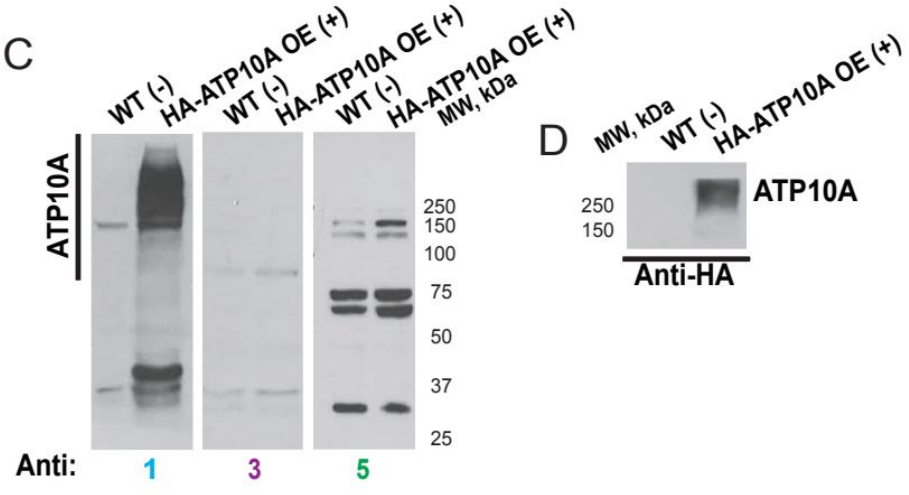

Supplemental Figure 9. Validation of ATP10A antibody: expression of ATP10A in HeLa cells with over-expressed HA-ATP10A. (A) Alignments of human (h), rat (r), and mouse (m) ATP10A, ATP10B, and ATP10D created using Clustal Omega with the ATP10A peptides that were chosen for antibody production highlighted. These peptides were chosen based on conservation between mouse and human ATP10A orthologs and lack of conservation with ATP10B and ATP10D paralogs. (B) Table indicating the sequences of the ATP10A peptides that were injected into rabbits to produce antibodies, peptides are color-coded according to the colors of the peptides in (A). (C,D) Representative images of total cell lysates from HeLa cells with (+) or without (-) over-expressed (OE) human HA-ATP10A (40 µg total protein) that were subjected to Western immunoblot analyses for expression of ATP10A using antibody produced against (C) ATP10A peptides or (D) HA. Peptides are color-coded according to the colors of the peptides in (A).

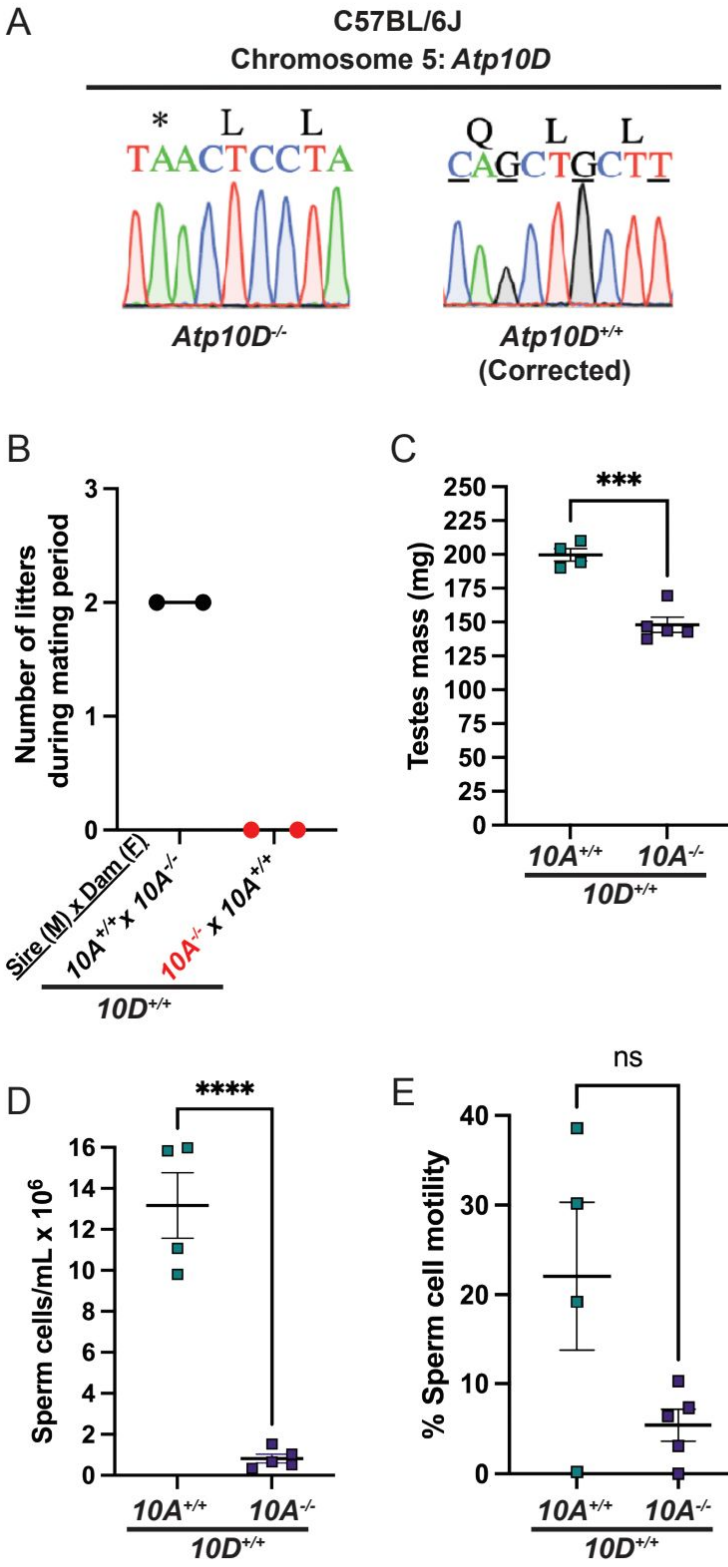

Supplemental Figure 10. Reintroduction of *Atp10D* does not rescue infertility, smaller testes, or low sperm cell count in *Atp10A* deficient mice. (A) Sequencing was performed to validate the genotype of the *Atp10D* mice. Briefly, CRISPR was used to replace the premature stop codon found in the *Atp10D* sequence in C57BL/6J mice (*, *Atp10D*$^{-/-}$ mice) to glutamine that is found in other mouse strains (Q, *Atp10D*$^{+/+}$ (corrected) mice). The underlined nucleotides indicate CRISPR-mediated changes to the DNA sequence, for the purposes of changing the amino acid or introducing restriction digest cut sites for genotyping purposes. (B) Mating studies were done by housing pairs of mice together (without separating) for approximately 9 weeks and recording the number of litters produced. (See supplemental table 1 for more details). (C) The wet mass of testes was measured in 14-21-week-old mice, ***P=0.0002. (D) Sperm cells collected from the caput epididymis were counted using a hemocytometer, ****P<0.0001. (E) % Sperm cell motility was measured using the equation: motile sperm/total sperm counted. P-value by unpaired t-test.

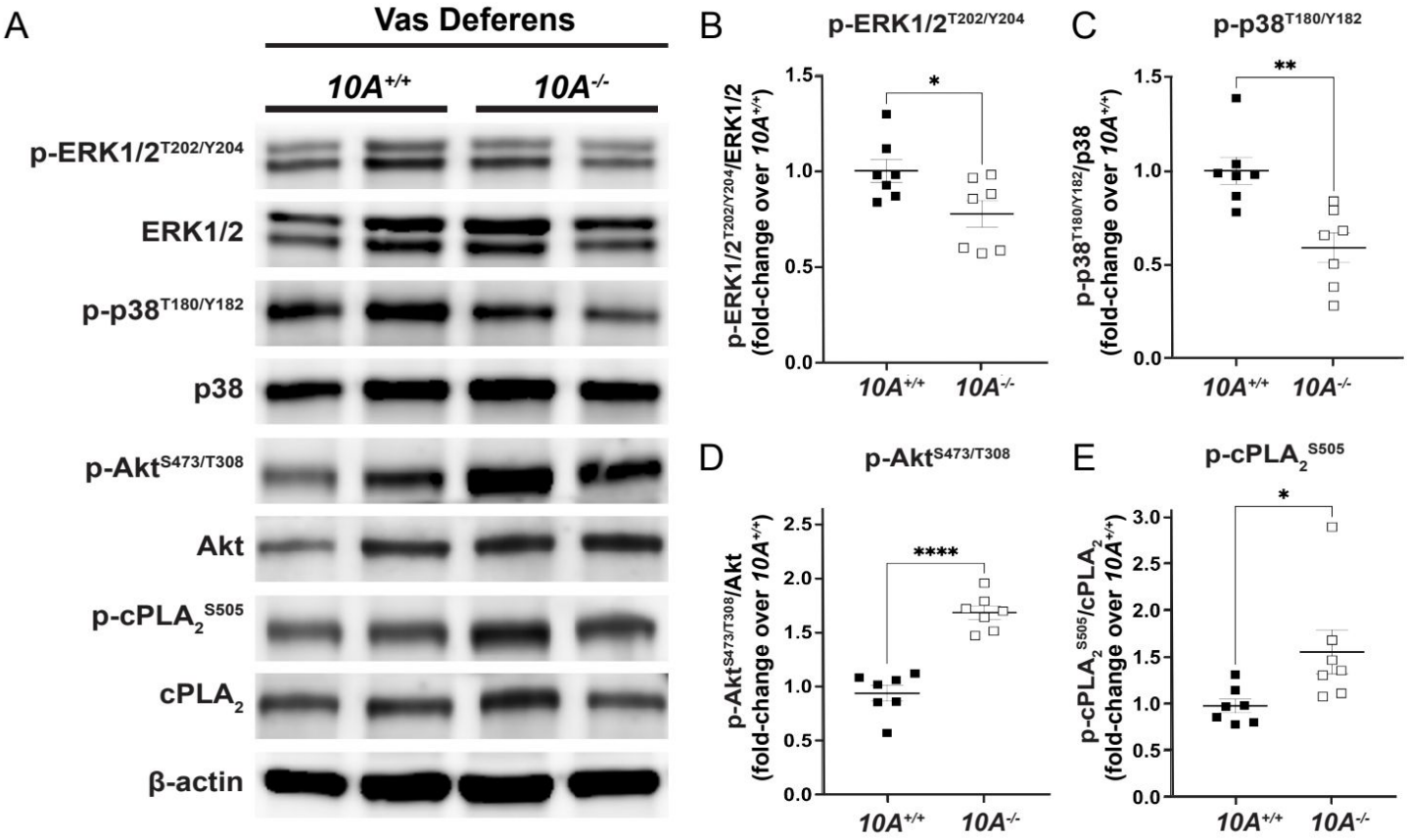

Supplemental Figure 11. *Atp10A* deficiency results in changes to signaling in the vas deferens. Total tissue lysates from vas deferens from the *10A*$^{+/+}$ and *10A*$^{-/-}$ mice were subjected to Western immunoblot analysis. (A) Representative blots for total and/or phosphorylated ERK1/2, p38, Akt, and cPLA$_2$. (B-E) The phosphoproteins were normalized to their respective total protein, β-actin levels, and total protein from *10A*$^{+/+}$ samples. Mean measurements of 4-6 independent experiments are shown. P value by unpaired t-test. (*10A*$^{+/+}$ n=7, *10A*$^{-/-}$ n=7, B: *P=0.0313, C: **P= 0.0024, D: ****P<0.0001, E: *P=0.0376).

Appendix D. Supplemental Table for Chapter 3

Supplemental Table 3

Figure 9 (all 10D -/-)	***10A+/+ (WT)***	***10A-/- (KO)***
(A) Vas deferens WB		
n	1	1
Body mass at sacrifice (g)	*did not measure*	*did not measure*
Age at sacrifice (weeks)	7	8
Outliers removed by ROUT analysis	N/A	N/A
(B) Testes WB		
n	1	1
Body mass at sacrifice (g)	23	24
Age at sacrifice (weeks)	8	8
Outliers removed by ROUT analysis	N/A	N/A
(C) Vas deferens IF		
n	1	2
Avg. body mass at sacrifice (g)	26	28.5
Avg. age at sacrifice (weeks)	11	15
Outliers removed by ROUT analysis	N/A	N/A
(D) Testes IF		
n	2	2
Avg. body mass at sacrifice (g)	27.5	28.5
Avg. age at sacrifice (weeks)	17	17
Outliers removed by ROUT analysis	N/A	N/A

(E) Mating studies	Red text= Sire is 10A -/-	
Order: Sire (M) x Dam (F)	**Average time parents housed together (weeks)**	**Average pups per litter**
10A +/+ x 10A +/+ (1 pair)	20.9	6
10A +/+ x 10A -/- (2 pairs)	6.6	5
10A -/- x 10A +/+ (3 pairs)	9.8	N/A
10A +/- x 10A -/- (1 pair)	19.6	6
10A -/- x 10A +/- (3 pairs)	15.9	8.5
10A +/- x 10A +/- (5 pairs)	12	7.1
10A -/- x 10A -/- (3 pairs)	10.9	N/A

Figure 10 (all 10D -/-)	***10A+/+ (WT)***	***10A+/- (Het)***	***10A-/- (KO)***
(A) Testes mass (mg), (B), Sperm cells/mL, (C) % sperm cell motility			
n	9	2	14
Avg. body mass at sacrifice (g)	26.8	25	26.7
Avg. age at sacrifice (weeks)	13.8	10.5	12
Outliers removed by ROUT analysis	0	0	0

Figure 11 (all 10D -/-)	***10A+/+ (WT)***	***10A-/- (KO)***
(C) Seminiferous tubule scoring		
n	6	12
Avg. body mass at sacrifice (g)	26	26.8
Avg. age at sacrifice (weeks)	12.2	11.6
Outliers removed by ROUT analysis	N/A	N/A

Figure 12 (all 10D -/-)	***10A+/+ (WT)***	***10A-/- (KO)***
(B) Plasma T		
n	16	18
Avg. body mass at sacrifice (g)	33.5	33.8
Avg. age at sacrifice (weeks)	14.1	15.4
Outliers removed by ROUT analysis	3	1
(C) LH	***10A+/+ (WT)***	***10A-/- (KO)***
n	11	17
Avg. body mass at sacrifice (g)	26	27
Avg. age at sacrifice (weeks)	11.5	11.1
Outliers removed by ROUT analysis	0	1
(D) FSH	***10A+/+ (WT)***	***10A-/- (KO)***
n	11	18
Avg. body mass at sacrifice (g)	26	27
Avg. age at sacrifice (weeks)	11.5	11.1
Outliers removed by ROUT analysis	1	0
(E) Inhibin B	***10A+/+ (WT)***	***10A-/- (KO)***
n	11	15
Avg. body mass at sacrifice (g)	26	27.3
Avg. age at sacrifice (weeks)	11.5	11.1
Outliers removed by ROUT analysis	0	0

Figure 13 (Testes, all 10D -/-)	***10A+/+ (WT)***	***10A-/- (KO)***
n	6-8	6-8
Avg. body mass at sacrifice (g)	27.4	28
Avg. age at sacrifice (weeks)	14.5	14.1
Outliers removed by ROUT analysis	0	LHR: 1, pAkt: 1

Supplemental Figure 10 (All 10D +/+)		
(A) Mating studies	Red text= Sire is 10A -/-	
Order: Sire (M) x Dam (F)	**Average time parents housed together (weeks)**	**Average pups per litter**
10A +/+ x 10A -/- (2 pairs)	8.9	5.8
10A -/- x 10A +/+ (2 pairs)	9.1	N/A
(B,C,D) Testes mass, Sperm cells/mL, sperm cell motility	***10A+/+, 10D +/+***	***10A-/-, 10D +/+***
n	4	5
Avg. body mass at sacrifice (g)	29.8	29.4
Avg. age at sacrifice (weeks)	18.5	17.8
Outliers removed by ROUT analysis	0	0

Supplemental Figure 11 (Vas deferens, all 10D -/-)	***10A+/+ (WT)***	***10A-/- (KO)***
n	4-7	4-7
Avg. body mass at sacrifice (g)	15.4	15
Avg. age at sacrifice (weeks)	27.9	28.6
Outliers removed by ROUT analysis	0	0

Appendix E: Supplemental Figure for Chapter 5

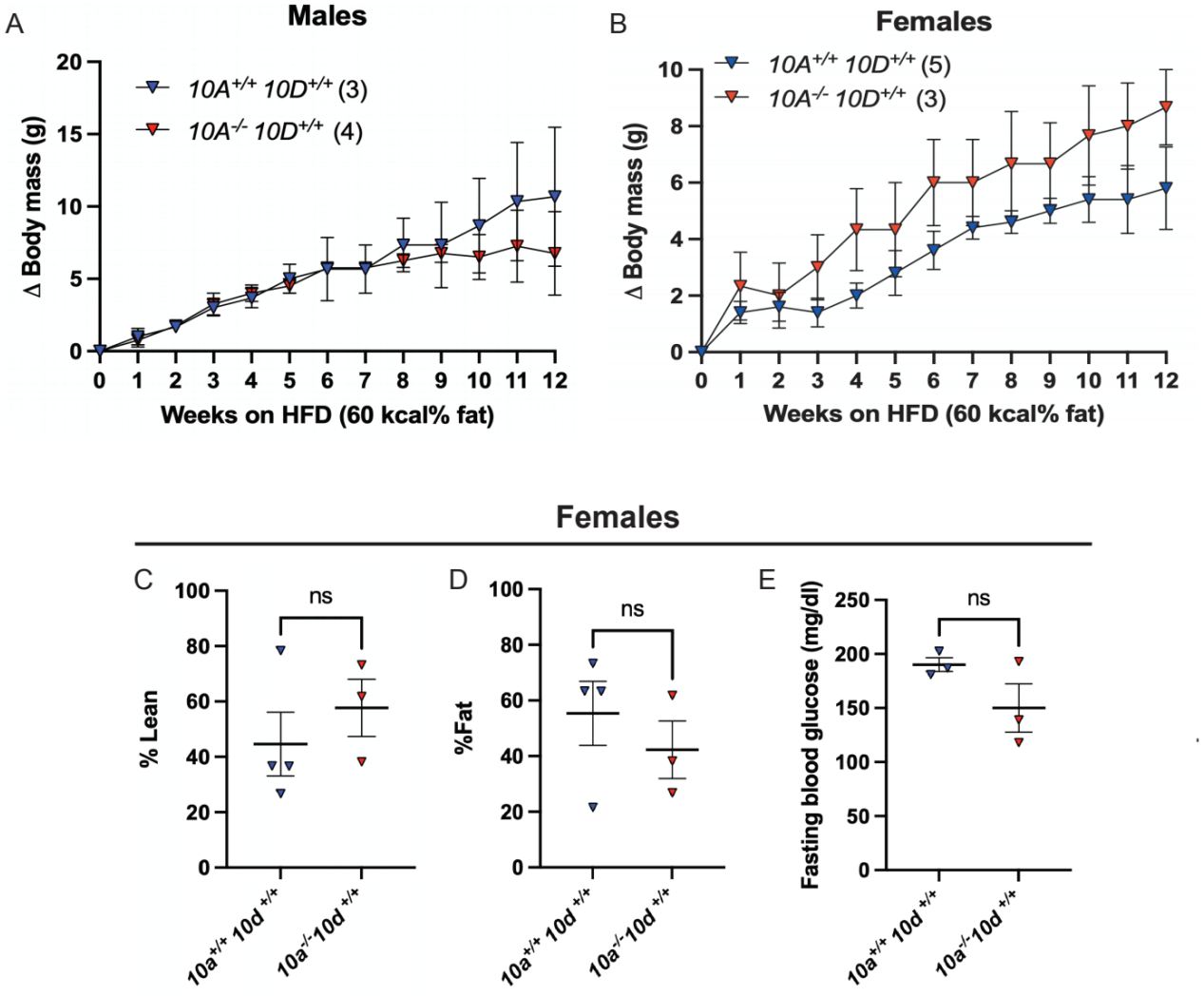

Supplemental Figure 12. Metabolic parameters in the 10A Deficient, 10D Correction mouse model (A, B) Weight gain of (A) male and (B) female *10A*$^{+/+}$*10D*$^{+/+}$ and *10A*$^{-/-}$*10D*$^{+/+}$ over the course of 12 weeks on a HFD (60 kcal% fat, Ad lib feeding). P value by 2-way ANOVA with Sidak's multiple comparison. (C) Lean and (D) fat body mass were normalized to the sum of lean mass and fat mass to calculate % Lean and % Fat mass (*10A*$^{+/+}$*10D*$^{+/+}$ n=4, *10A*$^{+/+}$*10D*$^{-/-}$ n=3). (E) Fasting blood glucose was measured after a 5 hour fast, via a glucometer (*10A*$^{+/+}$*10D*$^{+/+}$ n=3, *10A*$^{+/+}$*10D*$^{-/-}$ n=3). (C-E) P value by unpaired t-test. Average body mass (g) at end of HFD: Males: *10A*$^{+/+}$*10D*$^{+/+}$: 36 g, *10A*$^{-/-}$*10D*$^{+/+}$: 33.3 g, Females: *10A*$^{+/+}$*10D*$^{+/+}$: 24.5 g, *10A*$^{+/+}$*10D*$^{+/+}$: 29 g

Appendix F: Supplemental Tables for Chapter 6

Supplemental Table 4

	Primer sequence (5' to 3')	
Target	**F**	**R**
Pla2g5	TGG GGT TCT GAG ATG TCA CT	TCT TCC TCC TGT CTT GTT GC
SCD1	CTGTACGGGATCATACTGGTTC	GCCGTGCCTTGTAAGTTCTG
LPL	TGG CAT AAG TCA GGT CCA TT	GAG CCA TGT CTT CAA CTG CT
Pla2g6	ATC CAC ACA GCC ATG AAG TT	TGT TCC CTG AGG AGC TAG TG
FAS	GCGATGAAGAGCATGGTTTAG	GGCTCAAGGGTTCCATGTT
DGAT1	CCA GGT GGT GTC TCT GTT TC	AGA TGA TTG TGG CCA GGT TA
DGAT2	CTGTGCTCTACTTCACCTGGCT	CTGGATGGGAAAGTAGTCTCGG
PPARa	GCCTGTCTGTCGGGATGT	GGCTTCGTGGATTCTCTTG
PPARg	GCCCTTTGGTGACTTTATGGA	GCAGCAGGTTGTCTTGGATG
LXRa	CCGACAGAGCTTCGTCC	CCCACAGACACTGCACAG
Srebpc1	CGCGGAAGCTGTCGGGGTAG	AAATGTGCAATCCATGGCTCCGTGGTC
CGI58	GGT TAA GTC TAG TGC AGC	AAG CTG TCT CAC CAC TTG
Cyp7a1	cca ggg aga tgc tct gtg ttc AGCAACTAAACAACCTGCCAGTAC TA	acc cag aca gcg ctc ttt gat GTCCGGATATTCAAGGATGCA
Cyp8b1	GCCTTCAAGTATGATCGGTTCCT	GATCTTCTTGCCCGACTTGTAGA
Hprt1 (housekeeping gene)	GCTGACCTGCTGGATTACAT	TTGGGGCTGTACTGCTTAAC

Supplemental Table 5

Visceral Fat, Females, 12 weeks after HFD feeding									
qPCR results						RNA sequencing results (*10A+/+ n*= 3, *10A-/-* n=3)			
	Sample size (n)								
Target	***10A+/+***	***10A-/-***	**p-value (unpaired t-test of Relative mRNA level (2^-ΔΔCq))**	**Significant (Y or N)**		**Target**	***log2FoldChange***	**p-value**	**Significant (Y or N)**
Pla2g5	2	4	0.2526	N		Pla2g5	4.433277742	2.03E-17	Y
SCD1	2	4	0.8275	N		SCD1	0.355620653	0.242335	N
LPL	3	4	0.7678	N		LPL	0.294114678	0.123495	N
Pla2g6	3	4	0.8143	N		Pla2g6	0.234601663	0.309316	N
FAS	3	4	0.9077	N		FAS	-0.099676899	0.588441	N
DGAT1	3	4	0.6299	N		DGAT1	0.017153228	0.933198	N
DGAT2	3	4	0.6174	N		DGAT2	0.439107779	N/A	N/A
PPARa	2	4	0.3831	N		PPARa	not found in data	---	---
PPARg	3	4	0.3658	N		PPARg	not found in data	---	---
LXRa	3	4	0.824	N		LXRa	not found in data	---	---
SREBP-1C	2	4	0.824	N		Srebpc1	not found in data	---	---
CGI58	2	4	0.824	N		CGI58	not found in data	---	---
Liver qPCR Results, Females, 12 weeks after HFD feeding									
	Sample size (n)								
Target	***10A+/+***	***10A-/-***	**p-value (unpaired t-test of Relative mRNA level (2^-ΔΔCq))**	**Significant (Y or N)**					
PPARg	4	4	0.0474	Y *					
FAS	4	3	0.0067	Y **					
SCD1	4	5	0.4074	N					
Cyp7a1	4	4	0.7601	N					
Cyp8b1	4	4	0.1477	N					
LPL	4	3	0.2685	N					